Self-consistent predictions of electromagnetic and gravitational wave stellar transients

Max Merlijn Briel

Department of Physics
The University of Auckland

A thesis submitted in fulfilment of the requirements for the degree of Doctor of Philosophy in Physics, the University of Auckland, 2023.

July 2023

Abstract

Since 2015 gravitational-wave (GW) observations have provided valuable insight into the properties of the merging binary black hole (BBH) population. The most striking features of the observed primary black hole mass distributions are the extended tail up to $100\,M_\odot$ and an excess of masses at $35\,M_\odot$. However, traditional isolated binary population synthesis has difficulty explaining these two features.

To address this uncertainty, we have created a synthetic population of stellar transients using the detailed binary population synthesis, BPASS, and star formation histories (SFH) based on observations and cosmological simulations. This self-consistent approach allows for the prediction of multiple observables from the same population, providing robust constraints on the implemented stellar evolution. We are able to match supernova (SN) and GW observations simultaneously. Furthermore, various types of transients, including Type Ib/c and pair-instability SNe, probe the metallicity of star formation, while Type Ia SNe probes older star formation regions. The comprehensive matching of observations from a single cosmic population further validifies our approach.

In addition to matching the SN observations, the synthetic population reproduces the observed BBH mass distribution features, although not through the traditionally expected mechanisms of pulsational pair-instability. Instead, we identify the stability of mass transfer, quasi-homogenous evolution, and stellar winds as essential processes to reproduce the $35\,M_\odot$ excess, whilst the extended tail results from super-Eddington accretion during stable mass transfer at high mass ratios onto a black hole. These key features are independent of the SFH and remnant mass prescription, including (pulsational) pair-instability SNe. However, the $35\,M_\odot$ peak is redshift dependent and disappears at high redshift due to the delay time distribution of the formation channel.

Since the mass transfer stability allows for both features to occur, we explore this in detail and show that other binary population synthesis codes do not accurately capture it, thus missing the features in their populations. Future population synthesis codes should include detailed prescriptions for mass transfer and make predictions for multiple observables to constrain their implemented physics.

Acknowledgments

Writing acknowledgments is always a difficult taks, because you meet many people along the way who are amazing! I will start by thanking Jan for her guidance, support and kindness over the past three years. From my basic astronomy to critical science questions, never did I feel judged for expressing those thoughts and I feel very fortunate to have her as my PhD supervisor for the past few years. Without the guidance and advice from Heloise, this thesis would have taken much longer than it did. She helped me find my way in research and provided new perspectives in science and life when I needed them. Thank you for your support and guidance!

Of course, I want to thank all the people in the Stars and Supernovae group in Auckland for their ideas, science discussion, and banter during the course of my PhD. Although many people came and went, I want to thank the fellow PhDs Sean, Petra, and Sohan for their help and insights, but also for introducing me to Dungeons and Dragons.

There are so many nice people in the department of whom I want to say thank you to Darcey, Emma, Carlie, Liam, Caitlin, and many more. You made me feel welcome when I arrived to New Zealand and part of the physics community, even when we were stuck at home.

Finally, as well a thank you for my family, who I couldn't see for most of my PhD due to the COVID-19 pandemic. I've missed you but our consistent weekly calls have been a highlight throughout. And thank you Ana for being there through thick and thin.

Ik houd van jullie!

Contents

List of Figures

List of Tables

Chapter 1

Introduction

The night sky has fascinated humans for millennia and has fuelled mythologies all over the world, with origin stories dating back to the third millennium B.C. (Tassoul & Tassoul 2004). The earliest surviving records of events in the night sky date back to ∼1300 B.C.E. in present-day China, where bones were used to track solar eclipses. During the Middle Ages, the European view of the night sky was geocentric and the stars were considered static, even though sufficient evidence was available to the contrary (Tassoul & Tassoul 2004). While progress in Europe halted during this time, the Middle Eastern, Asian, and Pacific astronomy continued to record and explore the night sky. Although, eventually, in Europe, the Sun took center stage in our solar system, new questions about its heat source arose in the mid-19th century with the introduction of energy conservation in thermodynamics. For the Sun to continue shining, its energy had to originate from somewhere; otherwise, it would eventually stop shining. One of the first mechanical ideas was heating due to the gravitational energy of meteors falling into the Sun, as suggested by Mayer and Helmholtz (see references in Shaviv 2008; Kragh 2016). However, the mass required to heat the Sun sufficiently would drastically influence the orbits of the inner planets including the Earth. With no such evidence, Helmholtz concluded that the Sun must be losing its energy by contraction; an idea later adopted by Thomson, also known as Lord Kelvin (Helmholtz 1856; Thomson 1862). By contracting, the Sun converts gravitational energy into heat, and one can calculate the amount of radial shrinkage required to maintain the current solar luminosity. Although the calculations done by Helmholtz and Thomson assumed a liquid Sun, the proper gaseous calculation was done by Ritter in 1898 but provided a similar result (Ritter 1898). The time it takes for a star to radiate away its kinetic energy, which is now known as the Kelvin-Helmholtz or thermal timescale, is described by

$$\tau_{\rm KH/thermal} \approx \frac{\rm GM^2}{\rm 2RL} \approx 2\times10^7\,{\rm yr}\frac{({\rm M/M_\odot})^2}{({\rm R/R_\odot})({\rm L/L_\odot})}, \tag{1.1}$$

where M, R, and L are the mass, radius and luminosity of the star, and G is the gravitational constant. Performing the calculation using the solar properties ($_\odot$), we find an age of 20 million years for the Sun, which is at odds with the 4.5 billion year age of the Earth (Dalrymple 1991). Although, nowadays, we know the Sun is not powered by contraction, Equation 1.1 remains relevant in some stellar evolution phases, which we will discuss later in this thesis. Besides the age discrepancy, the Helmholtz-Thomson contraction would also require the Sun and other stars to shrink, contrary to any observations (Eddington 1917).

Despite the empirical evidence against the contraction theory, it was the preferred explanation in stellar physics for many years until significant improvements in nuclear physics were made. In 1939, Bethe formalised the theory of stellar energy production through hydrogen fusion into helium (Bethe 1939a,b; Bethe & Marshak 1939). We can calculate the age of the Sun with hydrogen fusion as the energy source following

$$\tau_{\rm nuc} \approx \frac{\rm M \times \mathit{X}}{\rm L/Q} \times 0.1 \approx 10^{10}\,{\rm yr}\frac{\rm (M/M_\odot)}{\rm (L/L_\odot)}, \tag{1.2}$$

where M and L are the mass and luminosity of the star, respectively, X is the hydrogen fraction, and Q is the amount of energy released per fusion. Approximately 10% of stellar matter can undergo fusion into helium, resulting in the factor of 0.1.

The process of fusion provides sufficient energy for the Sun to shine for more than 10 billion years; an age compatible with the age of the Earth. Observations of solar neutrinos produced during fusion provided the first direct proof for nuclear fusion as the energy source for the Sun and other stars (Bahcall 1964; Davis 1964; Ahmad et al. 2002). Nowadays, we know that stars are self-luminous bodies that are created, live, and die; our Sun being one of them.

The energy released from fusion creates an outwards pressure in the star that counteracts the inwards gravitational force. This is a self-regulating mechanism, known as hydrostatic equilibrium and is described by

$$\frac{dP}{dr} = -\frac{Gm(r)}{r^2}\rho(r), \tag{1.3}$$

where dP/dr describes the pressure change over the radius of the star, and $\rho(r)$ and $m(r)$ are the density and mass of the star at radius r from the centre of the star. If the gravitational force increases, the star shrinks, increasing the density and temperature in the center, leading to an increase in the outwards pressure. This is the first equation of stellar structure.

$$\tau_{\rm dyn} \approx \left(\frac{\rm R^3}{\rm GM}\right)^{1/2} \approx 5\,\text{minutes} \left(\frac{(\rm R/R_\odot)^3}{(\rm M/M_\odot)}\right)^{1/2} \tag{1.4}$$

describes the timescale at which the star responds to a change from this equilibrium and is known as the dynamical timescale, which is of the order of minutes for the Sun. In most cases, $\tau_{\rm nuc} \gg \tau_{\rm thermal} \gg \tau_{\rm dyn}$ holds.

1.1 Stellar Evolution

Stars are formed through the collapse of gas clouds, with the exact process being an active area of research (see McKee & Ostriker 2007, and references therein). During the collapse, the cloud heats until, at the center, densities and temperatures for hydrogen fusion are reached. Hydrogen ignition, also known as the zero-age main sequence (ZAMS), marks the start of the main-sequence, where hydrogen fusion is the primary energy source.

The time to reach the ZAMS is approximately the thermal timescale, as described by Equation 1.1. At the ZAMS, the star contains mainly hydrogen and helium with small amounts of other elements. The mass fraction of these heavier-than-helium elements is referred to as metallicity (Z). In our Sun, this is observed to be $Z_\odot \approx 0.014$, where $X + Y + Z = 1$ with X, Y being the hydrogen and helium fractions of 0.7438 and 0.2433, respectively (Asplund et al. 2009, 2021; Magg et al. 2022). The fraction of helium in the Sun is higher than in a ZAMS star since it has already fused hydrogen into helium for several billions of years.

The star spends nearly 90% of its life on the main-sequence, continuously fusing effectively four hydrogen nuclei into one helium nucleus. This is also referred to as 'hydrogen burning' and occurs predominantly through the proton-proton (PP) chain or carbon-nitrogen-oxygen (CNO) cycle, depending on the temperature and density of the given star. Moreover, if the stellar metallicity is low, the fraction of carbon is low, preventing the CNO cycle from functioning effectively (for more details, see stellar evolution textbooks, such as Salaris 2005; Kippenhahn et al. 2013; Eldridge & Tout 2019).

The energy produced by fusion in the star is equal to the energy loss at its surface, which is known as thermal equilibrium. If more energy is produced, the star expands, while if less is produced, the star contracts to maintain a similar luminosity. The star maintains a constant temperature, radius, and luminosity in thermal equilibrium. There are three main mechanisms through which the energy at the core of the star can be

transported to the surface, where it is radiated away: conduction, radiation, and convection.

Conduction, where hotter particles near the centre exchange energy with colder particles closer to the surface, is ineffective in a regular star due to its relatively low density. In radiative energy transport, photons carry the energy towards the surface instead. The distance the photons can travel is determined by the density and the absorption coefficient of the matter it travels through (κ), also known as the opacity. Due to a small mean free path of the photon, it takes about 170.000 years for a photon to leave the Sun through this diffusive process (Mitalas & Sills 1992). Regions within a star where this energy transport is dominant are referred to as radiative. However, radiative energy transport breaks down when the temperature gradient in the star becomes too large. This can occur because the opacity of the material is high or the energy generation is very localised, as is the case with the CNO cycle. Both cause energy to be transported through the bulk movement of hotter material upwards into cooler regions of the star, also known as convection. This process is very efficient in transporting the energy, as this is a dynamical timescale process compared to the slower thermal timescale radiative energy transport (see a review, such as Joyce & Tayar 2023)

Stars often contain radiative and convective regions, which depend on their mass, metallicity, and evolutionary phase. At the ZAMS, stars with $\mathrm{M} \lesssim 0.35\,\mathrm{M}_{\odot}$ are fully convective at solar metallicity (i.e. Chabrier & Baraffe 1997; Pols 2011; Kippenhahn et al. 2013). As a result of their low effective temperatures, the opacity of the stellar material is high, resulting in convection. With increasing mass, the temperature increases and only the outer regions of the star remain convective due to the high opacity, as shown in Figure 1.1. The PP-chain dominates the energy production in these low-mass stars, and the shallow temperature gradient keeps the central region radiative in the $M \lesssim 1.2\,\mathrm{M}_{\odot}$ regime. Above $\sim$1.2 $\mathrm{M}_{\odot}$, the CNO-cycle dominates the energy production (Kippenhahn et al. 2013). Due to the localised nature of the energy generation, the temperature gradient is steep, and convection is the dominant energy transport in the center of stars where the CNO-cycle is the dominant fusion process. As the total initial mass increases, the size of the central convective region increases further. As the ZAMS stars evolve, their structure changes further; the following sections cover the stellar evolution of stars at different masses and metallicities.

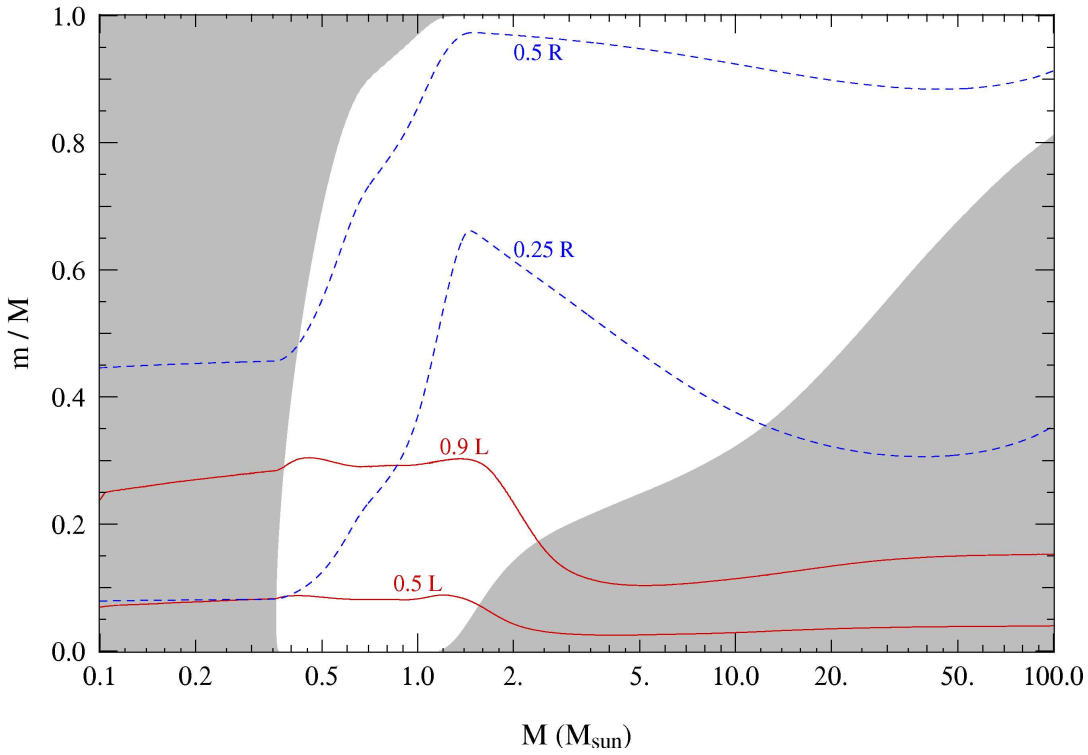

Figure 1.1: The ZAMS internal structure of over mass at a solar-like composition. The gray regions indicate energy transport through convection. The blue dashed lines indicate where 25% and 50% of the radius lies, while the solid red lines indicate the area where 50% and 90% of the luminosity is generated. Figure from Pols (2011).

1.2 Single Star Evolution

Direct observation of evolution in a given star is difficult due to its mass-dependent million- to billion-year timescale. As such, we require theoretical models to predict the past, future, and present of stars. Four fundamental differential equations are used to describe the stellar structure. Equation 1.3 is the first stellar structure equation, while the others are the equation of mass conservation, energy production, and radiation transport, which are respectively described by

$$\frac{dM(r)}{dr} = 4\pi r^2 \rho(r), \tag{1.5}$$

$$\frac{dL(r)}{dr} = 4\pi r^2 \rho(r) \epsilon(r), \tag{1.6}$$

$$\frac{dT(r)}{dr} = \frac{3\rho(r)\kappa}{64\pi r^2 \sigma T(r)^3} L(r), \tag{1.7}$$

where M, ρ, L, and T are the mass, density, luminosity and temperature of the star at radius r. ϵ, σ, and κ, on the other hand, describe the rate of energy generation, the Stefan-Boltzmann constant, and the absorption coefficient, respectively.

Although specific solutions exist for this system, numerical implementations are essential for solving these equations and evolving stars because no general analytical solution exists (for example, see Henyey et al. 1959; Eggleton & Tokovinin 2008; Kippenhahn et al. 2013). While stars spend most of their life on the main-sequence, their evolution diverge significantly based on their initial mass and metallicity.

In general, stellar evolution is divided into three categories based on the stellar mass: low-mass ($M_{ZAMS} \lesssim 2\,M_\odot$), intermediate-mass ($M_{ZAMS} \sim 2$—$8\,M_\odot$), and massive stars ($M_{ZAMS} \gtrsim 8\,M_\odot$). Stars below $0.08\,M_\odot$ cannot fuse hydrogen into helium and their gravitational energy is radiated away as a brown dwarf and are not considered in this thesis (Kumar 1963).

1.2.1 Low-Mass and Intermediate-Mass Stars

Low-mass and intermediate-mass stars both end their life as a white dwarf (WD), a compact object supported by electron-degeneracy pressure instead of fusion. However, their exact evolutionary pathways are slightly different. Initially, an intermediate-mass star will follow the evolution of a massive star (see Section 1.2.2) until the carbon-oxygen (CO) core becomes degenerate, after which it will follow the same evolution as a low-mass star. Instead of fusion, electron-degeneracy provides an outwards pressure inside electron-degenerate cores stopping the core from collapsing and can eventually result in a WD. Since our Sun with its $1\,M_\odot$ falls within the low-mass category, we will consider the evolution of a $1\,M_\odot$ star.

Figure 1.2 shows the evolution of the effective temperature and luminosity of a $1\,M_\odot$ star in a Hertzsprung-Russel (HR) diagram. The ZAMS is at **A**, where the star starts burning hydrogen through the PP-chain, which is dominant up to $1.1\,M_\odot$. It slowly increases luminosity and temperature during its main-sequence until hydrogen runs out in the core (**B**).

Figure 1.3 is a Kippenhahn plot that shows the internal structure of the star as it evolves. The green areas indicate convective energy transport, which is only at the surface during the main-sequence (**A** to **B**). The radius slowly expands during this main-sequence evolution, as shown in the Figure 1.2. Because the energy generation occurs through the PP-chain, the hydrogen burning smoothly transitions to a shell region above the core, known as the subgiant phase.

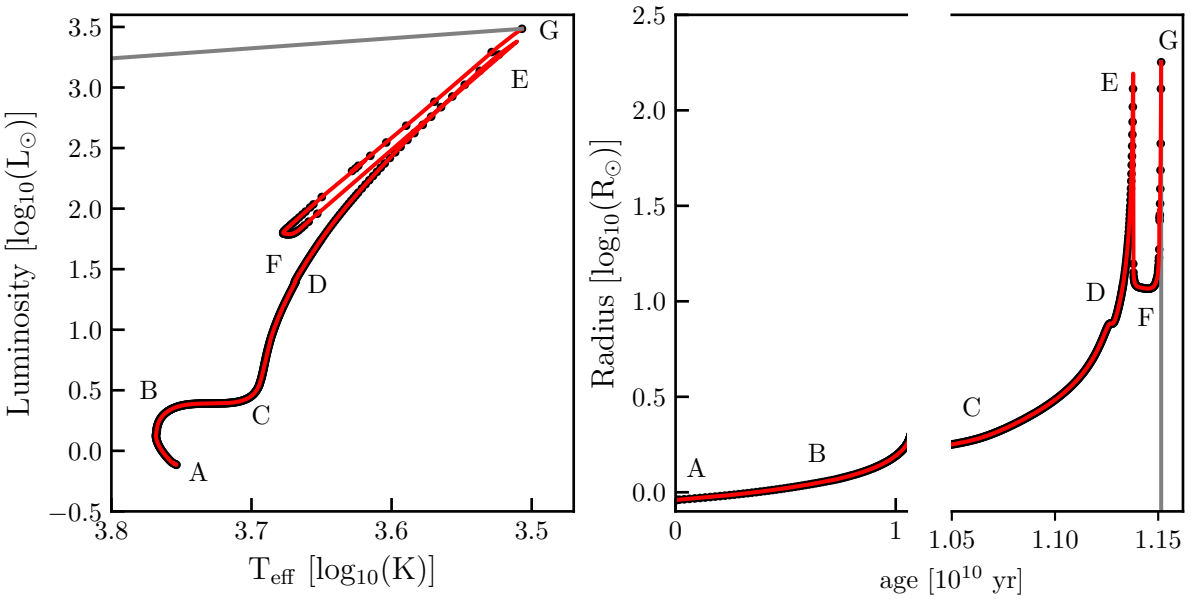

Figure 1.2: left: The HR diagram of a $1\,M_\odot$ star evolved through different stages of stellar evolution using the BPASS STARS code, as described in Section 2.1. right: The radial evolution of the same star. **A**-**G** indicate different evolutionary milestones. The red line is the detailed stellar model, while the grey line indicates the post-AGB approximation. The black dots are placed every 10^6 years to indicate where the star spends most of its time. The plot is split in two to allow for more detail in the later evolutionary phases.

Eventually, the star reaches the red giant branch (RGB) when the helium (He) core reaches $M = 0.1\,M_\odot$ (**C**) and has become degenerate. At the same time, the envelope has expanded and cooled significantly, allowing for convection to move helium to the surface and hydrogen to the shell-burning region, providing new fuel (**D**). This process is known as the first dredge-up. During the RGB, the star loses a significant amount of mass due to the opaqueness and extendedness of the envelope, while the core continues to grow to $0.45\,M_\odot$ to the tip of the red giant branch (**E**).

Due to the degenerate nature of the helium core, the helium ignition at $0.45\,M_\odot$ occurs in a runaway process known as the helium flash (Mestel 1952). The luminosity and radius of the star drop it to the horizontal branch (**F**). Eventually, helium is exhausted in the core too, and fusion moves to a shell around the CO core. Similar to the helium core, the CO core reaches a degenerate state, and the star evolves along the asymptotic giant branch (AGB) upwards to **G**.

The shell hydrogen and helium burning cause pulsations that eject much of the envelopes, which form a planetary nebula (see the review by Kwitter & Henry 2022). The star evolves towards the left side of the HR diagram, depicted as the grey line in Figure

1.2 becoming a CO white dwarf (CO WD). Lower mass stars that have lost their envelope on the RGB and did not undergo helium fusion can become He WD with $M \lesssim 0.45\,M_\odot$ However, the main-sequence lifetime of such stars is longer than the age of the Universe (Lequeux 2013). Consequently, most He WD result from binary interactions, which will be discussed in Section 1.3 (Rebassa-Mansergas et al. 2011; Brown et al. 2011). As we will see in Section 1.2.2, the CO core of massive stars does not become degenerate and can continue fusion to higher elements. However, some massive stars around $8\,M_\odot$ might undergo core carbon burning but form a degenerate oxygen-neon (ONe) WD with $M \gtrsim 1.2\,M_\odot$, which does not ignite. Since no nuclear fusion occurs inside a WD, it

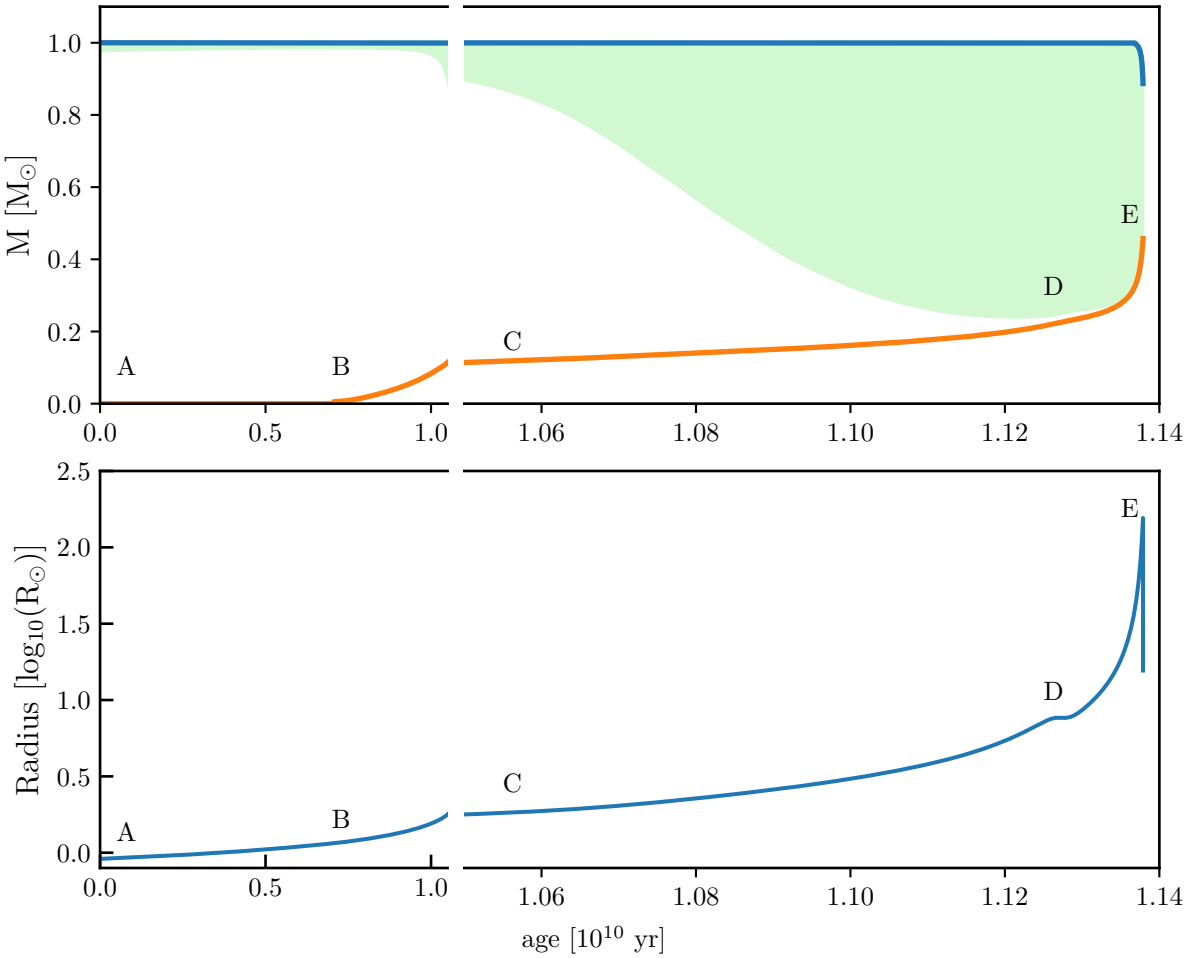

Figure 1.3: top: The internal structure of a $1\,M_\odot$ star displayed using a Kippenhahn diagram up to the helium flash (**E**). The blue and orange line indicate the total and helium core mass, respectively. Convective regions are shaded green. bottom: The radial evolution of the same star. The same as Figure 1.2 without the time indicators. The model ends at the helium flash due to numerical issues and is evolved using the BPASS STARS code, described in Section 2.1.

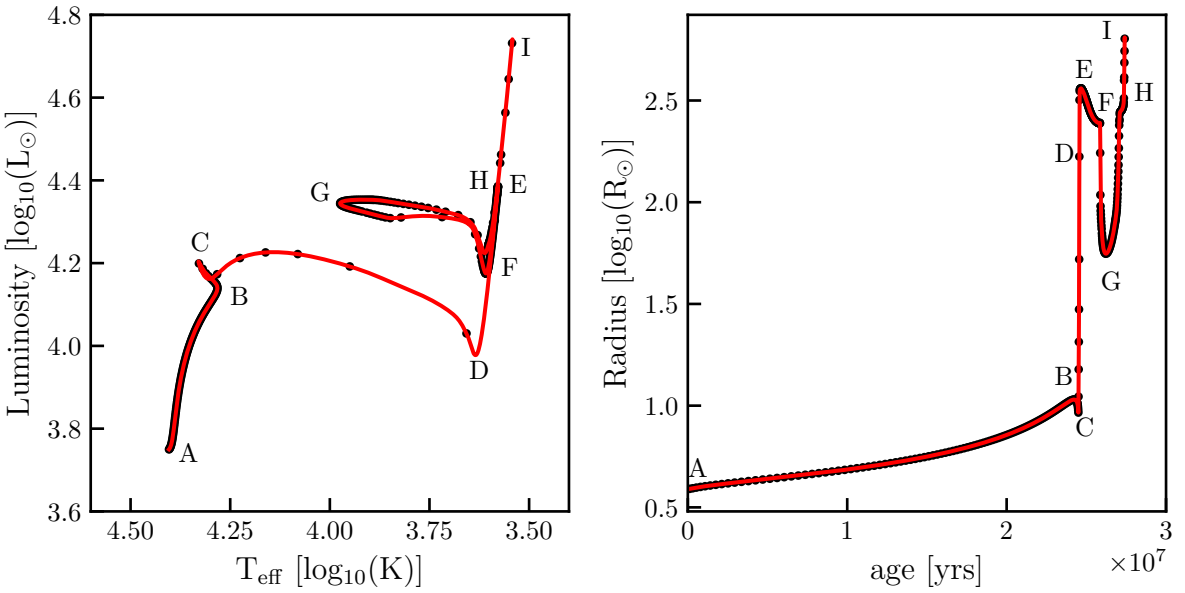

Figure 1.4: (left) The HR diagram of a $M_{ZAMS} = 10\,M_\odot$ star at $Z = 0.014$ metallicity evolved using the adapted Cambridge BPASS STARS code. (right) The radial evolution of the star over its lifetime. **A** to **I** indicate evolutionary phases within the model and correspond to the phases in Figure 1.5.

slowly emits the available thermal energy, while its radius remains constant due to its degenerate nature (for example, see Pols 2011). This process follows the WD cooling track, depicted in Figure 1.6 as the dashed grey line. The electron-degeneracy can support a WD with a maximum mass of $\sim$1.4 $M_\odot$, known as the Chandrasekhar mass (Chandrasekhar 1931; Schönberg & Chandrasekhar 1942). When approaching this mass through mass accretion, the WD collapses in a thermonuclear explosion, as we will discuss in Section 2.2.1.

1.2.2 Massive Stars

From theoretical studies and observations, we know that rare massive stars born with a mass larger than 8 times the mass of the sun ($M \gtrsim 8\,M_\odot$) are able to fuse elements all the way to iron. They can die in a dramatic fashion, known as a core-collapse supernova (CCSN), forming a neutron star or a black hole (e.g. Woosley et al. 2002; Smartt et al. 2009). Their evolution is quite different to the low-mass stars and Figure 1.4 shows the HR diagram of a $10\,M_\odot$ star.

The evolutionary track on the HR diagram starts again at hydrogen ignition (**A**) with the CNO cycle being the main fusion process and driving a convective core. The more massive the star, the larger the convective region is. Furthermore, at very high masses

($\sim$100 $M_\odot$) radiation pressure dominates the outwards pressure and the thermal timescale on the main-sequence becomes near constant (see Appendix B). Once hydrogen becomes depleted inside the core (**B**), the star starts to contract, and the hydrogen fusion ends (**C**). Unlike the low-mass stars, hydrogen shell burning does not slowly move outwards.

The hook in the HR diagram (**C**) is due to gravitational collapse providing additional energy, increasing the luminosity and temperature. Intermediate-mass star experience a similar hook, as can be seen for the 5 $M_\odot$ example in Figure 1.6. Shortly after, hydrogen starts to burn in a shell around the helium core, and the stellar radius becomes large, causing the surface temperature to decrease. This evolution happens on the fast thermal timescale and moves the star to the right side of the HR diagram becoming a red supergiant. Due to the short-lived nature, very few stars are observed in this transition region; thus, it is known as the Hertzsprung Gap (HG). During this phase, a convective region forms at the surface of the star (**D**) and the first dredge-up occurs. Because the core continues to contract during this phase, the central temperature increases and becomes sufficient for helium fusion (**E**), causing the outer convective zone to disappear (**F**). The stellar radius decreases (**G**), increasing its surface temperature and moving to the left in the HR diagram. During helium burning, the star slowly expands, similar to the main-sequence. The loop in the HR diagram is also known as the blue loop and occurs on the horizontal branch (for more information, see Walmswell et al. 2015).

For massive star above $\approx$ 15 $M_\odot$, helium ignition occurs on the HG, as the 20 $M_\odot$ example in Figure 1.6 shows. Eventually, the time between hydrogen depletion and helium ignition becomes negligible as the ZAMS mass increases and the overal lifetime decreases. At the same time, the blue loop disappears. At high masses, the star also becomes very extended, and the stellar wind removes a significant amount of matter during its evolution (Cassinelli 1979; Vink 2022). Although the mass loss mechanism is not fully understood, it is metallicity dependent and can drastically impact the stellar evolution, such as preventing the first dredge-up. If the whole outer hydrogen envelope is removed, the star becomes a Helium star, which can appear as a Wolf-Rayet star, if winds are sufficiently strong and its surface is obscurred, resulting in an emission spectrum. Such a star will continue to undergo fusion in its core untill fuel is exhausted and explodes as a stripped CCSN.

When helium runs out (**H**), the star expands again while its core contracts, eventually resulting in carbon ignition. The core carbon fusion phase is where most stellar evolution codes end the evolution (**I**) due to the intense and burst nature of the carbon burning. Further stages of stellar evolution are computationally intensive due to their

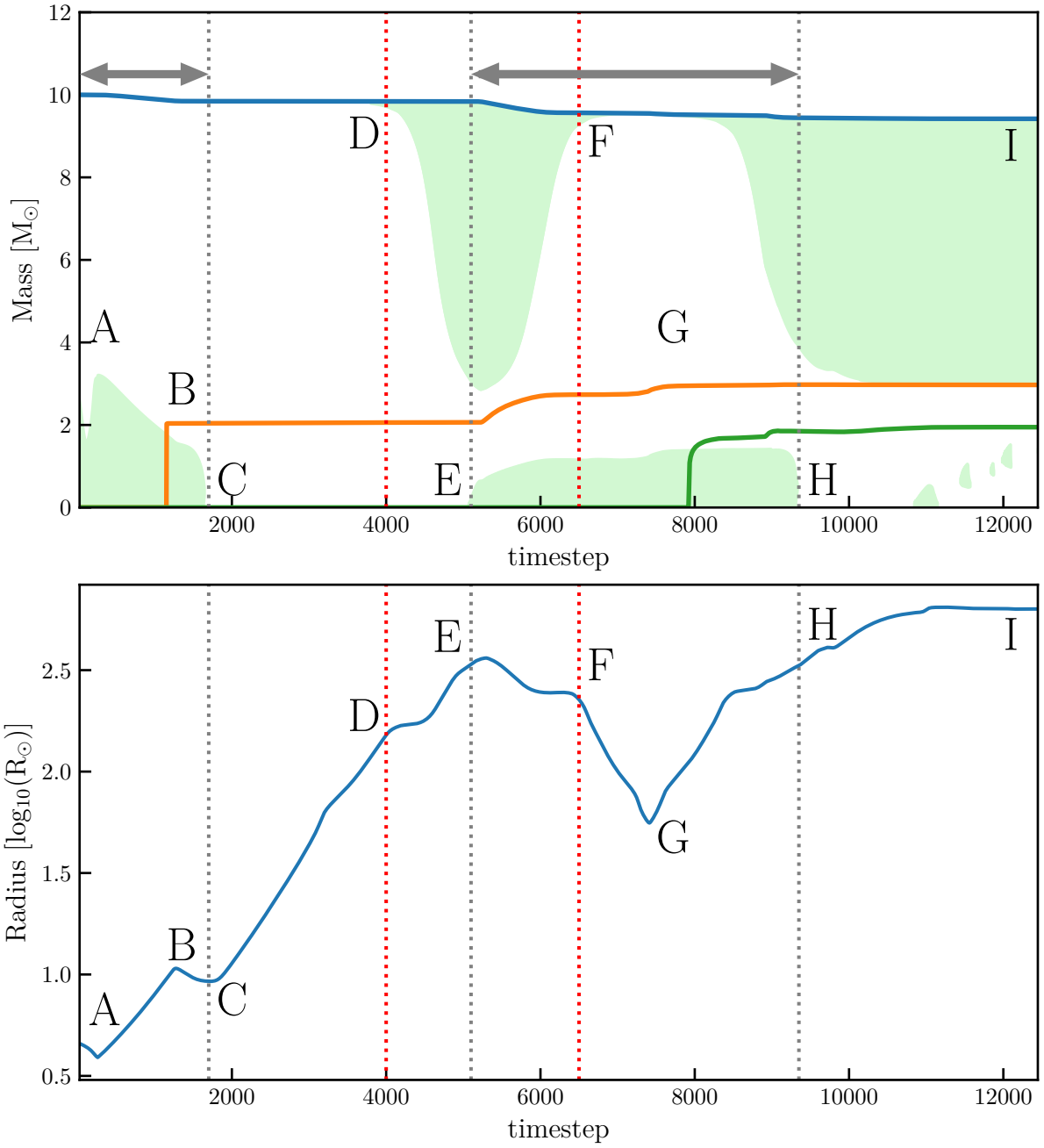

Figure 1.5: top: A Kippenhahn diagram of the internal structure of a $10\,M_\odot$ star at metallicity of $Z = 0.014$. The He core mass (orange), CO core mass (green), and total mass (blue) are shown with the convective regions (light green). The arrows between the vertical grey dotted lines indicate the core hydrogen and helium burning periods. The red dotted lines indicate the formation of a convective envelope in the outer layers of the star, also known as the first dredge-up. bottom: The radial evolution of the $10\,M_\odot$ star over timesteps. **A** to **I** indicate evolutionary phases within the model and correspond to the phases in Figure 1.4. The models comes from the BPASS STARS code, as described in Section 2.1.

short timescale and complex nuclear fusion rate. In reality, the star undergoes several additional stages of fusion to eventually develop an iron core. Without additional energy being able to be gained from iron fusion, the core collapses under the gravitational pressure, realising $\sim 10^{51}$ erg of energy as electromagnetic radiation while higher elements are formed in the explosion (Woosley et al. 2002; Heger et al. 2002). Depending on the mass of the core and amount of stellar material falling back on the core, a neutron star or a black hole can be formed. As the name suggests a neutron star consist almost entirely of neutrons that supply a neutron-degeneracy pressure, similar to how electrons-degeneracy supports a white dwarf (Landau 1932). Together with nuclear forces, it prevents further collapse of the star up to a mass of $\sim 2.5\,\mathrm{M}_{\odot}$, although this limit is dependent on the assumed physics (Rhoades & Ruffini 1974; Van Oeveren & Friedman 2017; Margalit & Metzger 2017; Shao et al. 2020; Tang et al. 2021; Fan et al. 2023). If the total mass is above the maximum neutron star mass, it collapses into a black hole where light can no longer escape (see for example Shapiro & Teukolsky 1983).

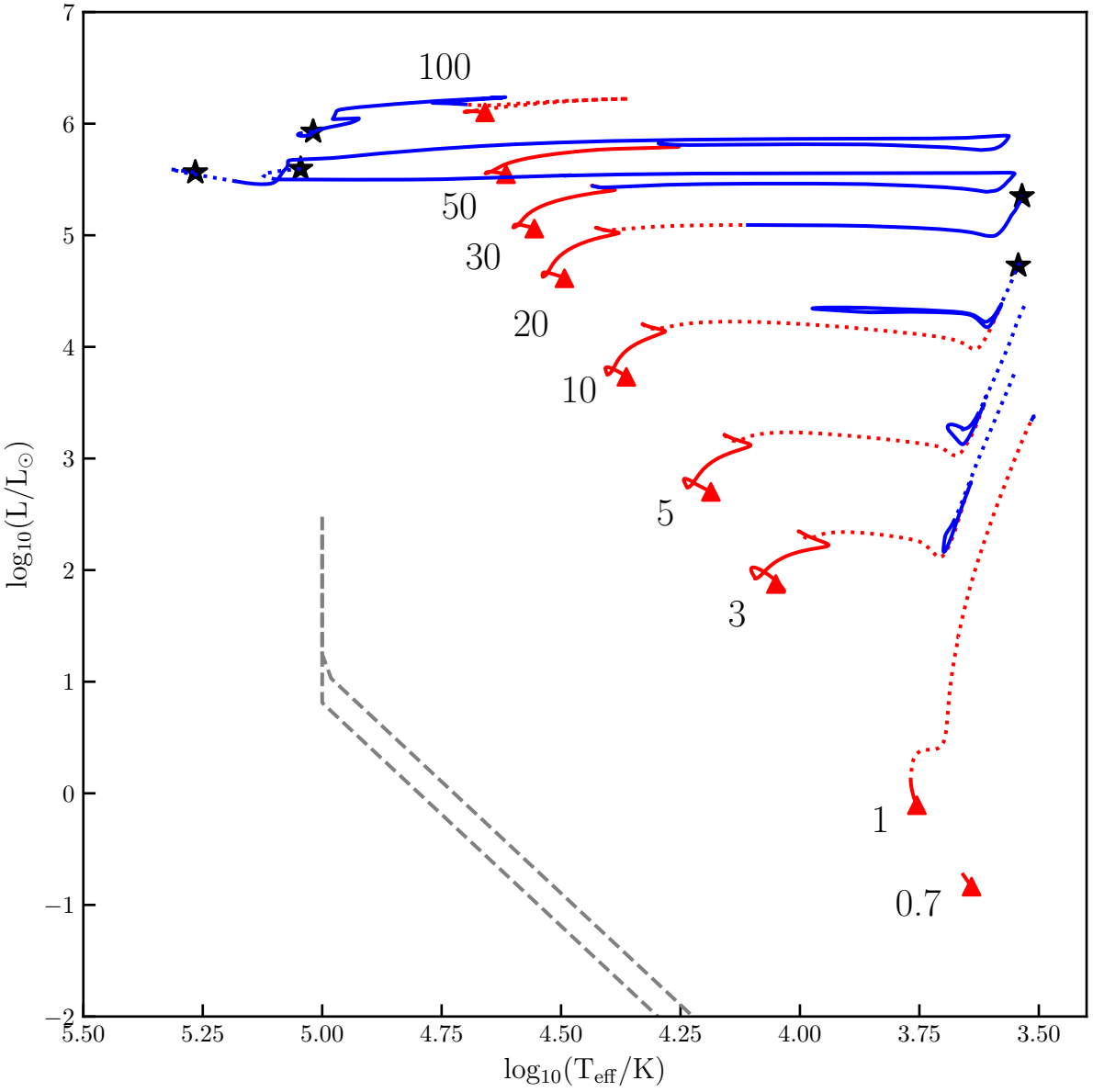

Figure 1.6: HR diagram of different ZAMS mass stars at a metallicity of $Z = 0.014$ indicating the start of the model (red triangle), core hydrogen (solid red line) and core helium burning (solid blue line). Dashed lines indicate no-core fusion, but shell burning might occur. Models are plotted up to the age of the Universe (13 billion years) or when they become a White Dwarf. The $1\,M_\odot$ star reaches the helium flash, but reaches the age of the Universe before core helium fusion drops the star to the horizontal branch. The WD cooling tracks for the 3 and $5\,M_\odot$ stars are shown as the top and bottom dashed grey lines, respectively. Stars indicate that the star ends its life in a CCSN. The small loop at the beginning of the stellar model is a numerical artefact, where the model finds a stable equilibrium with CNO nuclear burning being turned on. The numbers are ZAMS masses in $M_\odot$ of the models.

1.3 Binary Evolution

Before turning our attention to the explosive outcome of massive stars, we explore the impact of binary evolution. Most massive stars have a stellar companion defined by a mass ratio ($q = M_1/M_2$). The two stars are likely to interact during their lifetime (Sana et al. 2012, 2013). While single-star evolution already contains much non-linear physics, introducing a companion star further exacerbates the non-linear nature of the evolution.

For example, a side-effect of a SN in a binary is the occurrence of a natal kick (Blaauw 1961). A CCSN explosion can occur off-center resulting in a non-symmetric explosion giving the forming remnant a push in a particular direction. Although the exact mechanism is an area of active research (see references in Wongwathanarat et al. 2013), this can result in orbital changes and even unbinding from a stellar companion, which can be observed as runaway stars with a high peculiar velocity (e.g. Blaauw 1961; Gunn & Ostriker 1970; Hobbs et al. 2005). However, the most crucial difference from single-star evolution is mass gain and loss between the two stars during their lifetime.

1.3.1 Mass Transfer

When two stars are close enough, the outer layers of one star can be trapped in the gravitational potential of the companion. The gravitational potential takes the shape of a peanut, as shown in Figure 1.7. There are five points, known as Lagrange points (L_1-L_5), where the net effect of the gravity of both stars and the centrifugal force cancel. The region where the material is gravitationally bound to a star is known as the Roche lobe. While the exact mass transfer process is an active area of research, it is often approximated as material transfer through the inner Lagrange point, L_1 (Marchant & Moriya 2020, see references in). Although additional outflow of the outer Lagrange points (L_2 or L_3) is sometimes also considered (Pavlovskii & Ivanova 2015).

The onset of mass transfer through the L_1 point is when a donor star expands past its Roche lobe. The mass transfer is classified as Case A, B or C depending on when it occurs in the evolution. However, more sub-definitions are present in the literature (for example, see Eldridge & Tout 2019). During the main-sequence, the mass transfer is classified as Case A. If the star interacts when it leaves the main-sequence either during the HG or the RSG phase, it is defined as Case B mass transfer. Since the radius expands dramatically during this phase of the evolution, most binary interactions are expected to occur here. The star does not expand again until after core helium exhaustion, which is classified as Case C mass transfer. However, if the hydrogen envelope is already stripped

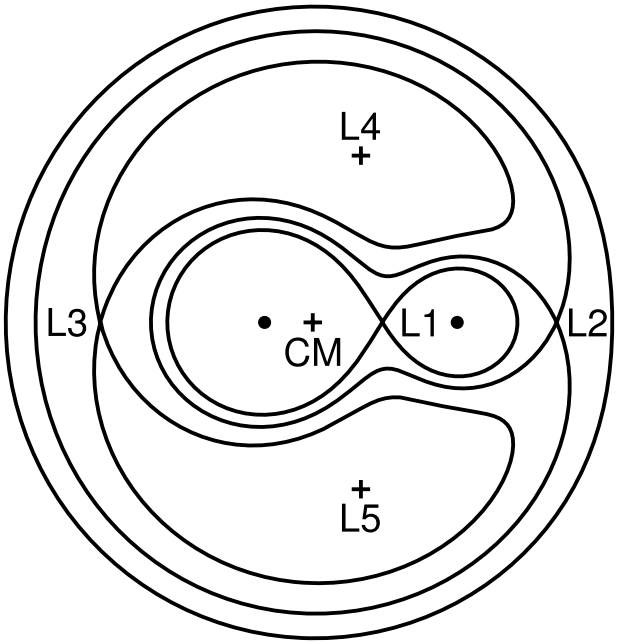

Figure 1.7: The graviational potential of a circular binary with $q = 1/3$ in the plane of the orbit. The lines are equipotential surfaces that go through the Lagrange points (L_1-L_5) except for the outer potential. The dots indicate the center of the stars, while CM indicates the center of mass in the system. Figure by Phillip Hall (2016).

from the donor star when the mass transfer occurs after helium exhaustion, it is referred to as Case BB.

Because the Roche lobe is asymmetric, the approximation from Eggleton (1983) for the spherical volume equivalent to the Roche lobe volume is widely used in 1D stellar evolution codes, which assume spherical symmetry to solve the equations of stellar evolution. It is formulated as:

$$R_{\mathrm{RL}} = a\frac{0.49q^{2/3}}{0.6q^{2/3} + \ln 1 + q^{1/3}}, \tag{1.8}$$

where $q = \mathrm{M}_1/\mathrm{M}_2$ with M_1 and M_2 being the more and less massive stars in the binary, respectively. a is the separation between the center of gravities of the stars.

The mass transfer between stars can spin up the accreting star, also know as the accretor, which can lead to rejuvenation where part of the hydrogen envelope is mixed back into the core, providing a new fusion fuel source (Vanbeveren & De Loore 1994) The accretor looks observationally younger than its lifetime would suggest due to the additional hydrogen gained from the donor star: such stars are known as blue stragglers (McCrea 1964). Furthermore, the mass transfer leads to Algol-type binaries, where a

massive star is accompanied by a low-mass Roche lobe overflowing companion (Budding 1989). At low metallicities, the stellar winds are unable to slow down the rotation of the accretor, and the star remains fully mixed throughout its main-sequence (Maeder 1987; Yoon & Langer 2005; Yoon et al. 2006; Meynet & Maeder 2007; Cantiello et al. 2007). No helium core is formed, and due to the higher mean molecular weight of the star, it remains compact throughout its main-sequence evolution.

If the donor star is sufficiently extended, it may also reach its outer Lagrange point, L_2/L_3, which leads to additional outflow of material and angular momentum of the binary (Shu et al. 1979). Besides spin-up and possible angular momentum loss due to mass transfer, the two components of the binary are also tidally locked during the mass transfer, with the stars rotating at similar velocities to their orbit, which requires angular momentum from the orbit. If the required angular momentum to spin up the star is larger than available in the orbit, the binary spirals in, initiates a common envelope, and possibly merges. This is known as the Darwin Instability, occurring around a mass ratio of $q \gtrsim 12$ depending on the mass transfer efficiency and stellar structure (Rasio 1995). The exact amount of stellar material transferred is an active area of theoretical research (Kolb & Ritter 1990; Marchant & Moriya 2020; Pavlovskii & Ivanova 2015; Cehula & Pejcha 2023), but, observationally, the mass transfer efficiency lies anywhere between inefficient (non-conservative) and efficient (conservative) depending on the observed system and the nature of the accretor (e.g. de Mink et al. 2007; Belloni & Schreiber 2023).

1.3.2 Stability of Mass Transfer

During mass transfer, the system can experience instability and the companion star becomes engulfed by the donor star's envelope to enter a phase known as common envelope (CE) (Paczynski 1976; Webbink 1984; Iben & Livio 1993; Podsiadlowski 2001; Ivanova et al. 2013). During this dynamical phase, the stellar material gains energy through drag, which causes the orbit of the binary to shrink. Whether this phase is reached depends on the criteria for CE chosen.

In its most basic form, the adiabatic response of the donor star is compared against the response of the Roche lobe due to the mass ratio changes, which are described as followed:

$$\zeta_{\rm ad} = \frac{{\rm d}\log R_{\rm d}}{{\rm d}\log {\rm M}_{\rm d}},\ \zeta_{\rm RL} = \frac{{\rm d}\log R_{\rm RL}}{{\rm d}\log {\rm M}_{\rm d}}. \tag{1.9}$$

In the adiabatic regime, it is assumed that the entropy profile in the star cannot readjust on the timescale of the mass transfer. If the response of the donor radius increases faster

or decreases slower than the Roche lobe, the donor star will engulf its companion in a CE, which is written as $\zeta_{\rm ad} < \zeta_{\rm d}$.

The classical approach used polytropic models to determine $\zeta_{\rm d}$ (Hjellming & Webbink 1987; Soberman et al. 1997). They found that stars with a convective envelope expand in response to mass loss, while radiative envelope stars shrink (Paczyński & Sienkiewicz 1972). While this approach is correct for fully convective stars, numerical detailed stellar models provide an entropy profile essential to determining the possible instability (Ge et al. 2020a; Temmink et al. 2023). A flat entropy profile leads to the expansion of the star, and an increasing profile provides radial shrinkage. These profiles are associated with a convective and radiative envelope, respectively.

However, a radiative star might be initially stable but contain a flat entropy profile deeper in the star. If the mass transfer reaches sufficiently deep, this flat entropy layer is reached, causing the star to expand, resulting in unstable mass transfer. This is also known as delayed dynamical instability (for more details, see Ge et al. 2010) and to avoid it, the critical mass ratio, $q_{\rm crit}$, was introduced. It is calculated using numerical stellar models, capturing the regimes in which a dynamical instability might occur (Ge et al. 2010, 2015, 2020a,b). Ge et al. (2020a) have shown it leads to a varying $q_{\rm crit}$ over mass, metallicity, and evolutionary phase. However, this approach requires defining mass transfer rates and efficiencies, and $q_{\rm crit}$ is only valid under these assumptions (Han & Podsiadlowski 2006). Furthermore, convective stars can contain a surface layer that can readjust on an adiabatic timescale, known as a super-adiabatic layer (Woods & Ivanova 2011). As such, a convective envelope star is able to remain within its Roche lobe, even though polytropes predict it will not. Only at very high mass loss rates is such a donor star unable to readjust (Temmink et al. 2023).

Detailed calculations of the stellar structure are required to properly model the response of the donor star to mass loss. Such an approach was performed by Pavlovskii et al. (2017). Using detailed stellar models, they determined the stability of mass transfer based on outflows from the outer Lagrange point (L_2/L_3). While this approach captures the delayed instability and super-adiabatic layer, L_2/L_3 outflow does not have to lead to unstable mass transfer (Temmink et al. 2023). Instead, a faster mass loss than the super-adiabatic layer timescale is more likely to result in a CE (Temmink et al. 2023). It is important to note that this does not include the response of the accretor due to the additional mass. Another approach is to set a maximum mass loss rate, as implemented by Marchant et al. (2021), which solves the issue of super-adiabatic layers by continuing the calculation. A limitation of this method is that a fixed mass loss rate does not

translate well to different donor masses. Each choice in mass transfer stability criteria has its benefits and drawback, but detailed mass transfer simulation provide valuable insight into the stability. Chapter 5 discusses the mass transfer stability and its criteria in more detail.

1.3.3 Unstable Mass Transfer: Common Envelope

Independent of the choice of stability criteria, once initiated CE evolution causes the orbit to shrink. Suppose sufficient energy or angular momentum is available to eject the envelope fully or partially. In that case, the binary survives with a tighter orbit than before the CE phase and a cloud of ejected material around the binary. If there is insufficient angular momentum in the binary, the CE system undergoes a merger and a single star with a unique composition remains. In stellar evolution codes, this dynamical timescale event requires a prescription to determine the outcome, focussing on energy or angular momentum conservation (for a detailed overview, see Ivanova et al. 2013). The choice for energy conservation is known as the α-formalism and is widely used in rapid population synthesis codes and the detailed stellar evolution code MESA (Paxton et al. 2011, 2013, 2015, 2018, 2019; Jermyn et al. 2023) to model the CE phase, which is typically formulated as:

$$\frac{GM_{1,\mathrm{env}}M_1}{\lambda R_1} = \alpha_{\mathrm{CE}} \left(-\frac{GM_1M_2}{2a_i} + \frac{GM_{1,\mathrm{c}}M_2}{2a_f} \right), \tag{1.10}$$

where $\mathrm{M_{env}}$ and $\mathrm{M_c}$ are the envelope and core of the star, respectively. a_i and a_f are the orbital separations before and after the CE. $\mathrm{M_1}$ and $\mathrm{M_2}$ are the primary and secondary masses, respectively. α_{CE} is the CE efficiency and determines how efficiently the orbital binding energy (right-hand side) gets used to eject the envelope (left-hand side). λ is a parameter that accounts for the stellar structure when calculating its binding energy. Hydrodynamical simulations have shown that depending on the choice of λ, the efficiency of the CE can be above 1, and additional energy sources, such as recombination energy, have been suggested as an origin for even higher efficiencies (see references in Ivanova et al. 2013)

The α-formalism is efficient in shrinking the orbit of binaries. However, post-CE white dwarf binaries have been measured with wide orbits, requiring a very high translation of orbital energy into envelope ejection. As a result, the γ-formalism based on the conservation of angular momentum was introduced (Nelemans et al. 2000), which takes the form of:

$$\frac{\Delta J_{\rm lost}}{J_i} = \gamma \frac{M_{1,\rm env}}{M_1 + M_2}, \tag{1.11}$$

where γ is the efficiency of angular momentum transfer, and J_i is the angular momentum in the system. A vast number of post-CE orbits map to a single γ value. However, this is an intrinsic property of the prescription (Ivanova et al. 2013).

The treatment of CE, mass transfer, and its stability are essential in understanding how binaries evolve and end their lives. Luckily, binaries also introduce a new array of stellar transients to understand the evolution of stars, which we will discuss in Section 2.2.1.

1.4 Stellar Transients

While most objects in the Universe change on a million to billion-year timescale, short timescale events, known as transients, have been observed throughout time. Some of these transients are related to physical processes in stellar evolution, such as the CCSN mentioned in Section 1.2.2, while others are related to binary evolution, for example, Type Ia supernovae (See Section 1.4.1). Because many of these transients are bright events, they have been observed for centuries and classifications of transients are observationally based (Kanas 2012). Because observations led the classification of supernovae (SNe), not all SNe originate from the core collapse of a massive star. Section 1.4.1 will discuss the transients related to stellar evolution with electromagnetic observations.

Not only do binaries allow for observation in the electromagnetic spectrum, but they also allow observations using gravitational waves (GW). These are fluctuations in space-time that occur when massive objects rotate around each other. Their effect was first indirectly observed in the orbital decline of the binary pulsar PSR1913+16 in 1982 by Taylor & Weisberg (1982). The first direct observation of a merging compact object was in 2015 by the LIGO/Virgo collaboration (Abbott et al. 2016). These mergers provide a new window into the understanding of the binary evolution of massive stars and are discussed in Section 1.4.2.

1.4.1 Electromagnetic Transients

The main classification of SNe is based on their light spectra indicating the presence or absence of elements. Type II SNe are hydrogen-rich, while Type I SNe lack hydrogen completely (Minkowski 1941). The Type II SNe originate from CCSN and are subdivided

into the Type II-P, II-L, IIb and IIn categories (Filippenko 1997). The Type II-P SNe contain plateau in their light curve evolution, where the luminosity decays slower and is likely caused by a recombination wave moving through the hydrogen envelope (Arnett 1980; Popov 1993; Kasen & Woosley 2009; Branch & Wheeler 2017). Type II-L and IIn SNe decay smoothly, but the latter contains narrow hydrogen emission lines in their spectra due to interactions with surrounding material (Schlegel 1990). If hydrogen is initially present but quickly fades, it is classified as a Type IIb SN (Filippenko 1988), indicating that the hydrogen envelope was stripped to $\lesssim 0.5\,M_\odot$ (Smith et al. 2011).

The hydrogen-poor Type I SNe contains the Ia, Ib and Ic subcategories. The latter two also originate from CCSN, like Type II SNe, but also exhibit either the presence or absence of helium, respectively (Filippenko 1997), and are also known as stripped-envelope SNe (SESNe). The Type IIb SNe are often included in this category since the hydrogen is no longer present late in the light curve evolution. The SESN are likely to originate from binary systems (Yoon et al. 2010; Eldridge et al. 2013, 2015; Yoon 2015), and it is thought that during some, a relativistic jet causes high-energy emission, detectable as a long Gamma Ray Burst (LGRB) (e.g. Heger et al. 2003; Langer 2012; Smartt 2015).

The spectrum of a Type Ia SNe contains strong silicon-II absorption lines (Filippenko 1997), and a Type Ia SN does not originate from a CCSN as the Ib and Ic categories do. They have a well-defined relationship between their peak luminosity and light curve broadness, and are, thus, used as a standard candle to measure distances to high redshift galaxies for cosmological measurement (Phillips 1993; Howell 2011). Observationally, Type Ia SNe come in many different subcategories (for an overview, see Taubenberger 2017; Jha et al. 2019; Ruiter 2019) and the exact progenitor nature of Type Ia is a long-standing unsolved problem in stellar physics (Maoz & Mannucci 2012). However, it is known that standard Type Ia's originate from binary progenitors that involve a CO WD. If, as a result of the added mass, the white dwarf approaches or exceeds the Chandrasekhar limit, a thermonuclear explosion occurs (Hoyle & Fowler 1960; Howell 2011; Maoz et al. 2014). The WD can gain mass from a companion (single-degenerate channel; SD) (Whelan & Iben 1973; Nomoto et al. 1984) or by merging with another WD through the emission of GW (double-degenerate channel; DD) (Webbink 1984; Iben & Tutukov 1984) (for a review, see Wang & Han 2012).

In the SD channel, as the mass of the CO WD increases, it either explodes through a delayed detonation at the Chandrasekhar mass limit (Whelan & Iben 1973; Khokhlov 1991) or at a sub-Chandrasekhar mass through double-detonation (Woosley & Weaver

1994; Livne & Arnett 1995). The mass transfer rate plays an important role in determining the explodibility of the WD (e.g. Wang & Han 2012; Ruiter 2019). For example, if the mass transfer rate is too high, the CO WD collapses into a NS (Nomoto & Iben 1985; Kawai et al. 1987; Timmes et al. 1994; Shen et al. 2012; Schwab et al. 2016).

The standard DD channel requires the formation of two CO WDs and their orbit to shrink through GW emission for them to merge (Pakmor et al. 2010, 2012). This is a much slower process than the SD channel but can create Type Ia SNe with a wide range of total masses below and above the Chandrasekhar limit (Tutukov & Yungelson 1981; Iben & Tutukov 1984; Webbink 1984). For example, if one of the WDs involved in the merger is a He WD, it is thought to produce sub-luminous Type Ia SNe (Ruiter 2019). If, on the other hand, it is a ONe WD, it is likely to undergo accretion-induced collapse into a NS and not produce a Type Ia SN (Miyaji et al. 1980; Saio & Nomoto 1985).

In the transition region between WD formation and CCSNe ($\sim 8\,M_\odot - 10\,M_\odot$), the degenerate core can collapse due to electron capture by magnesium and neon, also known as an electron-capture SN (e.g. Nomoto 1984; Jones et al. 2014) with a expected light curve less luminous than a typical CCSN and several observations matching their synthetic observables (Kozyreva et al. 2021).

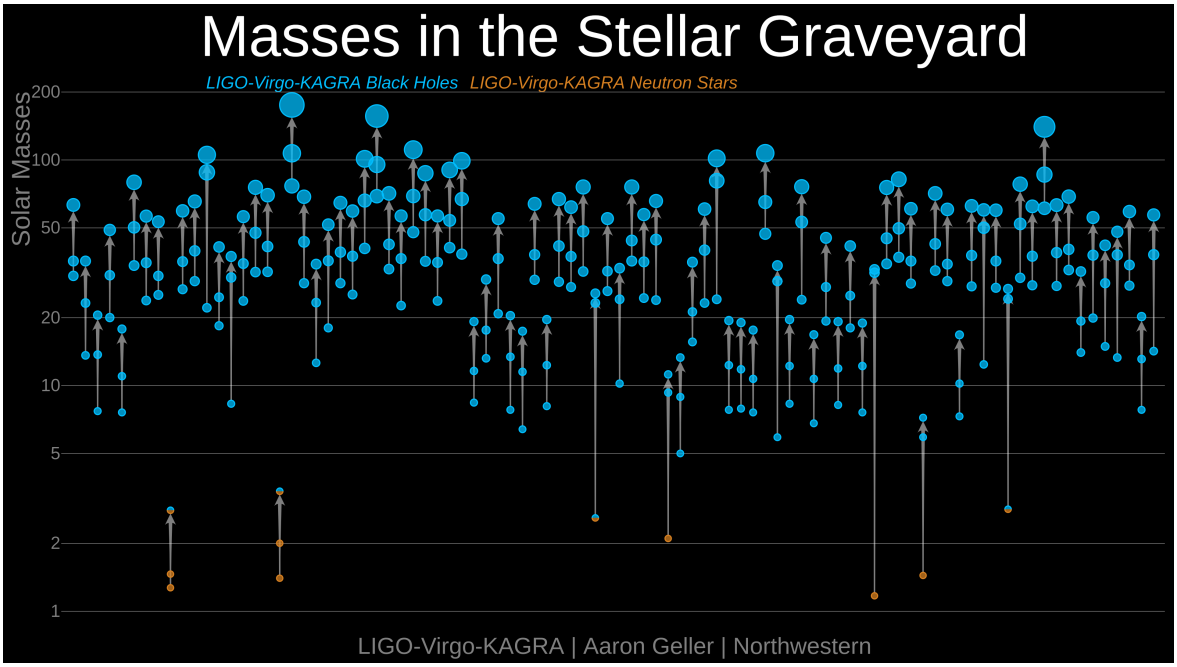

Figure 1.8: The observed merging compact objects by the LIGO-Virgo-KAGRA collaboration. Pre-merger masses of the BHs (blue) and NSs (orange) are connected and point to their post-merger mass. Credits: LIGO-Virgo-KAGRA Collaborations/Frank Elavsky, Aaron Geller/Northwestern.

A special theoretically predicted electromagnetic transient is the pair-instability SN (PISN; Fowler & Hoyle 1964; Rakavy & Shaviv 1967; Heger & Woosley 2002). Very massive stars ($M \gtrsim 100 - 130\,M_\odot$) have a high-density, high-temperature helium core at the end of their main-sequence evolution. This combination gives rise to electron-positron pair production and removes the radiative pressure that keeps the star from collapsing, resulting in an outburst and ejection of stellar material, known as a pulsational pair-instability (PPI). At lower helium core masses, this causes the pair production to cease, and the star will eventually undergo core-collapse in an explosion referred to as PPISN. Because stars with different initial masses exit this regime with similar masses, they form comparable compact objects. At higher He core masses, the pulsations can result in multiple outbursts and even complete disruption of the star in a single explosion without leaving behind a remnant, which is known as a PISN. Due to the short evolutionary timescale of massive stars, PISNe make a useful candidate for probing the star formation history (Fryer et al. 2001; Eldridge et al. 2018b). Specifically, their metallicity dependence makes them a probe for low metallicity star formation environments (Yusof et al. 2010, 2013; Dessart et al. 2013). While no confident detections of a PISN have been observed, several super-luminous Type I SNe (SLSN-I) have been identified as possible candidates (Woosley et al. 2007; Cooke et al. 2012; Gal-Yam et al. 2009; Terreran et al. 2017; Gomez et al. 2019; Schulze et al. 2023).

1.4.2 Gravitational Wave Transients

The double-degenerate channel for Type Ia SNe is driven by the emission of orbital energy through GW. This brings the white dwarfs closer and closer until they eventually merge, which can be calculated using the orbital evolution equations from Peters (1964). The same emission of GW drives the merger of other compact objects, such as black holes (BH) and neutron stars (NS). These objects are more compact, making the last phase of the inspiral and the merger itself measurable if the signal-to-noise ratio is sufficient to be observed by the LIGO, Virgo, and KAGRA detectors. The number of GW observations has increased significantly in the past few years since the first observation in 2015 (Abbott et al. 2016). After the second half of the third observing run (GWTC-3), the LIGO/Virgo/KAGRA collaboration measured 90 signals with an astrophysical origin of more than 50% (Abbott et al. 2023), which we can use to study the stellar population from which they originate. For a GW signal, an effective mass, the chirp mass ($\mathcal{M}$), can

be extracted, which depends on the individual masses of the binary systems like

$$\mathcal{M} = \frac{(m_1 m_2)^{(3/5)}}{(m_1 + m_2)^{(1/5)}}. \tag{1.12}$$

Figure 1.8 shows the extracted individual masses from the current GWTC-3 population of GW transients (Abbott et al. 2023).

The GW mergers are categorised by their pre-merger compact objects: binary neutron star (BNS), black hole-neutron star (BHNS), and binary black hole (BBH) mergers. The pre-merger BH masses cover a region between $\sim 5\,\mathrm{M}_\odot$ and $\sim 100\,\mathrm{M}_\odot$, while the NS mass range is unclear with GW190521_163120 having a mass component below $1.4\,\mathrm{M}_\odot$, while GW190814 and GW200210_092254 have components of $2.59\,\mathrm{M}_\odot$ and $2.83\,\mathrm{M}_\odot$, respectively. There might be a dearth of systems between ~ 2 and $\sim 5\,\mathrm{M}_\odot$, known as the lower mass gap, which is also supported by X-ray observations, where a compact object accretes material from a stellar companion (Bailyn et al. 1998; Özel et al. 2010; Farr et al. 2011). Although this could be a result of the core-collapse mechanism (Fryer et al. 2012, 2022b; Kochanek 2014, 2015), the existence of this mass gap is highly debated (see, for example, Kreidberg et al. 2012; Wyrzykowski & Mandel 2020; Jonker et al. 2021; Farah et al. 2022; Siegel et al. 2022).

Since no compact object is created during a PISN and more massive stars ($\mathrm{M} \gtrsim 260\,\mathrm{M}_\odot$; $\mathrm{M_{He}} \gtrsim 140\,\mathrm{M}_\odot$) directly collapse into a BH, the pair-instability disruption creates a gap in the isolated BH mass distribution, also known as the 'upper mass gap' or 'PISN mass gap' (Spera & Mapelli 2017; Marchant et al. 2019; Stevenson et al. 2019). The lower edge of this gap is at $\mathrm{M_{BH}} \approx 45\,\mathrm{M}_\odot$ (see Woosley & Heger 2021, and references therein) but can be raised using rapid rotation (Marchant & Moriya 2020; Woosley & Heger 2021) or altering the nuclear reaction rates (Woosley & Heger 2021; Mehta et al. 2022; Farag et al. 2022) to include more massive BHs, which have been observed in the PISN mass gap, such as GW190521 (Abbott et al. 2020a), GW190602_175927, and GW190519_153544 (Abbott et al. 2021a,b). Furthermore, a pile-up of events before the upper-mass gap is expected from theory due to PPI reducing the masses into a narrow pre-CCSN regime (see references in Yoshida et al. 2016; Woosley 2017; Marchant et al. 2019).

Observationally, however, the BBH merger, GW190521, contains a pre-merger component of $88^{+21}_{-14}\,\mathrm{M}_\odot$, which is confidently in the PISN mass gap (Abbott et al. 2020a). Figure 1.9 shows the mass distribution of the more massive BH, as predicted from GWTC-3 observations using assumptions about the BBH population (for more detail

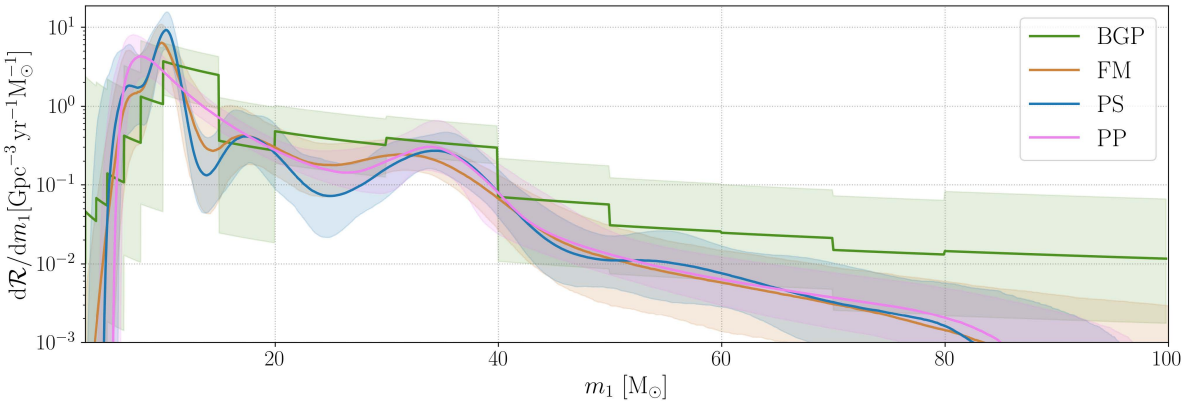

Figure 1.9: The distribution of the more massive BH as inferred from the observed BBH population. Different lines indicate different population models, as described in Abbott et al. (2023). The shaded areas are 95% confidence intervals of each population model. Figure taken from Abbott et al. (2023).

on the population models, see Abbott et al. 2023). The distribution shows an extended tail up to 80 to 100 $\mathrm{M}_\odot$ well into the upper mass gap. Although it shows an excess of systems with a more massive BH mass around 35 $\mathrm{M}_\odot$, this peak is not connected to a reduction of events, as expected by the PPI and PISN hypothesis. Increasing the lower mass limit of the PISN mass gap would also shift the pile-up associated with PPISN to higher masses, further decreasing any association with the observed 35 $\mathrm{M}_\odot$ excess. This observed mass distribution is in tension with theoretical predictions, which we will discuss in detail in Chapter 4.

GWTC-3 only contained 2 confident BHNS and 2 BNS observations because their signals are weaker than from BBHs. However, besides emitting GW, these systems can also emit in the electromagnetic spectrum. BNS mergers are associated with short and long gamma-ray bursts from a relativistic jet and kilonovae from the hot ejecta, which allows for a multi-messenger approach to the event analysis. For the BNS merger, GW170817, an electromagnetic counterpart in the ultraviolet-optical-infrared (Abbott et al. 2017b) and gamma-ray (Abbott et al. 2017c) has been measured (Abbott et al. 2017a). NSBH can also produce electromagnetic signals through the tidal disruption of the NS on the BH (Pannarale et al. 2011; Foucart 2012; Foucart et al. 2018; Pankow et al. 2020). So far, no electromagnetic counterpart has been found for the BHNS mergers (e.g. Hosseinzadeh et al. 2019; Goldstein et al. 2019; Coughlin et al. 2020; Anand et al. 2021) and predictions for multi-messenger observations from them are very dependent on the assumed neutron star equation of state (e.g. Fragione et al. 2021; Biscoveanu et al. 2023).

The multi-messenger approach of BHNS and BNS mergers provides a unique method

to probe binary stellar evolution and fundamental physics. While each GW merger provides a window into the binary massive star evolution, the number of BBH mergers allows for analysis of the population properties and the physics associated with the stellar population from which they originate.

1.5 Stellar Population

1.5.1 Simple Stellar Populations

Up to this point, we have discussed the evolution of single stars and binaries in isolation. However, the Universe contains many trillions of stars, and stellar transients originate from populations of stars. Stars tend to be born in groups from the same gas cloud within larger structures, like star clusters and galaxies (e.g. Ward-Thompson 2011; Smith 2004; Palla 2002).

A star cluster consists of gravitationally bound stars with a similar age and metallicity (e.g. Archinal & Hynes 2003) because they are born in a single starburst, creating a simple stellar population. Observationally, they also have the same redshift (z), which is a measure of how much the stellar spectrum has shifted, as shown in Equation 1.13. Due to the expansion of the Universe, galaxies appear to be moving away from us, and, as a result, their light is redshifted towards the infrared. Given an assumed cosmology, this cosmological redshift can be calculated using

$$1 + z = \frac{\lambda_{\text{obs}}}{\lambda_{\text{emitted}}}, \tag{1.13}$$

which uses the shift in wavelengths as an estimate for distance in space and time (e.g. Hogg 1999).

The single starburst nature of clusters makes them a perfect test for stellar evolution theory. Since different mass stars evolve on different timescales, stellar evolution features, such as the main-sequence and giant branch, show in the combined HR diagram of the stars of the cluster. Observational evidence shows that low-mass stars are more likely to be formed during star formation than massive stars (e.g. Scalo 1986; Chabrier 2003). This formation distribution is empirically described by the initial mass function (IMF), first introduced by Salpeter (1955) and later improved by Kroupa (2001), who included a turn-off towards lower masses.

While the IMF describes the formation of single stars, it does not describe the properties of binaries, such as their periods and masses, which are not independent of each

other and the stellar mass. These properties have been empirically described by Moe & Di Stefano (2017) using a collection of observable techniques, which shows that massive stars are likely to have one or more companions. However, triples, quadruples and higher order systems as triples and quadruples (see Toonen et al. 2016, 2020) are beyond the scope of this thesis.

1.5.2 Stellar Population Synthesis

Nearby stellar populations have been used to validation the model for stellar evolution. However, individual stars are unresolved in high redshift populations and only the combined spectrum of the population of stars can be observed. So it is only natural to also simulate simple stellar populations to make predictions about the unresolved population (e.g. Conroy 2013), which leads to predictions of the transients, such as Type Ia or GW transients from the same stellar populations (Toonen et al. 2014b; Mandel & Broekgaarden 2022). Initially driven by single-star population (for an overview, see Peletier 2013; Conroy 2013), binary population synthesis has taken the forefront since the first GW merger observation. The many binary population synthesis codes can be split into two main groups: rapid population synthesis codes and detailed population synthesis codes. The rapid population synthesis codes (BINARY_C (Izzard et al. 2004; Izzard & Jermyn 2023), BSE (Hurley et al. 2000, 2002), COMBINE (Kruckow et al. 2018), COMPAS (Riley et al. 2022), COSMIC (Breivik et al. 2020), MOBSE (Giacobbo et al. 2018; Di Carlo et al. 2020), SCENARIO MACHINE (Lipunov et al. 1996, 2009), SEBA (Portegies Zwart & Verbunt 1996; Toonen et al. 2012), SEVN (Iorio et al. 2023), STARTRACK (Belczynski et al. 2008)) use analytical formulae or interpolation tables to approximate the evolution of stars in a binary fashion (Hurley et al. 2000). These codes are able to quickly generate many stellar populations with different stellar evolution prescriptions and explore the associated parameter space.

The detailed population synthesis approach (BRUSSELS CODE (Mennekens & Vanbeveren 2014, 2016), BPASS (Eldridge et al. 2017; Stanway & Eldridge 2018), POSYDON (Fragos et al. 2023)) has a higher computational cost due to running many thousands of single and binary evolution stellar models and is less flexible to alteration in the assumed stellar physics, since the computationally expensive stellar models have to be recalculated. However, it does create a more robust stellar population with fewer assumptions about the stellar and binary evolution, which are instead replaced by choices in internal stellar physics.

1.5.3 Realistic Stellar Population

While a simple stellar population can describe a cluster, galaxies are considered complex stellar populations containing many different star clusters. The star formation history (SFH) of galaxies contains multiple starbursts and continuous star formation at different metallicities and ages. With billions of galaxies in the Universe, this makes describing the formation of stellar populations in the Universe difficult, but it has been approached observationally and theoretically.

Observationally derived relations have the advantage of being data-driven but are subject to uncertainties in observational completeness and model-dependence in the calibrations required to recover the star formation rate (SFR) or metallicity from the data. The cosmic star formation rate density (CSFRD) from Madau & Dickinson (2014) is fitted from empirically calibrated SFR indicators using UV and IR observations, which are sensitive to the assumed extinction from dust in distant galaxies (Wilkins et al. 2016, 2018). Early fits include a power-law time-dependence (e.g. Behroozi et al. 2013), but more recent fits typically use a parameterisation for redshift evolution introduced by Madau & Dickinson (2014):

$$\psi(z) = a\frac{(1+z)^b}{1+[(1+z)/c]^d}\ \mathrm{M}_\odot\ \mathrm{yr}^{-1}\ \mathrm{Mpc}^{-3}, \tag{1.14}$$

where for Madau & Dickinson (2014) $a = 0.001$, $b = 2.7$, $c = 2.9$, and $d = 5.6$. These parameters are dependent on the underlying data and processing. Section 2.3 shows other CSFRDs that use different analysis methods based on this parameterisation.

Observations of the metallicity over redshift have shown that it increases towards the current day, as expected from the chemical enrichment of the Universe through SNe and stellar feedback (for more information, see Langer & Norman 2006). However, metallicity measurements above $z \approx 3.3$ have only recently been possible with JWST (Curti et al. 2023), and limited information is known about the high redshift metallicity evolution.

In order to overcome these difficulties with data-driven relations, cosmic volume hydrodynamic simulations are used to simulate a universe in which the evolution of stars, metallicity and galaxies are precisely known. These cosmological simulations, such as the Illustris-TNG (Springel et al. 2018; Nelson et al. 2018; Pillepich et al. 2018b; Naiman et al. 2018; Marinacci et al. 2018), EAGLE (Schaye et al. 2015; Crain et al. 2015), or Millennium Simulation (Springel et al. 2005), evolve a patch of universe from initial condition to match observational properties over the age of the Universe, which is done using mass particles containing millions of stars and sub-grid prescriptions that

describe the star formation and feedback processes inside the mass particle. They capture observational trends and extrapolate to unexplored regions, such as the metallicity and CSFRD at high redshift. However, they require tremendous computational power and are subject to their own uncertainties in the assumed physical interactions or sub-grid prescriptions.

Empirically-driven or prescriptions from cosmological simulations for the SFH have advantages and drawbacks. Section 2.3 describes the CSFRD and metallicity evolution from five empirical prescriptions based on Equation 1.14 and those extracted from three cosmological simulations in more detail.

1.6 This Thesis

Since the first GW merger observation, BBH mergers originating from the cosmic population have become the focus of research for population synthesis studies to understand massive binary evolution (for an overview, see Mandel & Broekgaarden 2022). However, as mentioned in Section 1.4.2, the population properties of BBH mergers are not well understood. The stellar evolution and the SFH are recognised as the two main areas of uncertainty (Broekgaarden et al. 2022a), both required to create a synthetic population of BBH mergers.

Since BBH mergers from isolated massive binaries lie at the end of their evolution, as shown in Figure 1.10, several other observables, such as the CCSNe, can be used to constrain stellar physics. Since SNe observations have been made for centuries, their numbers are better constrained than the GW populations. Even Type Ia SNe can help constrain the physics governing binary interactions, such as mass transfer and its stability, especially since these systems do not contain core-collapse physics. The observations of these electromagnetic transients can help us constrain the physics resulting in the observed GW population. By doing this from the same stellar population, we create self-consistent predictions for the stellar transients, which should provide the strongest constraints on stellar and binary physics.

However, predicting electromagnetic stellar transients from a population requires detailed knowledge of the stellar structure of each star undergoing a CCSN and accurate modelling of binary interactions. Therefore, in this thesis, we use the Binary Population and Spectral Synthesis suite, BPASS (Eldridge et al. 2017; Stanway & Eldridge 2018), which contains populations of detailed single and binary stars. Chapter 2 discusses BPASS and how we extract the stellar transients from its simple stellar population. To create

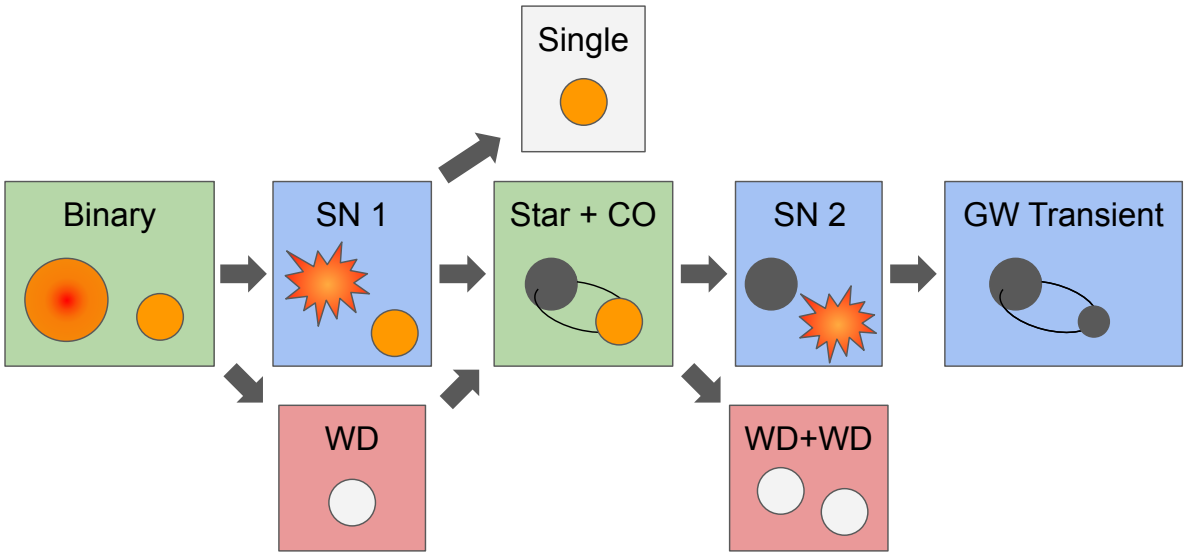

Figure 1.10: A simplified depiction of the binary evolution pathway leading to compact object mergers, with blue indicating electromagnetic and GW observational windows that can constrain the stellar and binary physics, while green indicates where the binary physics comes into play. Since WDs can result into Type Ia SNe, the formation pathway of WDs is shown in red. The SN natal kick can cause binaries to become unbound and result in runaway single star, depicted in gray.

complex stellar populations that represent the cosmic population of stellar transients, we will combine the BPASS simple stellar populations with SFHs from observations and cosmological simulations to account for uncertainty in the CSFRD and metallicity evolution, which we will discuss in Section 2.3. In Chapter 3, we make predictions for the electromagnetic and GW stellar transient population using the cosmological populations we have created in Chapter 2. We also compare these predictions against observations of transient rates across the age of the Universe. We dive further into the BBH population properties and formation pathways in Chapter 4. While each chapter quantifies uncertainties and caveats relevant to the topics it discusses, we go in-depth into the stellar and binary physics of the BPASS models and the possible impact on our self-consistent transient predictions in Chapter 5. Chapter 6 discusses the transient determination, remnant mass determination, supernova natal kick and CE prescription in the context of the complete thesis. There, we also summarise the conclusions of each chapter and discuss which areas binary population synthesis should focus on in the near future.

Chapter 2

Stellar Populations

In Chapter 1, we discussed the evolution of single stars and binaries, and the stellar transients originating from them. However, as mentioned in Section 1.5, stars are born in clusters and galaxies, which have vastly different SFHs. To predict the GW mergers and other stellar transients from the same cosmic stellar population, the stellar evolution and the SFH of the Universe are the essential components in creating a synthetic transient population. For the former, we use the Binary Population and Spectral Synthesis (BPASS) suite to create simple stellar populations (Eldridge et al. 2017; Stanway & Eldridge 2018). It uses a custom version of the CAMBRIDGE STARS code (Eggleton 1971; Pols et al. 1995; Eldridge & Tout 2004a; Eldridge et al. 2008) to evolve a grid of single and binary stars to or beyond carbon ignition over a range of metallicities. Section 2.1 covers the implemented single star and binary physics in detail.

Using this grid of stellar models, in this thesis we use BPASS TUI to create simple stellar populations, as described in Section 2.2, where we also describe how the theoretical models are linked to the observationally driven stellar transient definitions. Using the different SFHs described in Section 2.3, we create a complex stellar population of the universe. We describe this method in Section 2.4.

2.1 BPASS STARS

The adapted CAMBRIDGE STARS code in BPASS solves the full set of differential equations describing the structure of a star in 1D to simulate it up to carbon ignition, which we will refer to as BPASS STARS. To solve these equations, several standard approximations for 1D stellar evolution are made about, for example, the nuclear rates, metallicity abundances, and stellar wind mass loss.

The code uses nuclear reaction rates as described in Eldridge (2005) and uses the Schwarzschild convection criterion to determine the boundary between convective and radiative energy transport (for convection criteria, see Pols 2011; Eldridge & Tout 2019).

As part of the convection, overshooting can occur, where convective material mixes with the radiative layers around the convective zones, resulting in mixing of the abundances (for more detail on the implementation of the internal stellar physics, see Eldridge & Tout 2004a,b; Eldridge et al. 2008, 2017; Stanway & Eldridge 2018). BPASS STARS uses a metallicity composition from Grevesse et al. (1996).

During the post-main sequence evolution, a star is very extended and stellar winds remove a significant amount of stellar material, especially in massive stars, as described in Section 1.2.2. A higher initial metallicity causes the star to extended further due to higher opacity. As a result, more mass is lost through stellar winds compared to a low-metallicity star. Moreover, a higher metallicity provides more matter to run the CNO cycle. Therefore, higher metallicity massive stars have a shorter lifetime than low metallicity massive stars. The BPASS STARS code uses a metallicity-dependent wind mass loss from de Jager et al. (1988), Vink et al. (2001) and Nugis & Lamers (2000) for the more massive OB stars and hydrogen-depleted Wolf-Rayet stars, respectively. The combination of these prescriptions accounts for metallicity changes and adjustments in the hydrogen and helium composition.

2.1.1 Binary Physics

Modelling two stars and their interactions brings in new physics, which can be computationally difficult. Besides two stars of different masses evolving on different timescales, the mass transfer also introduces the CE, which occurs on a dynamical timescale. In that regime and the fact that a CE is a three-dimensional process, the BPASS STARS 1D stellar evolution code is unable to solve the stellar structure differential equations, and prescriptions are required to continue the evolution.

BPASS STARS has been adapted to include a unique method for evolving a binary system with two stars. While the primary, more massive, star is evolved in detail by the code, the companion, secondary, star is evolved using the rapid single star equations from Hurley et al. (2002). This reduces the computational time required per binary. Moreover, the binaries are assumed to be in a circular orbit. If the primary star survives until it becomes a WD or undergoes a SN, the secondary is evolved in detail. At this point, the companion has become a compact object and is assumed to be a point mass (Eldridge et al. 2017; Stanway & Eldridge 2018). In Section 2.2, we discuss how these models are combined and used to create simple stellar populations. Here, we discuss the details of the binary stellar evolution as they are implemented within the BPASS STARS code.

When the radius of the detailed primary extends past the Roche lobe radius, as defined in Equation 1.8, mass is removed according to Equation 2.1. This is an adapted version of the nuclear mass transfer rate prescription from Hurley et al. (2002). However, instead of using the minimum for stability, BPASS STARS uses the maximum between M_1 and 5, boosting mass loss rates at lower masses. The mass transfer starts slowly when the star expands pasts its Roche lobe, but the further the star expands, the higher the mass loss rate which follows

$$\dot{M} = F(M_1) \left[\ln(R_1/R_{L_1})\right]^3 \, M_\odot yr^{-1} \tag{2.1}$$

with

$$F(M_1) = 3 \times 10^{-6} \left[\max(M_1, 5.0)\right]^2 . \tag{2.2}$$

However, the maximum mass loss rate is limited to 0.1 $M_\odot$/yr for numerical stability.

The material removed from the donor star might be accreted by the companion, also known as the accretor. For the accretor to remain in hydrostatic equilibrium, it might not be able to accrete all the material lost from the donor. As such, BPASS STARS limits the accretion rate for stellar companions by their thermal (Kelvin-Helmholtz) timescale. If the companion is a compact object below $3\,M_\odot$, we limit the accretion by the Eddington luminosity. The Eddington luminosity ($L_{\rm edd}$) is the luminosity where the radiative pressure from the heat of spherically uniform infalling material counters gravity. As a result, material is pushed outwards and can no longer fall in. $M_{\rm edd} = L_{\rm edd}/\epsilon c^2$ is the accretion rate that would lead to this luminosity, where ϵ is the radiative efficiency; that is the fraction of energy released per $M_\odot$ as it falls towards the compact object and is often set to 0.1 for BH accretors. For a solar mass BH, this limit is approximately $2.2 \times 10^{-8}\,M_\odot yr^{-1}$.

In the context of disk-fed accretion, instead of spherically symmetric infall, an optically thick, slim disk structure allows for super-Eddington accretion rates (Johnson & Sanderbeck 2022; Ghodla & Eldridge 2023). Accretion above this limit can be used for BHs to grow sufficiently in the early Universe to become supermassive BHs, an unanswered astrophysical question. Because the exact accretion mechanism onto a BH is uncertain, BPASS STARS does not limit the accretion rate above $M_a \geq 3\,M_\odot$, which is contrary to other GW population synthesis codes (for example, see Bavera et al. 2021; Riley et al. 2022; Iorio et al. 2023). Unaccreted material is lost to the system with its angular momentum by treating it as a stellar wind from the donor star.

$$\dot{\mathrm{M}}_2 \leq \begin{cases} \mathrm{M}_2/\tau_{\mathrm{KH}} & (\text{stellar companion}) \\ \mathrm{M}_{\mathrm{edd}} & (\mathrm{M}_{\mathrm{rem}} \leq 3\,\mathrm{M}_\odot) \\ \infty & (\mathrm{M}_{\mathrm{rem}} > 3\,\mathrm{M}_\odot) \end{cases} \tag{2.3}$$

summarise the different accretion regimes depending on the companion type and mass, where $\mathrm{M}_{\mathrm{rem}}$ is the mass of the compact remnant accretor.

Determining if the mass transfer experiences instability is a non-trivial question, as discussed in Section 1.3.2. The BPASS STARS code uses a unique approach in determining mass transfer stability. It uses the definition of the radius of the donor star becoming larger than the separation of the system. This simple prescription allows for an initial mass transfer phase before initiating CE. However, the code does not yet consider the expansion of the accretor as a possible instability leading to CE.

Since the donor star is modelled throughout the interaction, it responds appropriately based on its entropy profile instead of approximating its response based on its evolutionary phase; the rapid population synthesis approach (Iorio et al. 2023; Riley et al. 2022). By progressively removing material and angular momentum, BPASS STARS implicitly accounts for delayed dynamical instabilities and super-adiabatic layers. Because BPASS STARS models the stellar structure, material is removed using Equation 2.1, and the angular momentum ($\mathrm{d}J$) required to remove this material (dM) comes from the orbit, which roughly follows

$$\mathrm{d}J \approx J\frac{\mathrm{dM}_1}{\mathrm{M}_1 + \mathrm{M}_2}. \tag{2.4}$$

We point to Section 6.4 for a more detailed explanation of the angular momentum loss during CE implemented in BPASS STARS.

Because the binary is evolved through the CE and material is removed per timestep, the core-envelope boundary and CE efficiency ($\alpha_{\mathrm{CE}}\lambda$) are not defined a priori (see Section 1.3.3 for these definitions). Instead, these follow from the implicit removal of material and differ based on the structure of the donor star. This also allows us to calculate the values for γ and $\alpha_{\mathrm{CE}}\lambda$ after the fact, which results in values of 0.5 to 4 for γ and 2-10 for $\alpha_{\mathrm{CE}}\lambda$ values (Stevance et al. 2023a). It is common in the BPASS models for part of the hydrogen envelope to be left behind, which has been found previously in detailed 1D calculations of CE with a NS companion (Fragos et al. 2019; Laplace et al. 2020). This contradicts stellar evolution assumptions in rapid population synthesis, where the envelope is entirely removed from the star, per definition (e.g. Iorio et al. 2023; Riley

et al. 2022).

To ensure the post-CE binary is in thermal equilibrium, the maximum mass-loss rate is limited to 0.1 $M_\odot$/yr, which increases the duration of the CE to unrealistic lengths but does not significantly impact the outcome of the CE (Eldridge et al. 2017). The CE prescription ends when the star shrinks back into its Roche lobe radius. This limit is chosen to ensure the system exits the common envelope properly. As a result, no accretion by the companion occurs until the star reinitiates mass transfer after ending the CE. The system merges if the orbital energy is insufficient to survive the CE, which occurs in BPASS STARS when the companion star fills its Roche lobe during a CE ($R_2 > R_{\rm RL}$). If the companion is a star, its mass is added to the primary using the surface composition of the primary.

2.2 Simple Stellar Populations: TUI

Because the single-star and binary star evolution is highly non-linear, BPASS stellar populations use grids of BPASS STARS with different ZAMS metallicities and parameters to create a synthetic population of the complete variety of evolution that single stars and binary systems lead to.

For the *single-star models*, a grid of masses between 0.1 and 300 $M_\odot$ over 13 metallicities ranging from $Z = 10^{-5}$ to 0.04 was calculated, with the exact values shown in Table 2.1. The *single-star models* are evolved up to the formation of a WD or up to core carbon burning for stars that might undergo a CCSN. Section 2.2.1 describes the stellar structure parameters required for a CCSN. If the star undergoes core-collapse, the remnant mass is determined by the prescription described in Section 2.2.2.

Because of the complex nature of binaries and the non-detailed companion in BPASS STARS, their evolution is split into *primary* and *secondary models*. The *primary model* follows the evolution of two stars up to the first SN or WD formation, while the *secondary model* contains a star with a compact object companion(WD/NS/BH).

BPASS contains simple stellar populations of 10^6 $M_\odot$, each with one at each of the 13 BPASS metallicities, as shown in Table 2.1. Each population is created by weighting the *single-star* and *primary models* according to a Kroupa et al. (1993) IMF extended up to 300 $M_\odot$ (Stanway & Eldridge 2018). The mass ratio and periods for the *primary models* are weighted according to empirical prescriptions by Moe & Di Stefano (2017).

The linking between the different models depends on the binary interactions, remnant masses, and possible supernova kick, and follows a similar process as depicted in Figure

Parameter	Values
Single-Star Models	
Mass ($M_\odot$)	0.02 $M_\odot$ steps: 0.1 to 2, 0.05 $M_\odot$ steps: 2 to 3, 0.1 $M_\odot$ steps: 3 to 10, 1 $M_\odot$ steps: 10 to 100, 100, 125, 150, 175, 200, 225, 250, 275, 300
Metallicity (Z)	10^{-5}, 10^{-4}, 0.001, 0.002, 0.003, 0.004, 0.005, 0.006, 0.008, 0.01, 0.014 0.02 ($Z_\odot$), 0.03, 0.04
Primary Models	
Primary star mass ($M_\odot$)	0.1 $M_\odot$ steps: 0.1 to 2.1, 2.3, 2.5, 2.7, 3, 3.2, 3.5, 3.7, 0.5 $M_\odot$ steps: 4 to 10, 1 $M_\odot$ steps: 10 to 25, 30, 35, 40, 50, 60, 70, 80, 100, 120, 150, 200, 300
Mass ratios ($q = M_1/M_2$)	0.1 steps: 0.1 - 0.9
Period ($\log_{10}(P/\text{days})$)	0.2 steps: 0 to 4.0
Secondary Models	
Primary masses ($M_\odot$)	0.1, 0.2, 0.3, 0.4, 0.5, 0.6, 0.8, 1, 1.4 1 $M_\odot$ steps: 2 to 25 25, 30, 35, 40, 50, 60, 70, 80, 100 120, 150, 200, 300, 400, 500
Compact object masses ($\log_{10}(M_{CO}/M_\odot)$)	0.1 steps: -1 to 2
BPASS age bins ($\log_{10}$(age/yrs))	0.1 steps: 6 to 11

Table 2.1: The parameters of the BPASS population grid for the *single-star*, *primary*, and *secondary models*. $Z_\odot$ indicates solar metallicity. For the *secondary models*, only models required to generate the simple population in the standard BPASS output are present, as such not all initial masses and periods might be available for them. Adapted from Eldridge et al. (2017).

1.10. In this thesis, they are combined using the population synthesis code TUI (Ghodla et al. 2022; Briel et al. 2023; Stevance et al. 2023b), for which the possible pathways in stellar evolution are shown in Figure 2.1.

Starting at the *primary model*, mass transfer can result in a merger, rejuvenation, quasi-homogeneous evolution (QHE), or slightly alter the companion mass. If a stellar companion accretes more than 5 per cent of its initial mass (Yoon et al. 2012), it is rejuvenated, as described in Section 1.3. However, a lower accretion fraction can already lead to a significant spin-up of the accretor (e.g. Ghodla et al. 2023). When the secondary star that has been rejuvenated is evolved in detail, it is modelled as if it was a ZAMS star. If this accretion occurs at a metallicity below $Z \leq 0.006$, the secondary model gets replaced by a QHE single-star stellar model (*QHE model*), where mixing is forced to occur (Eldridge et al. 2017). Mergers are considered implicitly inside BPASS STARS, and the model is treated as a single star for its SN and remnant mass determination.

If the more massive star in the *primary model* does not undergo a CCSN, a *secondary model* is selected based on the period and masses at the end of the *primary model*. If a SN does occur, the binary experiences a natal kick, as mentioned in Section 1.3. In this thesis, for each *primary model*, 1000 natal kicks are sampled from a Maxwell-Boltzmann distribution with $\sigma = 265$ km s^{-1} (Hobbs et al. 2005) for remnant masses below $3\,\mathrm{M}_\odot$. Otherwise, the kick is reduced by $\mathrm{M}_{\mathrm{remnant}}/1.4\,\mathrm{M}_\odot$. This can lead to systems becoming unbound, for which the stellar companion is evolved using a *single-star model*. For bound systems, their periods are calculated and *secondary models* are selected based on the masses and period distribution. Eventually, the secondary star becomes a WD or goes SN too. If the binary remains bound after the secondary evolution, its merger time from GW emission is calculated using

$$T \approx T_c \left(1 + 0.27e_0^{10} + 0.33e_0^{20} + 0.2e_0^{1000}\right)\left(1 - e_0^2\right)^{7/2}, \tag{2.5}$$

where

$$T_c = \frac{5c^5 a_0^4}{256\mathrm{G}^3\mathrm{M}_1\mathrm{M}_2(\mathrm{M}_1 + \mathrm{M}_2)}, \tag{2.6}$$

from Mandel & Farmer (2022) with its post-natal kick initial separation (a_0) and eccentricity (e_0) for BHs and NSs. If the system contains a double WD, we calculate its merger time using the equations from Peters (1964), described in Section 1.4.1.

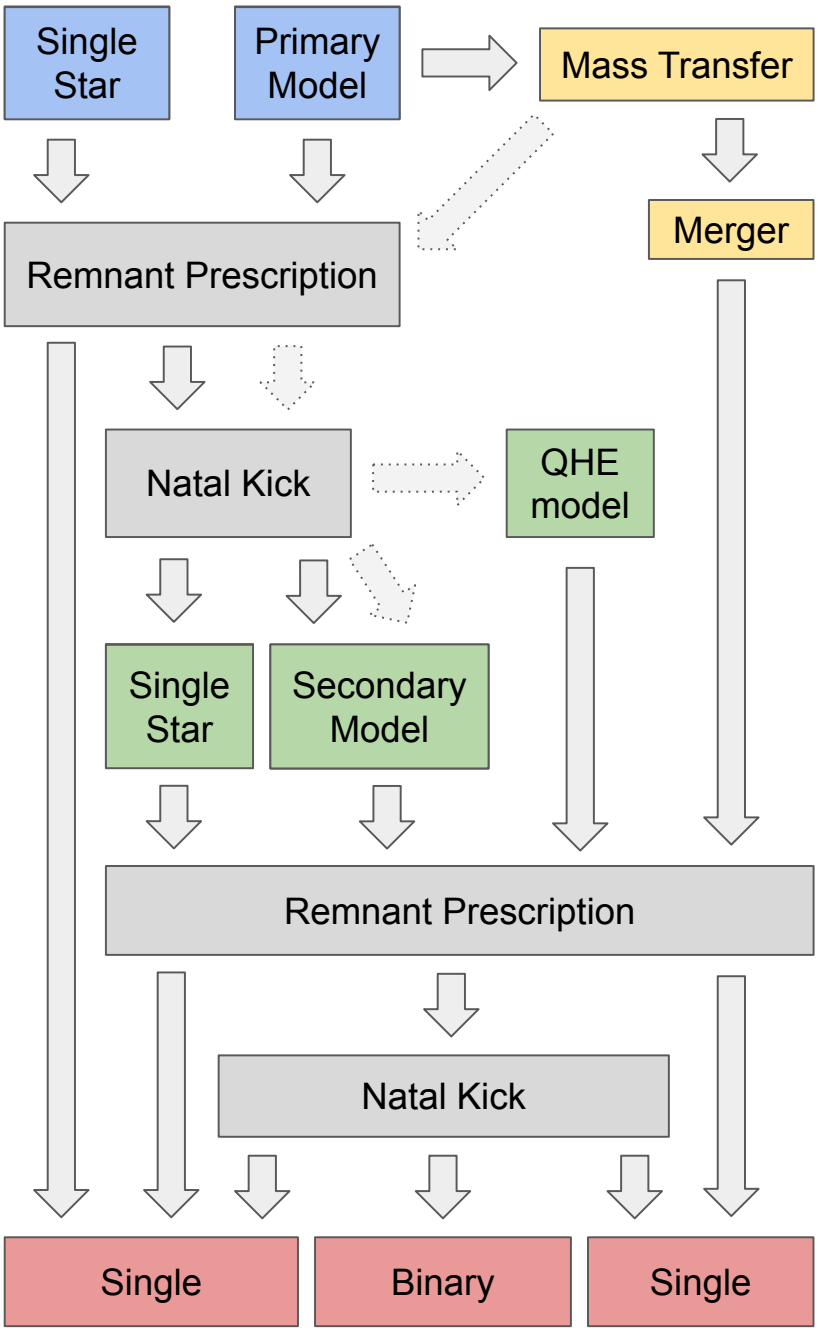

Figure 2.1: The TUI model to combine the *single-star*, *primary*, *secondary*, and *qhe models* to create a stellar population. Blue indicates the evolution of single stars and the primary star. Yellow indicates additional evolution inside the BPASS STARS code. Green indicates the evolution of the companion star, as a single star, binary system, or QHE star, depending on the mass transfer and natal kick. Gray indicates the TUI post-processing. The dotted arrow between Mass Transfer and QHE model indicates that the mass transfer influences if a QHE model is chosen. The remnant prescription contains both the SN detemination and remnant mass prescription.

2.2.1 Transient Determination

Although observationally a large variety of transient definitions exists, connecting them to the theoretical models is a non-trivial task. This thesis uses both theoretically and observationally motivated definitions to determine the transients originating from the single stellar populations.

In BPASS, a star undergoing a CCSN depends on the existence of a carbon-oxygen core larger than $1.38\,M_\odot$ and a total mass larger than $1.5\,M_\odot$. These models are expected to undergo carbon burning and generate a sufficiently large oxygen-neon or iron core to result in a supernova (Eldridge & Tout 2004b). In this thesis, we refine the definition that an ONe core must be present if the CO core is smaller than $3\,M_\odot$ to ensure the star undergoes iron core-collapse. Moreover, if the total mass is below $2\,M_\odot$, the star does not undergo iron core-collapse. Instead undergoes an electron capture core collapse and is not included in the CCSN category, as described in Section 1.4.1.

Within BPASS, the elemental abundances of the star are a proxy to determine the subtype of the CCSN and are shown in Table 2.2 (Eldridge et al. 2011, 2013, 2017). The parameters were chosen for each CCSN subtype to match the observed local relative rates within ~ 20 Mpc (Eldridge et al. 2013), the Ib/Ic rates in Shivvers et al. (2017), progenitor observations, and Type II light curve simulations Eldridge et al. (2018b).

BPASS only considers LGRB formation through chemically homogeneous evolution through fast rotation and mixing caused by low metallicity mass transfer to account for the metallicity dependence (Grieco et al. 2012; Perley et al. 2016b). If the stellar evolution of a QHE model leads to a CCSN with a remnant mass of $3\,M_\odot$, it is classified as a LGRB. We do not add tidal and magnetar-induced GRBs to the LGRB rate, as done previously in Briel et al. (2023), which we discuss in Section 6.1.

We define a PISN regime based on the He and CO core sizes. When they enter the regime where $M_{CO} > 60\,M_\odot$ and $M_{He} < 133\,M_\odot$, we tag the system as a PISN. The lower CO core limit is based on work from Marchant et al. (2019) and the He upper limit on work from Woosley et al. (2002). This is an updated PISN definition compared to BPASS v2.2.

We classify WDs into He ($M < 0.6\,M_\odot$), CO ($0.6\,M_\odot \leq M \leq 1.08\,M_\odot$), and ONe ($M > 1.08\,M_\odot$) WD based on their total mass, which adds a finer level of detail over the BPASS v2.2 definitions, see Appendix D for a comparison. These masses are chosen based on earlier work from van Zeist (2018), and the upper limit is close to the C ignition mass of $1.1\,M_\odot$ (Umeda et al. 1999; Siess 2006; Doherty et al. 2015, 2017). In reality, one WD type will transition into the other, and a more careful analysis of the structure

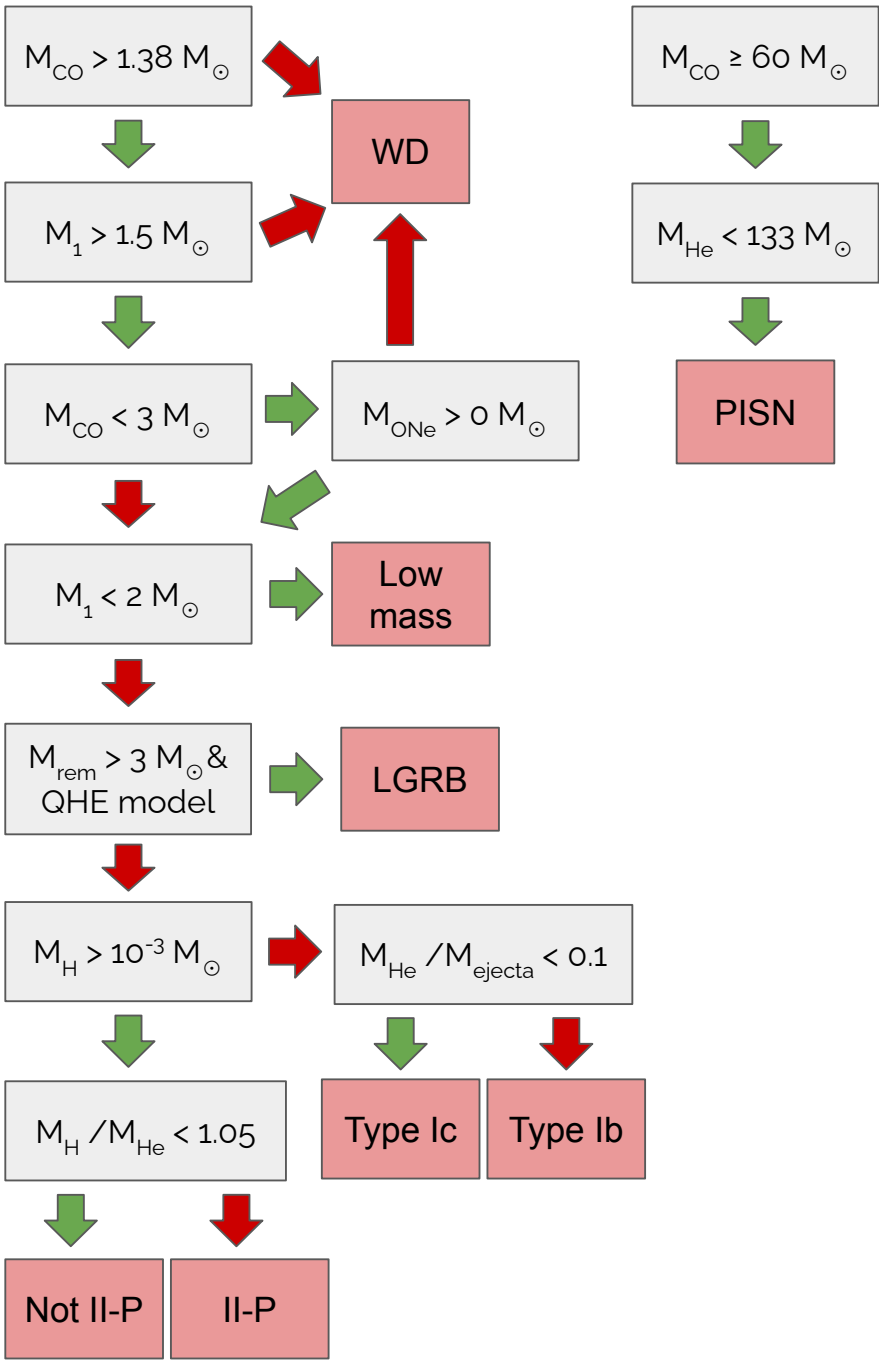

Figure 2.2: Selection criteria for CCSN, PISN, and LGRB transient determination in this work. Red arrows state show the flow if the binary does match the statement. Green arrows indicate matching the criteria. The PISN and CCSN definitions have been refined compared to Eldridge et al. (2013). For example, for a model with $M_{CO} < 3\,M_\odot$ a ONe core has to be present for the model to be classified as undergoing a CCSN. Low mass are not included in the CCSN rate and are systems that are likely to undergo an electron capture SN (see Section 1.4.1) The differences compared to BPASS V2.2 are discussed in Appendix D.

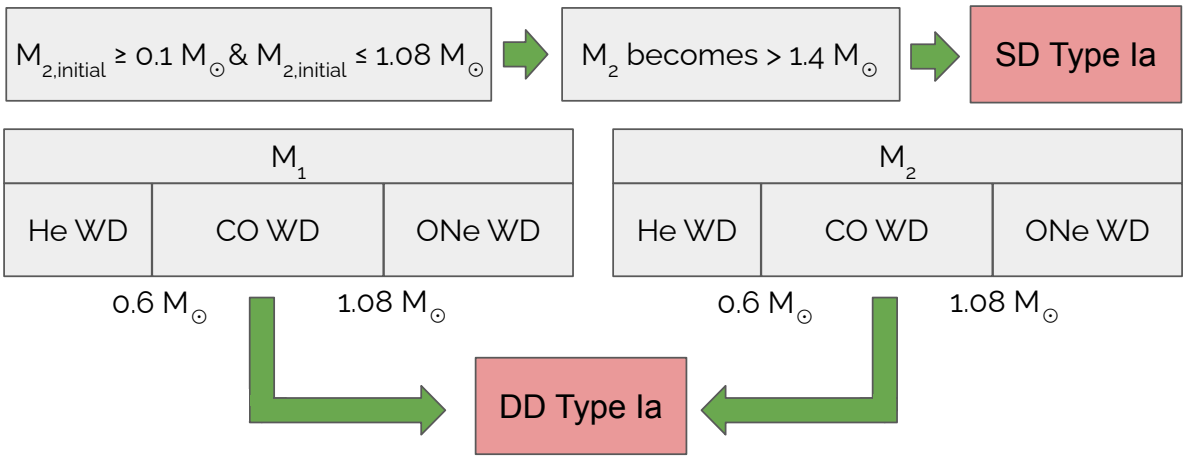

Figure 2.3: Type Ia selection criteria for the single and double degenerate formation channels based on the total masses of the models. M_1 and M_2 for the DD channel are WD masses, otherwise M_1 is the stellar object, while M_2 is the first formed white dwarf in the *secondary model*. Only if both models are CO WDs are they classified as a DD Type Ia event. The differences compared to BPASS V2.2 are discussed in Appendix D.

is required to determine its composition accurately, which is beyond the scope of this work, as we hope to capture standard Type Ia progenitors.

Because the stellar models might end before the second WD is formed, we set an upper limit of $M_1 < 1.5\,M_\odot$ and $M_2 < 1.4\,M_\odot$, and a helium core has to be present in the primary. Still, the CO core cannot be sufficient to explode in a core-collapse supernova ($M_{CO} < 1.38\,M_\odot$). The exact parameters are shown in Figure 2.3. The SD Type Ia channel contains accretion onto all types of WDs, while for the DD channel, we only include mergers between two CO WDs as the standard Type Ia SN. The orbital decay of the double WD systems is caused by the emission of orbital energy through gravitational GW, and we integrate over the orbital evolution equations from Peters (1964) till the lowest mass WD is ripped apart by the more massive WD, which is known as tidal disruption. This radius can be approximated as

$$R_{\rm td} \approx \left(\frac{6M}{\pi\rho}\right)^{1/3} \tag{2.7}$$

from Zou et al. (2020), where ρ is the average density of the less massive WD, which we approximate as $\rho = 10^9$ kg m^{-3}.

We use a different merger time calculation for the BBH, BHNS, and BNS mergers including eccentricity induced by the final natal kick. Although BPASS STARS divides BHs and NSs at $3\,M_\odot$, we use $2.5\,M_\odot$ for the maximum NS mass for the transient definitions;

more massive objects are defined as BHs. This more closely matches the maximum NS mass from multi-messenger observations (Abbott et al. 2017b) and predictions by the current equation of state models (Fattoyev et al. 2020)

2.2.2 Remnant Mass Determination

In this thesis, we use the BPASS remnant mass prescription, where the remaining bound mass is calculated by injecting 10^{51} erg into the star while considering its internal stellar structure (Eldridge & Tout 2004b). This value is close to the observed total energy released in most CCSNe (see Section 1.2.2). While BPASS does contain a PISN prescription Woosley et al. (2002), it does not contain a PPI prescription (see Section 1.4.1 for PPI and PISN definitions). These processes, however, are essential in determining the BBH population (Stevenson et al. 2019; Marchant et al. 2019), as it is thought to result in the upper mass gap and a pile-up of events, as described in Section 1.4.2. For this thesis, we implement the prescription from Farmer et al. (2019) based on the CO core of the progenitor for (P)PISNe. In the other regimes, we keep the BPASS prescription of energy injection. Since no upper limit based on the CO core is currently available (for an overview of limits, see Woosley & Heger 2021), we use the upper limit based on the He core mass from Woosley et al. (2002). As Figure 2.4 shows, this prescription transitions smoothly between regimes and can be described by

$$\begin{aligned} \mathrm{M_{CO}} < 38\ \mathrm{M_\odot} &\longrightarrow 10^{51}\ \text{erg injection} \\ 38\ \mathrm{M_\odot} \leq \mathrm{M_{CO}} < 60\ \mathrm{M_\odot} &\longrightarrow \text{Farmer et al. (2019)} \\ \mathrm{M_{CO}} \geq 60\ \mathrm{M_\odot}\ \text{and}\ \mathrm{M_{He}} < 133\ \mathrm{M_\odot} &\longrightarrow \mathrm{M_{rem}} = 0 \\ \mathrm{M_{He}} \geq 133\ \mathrm{M_\odot} &\longrightarrow 10^{51}\ \text{erg injection.} \end{aligned} \tag{2.8}$$

We change baryonic masses into gravitational masses, following Fryer et al. (2012) with $\mathrm{M_{grav}} = 0.9\mathrm{M_{bar}}$ for remnant masses above $3\,\mathrm{M_\odot}$ and for masses below we use

$$\mathrm{M_{grav}} = 2\frac{\sqrt{1+3\mathrm{M_{bar}}}-1}{3} \tag{2.9}$$

In Section 4.5.3, we also explore the effect of the Fryer et al. (2012) remnant mass prescriptions on the compact object population. They consider a rapid and delayed SN mechanism. In the former, the explosion occurs within 250 ms of the core bounce, while in the delayed mechanism, the explosion can occur on longer timescales, as described in

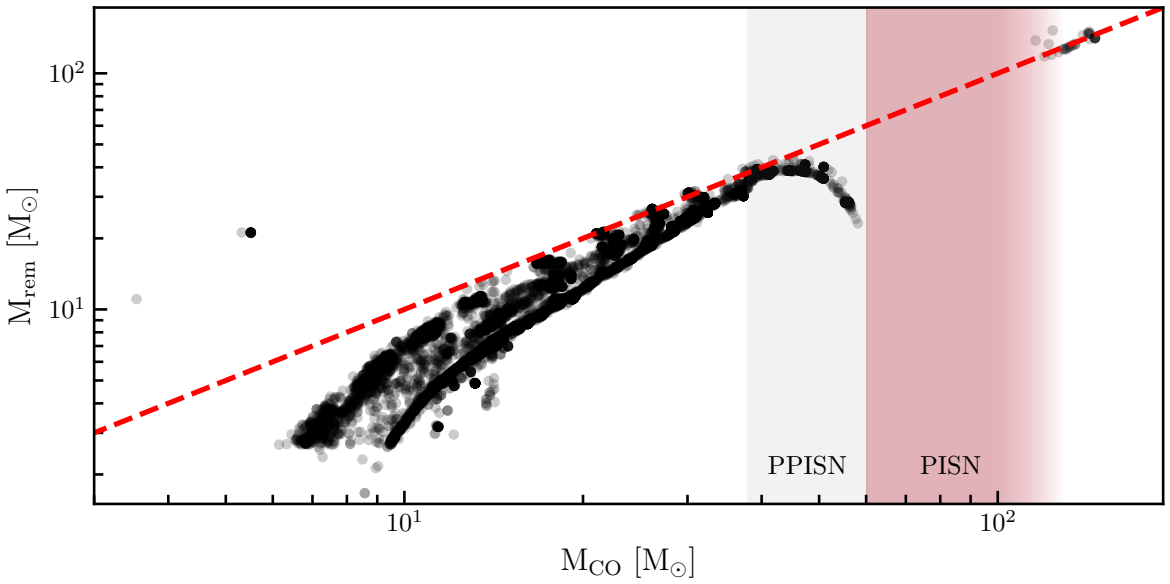

Figure 2.4: The remnant mass over M_{CO} for models resulting in BBH mergers to show the (P)PISN transition from the TUI fiducial remnant mass determination over all metallicities considered in the BPASS code suite. The dashed red line is where $M_{CO} = M_{rem}$. The models above this have large envelopes of which a large part falls back on the formed compact object. The grey PPISN region is between 30 and 60 $M_\odot$. Since the upper PISN boundary is defined by M_{He}, the PISN M_{CO} upper limit is a gradient.

Fryer et al. (2012). As a result, the delayed mechanism has lower explosion energy and more material falls back onto the formed compact object at low masses.

$$\begin{cases} M_{fb} = 0.2\,M_\odot & M_{CO} < 2.5\,M_\odot \\ M_{fb} = 0.286 M_{CO} - 0.514\,M_\odot & 2.5\,M_\odot \leq M_{CO} < 6.0\,M_\odot \\ f_{fb} = 1.0 & 6.0\,M_\odot \leq M_{CO} < 7.0\,M_\odot \\ f_{fb} = a_1 M_{CO} + b_1 & 7.0\,M_\odot \leq M_{CO} < 11.0\,M_\odot \\ f_{fb} = 1 & M_{CO} \geq 11\,M_\odot, \end{cases} \tag{2.10}$$

with $M_{fb} = f_{fb}(M - M_{proto})$, $a_1 = 0.25 - (1.275/M - M_{proto})$, $b_1 = -11a_1 + 1$, and $M_{proto} = 1.0\,M_\odot$, describes the amount of fallback (M_{fb}) onto the proto-compact object (M_{proto}) in the rapid prescription from Fryer et al. (2012) to calculate the remnant mass ($M_{rem} = M_{proto} + M_{fb}$). The gravitational remnant mass is calculated as above. Above 11 $M_\odot$, the differences between the rapid and delayed prescriptions minimise due to complete fallback. At lower masses, the differences originate from a different proto-compact object and amount of fallback. The delayed prescription contains multiple

M_{proto} depending on the CO core size:

$$\begin{cases} M_{proto} = 1.2\,M_\odot & M_{CO} < 3.5\,M_\odot \\ M_{proto} = 1.3\,M_\odot & 3.5\,M_\odot \leq M_{CO} < 6.0\,M_\odot \\ M_{proto} = 1.4\,M_\odot & 6.0\,M_\odot \leq M_{CO} < 11\,M_\odot \\ M_{proto} = 1.6\,M_\odot & M_{CO} \geq 11\,M_\odot. \end{cases} \tag{2.11}$$

It uses $a_2 = 0.133 - (0.093/M - M_{proto})$ and $b_2 = -11a_2 + 1$ to calculate the remnant mass with the following fallback prescription:

$$\begin{cases} M_{fb} = 0.2\,M_\odot & M_{CO} < 2.5\,M_\odot \\ M_{fb} = 0.5 M_{CO} - 1.05\,M_\odot & 2.5\,M_\odot \leq M_{CO} < 3.5\,M_\odot \\ f_{fb} = a_1 M_{CO} + b_1 & 3.5\,M_\odot \leq M_{CO} < 11\,M_\odot \\ f_{fb} = 1 & M_{CO} \geq 11\,M_\odot. \end{cases} \tag{2.12}$$

2.2.3 Delay Time Distribution

Based on the stellar transient definitions in Section 2.2.1 and the remnant mass determination in Section 2.2.2, we determine the delay time for each transient, which is the duration from birth until the transient occurs. In BPASS V2.2, these were binned in 0.1 logarithmic bins between 10^6 and 10^{11} yr. In this thesis, we keep each event separate and no longer bin the transient events into these time bins, except for plotting purposes.

For CCSN, this is the lifetime of the star, but for GW mergers, this contains the inspiral time due to gravitational wave emission. Similarly, the DD Type Ia delay time includes the time required for the system to merge. For the SD Type Ia SNe, we determine if mass transfer in the *secondary model* occurs after forming the WD according to the *primary model*. If this is not the case, the primary's lifetime is added to the delay time. However, due to a few numerically unstable models, some SD Type Ia progenitors still have extremely short delay times, which are unrealistic. Consequently, we also require SD Type Ia SNe to have at least a delay time of 10^7 yrs.

Different event types have significantly different delay time distributions (DTD) due to their formation pathways, as shown in Figure 2.5 (See Appendix A for DTDs of other metallicities). The delay time of a PISN is extremely short due to the fast rate of hydrogen burning, making it a great probe of the SFH (Fryer et al. 2001; Eldridge et al. 2018b). Moreover, they are also extremely metallicity dependent (Yusof et al. 2010, 2013;

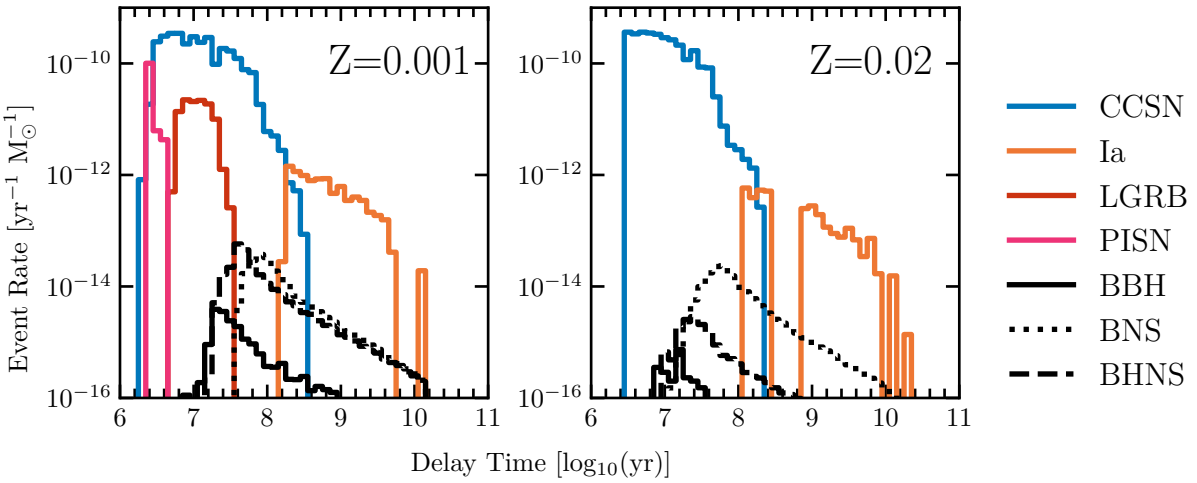

Figure 2.5: Delay Time Distributions at $Z = 0.001$ and $Z = 0.02$ for the transients discussed in this work. Type Ia SNe contain the SD and DD channels, while CCSN contains Type II, IIP, Ib, Ic. Due to the finite grid size of the stellar models, the delay time distribution might experience gaps in some regions.

Dessart et al. 2013). Similarly, LGRBs have short delay times and are very metallicity dependent (Grieco et al. 2012; Perley et al. 2016b). As such, both these transients probe star-forming and low-metallicity environments.

Type Ia SNe have relatively long delay times because a WD must be formed before a thermonuclear explosion occurs, with the DD channel requiring even longer delay times to form the secondary WD. As a result of this long stellar lifetime, Type Ia SNe take place a long time after star formation and, thus, probe older star formation environments. However, the DD channel in our population only contains a few merging double WDs, as its lack of contribution to the Type Ia SN delay time distribution in Figure 2.6 shows. While some double WD systems are formed within the age of the Universe in our stellar population, only a few have sub-day periods at the formation of the secondary WD (see Figure 2.7 and Section 6.1, respectively). As a result, the formed double WD systems are unable to emit sufficient GW emission between their formation and the age of the Universe to merge. Since double WDs with periods down to minutes have been observed (see Rebassa-Mansergas et al. 2017, and references therein), this result does not match observations and is unexpected, especially since the standard BPASS v2.2 population does contain a DD contribution to the Type Ia rate, albeit sub-dominant to the SD channel (Eldridge et al. 2019; Briel et al. 2022). In Section 6.1, we discuss the origin of the missing short-period double WD systems and improvements that need to be made to the TUI population synthesis to account for these systems in the future properly.

Even though the Type Ia population only contains SD events, the resulting Type

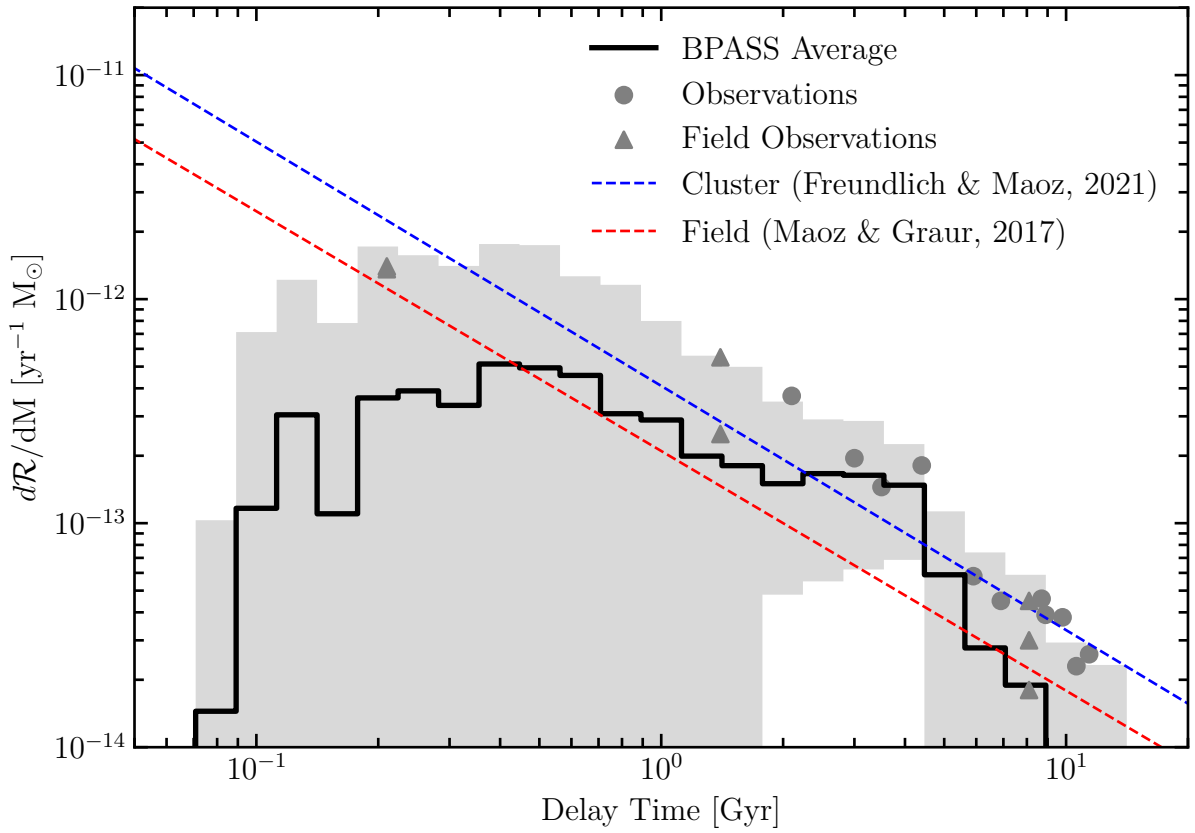

Figure 2.6: The delay time distribution of the Type Ia SNe averaged over metallicity (solid black) compared against observations from the field (Maoz & Graur 2017) (triangle grey) and cluster (Freundlich & Maoz 2021) (circle grey). The standard BPASS age bins are used to bin the delay time and the spread in rates per timebin is highlighted (grey area). Two t^{-1} relations have been fitted to these observations by Maoz & Graur (2017) and Freundlich & Maoz (2021) (dashed red and blue line respectively).

Ia DTD roughly follows a $\sim t^{-1}$ as is expected from observations (Totani et al. 2008; Maoz & Mannucci 2012; Maoz et al. 2014; Maoz & Graur 2017). Figure 2.6 shows the Type Ia DTD compared to observationally derived Type Ia DTD from field and cluster population by Maoz & Graur (2017) and Freundlich & Maoz (2021). These have a slope of ~ 1.09 and 1.07 and normalisation of $R_1 \approx 0.21 \times 10^{-12}\mathrm{yr}^{-1}\,\mathrm{M}_\odot^{-1}$ and $R_1 \approx 0.41 \times 10^{-12}\mathrm{yr}^{-1}\,\mathrm{M}_\odot^{-1}$. For the BPASS population, we have averaged all metallicities equally to produce an average DTD for comparison. The Type Ia rate is similar to the observations, especially when comparing directly to the field and cluster observations in Figure 2.6. Few Type Ia SNe occur below 100 Myr in BPASS due to the minimal duration to form a WD. It is, therefore, not unexpected that the BPASS DTD is lower than the empirical fits to Type Ia observations.

The observations from Maoz & Graur (2017) assume a single-burst star formation as many others do, while Freundlich & Maoz (2021) releases this parameter and instead fit the star formation history. The assumed SFH can introduce uncertainty in the actual delay time and rate. Moreover, the models used to extract the SFR are often based on single-star models and can overestimate the amount of star formation (Wilkins et al. 2019). Since the observations come from a collection of metallicities and star formation histories, this comparison indicates that the Type Ia DTD from BPASS is reasonable. In Chapter 3, we combine this DTD with the SFHs considered in this work and directly compare observed Type Ia rates to our predictions.

The fact that the BPASS DTD shapes are close to the observed distributions is even more surprising because, in BPASS, the SD channel dominates the Type Ia rate. We do not find a clear bimodal distribution in the SD channel, as often found in other binary population synthesis models (Hillebrandt et al. 2013; Ruiter 2019). Instead, we find a plateau at $\sim$ 2.5 Gyr, a t^{-1} relationship, and short delay times of $\sim$ 100 Myr at low metallicities. This might result from the detailed binary models and treatment of mass transfer stability. As shown in Section 5.1, most interactions in binaries with $M_d \leq 5\,M_\odot$ are stable and highly non-conservative. This results in wider orbits and longer delay times for the SD channel than evolution through a CE. However, further analysis beyond the scope of this thesis is required.

CCSNe have shorter delay times than Type Ia SN, and we can say that the CCSNe rate closely follows current star formation (Eldridge et al. 2018b; Botticella et al. 2008). However, different CCSN subtypes have different delay times (See Appendix A.2). Type Ic SNe have the shortest delay times because they originate from more massive stars than Type Ib and Type II SNe, where stellar winds are stronger. The delay times of GW events lie between the Type Ia and CCSN delay times, with BBH having shorter delay times than BNS, because the BH progenitors are more massive and thus have shorter lifetimes than NS progenitors. Moreover, the energy loss through GW emission from a BBH system is higher than from a BNS system due to their higher mass.

Besides having different delay times, the different transients also have different metallicity dependences. Figure 2.7 and Figure 2.8 show the metallicity distribution of EM and GW transients. The PISN and LGRB rates are only at low metallicities. The LGRB rate is limited by the QHE LGRB formation in BPASS. The PISN rate extends to higher metallicities because stellar mergers produce even more massive stars. Furthermore, due to increased stellar winds, the Type Ib rate increase and Type Ic start to take place, which results in a dip of Type II at higher metalicities. The GW rates are nearly flat over

metallicity until 0.002, where BBH and BHNS rates drop. Depending on the parameter choices, this is similar to rapid population synthesis codes, such as SEVN (Iorio et al. 2023). The BNs rate decreases slightly but remains mostly constant, even at super-solar metallicities, similar to other population synthesis results (Klencki et al. 2018; Chruslinska et al. 2018; Neijssel et al. 2019; Santoliquido et al. 2021; Broekgaarden et al. 2022a; Iorio et al. 2023).

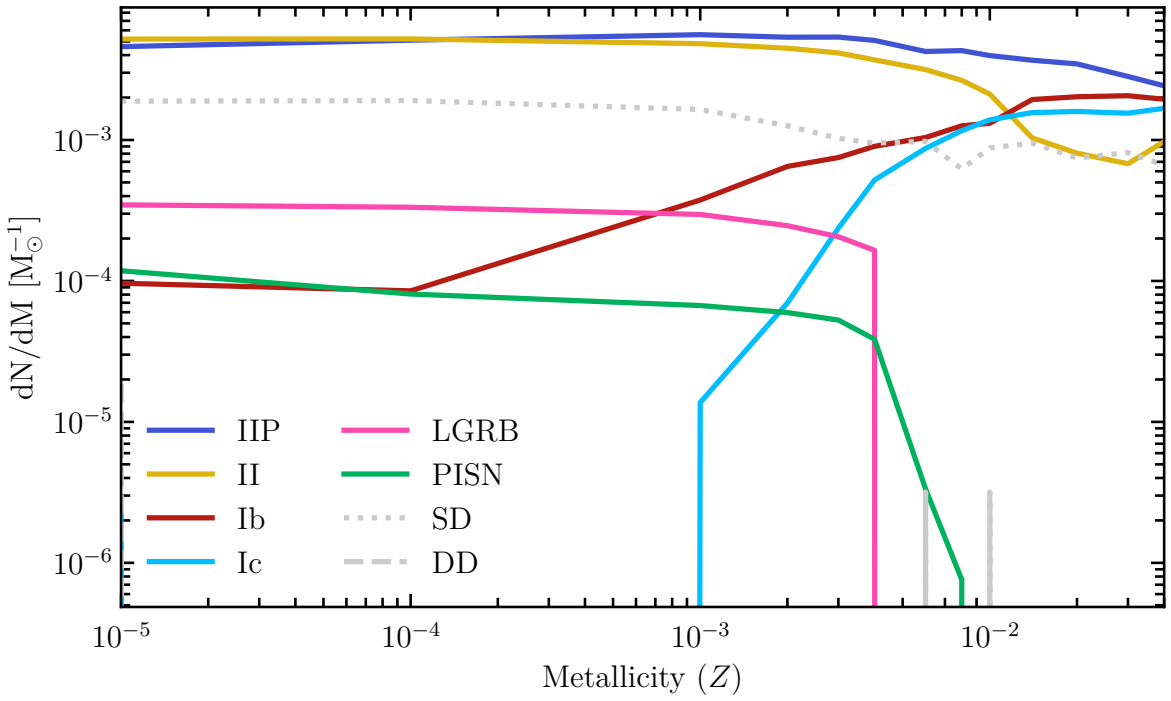

Figure 2.7: The number of electromagnetic transients per $M_\odot$ originating from a stellar population at each absolute metallicity within the Hubble time (13.8×10^9 yrs).

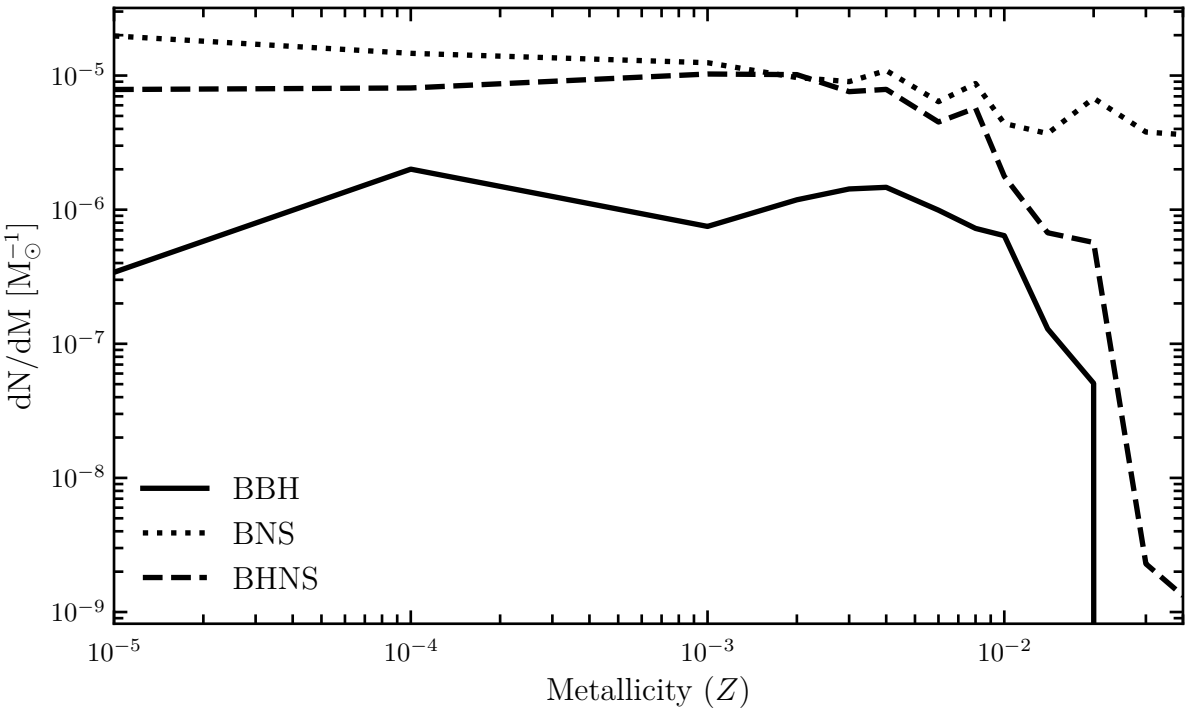

Figure 2.8: The number of gravitational wave transients per $M_\odot$ originating from a stellar population at each absolute metallicity within the age of the Universe.

2.3 Star Formation History

In reality, stellar populations in the Universe are not solely formed from 10^6 $M_\odot$ of at one specific metallicity, as created in Section 2.2. We require a prescription for the amount of stellar material, when it is formed, and its metallicity. For a prediction of the cosmic transient rates, we require a description of the star formation, which can significantly impact the number of SNe and GW mergers. Especially BBH merger and Type Ib/c SNe are sensitive to the metallicity at formation. To this end, we explore multiple SFH descriptions, including a prescription for the star formation rate and the metallicity over cosmic history

To compare the impact of the SFH on transient rates, we compare the MilliMillennium, EAGLE, and IllustrisTNG simulations to cover different release years, sizes, and physical models. We compare these to the often-used empirical prescription based on the star formation rate of Madau & Dickinson (2014) and the metallicity evolution of Langer & Norman (2006). We also include several updated prescriptions often used in GW transient predictions (Madau & Fragos 2017; Neijssel et al. 2019; van Son et al. 2023). We also include the Wilkins et al. (2019) prescription, which uses BPASS V2.2 population spectra to determine the CSFRD to account for the influence of binaries and create a self-consistent chain using stellar populations from BPASS.

2.3.1 Empirical SFHs

We transform Equation 15 from Madau & Dickinson (2014) from a Salpeter (Salpeter 1955) to a Kroupa IMF by multiplying by 0.66, and this function is shown in Figure 2.9 as the pink dashed line. It peaks at $z = 2$ while declining in the high and low redshift direction, with the current SFR being similar to $z \approx 6$. We also use the updated Madau & Fragos (2017), which includes additional observations and mostly updates the parameters from Madau & Dickinson (2014), influencing the peak and tail of the SFH: $a = 0.01$, $b = 2.6$, $c = 3.2$, and $d = 6.2$, as shown in Figure 2.9. One drawback of these SFH histories is the use of single-star models to determine the relation between luminosity and SFR. As such, we also include the CSFRD prescription of Wilkins et al. (2019), which uses the BPASS v2.2.1 models to recalibrate the CSFRD to $a = 0.0103$, $b = 2.48$, $c = 3.10$, and $d = 6.26$. This results in a similar prescription to Madau & Dickinson (2014), except that the pre-peak SFR is suppressed. We combine these CSFRD with cosmic metallicity distribution and evolution from Langer & Norman (2006) as used in Eldridge et al. (2019) and Tang et al. (2020):

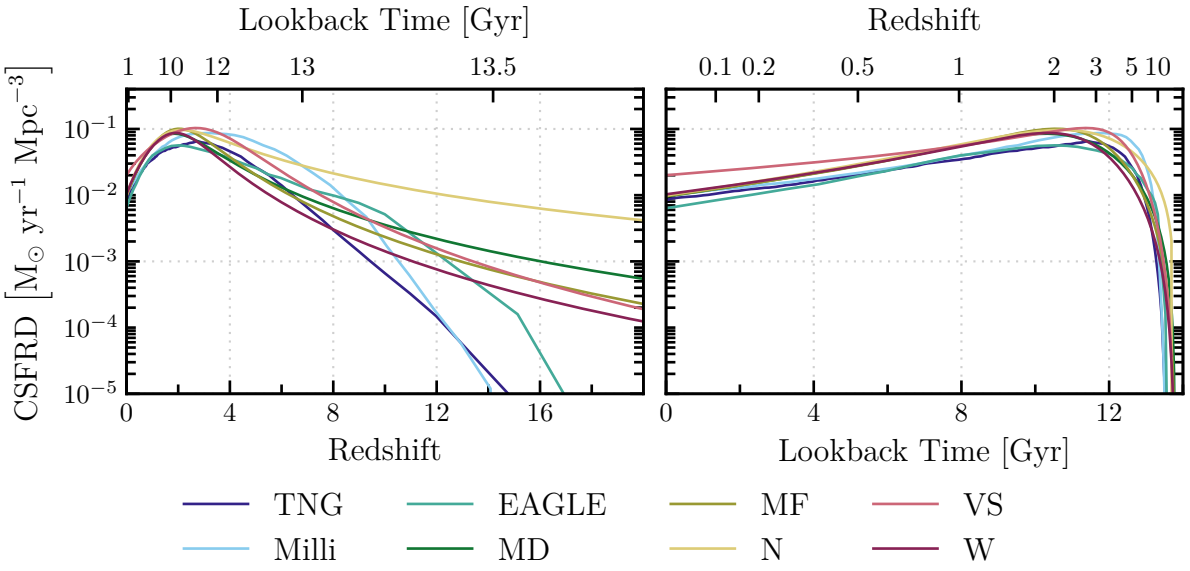

Figure 2.9: The CSFRD over redshift (top) and lookback time (bottom) for the empirical prescriptions from Madau & Dickinson (2014), Madau & Fragos (2017), Wilkins et al. (2019), Neijssel et al. (2019), van Son et al. (2023), and SFRs extracted from the MilliMillennium, EAGLE, and IllustrisTNG-100 simulations. Most prescriptions predicts similar rates at low redshifts. As observations become more scarce at higher redshift, the rates start to deviate with drastically different evolutions at $z > 8$.

$$\Psi\left(\frac{Z}{Z_\odot}\right) = \frac{\hat{\Gamma}\left[0.84, (Z/Z_\odot)^2 10^{0.30z}\right]}{\Gamma(0.84)}, \tag{2.13}$$

where Γ and $\hat{\Gamma}$ are the complete and incomplete gamma functions, respectively, and Z is the volume-averaged metallicity of newly formed stars at redshift z.

We consider two more CSFRDs with their own metallicity distributions. Both use the Madau & Dickinson (2014) CSFRD shape of Equation 1.14 but recalibrate the parameter. Neijssel et al. (2019) use the BBH population to calculate the CSFRD and use a log-normal distribution for the metallicity evolution. As shown in Table 2.2, their parameters result in an very high SFR at high redshifts and peaked metallicity evolution, as shown in Figures 2.9 and 2.11, respectively.

van Son et al. (2023) improved upon this prescription by altering the metallicity evolution into a skewed-lognormal distribution and by matching the parameters of the prescription to the TNG-100 simulation. This improves the CSFRD match with observations and creates a unique metallicity evolution with metal-rich star formation already at high redshifts. We note a difference in the TNG simulation CSFRD in this work and van Son et al. (2023) due to the extraction of SFR. We extract the SFR and mean stel-

	CSFRD				Metallicity Evolution
M&D	$a = 0.001$	$b = 2.7$	$c = 2.9$	$d = 5.6$	Langer & Norman (2006)
M&F	$a = 0.01$	$b = 2.6$	$c = 3.2$	$d = 6.2$	"
Wilkins	$a = 0.0103$	$b = 2.48$	$c = 3.10$	$d = 6.26$	"
Neijssel	$a = 0.01$	$b = 2.77$	$c = 2.9$	$d = 4.7$	log-normal
Van Son	$a = 0.02$	$b = 1.48$	$c = 4.44$	$d = 5.90$	skewed log-normal

Table 2.2: The empirical CSFRD and metallicity evolution parameters, where a, b, c, d are the parameters from Equation 1.14.

lar metallicity from the individual galaxies and their merger trees to retain the history of individual galaxies, while van Son et al. (2023) extract the SFR and gas metallicity from individual gas particles. Due to the averaging of the metallicity, we miss more extreme pockets of high and low metallicity. However, we can trace back the SFH for an individual galaxy, allowing us to determine transient rates per galaxy.

Throughout this thesis, we use the Aghanim et al. (2020) results as our assumed cosmology ($h = 0.6766$, $\Omega_{\rm M} = 0.3111$, and $\Omega_\Lambda = 0.6889$). All SFH must be brought to this cosmology to compare all the final rates. The empirical SFH extracted from UV observations has a h dependence coming from a $1/h^2$ for the SFR and a $1/h^3$ from the comoving volume. Since the empirical CSFRDs are given in $\rm M_\odot yr^{-1}Mpc^{-3}$, we transform these by first reintroducing the h dependence followed by applying our cosmology. The SFHs from the cosmological simulations and cosmic event rate observations, on the other hand, have an h^3 dependence coming from the comoving volume, but similar to the empirical CSFRD we transform them to our assumed cosmology.

2.3.2 SFHs from Cosmological Simulations

Cosmic volume hydrodynamic simulations start with dark matter and baryonic particles distributed through a simulation box according to initial conditions based on cosmic microwave background observations. The boxes are evolved up to the current time using simulated large-scale interactions, semi-analytical models for small-scale influences and, in some cases, also hydrodynamical gas modelling. The assumed strength of interactions and subgrid physics are tuned to match observations or according to theoretical prescriptions.

MilliMillennium Simulation

The MilliMillennium Simulation is a subset of the N-body dark matter Millennium Simulation with ΛCDM cosmology with parameters $h = 0.73$, $\Omega_{\rm M} = 0.25$, and $\Omega_\Lambda = 0.75$ (Springel et al. 2005). Released in 2005, it contains 270^3 particles in a $62.5\,h^{-1}\,{\rm Mpc}$ box, with each particle representing $8.6 \times 10^8\,h^{-1}\,{\rm M}_\odot$ dark matter with a spatial resolution of $5\,h^{-1}\,{\rm kpc}$. We will refer to the MilliMillennium as Millennium in this paper. As demonstrated by Stanway et al. (2018), this box is sufficiently large to recover the volume-averaged properties of the bulk galaxy population, although the full simulation would be required to recover rare systems such as extremely massive large-scale structures. Starting at $z = 127$, 64 selected time steps, known as snapshots, are stored with their gravitationally bound substructure, subhaloes. These are identified by the SUBFIND algorithm (Springel et al. 2001) and used to build a merger tree of subhaloes, which is the basic input for the semi-analytical models of galaxy formation (De Lucia & Blaizot 2007). When the gas surface density is higher than a critical value, star formation in a disk takes place and follows the parameterisation by Croton et al. (2006); bulge star formation, however, only occurs during the merger of subhaloes and follows the Somerville et al. (2001) collisional starburst model, which is only able to reproduce the observed gas fraction as a function of galaxy luminosity.

EAGLE Simulation

Evolution and Assembly of GaLaxies and their Environments (EAGLE) (Schaye et al. 2015; Crain et al. 2015) is a hybrid N-body and hydrodynamical simulation. It contains dark matter particles with a mass of $9.70 \times 10^6\,{\rm M}_\odot$, and baryonic gas particles of $1.81 \times 10^6\,{\rm M}_\odot$ in a $100\,{\rm Mpc}^3$ box for the fiducial model (L0100N1504). The EAGLE simulation has a $\Omega_{\rm M} = 0.307$, $\Omega_\Lambda = 0.693$, and $h = 0.6777$ cosmology and does not provide their output with explicit dependence on the Hubble parameter. Therefore, we use the simulations cosmology to reintroduce the h^3 dependence and then apply our cosmology to allow for comparison. While only 29 snapshots were recorded between $z = 127$ and $z = 0$, 1504^3 particles were used to study galaxy formation. The stellar formation is resolved using sub-grid physics and depends on the pressure in dense gas, and is tuned to reproduce the observed Kennicutt-Schmidt relation (Schmidt 1959). The simulation includes prescriptions for black hole and SN feedback mechanisms that return baryons to the intergalactic medium and enrich the environment. A full description can be found in Wiersma et al. (2009). The feedback mechanisms and star formation rate (SFR) are calibrated to reproduce the galaxy luminosity function at $z = 0.1$, BH-stellar mass

relation, and galaxy size (Crain et al. 2015). A merger tree is constructed using the same SUBFIND algorithm as the Millennium simulation, but with slight adjustments and inclusion of baryonic matter in substructure identification (Dolag et al. 2009).

IllustrisTNG Simulation

Similar to EAGLE, The Next Generation Illustris simulation (IllustrisTNG) is a hybrid simulation that contains dark matter and baryonic matter. These have particle masses $7.5 \times 10^6\,\mathrm{M}_\odot$ and $1.4 \times 10^6\,\mathrm{M}_\odot$, respectively, in the TNG100-1 simulation (Springel et al. 2018; Nelson et al. 2018; Pillepich et al. 2018b; Naiman et al. 2018; Marinacci et al. 2018), which we shall refer to as the TNG simulation in this paper. 1820^3 dark matter and 1820^3 baryonic particles are included in the simulation volume of 110.7^3 comoving Mpc and are evolved from $z = 127$ to present day in a $h = 0.6774$, $\Omega_\mathrm{M} = 0.30897$, and $\Omega_\Lambda = 0.6911$ ΛCDM Universe from Ade et al. (2015). Again, we scale to our own cosmology. Like the other two simulations, the IllustrisTNG is a hydrodynamic simulation but also includes magnetic fields and new feedback prescriptions. These and the galaxy formation models are fully described in Weinberger et al. (2017) and Pillepich et al. (2018a) and aim to agree with observational constraints, such as the CSFRD and the stellar mass content of galaxies at $z = 0$. Again, the SUBFIND algorithm finds subhaloes (galaxies), but the IllustrisTNG introduces a "SubhaloFlag" to identify gravitationally-bound clusters that are numerical artefacts and not of cosmological origin (Nelson et al. 2019). We remove non-cosmological subhaloes from our sample. By tracing the baryonic content of each galaxy, the SUBLINK algorithm generates merger trees (Rodriguez-Gomez et al. 2015).

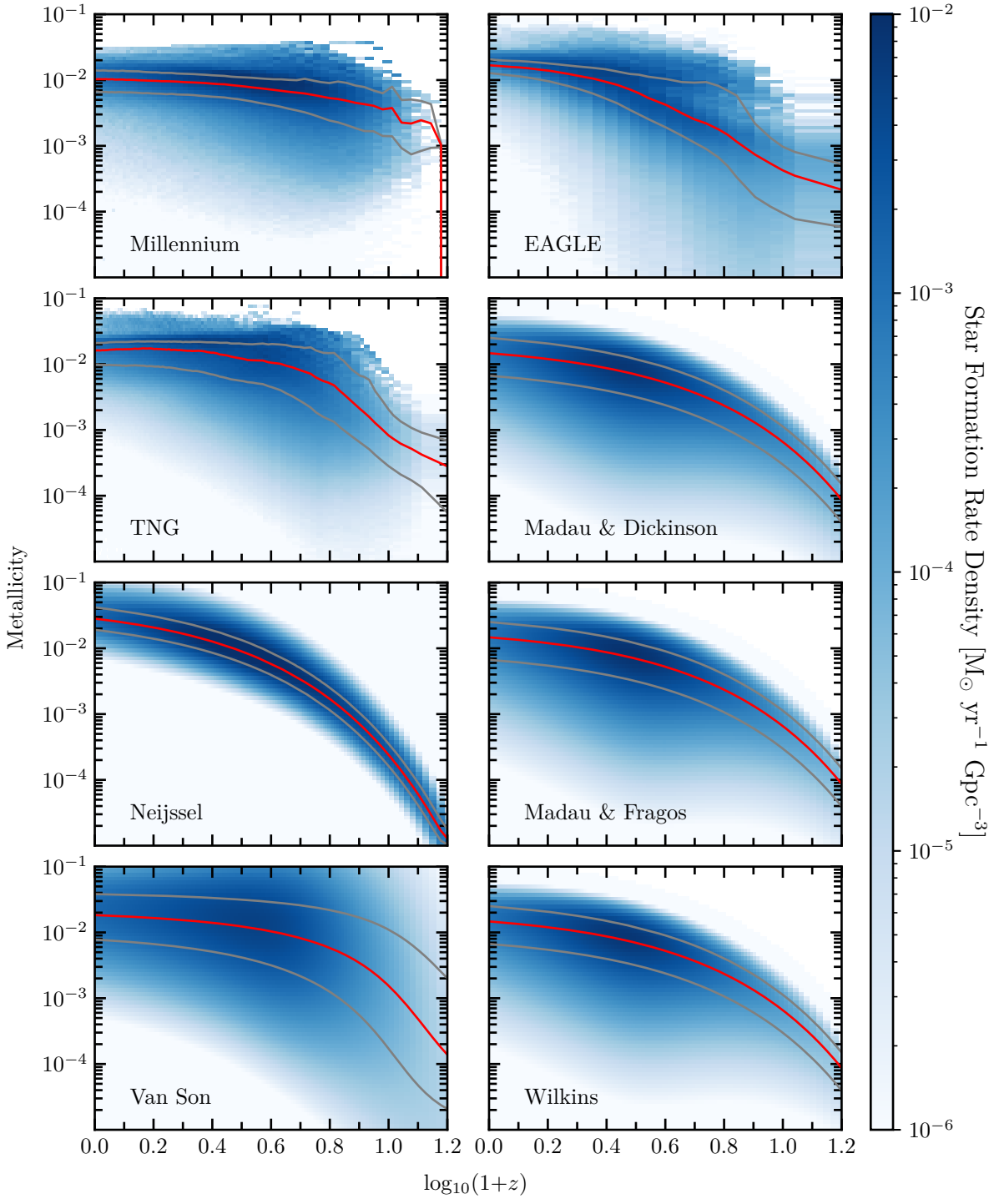

Figure 2.10: The SFR density distributions over metallicity and over $\log_{10}(1+z)$. The median SFR weighted metallicity is indicated with the red solid line with the 1σ spread shown by the solid grey lines. The metallicity is logarithmically binned in 100 bins between $Z = 10^{-5}$ and 1. Neijssel et al. (2019) and van Son et al. (2023) use a different metallicity distribution to the other empirical prescriptions. Their parameters are shown in Table 2.2.

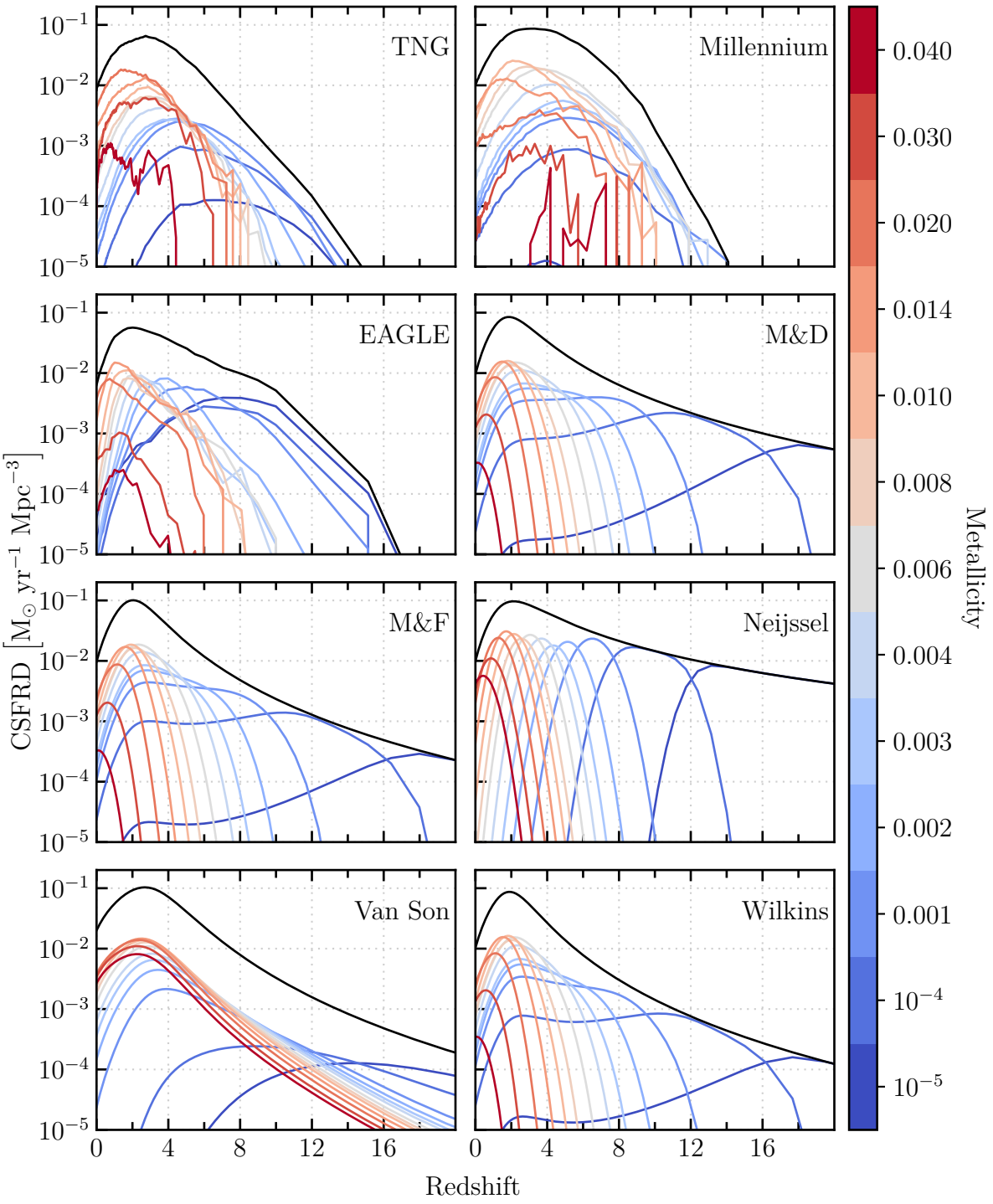

Figure 2.11: The SFR density distribution over redshift (z) split per metallicity. The colors indicate the BPASS metallicities and the black line is the total SFR.

2.4 Complex Stellar Populations

For the cosmological simulations, we extract the merger trees of each non-zero stellar-mass galaxy at $z = 0$ using the public APIs [EAGLE (McAlpine et al. 2016), TNG; (Nelson et al. 2018), Millennium (Lemson 2006)]. Each galaxy has its own individual metallicity and SFR evolution influenced by stellar evolution and galaxy interactions, allowing for a broader range of galaxy metallicities than the empirical CSFRD. The SFR distribution over metallicity and redshift in Figure 2.10 shows that the cosmological simulations have a wider metallicity spread and faster enrichment of the Universe than the empirical parameterisation. The latter is especially true for the Millennium simulation, which achieves a mean metallicity of 0.004 at $z = 10$ and stays nearly flat throughout cosmic history, only increasing to 0.01 at $z = 0$. This is similar to the mean metallicity evolution of the TNG simulation, which remains mostly flat with only a fast increase between $\log_{10}(1 + z) = 0.8$ and $\log_{10}(1 + z) = 1.0$. The EAGLE and empirical distributions, on the other hand, have a gradual increase in their mean metallicity towards current time. In the case of the EAGLE, we even see evidence for a bimodal distribution in the metallicity evolution with a constant high metallicity population at $Z = 0.015$ from $\log_{10}(1+z) = 0.8$ to current time, and a second lower metallicity population that is present from the start of star formation and slowly increases in metallicity over redshift. This complex behaviour cannot be reproduced in the analytical models typically used. This, for example, allows for low metallicity events to still occur when high metallicity events are more prevalent.

Using the metallicity and star formation at each snapshot for each galaxy and the dimensions of the simulation, we construct a volume-averaged CSFRD, as shown in Figure 2.9. At redshifts below $z = 2$, the shapes of the CSFRDs are similar but differ in normalisation with the Millennium CSFRD and semi-analytical prescription having the highest SFRs at $z = 0$ followed closely by the TNG and EAGLE CSFRD. Above $z = 2$, the shape of the Millennium CSFRD and the long tail of the empirical CSFRD stand out. It is significantly different than the other CSFRD by peaking later with a broader spread at $z = 3.31$. The empirical CSFRD, on the other hand peaks sharply at $z = 1.87$ with the tail continuing into high redshift, while the rates of the cosmological simulations at these early times, when we expect low metallicity to dominate, are low to non-existent. Based on the mean stellar metallicity reported by the simulation, individual galaxies are binned into one of the 13 BPASS metallicities, resulting in metallicity-specific SFR over redshift, as shown in Figure 2.11. The empirical SFH are split into the same metallicity

redshifts	[0.00, 0.01, 0.02, 0.03, 0.05, 0.06, 0.07, 0.08, 0.10, 0.11, 0.13, 0.14, 0.15, 0.17, 0.18, 0.20, 0.21, 0.23, 0.24, 0.26, 0.27, 0.30, 0.31, 0.33, 0.35, 0.36, 0.38, 0.40, 0.42, 0.44, 0.46, 0.48, 0.50, 0.52, 0.55, 0.58, 0.60, 0.62, 0.64, 0.68, 0.70, 0.73, 0.76, 0.79, 0.82, 0.85, 0.89, 0.92, 0.95, 1.00, 1.04, 1.07, 1.11, 1.15, 1.21, 1.25, 1.30, 1.36, 1.41, 1.50, 1.53, 1.60, 1.67, 1.74, 1.82, 1.90, 2.00, 2.10, 2.21, 2.32, 2.44, 2.58, 2.73, 2.90, 3.01, 3.28, 3.49, 3.71, 4.01, 4.18, 4.43, 4.66, 5.00, 5.23, 5.53, 5.85, 6.01, 6.49, 7.01, 7.24, 7.60, 8.01, 8.45, 9.00, 9.39, 10.00, 10.98, 11.98, 14.99, 20.05]

Table 2.3: The redshifts at which the cosmic stellar transients are calculated. These come from the TNG simulation, see Section 2.3.2.

bins.

The metallicity distributions in Figure 2.11 indicate an early start in high metallicity star formation in the cosmological simulations. At $z \sim 6$ solar metallicity star formation is ongoing, while the empirical prescription only starts formation at this metallicity at $z = 4$. The faster enrichment significantly impacts the rate of specific transients due to their sensitivity to metallicity, see Section 2.2. Furthermore, a late start in star formation in the cosmological CSFRD reduces the amount of low-metallicity star formation at high redshift.

To estimate transient rates, the metallicity-specific SFHs must be combined with the associated transient DTDs from Section 2.2.1. This is achieved by sampling the final lookback time into 100 points (j) based on the snapshot redshifts of the TNG simulation, as shown in Table 2.3. These provide enough detail at the redshift ranges considered in this thesis and are transformed into lookback time using our assumed cosmology in Section 2.3.

Together with the delay time of each individual transient/system, the moment of stellar birth can be calculated. The weight of the transient (w_i) is recalculated by the metallicity-specific star rate at the moment of the stellar birth. The SFR at this moment in time is calculated by linearly interpolating between the given lookback times and SFR from the SFH prescription:

$$R_j = \sum_i^N w_i * \mathrm{SFH}(t_i + t_j), \tag{2.14}$$

where SFH is a function of the SFR at a specific metallicity over lookback time, t_i is the delay time of event i, t_j is the lookback time at which the transient rate is calculated.

R_j is the transient rate at t_j at a specific metallicity, and N is the total number of this transient type. The total transient at t_j is the sum of R_j over the 13 BPASS metallicities. Using the combintation of star formation history, metallicity evolution and stellar evolution, we are able to create a simulated cosmic stellar population and in Chapter 3 we look at the predicted population from each of the different CSFRD prescriptions.

Chapter 3

Estimating Transient Rates

With the complex stellar and transient populations from Chapter 2, we can predict stellar transient rates on a cosmological scale and compare them against observations over a range of redshifts using the method introduced in Section 2.4. To validate the physics involved in the predictions of BBH transients, we can compare the other stellar transients against observations to understand where our predictions are limited.

Since the observations for GW transients are still limited and SNe observations are plentiful, they provide the perfect test for our population synthesis. The CCSN and PISN rates originate from massive stars and could leave an imprint on the BBH rate. At the same time, Type Ia SNe come from binary systems, like GW transients, and probe the mass transfer properties. With each of these transients probing a different component of the same cosmic stellar population, we can identify areas in the stellar physics or the SFH that require attention and improvement.

We employ the SFHs described in Section 2.3 to account for the variation and differences in the CSFRD and metallicity evolution, which we hope to constrain using a variety of transients. First, we will discuss the stellar transients individually and compare them against their observations before moving on to joint analysis.

3.1 Type Ia Supernovae

The formation of a white dwarf and subsequent accretion or merger leading to a thermonuclear explosion takes at least a few 10^7 years in BPASS, depending on metallicity and stellar evolution, due to the low-mass progenitors and inherent binary nature of this event. With the long time between stellar birth and SN, the Type Ia rate probes earlier star formation (Ruiter et al. 2009; Mennekens et al. 2010; Ruiter et al. 2011; Maoz & Mannucci 2012; Eldridge et al. 2019), which we confirm by comparing the peaks of star formation against the peaks of the Type Ia rate in Table 3.1. The peak Type Ia SN rate occurs $\Delta(z) \approx 1 - 2$ later than the peak in star formation, with the exact delay

	SFH	Ia	CCSN	PISN	LGRB	BBH	BHNS	BNS
	redshift (z)							
Millennium	3.31	1.00	2.89	4.01	4.01	2.00	2.32	2.10
EAGLE	2.01	0.92	2.00	3.49	3.49	1.90	2.21	1.90
TNG	2.73	1.00	2.73	4.43	4.42	2.31	2.58	2.10
M&D	1.87	0.85	1.90	2.73	2.73	1.53	1.74	1.53
M&F	2.04	0.89	2.10	2.73	2.73	1.74	1.90	1.67
Neijssel	2.13	1.00	2.32	4.66	5.00	2.58	2.90	2.10
Van Son	2.68	0.95	2.73	3.28	3.28	2.00	2.32	2.00
Wilkins	1.89	0.82	1.90	2.44	2.44	1.60	1.74	1.60

Table 3.1: The redshift (z) of the peak in SFH, Type Ia, CCSN, PISN, and BBH rates.

depending on the simulation and its metallicity evolution.

The rates over redshift are shown in Figure 3.1 together with a collection of observations, which are summarised in Table F.1. As mentioned in Section 2.2.3, the SD channel dominates the Type Ia SN predictions with no contribution from the DD channel and, because of this, these predictions are an underestimation of the Type Ia SN rate (see Section 6.1 for more details).

Furthermore, the definition of what BPASS models undergo a thermonuclear explosion can drastically alter the type of SNe contributing to the Type Ia rate. Only a narrow accretion rate range of a few $10^{-7}\,\mathrm{M}_\odot\,\mathrm{yr}^{-1}$ should lead to WD growth and a thermonuclear runaway (e.g. Ruiter et al. 2011). Most BPASS models tagged as Type Ia have accretion rates between $10^{-7}\,\mathrm{M}_\odot\,\mathrm{yr}^{-1}$ and $10^{-5}\,\mathrm{M}_\odot\,\mathrm{yr}^{-1}$. However, a more careful consideration of the accretion rate is required for a stronger conclusion on the Type Ia rate. Another option would be to more accurately determine the type of WD formed based on the composition in the detailed stellar models, but this is beyond the scope of this thesis.

The SD channel alone achieves Type Ia rates comparable to observations, as shown in Figure 3.1. The TNG and EAGLE simulations go through most observations at low redshifts but are at the lower end of the observations around $z = 1$. At the same time, the empirical prescriptions are closer to the observations, which results from general CSFRD shape, where the empirical prescriptions have higher SFR at their peak than the TNG and EAGLE simulations. However, the uncertainty of these observations is large and corrections for dust can alter the rate significantly.

The model predictions only differ around a factor of 2. To assess the goodness of the predictions, we calculate the reduced χ^2 and see in Table 3.2 that the EAGLE and TNG have reduced χ^2 closest to 1. However, we note that due to the large uncertainties

of the observations, all reduced χ^2 of the Type Ia predictions are close to 1. The fact that the difference between prescriptions using different metallicity evolutions is small indicates that it is minimally important in predicting the Type Ia rate. Instead, the stellar evolution and overall shape of the CSFRD determine the shape and rate of the Type Ia rate.

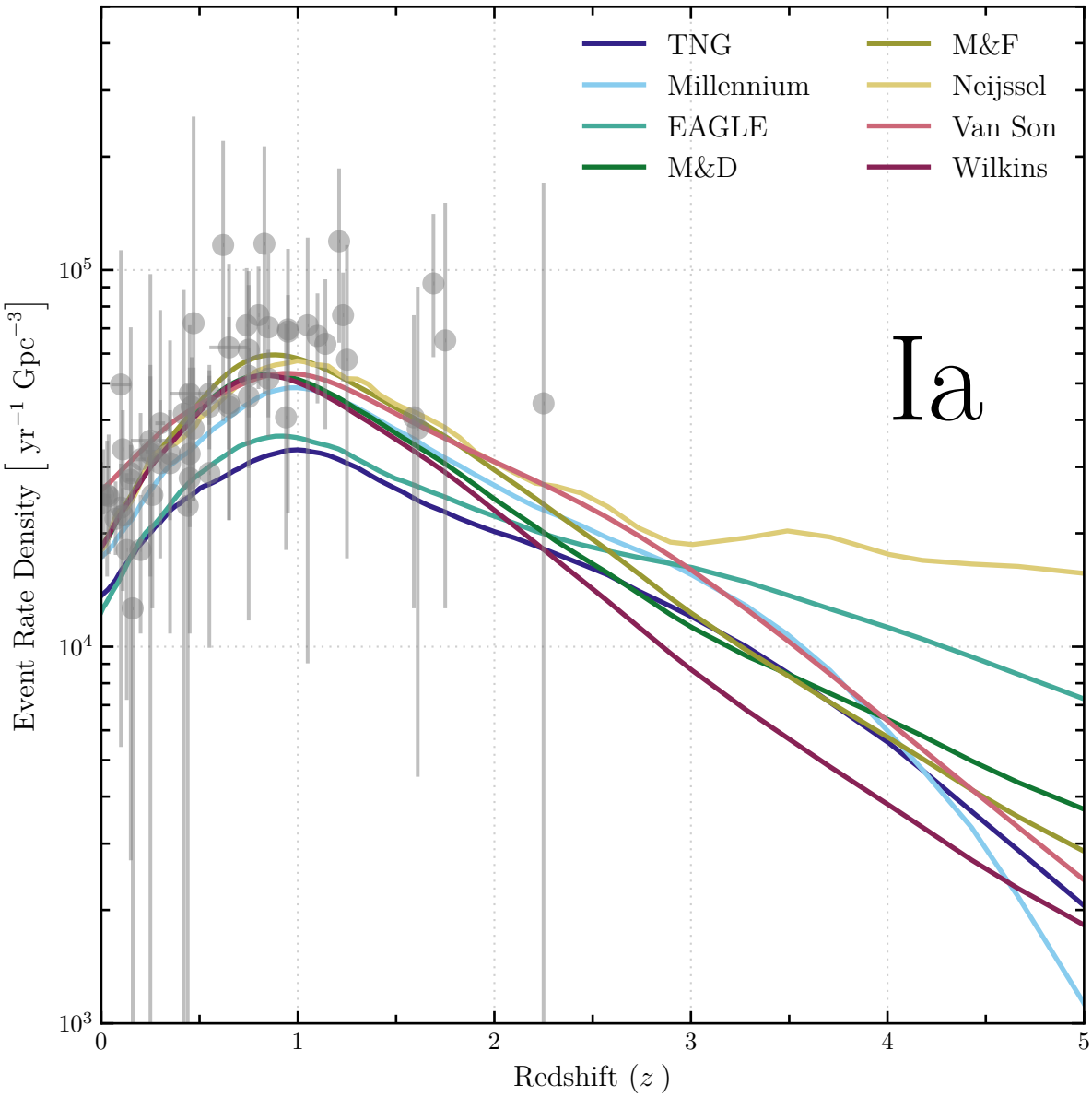

Figure 3.1: Type Ia SN rate predicted from the star formation histories, compared with observations drawn from a collection of surveys described in Table F.1.

	Type Ia	**CCSN**	**PISN[a]**	**LGRB***	**Combined**
N	60	25	5	10	90
TNG	1.06	0.56	0.41	10.20	0.89
Millennium	0.39	0.99	4.19	9.34	0.76
EAGLE	0.93	0.70	9.31	8.94	1.33
Neijssel	0.36	0.95	3.51	9.99	0.63
Wilkins	0.28	1.32	21.69	7.61	1.77
M&D	0.30	1.17	23.49	7.49	1.82
M&F	0.25	1.36	31.43	7.04	2.31
Van Son	0.30	7.14	8.15	8.88	2.67

Table 3.2: The reduced χ^2 value from each model using the given data, where N is the number of observed cosmic event rates for the specific event type. **Combined** weights each observed rate equally. $\star$ is not included in **Combined**, because the BPASS models from Chrimes et al. (2020), where used to normalise the LGRB observations. [a]: the calculated rate from Zhao et al. (2021) is left out due to the absence of an uncertainty on the observation. The SFHs are sorted based how close their reduced χ^2 is to 1.

3.2 Core-Collapse Supernovae

CCSNe occur in young stellar populations because the CCSN progenitors are massive stars that burn through their nuclear fuel quickly and, thus, have short delay times ($10^{6.5}$- $10^{8.3}$ years). This creates a tight relationship between the SFR and cosmic CCSN rate, as the alignment of the peaks between the CCSN rate and SFH peaks in Table 3.1 shows. Not only do the peaks align, but the CCSN predictions over redshift also closely track the shape of the associated CSFRD, as shown in Figure 3.2 with observations from Table F.4. The exception again seems to be the SFH from van Son et al. (2023), which overestimates the CCSN at $z = 0$. This is most likely a result of a higher SFR at $z = 0$ caused by the usage of the particle data, as described in Section 2.3.1, and results in a reduced χ^2 value of 7.14.

Below $z = 0.5$, the other prescriptions follow observations closely until around $z = 0.9$, after which the observations are split into two trend lines. The first has data points around $z = 1$ and $z = 1.5$ with high CCSN rates originating from a collection of surveys (Melinder et al. 2012; Dahlen et al. 2012; Graur et al. 2011). At these redshifts, the empirical CCSN rate predictions have the best fitting rates. The cosmological CCSN rate predictions align better with the second group of data points, located between $z \sim 1 - 2.5$, have lower rates, and originate from a single survey by Strolger et al.

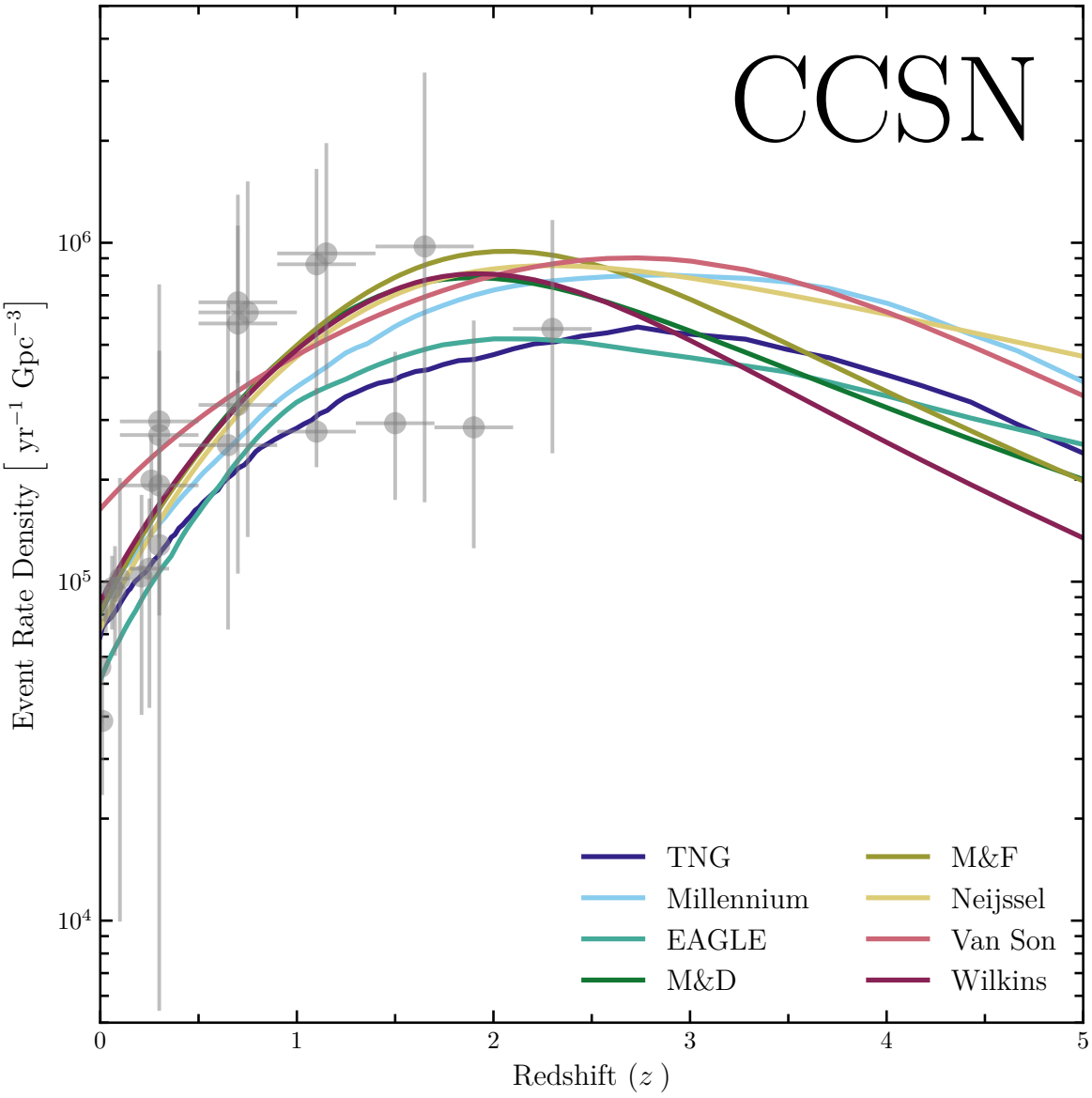

Figure 3.2: Predicted CCSN rates with a compilation of observational estimates in grey for comparison (see Table F.4).

(2015). Different approaches in correcting for missed SNe due to high extinction could result in this grouping. Because the CCSN rate follows star formation closely, they often happen in very dusty star-forming regions and can be obscured, especially at high redshifts. Hence the fraction of missed SNe has to be accounted for. The higher estimates use a prescription from Mattila et al. (2012), which can increase the CCSNe rate significantly. Local overdensities of star formation in the survey fields might also cause these observations to be overestimated (Dahlen et al. 2012). Strolger et al. (2015), on the other hand, use their own method based on the Calzetti et al. (2000) extinction law. These high redshift observations are challenging and only survey a small area compared to other SN surveys leaving them more vulnerable to cosmic variance and low number counts. Finally, this grouping and the large standard deviation of the first group results in a 0.56 reduced χ^2 for the TNG simulation and slightly worse values for the simulations and Neijssel et al. (2019) prescription, as shown in Table 3.2.

3.2.1 CCSN Subtypes

Although the same explosion mechanism causes CCSNe, the subtypes come from progenitors with different mass ranges and mass loss histories, as described in Chapter 2. By looking at the rate of the subtypes and their fraction to the total CCSN rate, we extract more information about the progenitors. However, the limited number of SESN events restricts the calculation of an observed rate. Frohmaier et al. (2021) is one of the few studies to calculate the total combined rate for Type IIb, Ib, and Ic events. Since BPASS does not distinguish between Type II subtypes except for Type IIP events, we use the fraction from Eldridge et al. (2013) of 0.6541 to estimate the Type IIb rate from the non-IIP Type II events. This fraction is not well constrained and differs from other surveys (e.g. Smith et al. 2011; Li et al. 2011a).

Figure 3.3 shows that the predicted rates lie above the Frohmaier et al. (2021) observed rate estimate of 2.18×10^4 yr^{-1} Gpc^{-3} in our cosmology at $\langle z \rangle = 0.028$. Rates calculated using the EAGLE model approach this rate with 2.40×10^4 yr^{-1} Gpc^{-3}, but the other SFHs overpredict the observed rate with van Son et al. (2023) deviating the most with a rate of 8.23×10^4 yr^{-1} Gpc^{-3}.

Most Type II rate predictions align with observed rates from Li et al. (2011b) and Cappellaro et al. (2015) in Table F.3. For the other CCSN subtypes, Type Ib and Type Ic, no observational cosmic rates are available for comparison. Instead, we note that the Type Ib and Ic rates have similar shapes due to similar progenitors and sensitivity to the metallicity evolution. The absolute rate of Type Ib events, however, is slightly higher

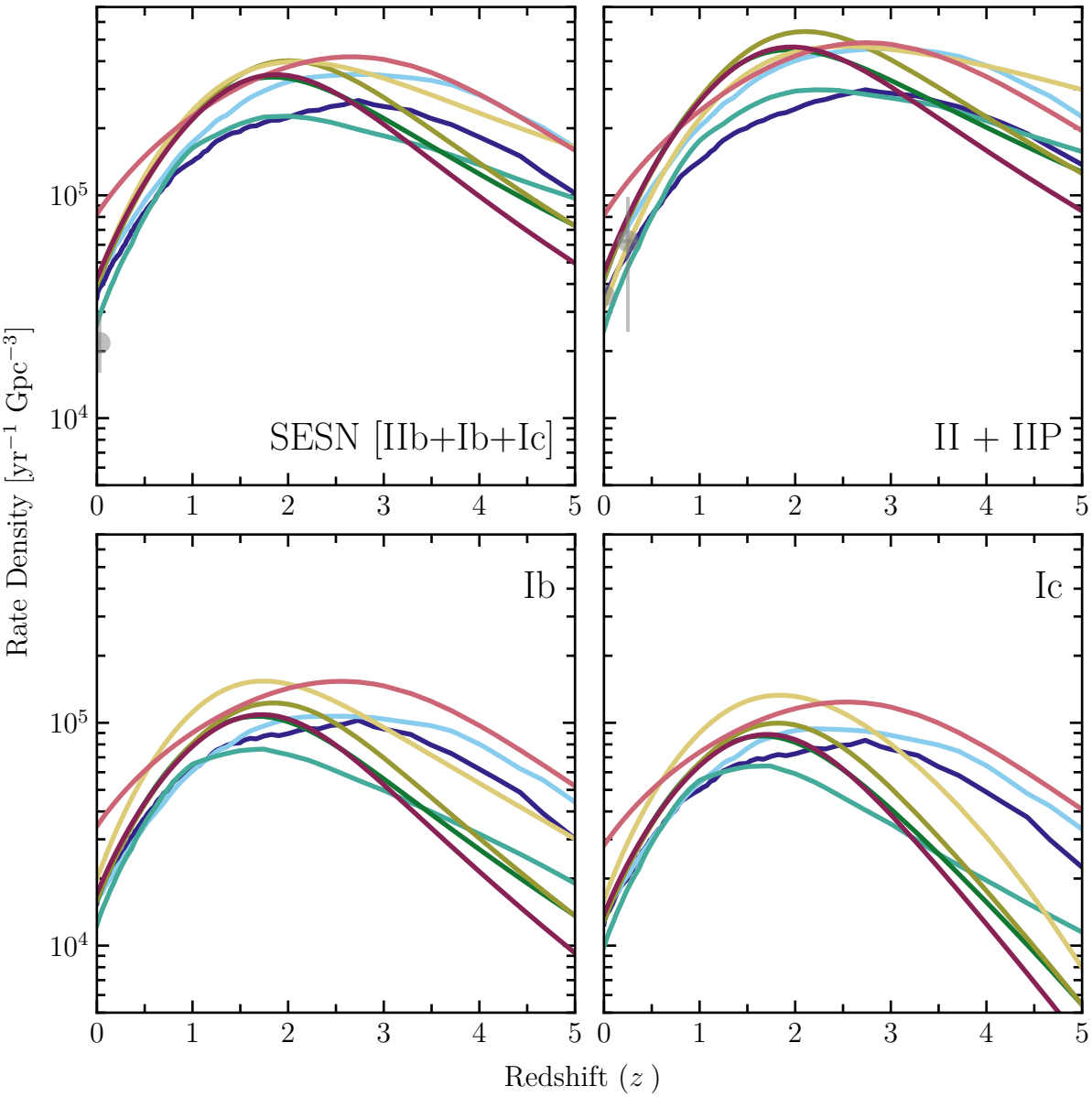

Figure 3.3: The CCSN events split up by possible subtypes with a single observed stripped-envelope SN (SESN) rate by Frohmaier et al. (2021), and two Type II observations (See Table F.3). The SESNe rate contains Type IIb SNe according to the fraction from (Eldridge et al. 2013), while the Type II+IIP has this fraction removed, since the observations are classified as such. Colours are the same as Figure 3.2.

than Type Ic due to the difficulty of stripping the helium envelope required for a Type Ic SN. Distinguishing between the individual predictions for either of these SN types is impossible at low redshift due to the minimal difference in the rates, which could be attributed to a small difference in metallicity between the predictions. The metallicity distributions in Figure 2.10 shows that the EAGLE, TNG and empirical CSFRDs have

	II	Ib	Ic
	CCSN Fraction		
M&D	0.65	0.20	0.16
Millennium	0.67	0.18	0.15
EAGLE	0.57	0.24	0.19
TNG	0.59	0.22	0.18
M&F	0.65	0.20	0.16
Neijssel	0.51	0.27	0.22
Van Son	0.62	0.21	0.17
Wilkins	0.64	0.20	0.16
Shivvers et al. (2017)	0.80	0.11	0.09
Perley et al. (2020)	0.748	0.251	
Smith et al. (2020)	0.766	0.234	
Eldridge et al. (2013)	0.74	0.09	0.17

Table 3.3: Fraction of CCSN subtypes at $z = 0$ for predicted rates. Shivvers et al. (2017) is volume-limited to 60Mpc. Due to rounding, the fractions do not add up to 1. Perley et al. (2020) and Smith et al. (2020) are corrected to only include Type II and Ib/c SNe.

similar metallicities at these low redshifts, while the Millennium simulation has a slightly lower mean metallicity. However, above a metallicity of half solar, the Ib/c rates in the DTD are near constant, which, together with the similar CSFRD, results in similar rates for the cosmic Type Ib/c predictions. At higher redshifts, the metallicity and CSFRDs become more distinct, separating the cosmic Type Ib/c rates, seen in Figure 2.9 and 3.3.

The Type II SN rates are an order of magnitude higher than the Type Ib and Ic rates and dominate the CCSN predictions because the progenitor systems do not need to undergo envelope stripping and can be of effectively single or binary star nature, resulting in the predicted rates more closely following the CSFRD.

3.2.2 CCSN Subtype Fraction Evolution

While the cosmic rates of CCSN subtypes are hard to come by, the fractions of Ib, Ic, and IIb with respect to the total number CCSNe are available from several surveys (Li et al. 2011a; Smith et al. 2011; Shivvers et al. 2017; Perley et al. 2020). Therefore, we show our predictions and the fractions from the volume-limited survey up to 60 Mpc from Shivvers et al. (2017) in Table 3.3. Our Type II predictions are significantly lower than the observed fraction. However, we only consider the rate at $z = 0$, which could reduce our Type II rate since the local metallicity might be higher than out to 60 Mpc.

The magnitude-limited survey from Perley et al. (2020), however, predicts a lower Type II fraction of 0.722, which is closer to our predictions, although still significantly higher than the 0.65 and 0.67 fractions for the Madau & Fragos (2017) and Millennium predicted fractions. A slightly higher fraction of 0.766 is found in the 100 Mpc volume-limited survey by Smith et al. (2020). Eldridge et al. (2013) contain a complete sample within 20 Mpc but is used to determine the Type Ib/c parameters in BPASS.

Instead of the Type II events, there are fractionally more Type Ib/c events in our predictions, of which the bulk is Type Ib events. This discrepancy could indicate too swift an enrichment, a too strong stellar wind prescription, a different mass transfer efficiency, or a combination of the above. While the EAGLE and TNG simulations enrich faster than the Millennium simulation and empirical description, the Type Ib/c rate is most likely closely linked to stripping due to binary interactions with the ratio between Type Ib and Ic being linked to stellar winds (Dessart et al. 2012a, 2020; Yoon et al. 2022; Aguilera-Dena et al. 2023). Although the Type Ib/c definition is observationally motivated in this thesis, uncertainty remains in what fraction of hydrogen or helium left in the theoretical model relates to each observational classification, which we will discuss more in-depth in Section 6.1.

Looking at the evolution of the relative fractions of CCSN SNe over redshift in Figure 3.4, makes it clear that the Type IIP remains constant over redshift because these typically come from single stars and wide binaries. In comparison, the other type II SN fraction decreases with decreasing redshift, being replaced by Type Ib/c. The reason for this is that while binary interactions remove much of the envelope, stellar winds play a significant role in further evolution. Thus, more metal-rich stellar populations are dominated by SNe that have experienced more mass loss. The scale of this change depends on the metallicity distribution, as shown in Figure 2.10, where the mean metallicity evolution of the Millennium simulation is nearly flat, as is the evolution of the Type Ib/c rate in Figure 3.4. The other SFHs, on the other hand, have a clear metallicity evolution, which shows in the relative fraction change indicating that the Type Ib/c fractions over redshift are good tracers for the metallicity evolution and might allow future observations of these rates to constrain the IMF and cosmic metallicity evolution, despite model uncertainty (Fryer et al. 2022a).

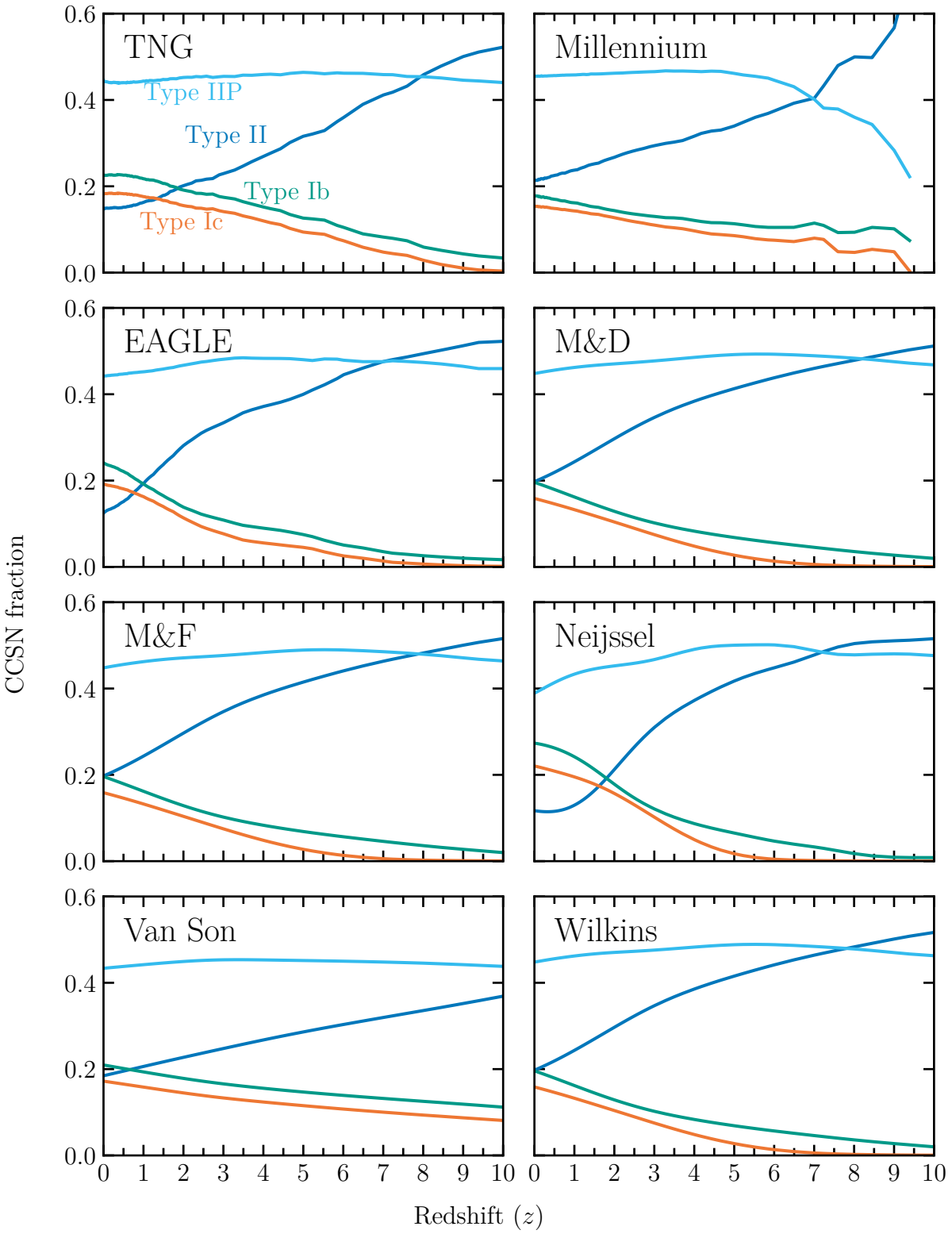

Figure 3.4: The relative fraction of all CCSN subtypes with Type IIP (light blue), II (dark blue), Ib (orange) and Ic (green) SNe. As metallicity increases towards $z = 0$, Type Ib/c SNe become more prevalent.

3.3 Long Gamma-Ray Bursts

LGRB afterglows have been observed as coincident with broad-lined Type Ic (Ic-BL) and represent a subset of energetic Ic events, where a relativistic jet is launched from the surface of a nascent black hole or magnetar formed during core-collapse (e.g. Heger et al. 2003; Langer 2012). The furthest GRB has been measured at $z = 9.4$ (Cucchiara et al. 2011), but it is difficult to derive a volumetric rate for such sources because their emission is highly beamed. As a result, their observability depends on the event geometry, specifically the jet opening angle and inclination.

We use the observed GRB rate over redshift from the SHOALS sample (Perley et al. 2016a) that we correct for the event geometry and missed low-luminosity events. To achieve this, we adopt the method from Chrimes et al. (2020) and integrate over the GRB luminosity function of Pescalli et al. (2016) from an isotropic equivalent energy of $E_{low} = 10^{48.1}$ erg to $E_{max} = 10^{56}$ erg while correcting for an opening angle of $\theta = 9.9°$. The grey triangle in Figure 3.5 shows the corrected SHOALS rate.

The predicted LGRB rates from BPASS, shown as solid lines in Figure 3.5, only contain events formed through chemically homogeneous evolution at low metallicities (Eldridge et al. 2017), which is lower than observed, as expected. Although in Briel et al. (2022) we implemented tidal LGRB sources in our predictions based on the models from Chrimes et al. (2020), we do not do so here due to the remnant mass determination and remnant mass being altered significantly in this thesis compared to the standard BPASS output. Instead, the tidal LGRB pathway mostly contributes at low redshifts, altering the gradient of the predictions and possibly peaking at lower redshifts. Due to the difficulty in constraining the observed rate and because the agreement is, of course, in part a consequence of the tuning of the LGRB opening angle parameters with a similar empirical CSFRD prescription as adopted here (Chrimes et al. 2020), it is not possible to distinguish between the SFHs as of yet. As such, we also show the observations with a 20° opening angle to indicate the uncertainty in event geometry.

Although the LGRB are related to the Type Ic, their relative fractions evolve oppositely in Figure 3.4. While the Type Ic increase over redshift, the LGRB rate drops significantly because the angular momentum required for the LGRB is removed by the stronger stellar winds in a more enriched Universe (Woosley et al. 2002; Vink et al. 2001). Therefore, LGRBs are sensitive to low metallicity star formation. This relation between the two event rates can help us probe the metallicity distribution of a stellar population, especially since the chemically homogeneous LGRB event have a short delay allowing us

to probe the change in low metallicity star formation (Metha et al. 2021).

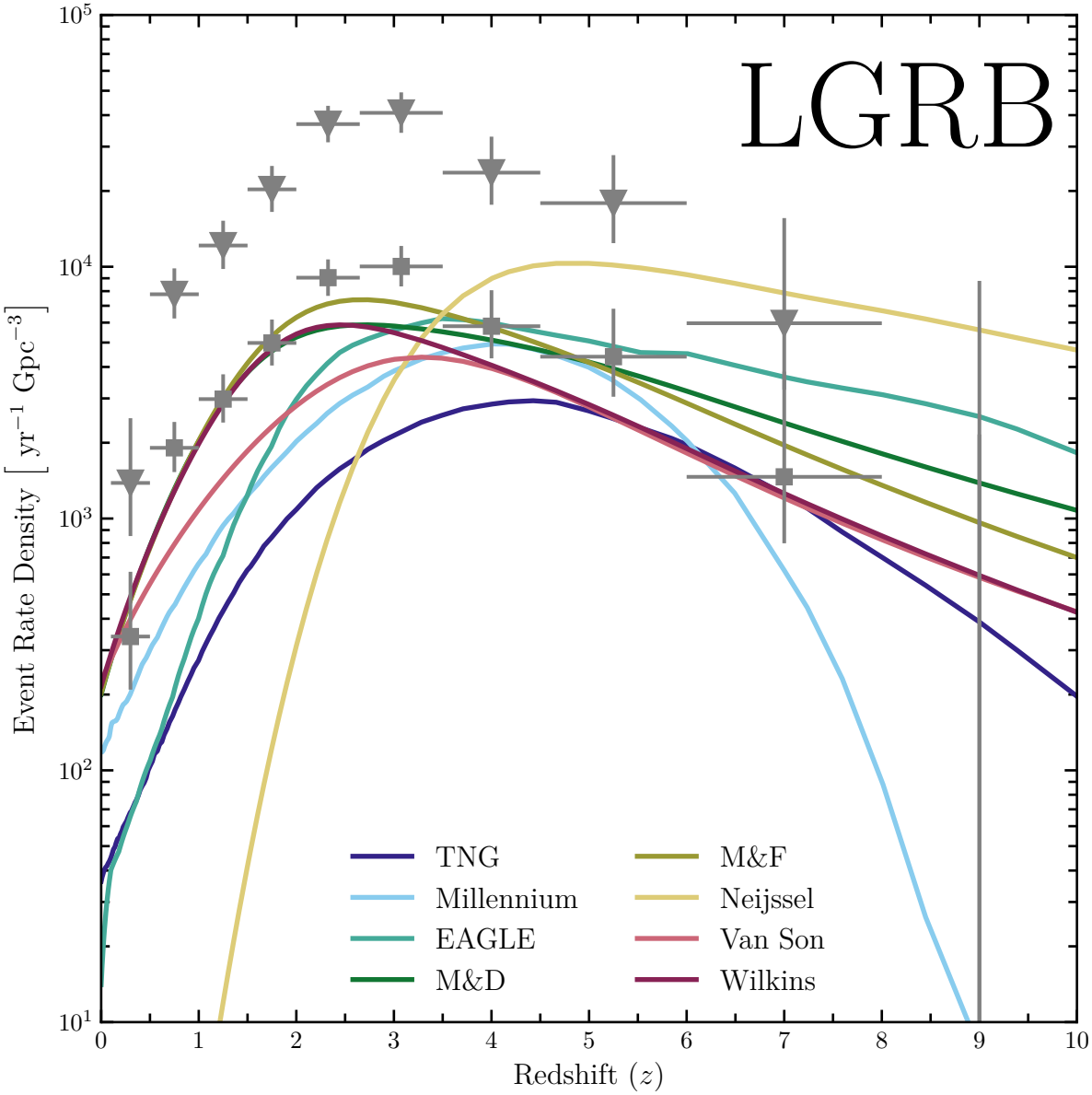

Figure 3.5: The predicted LGRB rates from the standard BPASS output for the considered SFH. The opening angle and luminosity corrected SHOALS rates are shown for comparison using the parameters from Chrimes et al. (2020) with $\theta = 9.9°$ (grey triangles) and $\theta = 20°$) (Perley et al. 2016a).

3.4 Pair Instability Supernovae

As mentioned in Section 1.4.1, no smoking-gun evidence of a PISN has been observed, although a few hydrogen-poor SLSN-I have been identified as possible candidates (Woosley et al. 2007; Cooke et al. 2012; Gal-Yam et al. 2009; Terreran et al. 2017; Gomez et al. 2019). Their energy requirements are too high to be consistent with the classical core collapse mechanism, but this remains unproven (Kozyreva & Blinnikov 2015), and alternative explanations, such as magnetars (Howell 2017; Kasen & Bildsten 2010; Woosley 2010; Inserra et al. 2013), rotational PISN (Renzo et al. 2020b), and late leakage from pulsar wind nebula (Dessart et al. 2012b), are also likely. Nonetheless, in Figure 3.6, we have used the observed rate of hydrogen-poor Super-Luminous SNe (SLSN-I) that are possible PISNe, summarised in Table F.2, for comparison. The simulation event rates show the non-smooth nature of the low metallicity SFR at low redshift, specifically the EAGLE simulation. Its event rate has a significant drop at $z = 0.1$, which is caused by a drop in the low metallicity star formation. Since they have limited star formation at low redshift and PISN mostly occur in low metallicity environments, only the predicted event rate from the TNG simulation aligns with the observations. The uncertainty in the formation pathway of SLSN-I makes it not possible to state if SLSNe-I are a good indicator for the PISN rate, except that their observed rate is within an order of magnitude of our predictions. However, if there is a relation between the PISN rate and SLSN-I, the CSFRD from Neijssel et al. (2019) does not accurately follow the same gradient as the observations. It does not have sufficient low metallicity star formation at low redshift and is higher than the other CSFRD at high redshifts, which is a consequence of the log-normal metallicity distribution.

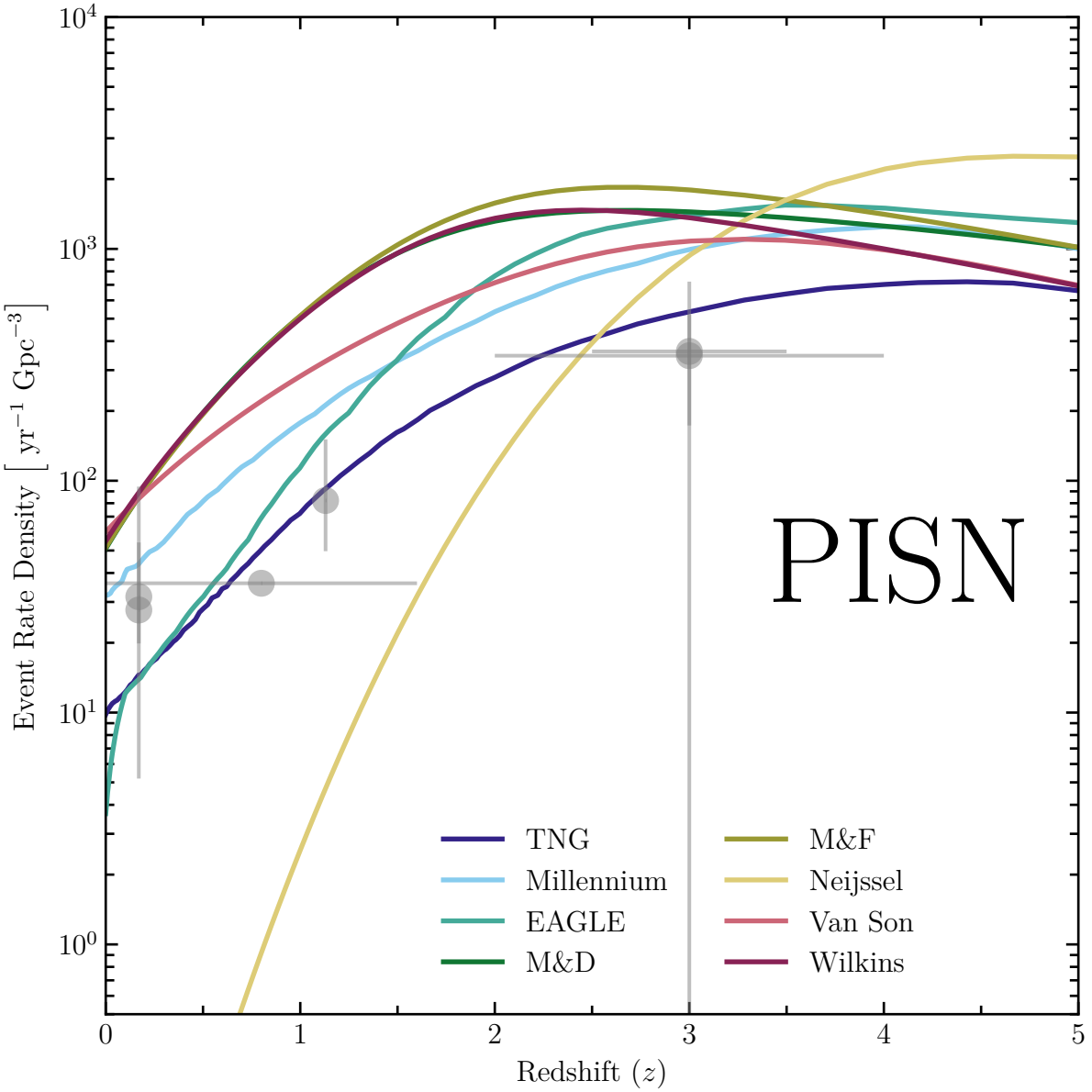

Figure 3.6: Predicted PISN rates with observational rates from SLSN-I measurements (see Appendix Table F.2).

3.5 Compact Objects

3.5.1 Binary Black-hole Mergers

The massive star nature of BBH progenitors lead to fast compact object formation, but orbital decay through GW emission is a slow process, which should result in the peak of BBH mergers occurring after the peak SFH. However, since the BBH merger rate is sensitive to metallicity and mostly occurs at low metallicity, this does not have to be the case, as is the case for the prescription from Neijssel et al. (2019). Due to its peaked metallicity distribution, its peak of BBH mergers occurs before the peak of star formation. For all other prescriptions, the BBH rate peak occurs after the SFR peak.

A more direct comparison is possible with recent results from GWTC-3, as described in Section 1.4.2, which includes estimates for a variety of population models at $z = 0$ for non-evolving merger rates and at $z = 0.2$ for redshift-dependent rates (Abbott et al. 2023). Figure 3.7 shows their range when only considering the lowest 5% and highest 95% credible boundaries out of the `PDB (ind)`, `MS`, and `BGP` models (for a description of the models, see Abbott et al. 2023), whose ranges are shown in Figure 3.8. All predictions fall within the combined 90% credible interval from 16 to 129 yr^{-1} Gpc^{-3} for the non-evolving merger rate at $z = 0$, although the Millennium and Empirical predictions are at the higher end of the observational range. However, the merger rate increases over redshift, and when this is taken into consideration, the observed rate decreases to 17.1-45 yr^{-1} Gpc^{-3}, as the bar at $z = 0.2$ in Figure 3.7 shows. This combined credible interval has been constructed in a similar fashion to the region at $z = 0$ but considers three BBH population models: `PP`, `FN`, and `PS` (For a description of the models see Abbott et al. 2023), which evolve over redshift. At $z = 0.2$, the observational constraints from Abbott et al. (2023) are the strongest, and the combined 90% credible range from their collection of models lies above most predicted merger rates, except for several empirical prescriptions. Despite that, the simulations with a fast enrichment, the EAGLE and TNG simulations, approach this range, which shows the strong correlation between the BBH rate and metallicity evolution.

More detail can be obtained by looking at the specific population models used by Abbott et al. (2023) instead of the combined credible interval. The conversion from measured to intrinsic rates introduces several model-dependent uncertainties in the BBH rate and can move the observed rate towards and away from our predictions. For the constant merger rate at $z = 0$, shown in the left-most panel in Figure 3.8, most uncertainty in the credible interval comes from the `Mixed-Source model`, while the other models are

clustered around the same rate of ~ 25. Most empirical rates and the Millennium simulation are close to the observations, while the TNG, EAGLE, and Neijssel et al. (2019) prescriptions are significantly lower than the observations. Since we only consider the isolated binary evolution formation pathway, all rates being underpredicted is an improvement from overpredicting, which is common in other population synthesis codes

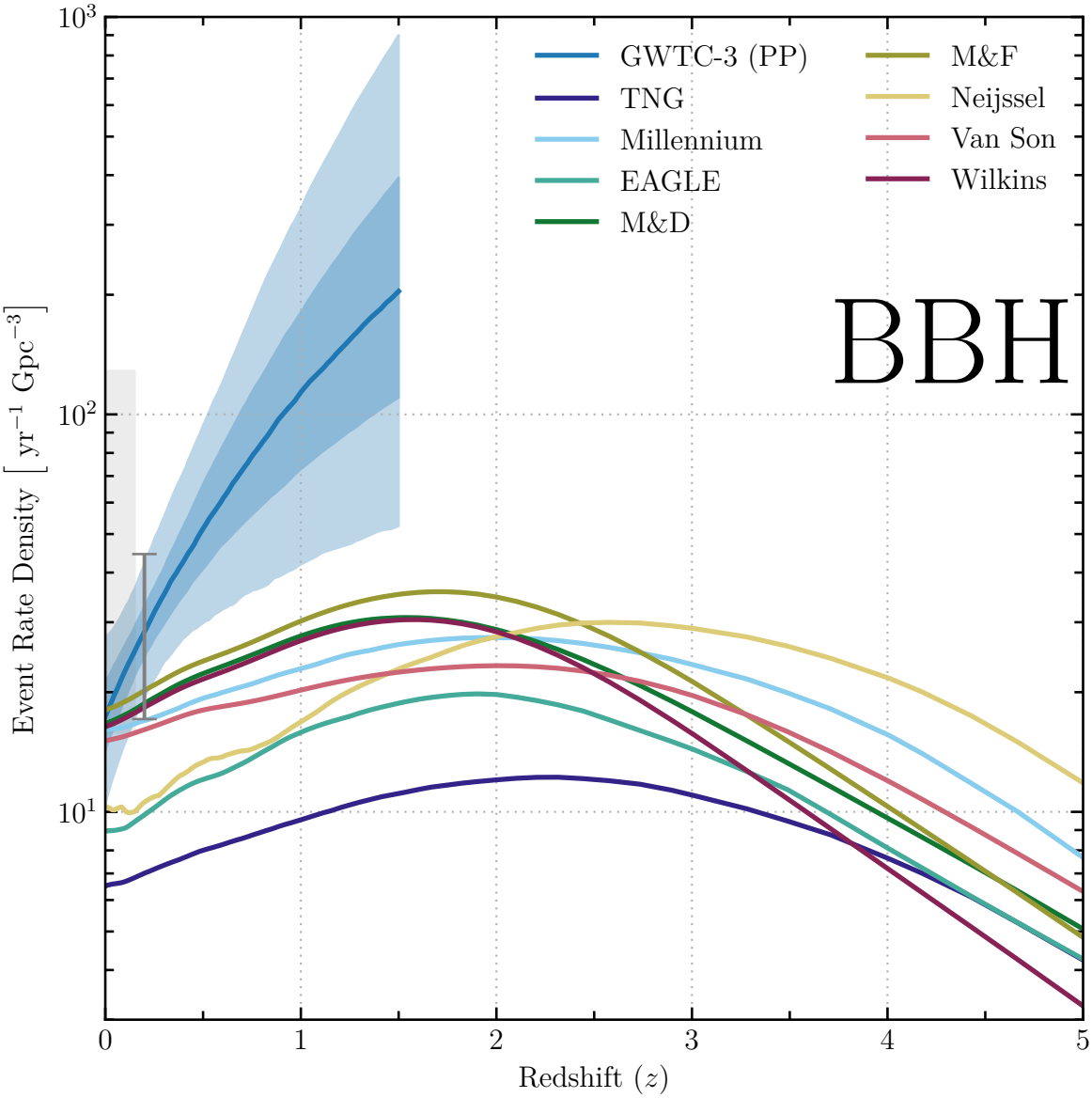

Figure 3.7: BBH merger rate predictions with observations from Abbott et al. (2023) with the lowest 5% to highest 95% credible interval at $z = 0$ and $z = 0.2$ in grey. The redshift evolving population model is shown as the blue region. The $z = 0$ rates are shaded and extended out to $z = 0.15$ for clarity.

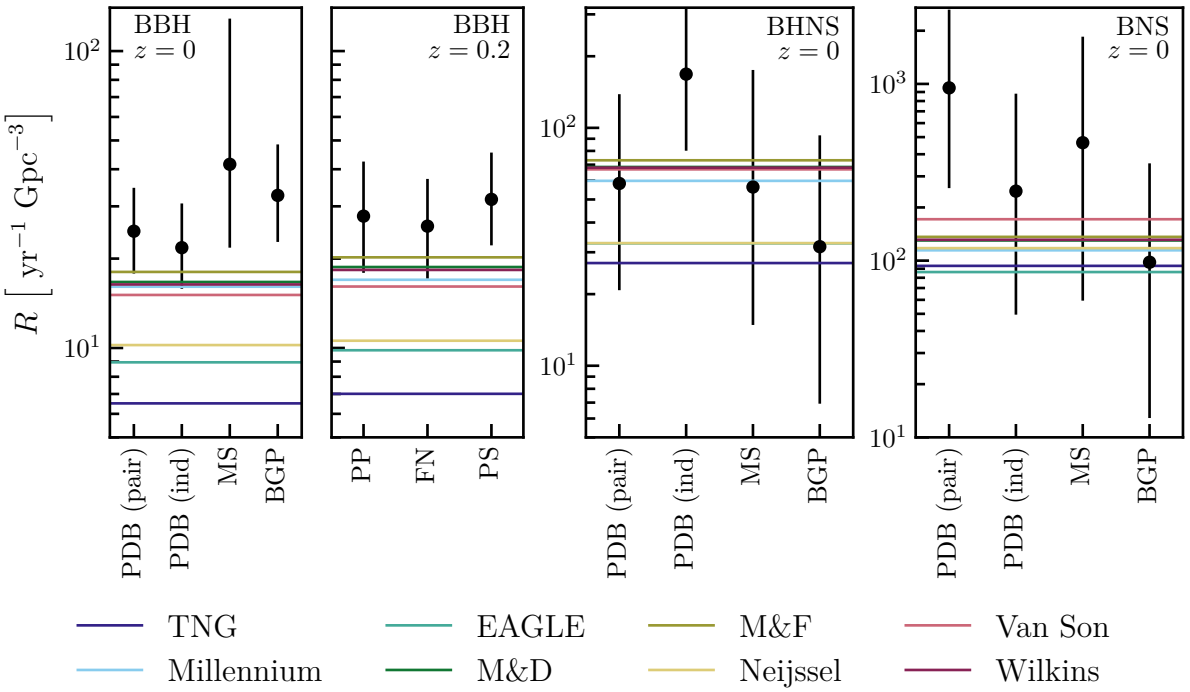

Figure 3.8: Observed BBH, BHNS, BNS merger rates from different assumed population models by Abbott et al. (2023) as black circles with their 90% credible interval marked. At $z = 0$, these population models assume a non-evolving BBH rate, while the $z = 0.2$ observed rates assume an evolving merger rate over redshift. The predicted rates, which evolve over redshift, are sampled at the relevant redshift to compare against the observed rates.

without tweaking the parameters (e.g. Mandel & Broekgaarden 2022). It allows for the inclusion of other BBH formation channels, as described in Section 4.6.5. This might be the effect of the mass transfer stability, natal kick, or QHE treatment, especially since more low-mass BHs are formed in the BPASS populations (Ghodla et al. 2022). We explore the stellar physics resulting in the predicted BBH population in Chapter 4.

While several prescriptions are able to get the current rate of BBH merger at $z = 0$ and $z = 0.2$, they cannot follow the gradient of the redshift evolving merger rate model. Abbott et al. (2021b) found that the BBH rate increases with $(1 + z)^{\kappa}$ with $\kappa = 2.7^{+1.8}_{-1.9}$, which is a slope of 5.50 per z between $z = 0$ and $z = 1$. This lies between the slopes of the predictions. The TNG (3.04), Wilkins et al. (2019) (10.59), Madau & Dickinson (2014) (11.02), and Madau & Fragos (2017) (12.16) prescriptions have values far deviating from the observed slope. The van Son et al. (2023) (5.16), Neijssel et al. (2019) (6.61), Millennium (6.84), and EAGLE (6.90) prescriptions are within the uncertainty range of the observations. This indicates that the rate only requires a small upward adjustment

to be within the observed range, which can be achieved using the methods below.

First, the BBH merger rate is sensitive to the SFH parameters, such as the SFR and metallicity evolution in the early Universe (Dominik et al. 2013; Mapelli et al. 2017; Lamberts et al. 2018; Mapelli et al. 2019; Neijssel et al. 2019; Santoliquido et al. 2021; Artale et al. 2020; Tang et al. 2020), where the differences between SFH in our simulations are most apparent. This effect shows in the predicted rates, with the TNG and EAGLE simulation having a faster enrichment and lower BBH rates. An even faster increase in mean metallicity could further reduce the BBH cosmic rate, but this would also increase the overpredicted Type Ib/c fraction and further underestimate the LGRB rate. Although the constraints on the observed fraction and LGRB rate are limited, we should also focus on other influences on the cosmic BBH merger rate, such as the assumed constant binary fraction over redshift and metallicity. For close binary systems with solar-type stars, the binary fraction decreases significantly with metallicity (Moe et al. 2019). A similar relation might hold for massive stars, but the binary fraction is difficult to infer from early Universe observations, although more observations are becoming available (Moe et al. 2019).

The second area of interest is the physics and parameters assumed in the stellar evolution models. While the BNS merger rate is most sensitive to these parameters (Broekgaarden et al. 2022a), specific processes could contribute to a lower BBH rate but an unchanged BNS rate. For example, altering the prescription used to predict SN outcomes (Dabrowny et al. 2021) or increasing the stellar winds at low metallicities (Mapelli et al. 2022, and references therein) can decrease the compact remnant masses, making it easier for systems to become unbound; thus, possibly reducing the BBH and BHNS rate. However, untangling the effect and strength of each component of the assumed physics of the natal kick (du Buisson et al. 2020; Tang et al. 2020; Igoshev et al. 2021), mass transfer efficiency, and common envelope prescription (van Son et al. 2020; Marchant et al. 2021; Bavera et al. 2021; Klencki et al. 2021) on the resulting BBH, BHNS, and BNS rates is non-trivial and an active area of research (Santoliquido et al. 2021; Broekgaarden et al. 2022a; Olejak et al. 2021). In Chapter 4, we discuss the BBH population and their formation pathways in more detail.

Including GW190814 in the BBH merger rate can drastically change the observed intrinsic rate. For example, in Abbott et al. (2023), the inclusion of GW190814 changes the observed rate to 57^{+52}_{-29} Gpc^{-3} yr^{-1} in the cosmology used in this thesis due to an increase in the expected number of low mass black holes resulting in a larger discrepancy with our predicted rates at $z = 0$. The nature of GW190814, however, is an area of

active discussion and the models by Abbott et al. (2023) do not extrapolate well to the GW190814 masses ($M < 3\,M_\odot$).

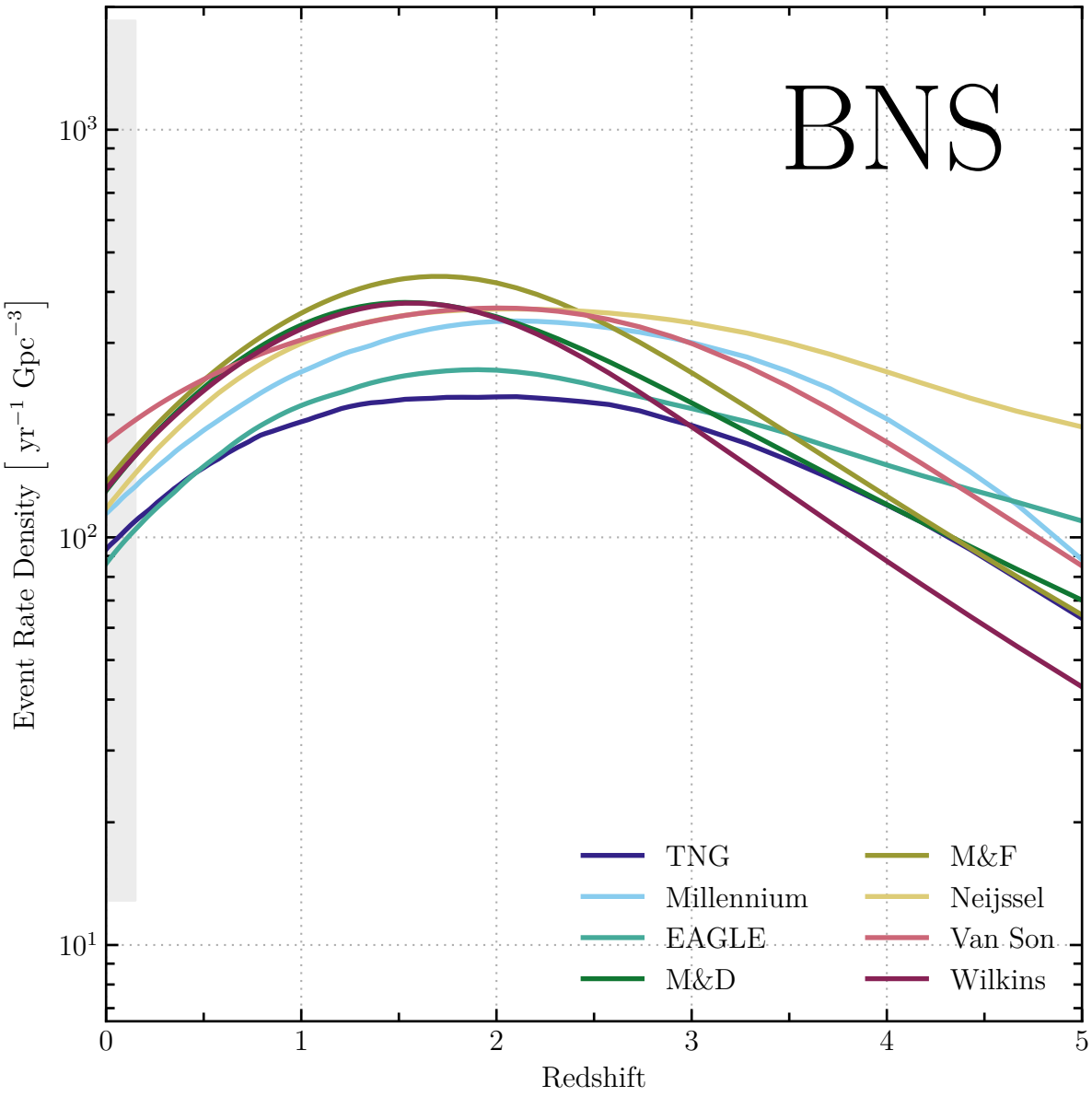

Figure 3.9: BNS merger rate with maximum credible range at $z = 0$ from Abbott et al. (2023). The $z = 0$ rates are shaded and extended out to $z = 0.15$ for clarity.

3.5.2 Binary Neutron Star Mergers

Like the BBH population, the BNS rate has been directly measured at $z = 0$ using GW measurements. While short gamma-ray bursts can provide observations at higher redshift, the conversion from measurement to intrinsic rate suffers from a similar dependence on the opening angle as the LGRB rates. The intrinsic merger rate is mostly independent of metallicity (Giacobbo & Mapelli 2018; Tang et al. 2020), as shown in Figure 2.8, but is highly sensitive to the natal kick and CE evolution prescription (Dominik et al. 2013; Giacobbo & Mapelli 2018; Chruslinska et al. 2018; Tang et al. 2020; Santoliquido et al. 2021; Richards et al. 2023). Figure 3.9 shows that all our predictions lie within the maximum credible region at $z = 0$, which is a positive sign for the implemented physics model. Breaking down the measured interval further in Figure 3.8, we see that the rates fall within the boundaries of most populations models considered by Abbott et al. (2023), except for the `PDB (pair) model`, which has a higher BNS merger rate than any of the models predict. Our predictions agree with the other population models, but no SFH is preferred by the BNS rate, which is as expected since it is mostly independent of metallicity (Tang et al. 2020). Instead, better constraints can be placed by looking at the BNS chirp mass distribution and surviving BNS systems (see, for example, Willcox et al. 2021; Richards et al. 2023). However, such comparisons go beyond the scope of this thesis.

3.5.3 Black Hole - Neutron Star Mergers

After observations from Abbott et al. (2021c) produced a weak constraint on the BHNS merger rate, Abbott et al. (2023) improved upon this by using a joint analysis of the BBH, BHNS, and BNS populations with multiple population models. As shown in Figure 3.10, all predictions lie within the maximum credible region of the models considered. Although similar to the BBH merger rate, the TNG and Neijssel et al. (2019) prescriptions are lower than the other prescriptions, which is most likely a result of the low metal-poor SFR since black hole formation is dependent on the metallicity of the star formation environment (Tang et al. 2020; Mapelli et al. 2022). However, the difference is more pronounced in the BBH rate than the BHNS rate, which agrees with the finding of Drozda et al. (2022) and Broekgaarden et al. (2021) that show a stronger influence of stellar physics on the BHNS rate than the SFH. The interplay between the cosmic BBH, BHNS, and BNS rates is essential in finding the exact origin of the high black hole formation estimation but requires further investigation into the influence of the remnant

mass determination, mass transfer efficiency, and natal kick.

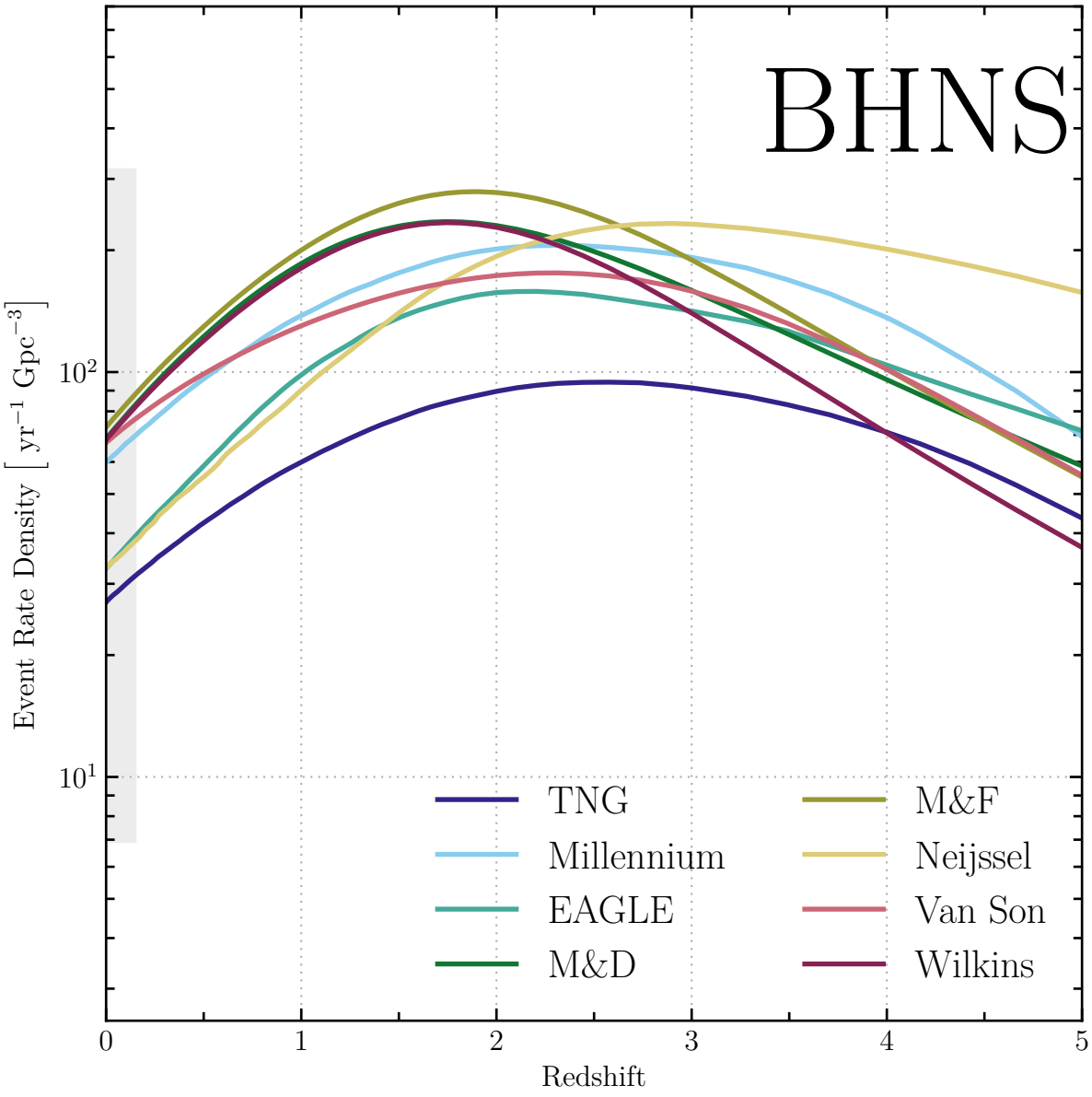

Figure 3.10: The observed maximum credible range of the BHNS merger rate at $z = 0.2$ from (Abbott et al. 2023) compared against the TNG, EAGLE, Millennium, and empirical predictions. The $z = 0$ rates are shaded and extended out to $z = 0.15$ for clarity.

3.6 Combined Rates Analysis

Individually, each transient rate prediction only provides limited information about the different factors that affect it, but taken together, it becomes possible to disentangle these influences. To this end, we have performed a reduced χ^2 calculation on the electromagnetic event rates with observation available except for the LGRB rates. The reason for this exclusion is the fact that the geometrical parameters for the observed rate normalisation are fitted using the same metallicity distribution and a similar CSFRD as our empirical prescription. They will therefore be biased towards the empirical CSFRD.

Although the reduced χ^2 statistic assumes a Gaussian distributed error, the SN rates will be Poisson distributed, which only resembles a Gaussian distribution at high observational counts. At low redshift, the counts should be sufficient, but at high redshift observations are limited and the reduced χ^2 statistic has to be used with care. Moreover, we do not include any uncertainty or binning from the redshift, which can further reduce the accuracy of the statistic. As such, we primarily use the reduced χ^2 as an indicator where the predicted rates from a SFH do not match observations instead of a definite decider for best fit.

Looking at the combined reduced χ^2 of the electromagnetic transients in Table 3.2, the TNG simulation has the closest χ^2 to 1 with a value of 0.89, followed by a reduced χ^2 of 0.76 of the Millennium simulation, while the Neijssel et al. (2019) and EAGLE simulation predictions have reduced χ^2 of 0.63 and 1.33, respectively. Other prescriptions have values further away from 1. Although the TNG simulation provides the best match to the data, the limited difference in reduced χ^2 values does not allow us to distinguish between the predictions. However, the prescription from van Son et al. (2023) has the largest reduced χ^2 of 2.67, which is significantly higher than the other prescriptions. This is due to a higher normalisation of the SFR, resulting in a higher CCSN rate than observed but better matching the Type Ia observations with just the SD contribution.

The compact objects are excluded in the χ^2 calculation because there is no robust method to include the credible intervals without knowing their distributions. Instead, we look at these rates qualitatively by considering the population models in Abbott et al. (2023), with each having its advantages and disadvantages that can drastically alter the observed rates. For example, the fiducial BBH population model (`PP`) evolves over redshift but does not consider the neutron star masses as part of the same population. On the other hand, the `PDB (ind)` model fits the black hole and neutron star masses but assumes a non-evolving merger rate over redshift. To show the influence of these

assumptions, we showed in Figure 3.8 the rates for each population model and compared them against the predicted GW rates in Section 3.5. Here, we consider all GW transients simultaneously and see that all prescriptions underestimate the BBH rates compared to the majority of the population models, even though the BNS rate does not provide additional constraints due to the limited number of observations. The TNG, EAGLE, and Neijssel et al. (2019) prescriptions are significantly underpredicting the rate compared to the other prescriptions, which is most likely a result of the fast enrichment over redshift. Although this allows for the inclusion of additional BBH formation pathways, it is unclear what their contribution should be to the total BBH merger rate (Zevin et al. 2021; Broekgaarden et al. 2022a). However, no prescription is able to match the rate and gradient of the evolving merger rate correctly, as shown in Section 3.5.1.

Because the CSFRD of the Millennium simulation aligns with SFR observations at $z < 2$, short delay time events, such as PISNe and CCSNe, are reasonably well predicted at these redshifts. However, at higher redshifts, its CSFRD does not align with SFR observations, and the estimated PISN and CCSN rates deviate from the other predictions, which is not taken into account in our χ^2 calculation due to the limited rate observations in this redshift regime. On the other hand, metallicity-independent event types with long delay times, such as Type Ia and BNS, do align with observations, which indicates that the total amount of stellar material formed over the history of the Universe is most likely correct. Together with the SFR observations misalignment, this indicated that the Millennium CSFRD distribution over redshift is incorrect. This is further motivated by the short delay time and metallicity-dependent LGRB rate, whose shape over redshift does not align with observations and peaks at a higher redshift than observed. In summary, the total star formation of the Millennium simulation is correct, but its distribution over redshift and its metallicity evolution result in transient rates that deviate from observations.

The Madau & Dickinson (2014) and Madau & Fragos (2017) CSFRDs solve the SFR observation misalignment but still have a significantly different metallicity distribution over redshift than the simulations, as shown in Figure 2.10. Its slow metallicity increase over redshift leads to an overestimation of PISN and possibly LGRB events. The prescription from (Wilkins et al. 2019) removes some of the overprediction at high redshifts but is similar to (Madau & Dickinson 2014) at low redshifts. Neijssel et al. (2019) and van Son et al. (2023) prescriptions use a significantly different metallicity distribution than the other prescriptions and show unique behaviour. These SFHs were calibrated against other GW population synthesis codes and, therefore, cannot be used by other

	SF		metallicity	
	old	**young**	**low**	**high**
Type Ia	✓	×	✓	✓
SD	✓	×	✓	✓/×
DD	✓	×	✓/×	✓
CCSN	×	✓	✓	✓
(non) II-P	✓	✓	✓	✓
Ib	×	✓	✓/×	✓
Ic	×	✓	×	✓
LGRB	×	✓	✓	×
PISN	×	✓	✓	×
BNS	✓	×	✓	✓
BHNS	✓	×	✓	✓/×
BBH	✓	×	✓	×

Table 3.4: General relations between the stellar transients in this thesis and what star formation (SF) and metallicity they probe. Type II-P and Type II SNe are combined since they probe similar regimes of the SFH.

population synthesis codes to predict similar GW sources. Furthermore, van Son et al. (2023) use the gas particle SFR to calculate the full SFH, which results in a higher CSFRD and transient rates, as discussed in Section 2.3.1. While the total is high, the metallicity distribution is more accurate than the Neijssel et al. (2019) prescription, which consistently underestimates the metal-poor star formation at low redshift.

The EAGLE and TNG simulations, on the other hand, underestimate the BBH and BHNS rates due to faster enrichment in the early universe, even when considering an evolving BBH merger rate. Although subject to model uncertainties (See Section 3.7), this means that more detailed observations of the BHNS and BBH rates can be used to constraint the metallicity-specific CSFRD at high redshift, where observations of metallicity-specific SFRs are limited, providing us with a more complete understanding of the Universe.

Table 3.4 summarises the dependencies of each transient and what regime of metallicity and star formation it probes. Together, the transients from a single cosmic stellar population cover most of the parameter space, but limited observations of some transients, such as PISNe, limit their current use in constraining the SFH.

3.7 Caveats in the Estimations

While the Millennium and empirical CSFRD predictions are able to reproduce the observed BBH merger rates, we only considered isolated binary formation. In reality, a mixture of isolated systems and dynamical interactions in globular clusters, young stellar clusters, nuclear clusters, isolated triples, and systems in active galactic nuclei disks could contribute to the total cosmic merger rates (Zevin et al. 2021; Santoliquido et al. 2020; Bouffanais et al. 2021, and references therein for dynamical interactions). This provides support for the EAGLE and TNG CSFRD predictions, which underestimate the BBH rate.

However, the rates can be adjusted by altering the natal kick, remnant mass distribution, mass transfer efficiency, or common envelope prescription, as described in Section 3.5.1, and possible differences in mass distributions could identify areas of improvement (Mapelli et al. 2019; Ghodla et al. 2022). Especially as the distribution of masses and spins become available with more observations from the LIGO/Virgo/KAGRA collaboration, they provide an additional window and new constraints for the formation of binary compact objects, which can be compared against binary population synthesis models, since formation pathways leave imprints on the observed population (Barrett et al. 2018; Neijssel et al. 2019; Arca-Sedda et al. 2020; Zevin et al. 2021; van Son et al. 2022; Bavera et al. 2021) In Chapter 4, we go in-depth into the properties of the BBH merger population to identify areas of improvement.

Besides the underestimation of the BBH and BHNS rates, the EAGLE and TNG simulations have high Type Ib/c fractions at $z = 0$ compared to the empirical and Millennium predictions due to the higher mean metallicity resulting in stronger stellar winds (e.g. Vink et al. 2001). All SFH prescriptions have significantly higher Type Ib/c SN fraction compared to observations, which can either be a result of too high typical metallicity at low redshift or an area for improvement in determining the transition between Type II, Ib, and Ic SNe. We discuss the latter in Section 6.1. Since the local metallicity distribution is relatively well understood (e.g. Kewley & Ellison 2008; Zahid et al. 2014) and this is matched by the TNG simulation (Torrey et al. 2019; Naiman et al. 2018; Hemler et al. 2021), the low-redshift metallicity is unlikely to be the cause for the high Type Ib/c fraction.

However, the available observations for the Type Ib/c fractions are currently limited, but the continuation of surveys from the Zwicky Transient Facility (Perley et al. 2020), ATLAS (Smith et al. 2020) will provide better constraints on the Type Ib/c fractions

and SLSN observations. At the same time, next-generation observational facilities, such as THESEUS (Tanvir et al. 2021), Vera Rubin (Andreoni et al. 2019), Euclid (Moriya et al. 2022a), and Nancy Grace Roman Space Telescope (Spergel et al. 2015; Moriya et al. 2022b), will be able to detect large numbers of CCSNe, PISNe, LGRBs. With these future observations, it might become possible to distinguish between the similar predictions and provide us with more understanding of the metallicity evolution at high redshift.

3.8 Conclusion

We have predicted electromagnetic and GW cosmic transient rates using detailed stellar models from BPASS and several prescriptions of the star-forming environment from well-known cosmological simulations. These include an empirical prescription and three numerical models originating from the MilliMillennium, EAGLE, and Illustris-TNG simulations, which provide detailed SFH and metallicity evolution for each simulated galaxy over the history of the Universe. These additional details lead to significantly different cosmic transient rate predictions, which we compared against observations and each other, focusing on the difference between the simulations and the empirical prescription.

1. There can be up to an order of magnitude difference between the predicted rates from the empirical model and those from the cosmological simulations. While most event types differ by a factor of 2, the predicted rates are significantly altered when the delay-times distribution for the events are extended or when the rates are highly metallicity dependent, up to a factor of 2.38 for the BBH transient rate, and up to 9.66 for the LGRB rates. This result suggests that care should be taken in choosing which cosmic SFH to use, especially how the metallicity evolution is modelled when predicting transient rates. Those that are most sensitive are events with long, > 1 Gyr, delay times and strong dependence on metallicity.

2. The cosmological simulations have metallicity-specific CSFRD with reduced early star formation and faster enrichment than the empirical prescription. Of the SFH considered, the Millennium simulation has the most uniquely shaped CSFRD, which does not agree with SFR observations, and has a nearly constant mean metallicity over redshift resulting in distinct cosmic transient rates. Compared to observations, the predictions from the Millennium simulation agree with the observations for the Type Ia, CCSN, PISN, and BNS rates but overestimate the BHNS

and BBH rates. The TNG and EAGLE simulation solve this overestimation with an increasing mean metallicity evolution and an observationally constraint CSFRD resulting in BHNS and BBH rates closer to observation irrespective of the assumed black hole and neutron star population model. At the same time, the Type Ia, CCSN, and BNS rates are minimally affected. However, the PISN and LGRB rates decrease significantly due to the higher metallicity, but the number of observations is limited or hard to constrain. Moreover, the inclusion of star formation on a per-simulation particle basis instead of mean galaxy metallicity can solve the discrepancy between current observations and our LGRB prediction from the TNG simulation (Metha et al. 2021). Future observations, like long-term deep transient surveys (Moriya et al. 2021) and next-generation observational facilities, such as THESEUS (Tanvir et al. 2021), will put better constraints on the SLSN and LGRB rates and, through these events, a better understanding of the metallicity evolution over redshift (Fryer et al. 2022a).

3. We find that the predictions of the empirical prescription, based on the CSFRD from Madau & Dickinson (2014) and metallicity evolution from Langer & Norman (2006), align well with observed CCSN and Type Ia rates from multiple surveys. Moreover, the predicted fraction of Type Ib/c at $z = 0$ of 0.71 is similar to 0.722 found by Perley et al. (2020), and the predicted LGRB, PISN, and BNS rates align well, although the observations for the LGRB and PISN are not well constrained. Furthermore, the BHNS and BBH rates are significantly overestimated compared to observations up to almost an order of magnitude, which can be a result of our assumptions in stellar physics, mass transfer, common envelope evolution, or natal kick (Zevin et al. 2020; du Buisson et al. 2020; van Son et al. 2020; Santoliquido et al. 2021; Marchant et al. 2021; Bavera et al. 2021; Olejak & Belczynski 2021; Olejak et al. 2021; Igoshev et al. 2021; Klencki et al. 2021; Belczynski et al. 2022).

4. The additional detail in the metallicity-specific CSFRD provided by the TNG and EAGLE simulations results in reasonable cosmic rate estimations across the board but especially improves upon the BHNS and BBH rates compared to the standard empirical prescription. These new cosmological simulations have been improved to fit a variety of observations. The semi-analytical models from the Millennium simulation, on the other hand, are older and unable to match the observed CSFRD over redshift. Together with the near-flat metallicity evolution, it significantly overestimates the BBH and BHNS rate with minimal changes in the other rates compared to the empirical prescription.

5. In this thesis, we have only considered isolated binary evolution for the BBH and BHNS rates. The Universe has more than one way to make compact object mergers happen with the contribution of each pathway, such as isolated and dynamic formation being undetermined, as described in Section 1.4.2. The rate estimations from the EAGLE and TNG simulations leave room for other formation channels to contribute to the observed BBH merger rate. However, adjusting of the CEE or natal kick might be necessary for more accurate redshift evolution.

Altogether, we find that the EAGLE and TNG simulation provide the best metallicity-specific CSFRD based on the predicted cosmic rates for electromagnetic and GW transients. The additional detail provides clear benefits over the empirical prescription, closer matching the irregular and complex metallicity and SFR evolution of the real Universe, constraining environmental and evolutionary parameters. As the observational constraints improve over the coming decades for the SFH and cosmic transients rates, we expect the true complexity of their variation over redshift to be revealed. In this chapter, we have probed the influence of the SFH on the population of stellar transients and validated our predictions against observations. With confidence in our stellar population, we turn our attention to the formation pathways of BBH mergers.

Chapter 4

The Population Properties of Binary Black Hole Mergers

In the years following the first observed BBH merger in 2015, the number of observations has increased dramatically to a total of 69 BBH events with a False Alarm Rate of less than 1 per year from the release of GTWC-3 (Abbott et al. 2023).

This growing population is a window into the stellar physics governing the life and death of their progenitors. We have seen in Chapter 3 that depending on the SFH prescription, the observed cosmic BBH rate can be accurately predicted by the BPASS models. However, GWTC-3 has shown that the merging BBH population is not yet well understood with the observed primary BH mass ($M_{1,BH}$) distribution extends up to $100\,M_\odot$ - beyond the expected maximum (Heger & Woosley 2002; Woosley et al. 2002; Woosley 2017; Farmer et al. 2019; Renzo & Zapartas 2020; Woosley & Heger 2021; Mehta et al. 2022; Farag et al. 2022) - and an excess at $35\,M_\odot$ that is not connected to the turn-off of the distribution. The assumed evolutionary physics in the stellar evolution and population synthesis leaves imprints on the primary remnant mass, spin, and mass ratio distributions of the BBH population.

Depending on the SN prescription, the primary remnant mass distribution can be drastically different (Mandel et al. 2020; Shao & Li 2021; Ghodla et al. 2022), with PPISN and PISN leaving the largest imprint on the distribution at high black hole masses (Spera & Mapelli 2017; Marchant et al. 2019; Stevenson et al. 2019). In Section 1.4, we discussed it is expected that they create a dearth of systems above $M_{BH} \approx 45\,M_\odot$ with a pile-up at lower masses before it. While changing the internal stellar physics can change the predicted location of the peak and upper mass gap, the association between them remains. Observationally, however, they are not connected, since the $35\,M_\odot$ excess is at a lower mass and the dearth of systems starts at a higher mass.

Without altering the stellar physics, such a massive BBH merger could also be explained by non-isolated binary formation pathways (Yang et al. 2019; Rodriguez et al.

2019; Santoliquido et al. 2020; Di Carlo et al. 2020; Renzo et al. 2020c; Mapelli et al. 2021; Bouffanais et al. 2021; Zevin et al. 2021; Arca-Sedda et al. 2020, 2023; Costa et al. 2022; Ballone et al. 2023; Banerjee 2022). Each would leave imprints on the properties of the merging BBH population and could challenge the standard isolated binary evolution formation pathway.

Another possibility for the existence of BHs in the PISN mass gap is mass transfer onto the BH from a companion (van Son et al. 2020; Woosley & Heger 2021). This occurs when the radius of the star, the donor star, expands beyond its Roche lobe radius and, thus, mass is transferred to the companion, the accretor. This can drastically alter the mass ratios and evolution of the star, with the stability and the accretion efficiency determining the outcome of this mass transfer.

If the radius of the donor star contracts or remains constant as a response to mass loss during the Roche lobe overflow, the mass transfer is stable. If, on the other hand, the star expands as a response to mass transfer, the positive feedback-loop results in the donor star engulfing the whole system in a CE phase, as discussed in Sections 1.3.3 and 2.1.1. The accretion onto the BH during the CE phase is limited (De et al. 2020), but Roche lobe overflow before the CE can result in accretion onto the BH and its effects is poorly explored for high-mass stars.

Systems undergoing CE have historically been considered the main formation channel for merging BBH systems (Dominik et al. 2012; Belczynski et al. 2016; Bavera et al. 2021; Zevin et al. 2021; Zevin & Bavera 2022; van Son et al. 2022), with only the high-mass primary mass systems being formed through stable mass transfer (SMT) (Neijssel et al. 2019; van Son et al. 2022). However, stable mass transfer (SMT) has been shown to play a more important role than previously thought, with accretion being more stable in detailed stellar models than those used in rapid population synthesis (Marchant et al. 2021; Gallegos-Garcia et al. 2021; Klencki et al. 2021), like COMPAS (Riley et al. 2022), STARTRACK (Belczynski et al. 2016), MOBSE (Giacobbo et al. 2018), and COSMIC (Breivik et al. 2020) which use stability criteria based on the evolutionary phase of the star from Hurley et al. (2002). Using improved stability criteria Olejak et al. (2021) has shown that more stable mass transfer takes place in STARTRACK. While this results in an extended primary BH mass range up to $55\,M_\odot$, it is unable to predict more massive primary mass BHs.

Super-Eddington accretion onto the BH during SMT could allow the primary BH to gain a significant amount of mass to become a PISN mass gap BH (van Son et al. 2020). However, for SMT systems to merge within the Hubble time, they need to lose

angular momentum to reduce the size of their orbit. With Eddington luminosity limited accretion, this happens through mass loss from the system during Roche lobe overflow, but this does not occur for super-Eddington accretion, and BHs in the PISN mass gap are unable to merge within the Hubble time (van Son et al. 2020; Bavera et al. 2021; Zevin & Bavera 2022). Thus, most BBH population synthesis codes limit the accretion onto the BH to the Eddington luminosity. On the other hand, super-Eddington accretion onto a BH is a candidate for ultra luminous X-ray sources (Woosley & Heger 2021) and is theoretically possible (Begelman 1979; Sądowski & Narayan 2016; Woosley & Heger 2021; Johnson et al. 2022; Ghodla & Eldridge 2023).

Since the high end of the primary BH mass distribution is not yet well understood, we predict the properties of the BBH population using our detailed stellar populations, as described in Chapter 2. Using the IllustrisTNG-100 SFH and metallicity evolution, we predict the primary mass and mass ratio distributions of the merging BBH population. While observations are limited, one has to be cautious in drawing strong conclusions from these comparisons, but the most constrainted observables from GWTC-3 are the primary mass and mass ratio distribution. We limit ourselves to the SFH of the TNG simulation for our detailed analysis but show the impact of other SFH prescriptions in Section 4.5.1.

We explore the formation pathways of the merging BBH systems and describe the formation of features matching observation in the high BH mass range in Section 4.2. We look at the impact of the remnant mass prescriptions (including PISN and PPISN), quasi-homogeneous evolution, and SFH on the $M_{1,BH}$ distribution and its features in Section 4.5. In Section 4.6, we discuss how this relates to the current view and what limitations our predictions have.

4.1 Population Properties

In Figure 4.1 we compare the predicted population against the intrinsic observed population from the PP model from Abbott et al. (2023). We split the $M_{1,BH}$ space into 40 logarithmically spaced bins between 2 and 200 $M_\odot$. Unless otherwise stated, we use this binning for all $M_{1,BH}$ distributions. In Appendix C, we perform a Poisson error calculation, bootstrap sampling, and apply a kernel density function to determine the uncertainty associated with this distribution, which is limited.

While the predicted rate over mass ratio with $q_{BH} = M_{2,BH}/M_{1,BH}$, where $M_{2,BH}$ is the mass of the secondary BH in Figure 4.1 does increase rapidly at low q_{BH}, it does

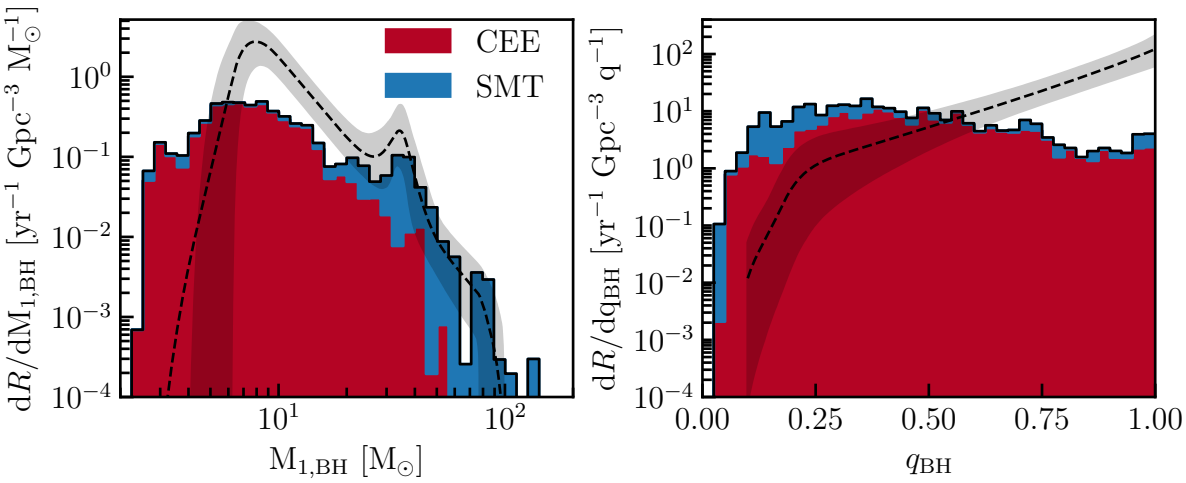

Figure 4.1: The event rate density over the primary BH mass (left) and the mass ratio (right) at $z = 0$ with the results from the PP model from Abbott et al. (2023) as the black dashed line. The grey area is the 90% credible interval. The presence of a CE in the evolution of the BBH merger progenitor has been marked with red, while blue indicates that no CE has taken place and only stable mass transfer has occurred during the life of the BBH progenitor system. The vertical dotted line indicates the $35\,\mathrm{M_\odot}$ BH mass. $\mathrm{q_{BH}}$ is split into 40 linear bins between 0 and 1.

not continue to increase with increasing q_{BH} and instead drops beyond $q_{\mathrm{BH}} \sim 0.4$. This might be due to our CE prescription, which dominates the mass ratio distribution, or the remnant mass prescription, see Section 6.4 and Section 4.5.3, respectively.

Although the mass ratio distribution does not agree with the observed values, we find good agreement in the high-mass regime of the $\mathrm{M_{1,BH}}$ distribution between our predictions and GWTC-3. The predicted distribution contains a double peak structure with a peak near $5\,\mathrm{M_\odot}$ and $35\,\mathrm{M_\odot}$, with the latter agreeing with observations. Moreover, it extends into the PISN mass gap with masses over $100\,\mathrm{M_\odot}$, as shown in Figure 4.1. However, it does overpredict the low mass BBH mergers ($\mathrm{M_{1,BH}} \lesssim 5\,\mathrm{M_\odot}$) and underestimates the number of systems near $10\,\mathrm{M_\odot}$.

The well-matched nature of the predictions to observations in the high BH mass regime raises questions about the formation of the high-mass BHs and their merger time. Moreover, the peak at $35\,\mathrm{M_\odot}$ seems to be disconnected from the turn-off of the $\mathrm{M_{1,BH}}$ distribution, as observed; this calls into question its connection to PPISN, which is thought to lead to a pile-up at the end of the primary BH mass distribution near $\sim 40-50\,\mathrm{M_\odot}$ (Marchant et al. 2019; Renzo et al. 2020a; Woosley & Heger 2021). Because these questions are linked, the Section 4.2 will cover these components in detail, but here we will discuss the formation channels giving rise to the $\mathrm{M_{1,BH}}$ distribution.

To this end, we tag BBH merger progenitor models that undergo CE during their evolution as CEE and models that only experience SMT as SMT. If multiple mass transfer phases take place during the evolution, we check if any of them is unstable. If so, we tag the model as undergoing CEE. If no interactions take place, the model is tagged as NON. We perform the tagging for the primary and secondary models.

In Figure 4.1, we separate the $M_{1,BH}$ distribution into a formation channel with a CE in their evolution and in a pure SMT sample that only contains systems (primary and secondary models) with stable mass transfer. We find that high-mass BH ($20 - 115\,M_\odot$) are increasingly formed through systems only undergoing SMT, which is in agreement with Neijssel et al. (2019) and van Son et al. (2022). The majority of these events have mass ratios below $q_{BH} < 0.4$.

To see what models these systems come from, Figure 4.2 shows that the main channels contributing to the SMT-only channel are SMT+SMT with SMT in the primary and secondary model, and SMT+NON, where after SMT in the primary model, no interaction in the secondary model takes place. Both channels originate from massive stars ($M_{1,ZAMS} > 60\,M_\odot$) with a slightly less massive companion ($M_{2,ZAMS} > 35\,M_\odot$). This is further motivated by the central figure, which shows the fraction of events going through a formation pathway at a given $M_{1,ZAMS}$ and $M_{2,ZAMS}$. While these systems originate from similar populations, they undergo drastically different evolution. The NON+SMT systems only contribute 0.30% to the total merging BBH rate but originate from a wide variety of initial masses.

Nearly all BBH merger progenitor systems interacted during their lifetime, and the CE and SMT channels result in different remnant mass outcomes. Figure 4.3 shows the period evolution separated per evolutionary phase and mass transfer case. In the left column, i.e. the evolution of the binary before the first SN where the primary star, M_1, initiates mass transfer, while the right column shows the period evolution of the secondary binary models, where the initial primary star has become a compact object and the secondary star, M_2, fills its Roche lobe. Throughout the evolution, we keep the definition of the primary (1) and secondary (2) star the same. As such, in the PRIMARY (SECONDARY) MODELS, M_1 is M_d (M_a) and M_2 is M_a (M_d).

In the initial phase of the evolution (left), we see that SMT (top) leads to larger periods and, thus, larger separations than systems experiencing CEE (bottom). This is a result of material being transferred from the more initially massive star to the less massive in the system. At the start of mass transfer, this results in an orbit shrinkage, but once the mass ratio becomes more equal, the orbit starts to widen (Soberman et al.

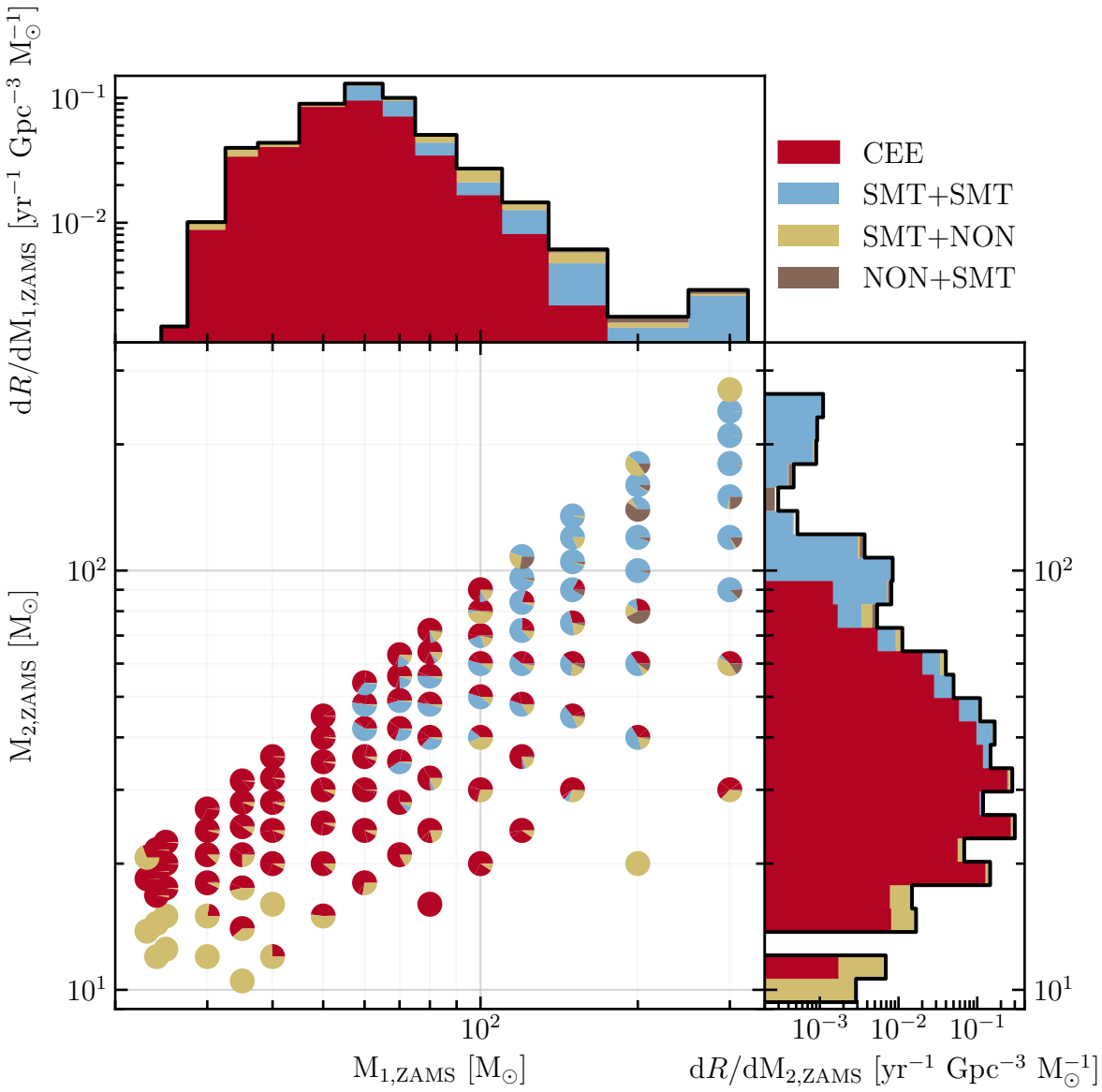

Figure 4.2: The ZAMS distributions of M_1 and M_2 for systems leading to a BBH merger at $z = 0$. The SMT channel has been split into its individual formation channels since it dominates the high $\mathrm{M}_{1,\mathrm{BH}}$ regime. Each circle contains the systems at those $\mathrm{M}_{1,\mathrm{ZAMS}}$ and $\mathrm{M}_{2,\mathrm{ZAMS}}$ and are split into their formation pathways, weighted according to the systems weight w.r.t. total weight at this $\mathrm{M}_{1,\mathrm{ZAMS}}$ and $\mathrm{M}_{2,\mathrm{ZAMS}}$. $\mathrm{M}_{1,\mathrm{ZAMS}}$ is split into 16 bins, which are the ZAMS masses in the BPASS grid. $\mathrm{M}_{2,\mathrm{ZAMS}}$ is split into 40 bins between 2 and 300 $\mathrm{M}_\odot$.

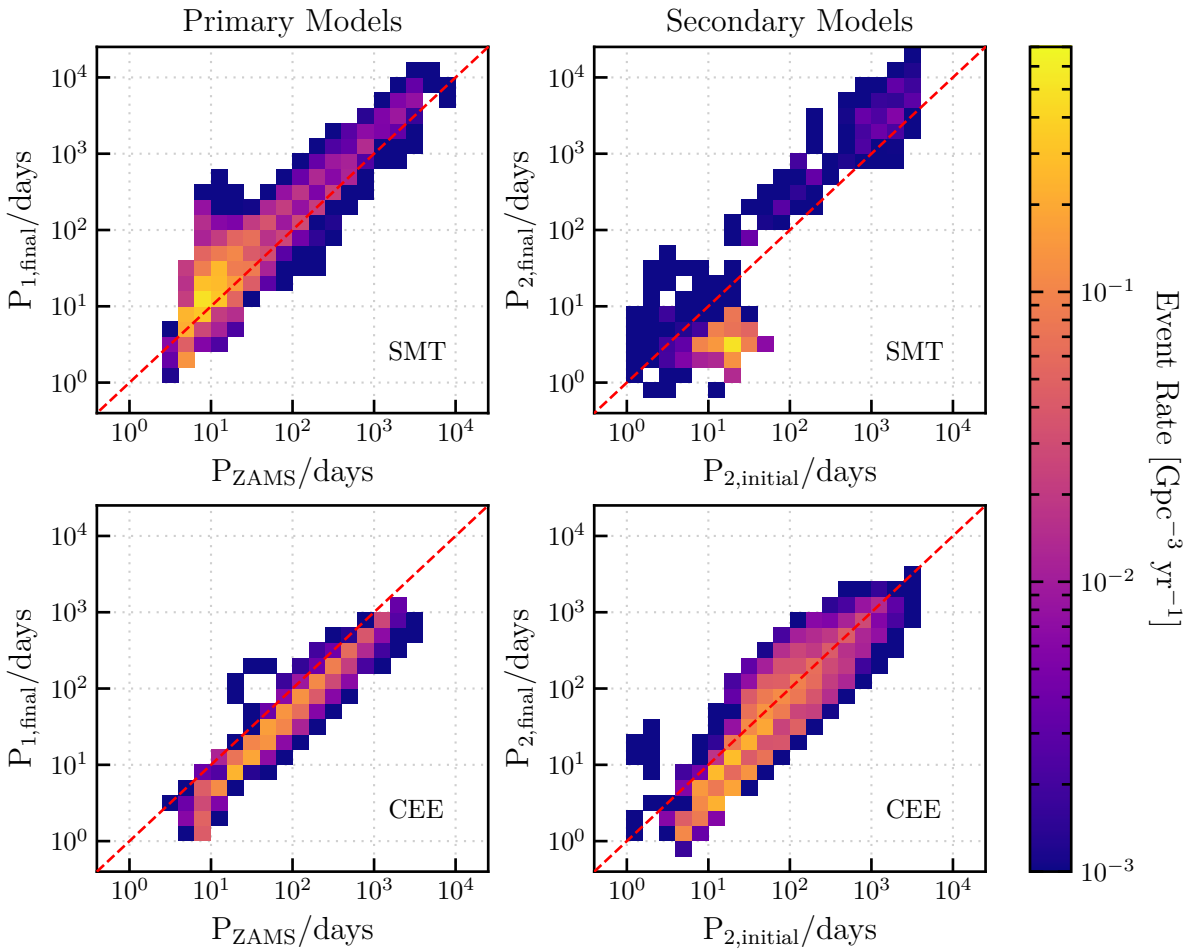

Figure 4.3: The period evolution of the merging BBH progenitors. The left column contains the primary binary models in the simulation, i.e. the evolution before the primary SN. The right column contains the secondary binary models after the first SN. The horizontal axis represents the period at the start of the model. This means that the P in the left column represents the ZAMS period of the systems. The vertical axis represents the period at the end of the model evolution, which does not include the SN. Between the primary (left) and secondary (left) binary models, the remnant mass prescription is applied to the primary star. The primary (1) and secondary (2) stars are defined at the beginning of the evolution and we do not change this definition throughout the evolution. The final mass ratio is not the BBH mass ratio since the remnant mass prescription still needs to be applied to the secondary star. The rows are split between SMT and CEE taking place in this model. The periods are logarithmic binned in 30 bins between 10^{-1} and 10^{5}. The dashed red line indicates that the period has remained unchanged throughout the evolution, e.g. $P_{initial} = P_{final}$.

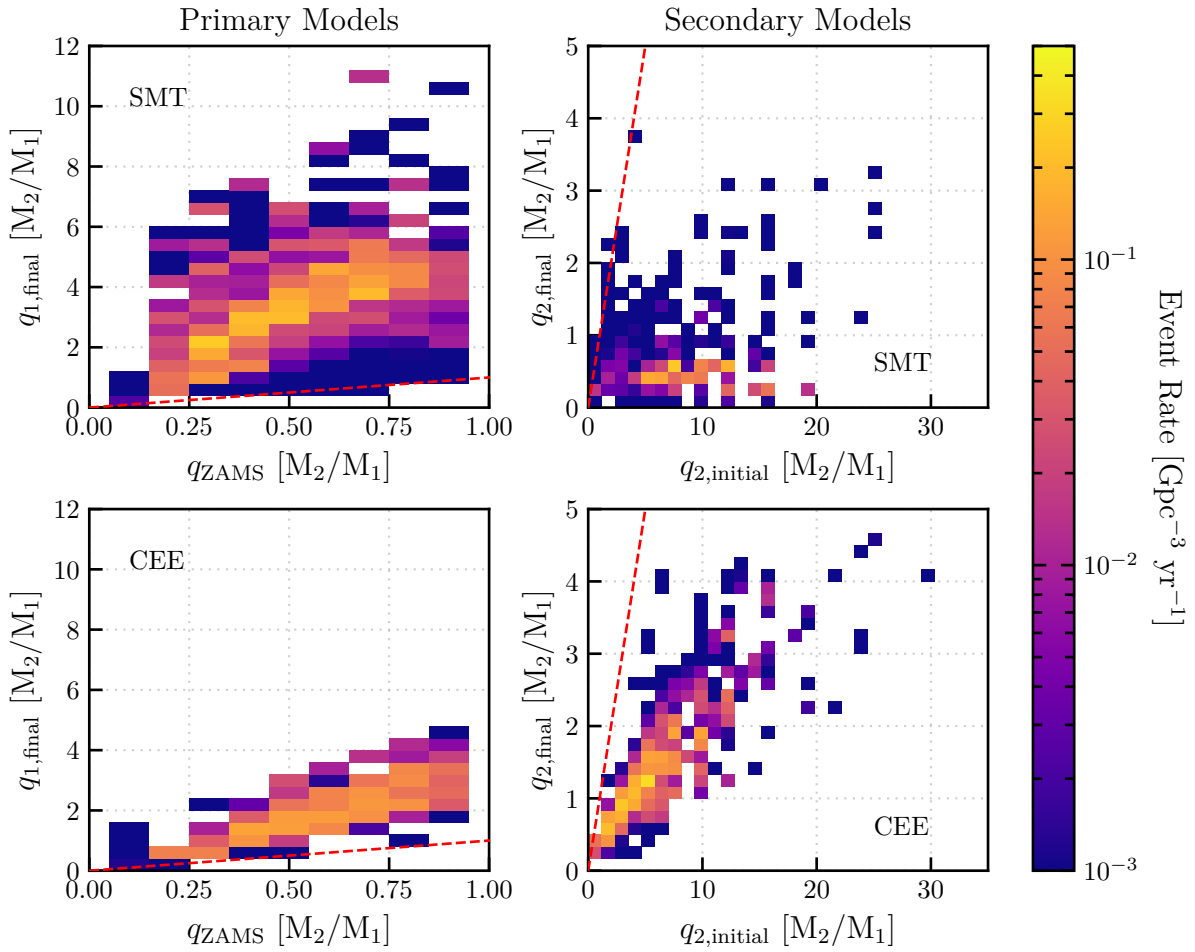

Figure 4.4: Same as Figure 4.3, but for the mass ratio. Depending on the q value, the binning is different. The q_{ZAMS} bins are centred around the q values used by BPASS, 0.1 to 0.9 with steps of 0.1. $q_{1,\mathrm{final}}$, $q_{2,\mathrm{initial}}$, and $q_{2,\mathrm{final}}$ each contains 30 bins linearly spaced between 0–12, 0–35, and 0–5, respectively. The dashed red line indicates that the period has remained unchanged throughout the evolution, e.g. $q_{\mathrm{initial}} = q_{\mathrm{final}}$.

1997; van Son et al. 2020).

Looking at the mass ratio evolution of SMT systems during the primary phase of the binary evolution in Figure 4.4 (top left), we see that the mass ratios flip and increase up to $q_{1,\mathrm{final}} = M_2/M_1 = 11$ when the primary star dies, with most systems laying between 2 and 6. The CEE channel (bottom left) is only able to achieve a maximum mass ratio of $q_{1,\ \mathrm{final}} = 5$ with most models between 0.5 and 4, but does reduce the periods for most systems, as expected.

The remnant mass prescription further increases the mass ratio up to $q_{2,\ \mathrm{i}} = 30$ by reducing the primary mass, as can be seen in the right column in Figure 4.4. This column contains the secondary models split between those experiencing SMT and CE. Thus, a

model in SMT could have experience SMT, CE, or not interacted in the primary model. Most of the systems undergoing only SMT after the first SN have an initial mass ratio between $5 < q_{2,\mathrm{i}} < 20$. A few low contributing systems have more extreme mass ratios up to $q_{2,\,\mathrm{i}} = 25$, which are unexpected in the context of SMT, and we will explore these further in Section 4.4. Eventually, the mass transfer stops and the systems reach mass ratios between 0 and 1, which will be further reduced by the remnant mass prescription. Thus, super-Eddington accretion onto the BH leads to a mass reversal, such that the $\mathrm{M}_{1,\mathrm{ZAMS}}$ also becomes $\mathrm{M}_{1,\mathrm{BH}}$. This results in limited mass ratio reversal (Zevin & Bavera 2022; Broekgaarden et al. 2022a; Mould et al. 2022), as will be discussed in Section 4.6.3.

The CE in the second phase of the systems evolution decreases the mass ratio linearly, e.g. a higher initial mass ratio leads to a higher final mass ratio. Since we tag a system as CEE if the undergoes a single CE phase during the phase of the systems evolution, we do not identify multiple mass transfer phases in the system, which occur in our model. Therefore, phases of SMT in a system undergoing CE can alter the mass ratio and periods.

In general, systems experiencing only SMT in the secondary model have, on average, smaller periods at the end of the model than those that have experienced CE. The reason for the orbital shrinkage depends on the binary model parameters, but most shrinkage is caused by tidal synchronisation reducing the angular momentum in the orbit. Most systems are below the critical mass ratio for the Darwin Instability ($q > 12$) (Eggleton 2011), but those above are able to avoid it due to rapid changes in the mass ratio (Stępień 2011), the rapid shrinkage of the donor radius, and/or increased winds due to high helium surface abundance. We further discuss the stability of these models in Section 5.1.

The right column of Figure 4.3 shows that the period change during the CEE interaction spreads out its original distribution and reduces the period for systems with period $\lesssim 10^{1.5}$. The SMT channel reduces the period of such systems more significantly than the CEE channel. Furthermore, two main clusters of periods can be identified around 10^1 and around 10^3 with limited systems between these periods. This is a result of interaction on the Hertzsprung gap being mostly unstable and will be discussed more in Section 5.1. However, both channels have systems with final periods that are unable to merge when assuming a circular orbit, e.g. 10^4 days. We find that these systems come from higher metallicity populations and have eccentricities near unity due to the natal kick they received. As a result, they are able to merge within the Hubble time. This shows that it is possible to get BBH systems merging within the Hubble time, even when considering super-Eddington accretion, while retaining a significant amount

of mass, thus resulting in more massive BBH systems.

We further separate the formation pathways per metallicity and per evolutionary model in Figure 4.5. The highest contribution comes from the SMT+CEE (34.29%), where the primary model only experiences SMT and the secondary contains a CE phase. The next largest formation channel is CEE+CEE (26.16%) channels, where a CE takes place in both the primary and secondary model. The dominance of CE in the formation of merging BBHs is in agreement with other population synthesis codes (Dominik et al. 2012; Belczynski et al. 2016; Bavera et al. 2021; Zevin et al. 2021; Zevin & Bavera 2022; van Son et al. 2022). The SMT+CEE distribution contains mergers originating from a variety of metallicities, but lower mass primary mass systems originate from higher metallicities than the higher primary mass systems due to the mass loss from stellar winds. The CEE+CEE distribution, on the other hand, has a higher contribution from low metallicity star formation.

The SMT+NON channel, where the binary only interacts before the first SN (9.15%), is dominated by mergers from low metallicity ($Z < 0.006$) star formation with a large contribution between 30 to 40 $M_\odot$ from $Z = 0.0001$. While this channel contains the largest primary BH mass, most other events are constrained to $M_1 < 40\,M_\odot$ because of the PISN mass limit. The next largest formation pathway, the CEE+NON channel (6.48%), is also limited to $M_1 < 40\,M_\odot$ and low metallicity. Similarly, CEE+SMT only occurs at low metallicity, but has a specific mass regime (15 to 55 $M_\odot$) and only contributes 0.28%. The events only interacting in the primary preferentially come from low metallicity events, while systems interacting only in the secondary phase originate from higher metallicity environments. The SMT+SMT channel (20.08%) forms most of the high primary mass BH systems, similar to the distribution shown by van Son et al. (2022). We note a metallicity dependence in the primary mass with low primary mass BHs originating from higher metallicity environments, as a result of the formation pathway discussed in Section 4.2.1.

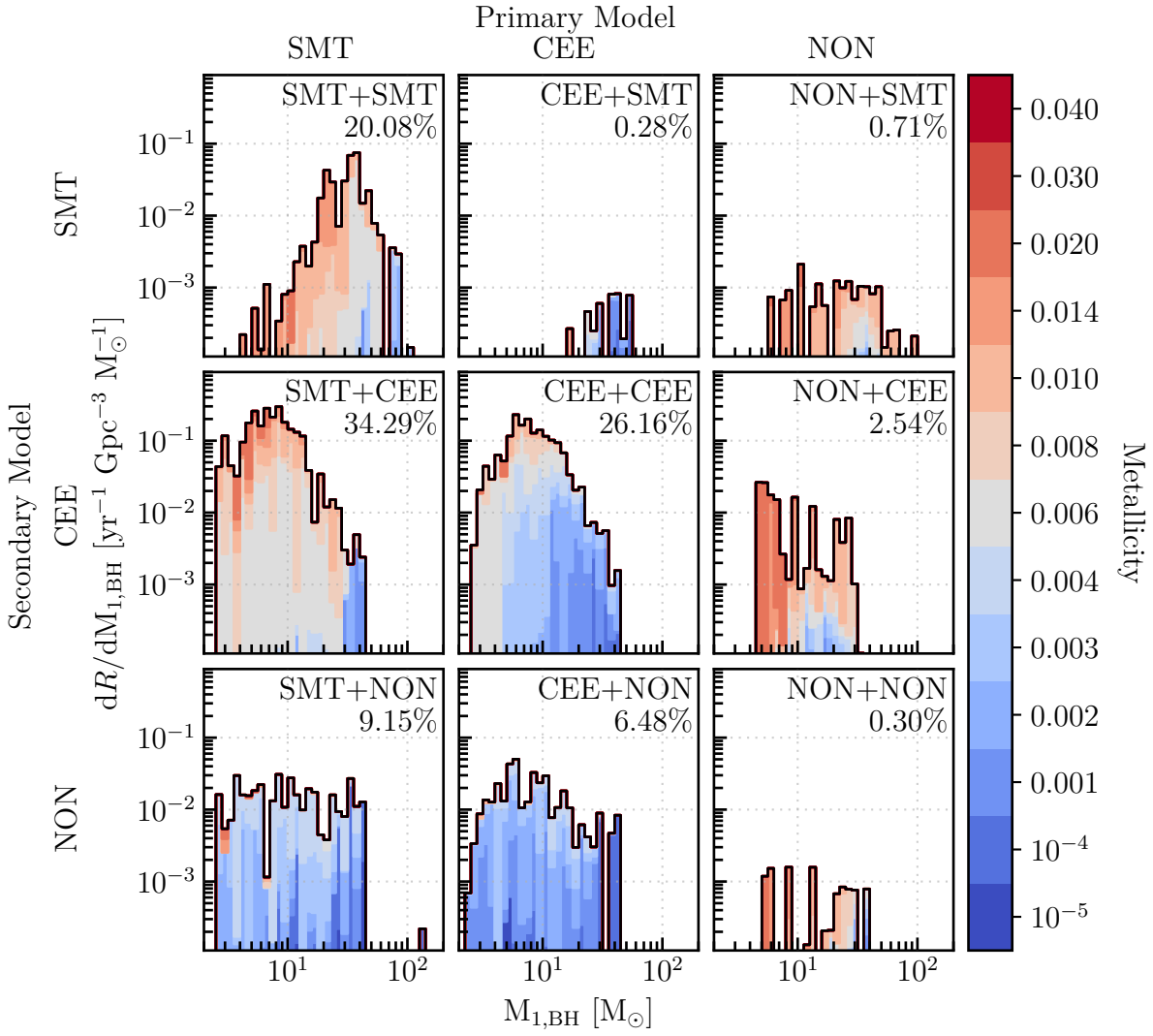

Figure 4.5: The predicted event rate at $z = 0$ over primary BH mass separated by formation channels coloured by the metallicity at which the binary system was formed. The columns are split based on only SMT, CEE, or NON occurring in the primary model, as described in Section 4.1. The rows are the same but for the secondary models. The percentages are the contribution of that formation channel to the total BBH merger rate.

4.2 Primary Remnant Mass Distribution Features

Mass transfer is a defining feature of the outcome of the binary system and SMT leads to higher mass systems. We find a distribution that matches the high-mass properties of the observed intrinsic primary mass distribution. These are the extended mass range and an excess at $35\,M_\odot$. In the next sections, we cover these two findings in more detail.

4.2.1 The $35\,M_\odot$ Excess

In Figure 4.1, we find an excess of systems near $M_1 \approx 35\,M_\odot$, similar to observations, which previously has been attributed to a pile-up of PPISN events. We tag the systems undergoing PPISN and find that only the high end of the peak has a strong contribution from PPISN at $40\,M_\odot$. As shown in Figure 4.6, the majority of $\sim 35\,M_\odot$ BH progenitors do not experience PPISN. Instead, we find that the peak consists of systems only undergoing SMT. The CEE channel, on the other hand, has a decreasing rate until $35\,M_\odot$, after which it slightly increases due to PPISN events. Since CEE systems dominate other population synthesis codes, the pile-up is logically attributed to PPISN. However, since in this mass regime BPASS is dominated by SMT, this is not the main formation process for the $35\,M_\odot$ peak.

The main contributors to the $35\,M_\odot$ peak within the SMT channel are the SMT+SMT and SMT+NON formation pathways. These channels originate from massive stars ($M_1 > 60\,M_\odot$) with a slightly less massive companion ($M_2 > 35\,M_\odot$), as shown in Figure 4.2. While these systems originate from similar populations, they undergo drastically different evolution. Therefore, we look at each pathway separately in the following sections.

Single Stable Mass Transfer Only (SMT+NON)

Because these systems only interact before the first SN, the first formed BH remains unchanged in mass after its formation and, thus, comes from an initially massive star that has experienced or is close to the lower limit of PPISN.

The non-interacting nature after the first SN in this system makes that the primary BHs do not continue to grow after their formation. This is a result of the companion experiencing QHE, which occurs in BPASS V2.2 when 5% of its initial mass is accreted from the primary at low metallicities. This explains the low average metallicity of this channel in Figure 4.5 since QHE is limited to systems with a metallicity of 0.004 or below. The majority of systems in this channel undergo QHE. Our QHE models are assumed to be fully mixed during hydrogen burning. Thus, their mean molecular weight increases

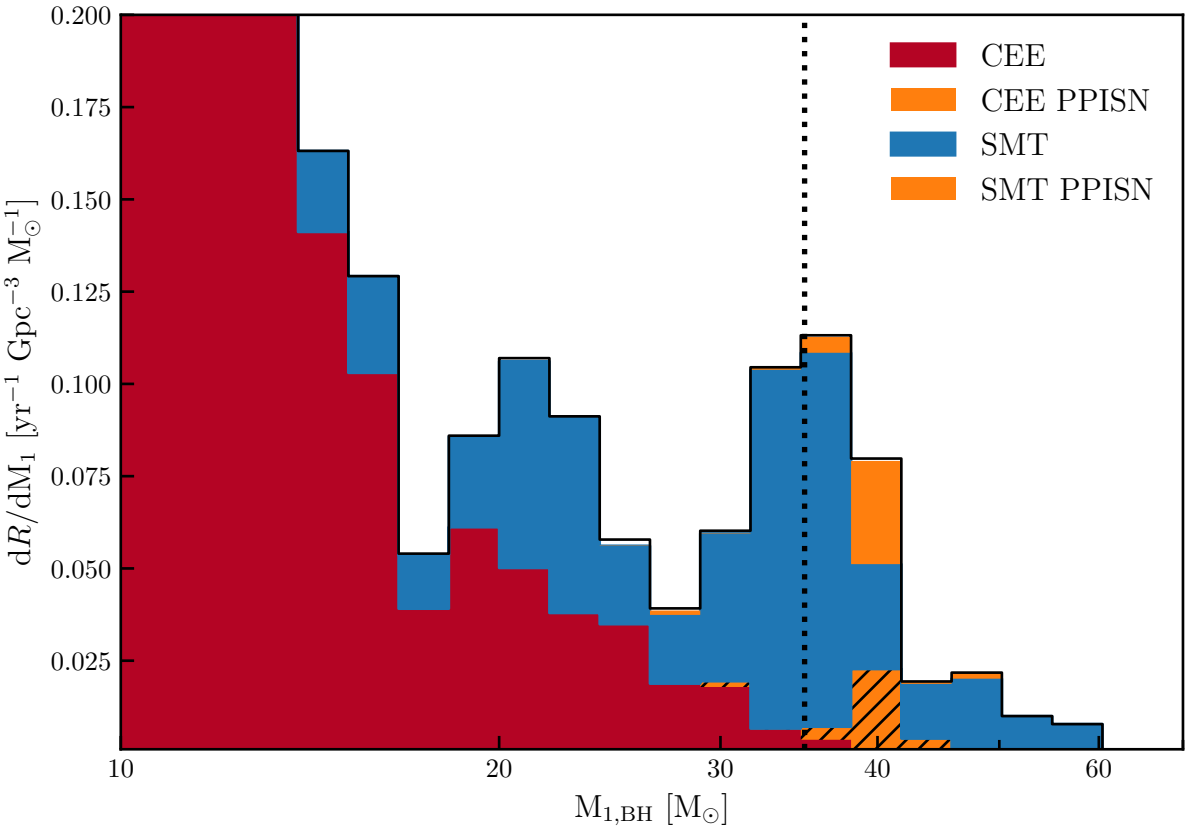

Figure 4.6: The primary remnant mass distribution at $z = 0$ rebinned to 50 logarithmic spaced bins and zoomed in on the $35\,M_\odot$ excess, where the systems are split into the SMT and CEE channels with the PPISN tagged per channel. The systems experiencing PPISN are above $35\,M_\odot$ (dashed line). The majority of the peak is formed through the SMT channel. The black line represents the total event rate, which also contains non-interacting systems. An additional excess near $20\,M_\odot$ can be identified and is discussed in Section 4.6.4.

with the progression of nuclear burning. This leads to the radius of the star shrinking rather than expanding, as would occur with normal main-sequence stars. QHE stars fail to fill their Roche lobe and do not interact with their companion. The BH companion will be unable to grow further and PPISN systems only contribute to the high end of the peak near $35\,M_\odot$ through the SMT+NON formation channel.

Double Stable Mass Transfer Only (SMT+SMT)

The SMT+SMT formation pathway is more complicated than the SMT+NON channel due to interactions in multiple evolutionary phases. Similar to SMT+NON, these merging BBHs come from very massive ZAMS stars, but they do not all experience PPISN.

Instead, limitations from mass transfer stability, QHE, and stellar winds restrict the SMT+SMT channel to form BHs around 35 $M_\odot$. Most low ZAMS primary and secondary masses will not form a BH or merge within the Hubble time. We distinguish between the regime with QHE ($Z < 0.006$) and without, because QHE restricts further interactions in BPASS.

Figure 4.7 shows a cartoon depiction of how each process in the QHE regime restricts the SMT+SMT formation pathway. The high mass end of the $M_{1,ZAMS}$ is restricted due

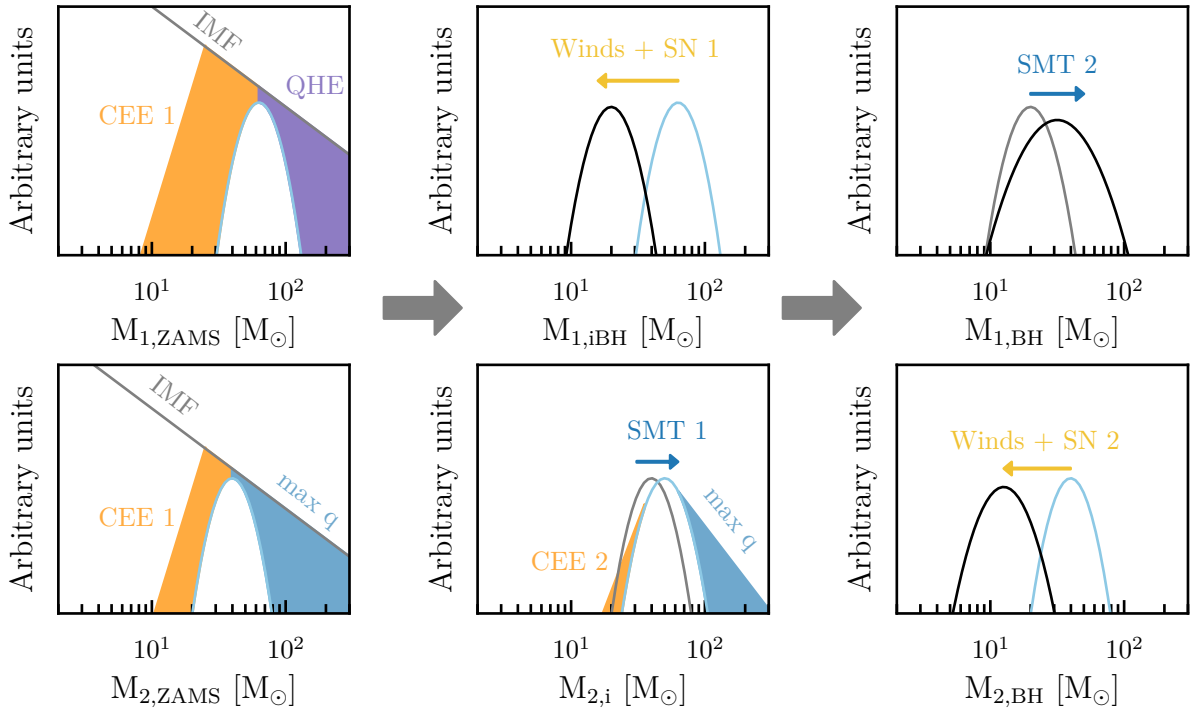

Figure 4.7: A cartoon depiction of the BBH distribution and the stellar physics that restricts SMT at low metallicity. The peaks represent the SMT channel at each stage. From the Kroupa IMF (grey), most systems do not result in a BH or merge within the Hubble time. In the primary models, the low ends of the $M_{1,ZAMS}$ and $M_{2,ZAMS}$ distributions are limited by mass transfer stability (CEE 1; orange), while the high-mass regime is limited by QHE (purple). As a result of limited high-mass contribution, the secondary is also limited (max q; blue). As metallicity increases, the $M_{1,iBH}$ shifts towards lower masses due to stellar winds. Also, in the primary model, $M_{2,ZAMS}$ increases due to SMT onto it, resulting in the $M_{2,i}$ distribution. In the secondary model, CE restricts $M_{2,i}$ at the low end (CEE 2; orange), while the maximum mass ratio limits the low end. During this phase, $M_{1,iBH}$ increases in mass due to SMT to give the $M_{1,BH}$ distribution in the top right Figure. $M_{2,i}$ losses material due to SMT, stellar winds, and the SN, and results in the $M_{2,BH}$ distribution in the bottom right Figure. Black and blue peaks lines peaks indicate the BH and stellar distribution, respectively. Grey distributions are the distributions from the previous phase.

to QHE (see Section 4.5.2 for more details), since mass transfer is stable and highly conservative at these donor masses (see Section 5.1). QHE restricts further interactions and makes it impossible for the system to merge within the Hubble time. As a result of this upper mass restriction in $M_{1,ZAMS}$, $M_{2,ZAMS}$ is also restricted since per definition $M_{2,ZAMS} < M_{1,ZAMS}$.

The low end of $M_{1,ZAMS}$ is limited by CE. If the donor star is less massive, it is more likely to undergo unstable mass transfer and, thus, does not contribute to the SMT channel (see Section 5.1 about the stability). Similarly, if the companion star is too small compared to the primary mass, it will experience CE due to the large mass ratio and restricts the bottom of $M_{2,ZAMS}$. Since the accretion before the first SN is limited due to QHE, the secondary mass distribution ($M_{2,i}$) is similar to the ZAMS distribution ($M_{2,ZAMS}$).

Further limitations are introduced at later stages of the evolution due to the stability of mass transfer between the star and compact object. At low secondary masses, the system is likely to undergo a CE, while higher mass systems are more likely to interact stably, as CEE2 in Figure 4.7 indicates. Together with PISN limiting the maximum formation mass of $M_{1,iBH}$, at low metallicities this leads to systems with mass ratios close to unity.

As metallicity increases within the QHE regime, stellar winds now limits the maximum $M_{1,iBH}$ mass. Moreover, they also increase the stability and non-conservative nature of mass transfer during core-helium burning. As a result, QHE can be avoided, while $M_{2,i}$ can still transfer a significant amount of material onto $M_{1,iBH}$. We discuss this further in Section 4.2.2. At metallicities above 0.004, QHE no longer restricts the maximum $M_{1,ZAMS}$. Instead, it is restricted by the IMF, and higher mass primaries and secondaries can interact stably. This increases the systems contributing to the merger rate and the material available for the formation of BHs. At the same time, mass loss due to stellar wind has also increased, which decreases $M_{1,iBH}$ and $M_{2,BH}$. The interplay between the mass transfer and stellar winds results in an initial increase in BH mass with increased metallicity until the stellar winds become stronger and reduce the BH mass again. Since mass is stored on the companion and transferred back onto the BH, a transition to BBH systems with high $M_{1,BH}$ and small $M_{2,BH}$ (q closer to 0) takes place as metallicity increases.

We now turn our attention to the actual distributions in the SMT+SMT channel in Figure 4.8. The leftmost Figures show that most of the systems originate from $Z > 0.004$, above the QHE limit. While the contribution of systems below the QHE limit to the

peak is limited, these systems play an important role in the high-end of $M_{1,BH}$ and will be discussed in Section 4.2.2. Above the QHE limit, systems with $Z = 0.006$ (grey) cover a large range of $50 < M_{1,ZAMS} < 300$. As metallicity increases (redder), the high end of $M_{1,ZAMS}$ becomes restricted due to stellar winds keeping the radius of the star small and limiting interactions. Furthermore, the material available for mass transfer and $M_{1,iBH}$ formation reduces. Thus, as metallicity increases, $M_{1,iBH}$ decreases and the change in mass between $M_{2,ZAMS}$ and $M_{2,i}$ decreases.

The $M_{1,iBH}$ distribution after the first SN is similar to the single star remnants with the same ZAMS mass but is more extended to the low and high end. The less massive BHs are due to enhanced mass loss, reducing the core mass of stars and leading to less massive remnants as discussed by Laplace et al. (2021). The more massive BHs are surprising, but were also found in Eldridge & Stanway (2016). These are a consequence of mass transfer preventing the formation of a convective zone at the edge of the helium core post-MS. This convective region would normally dredge-up core material, decreasing

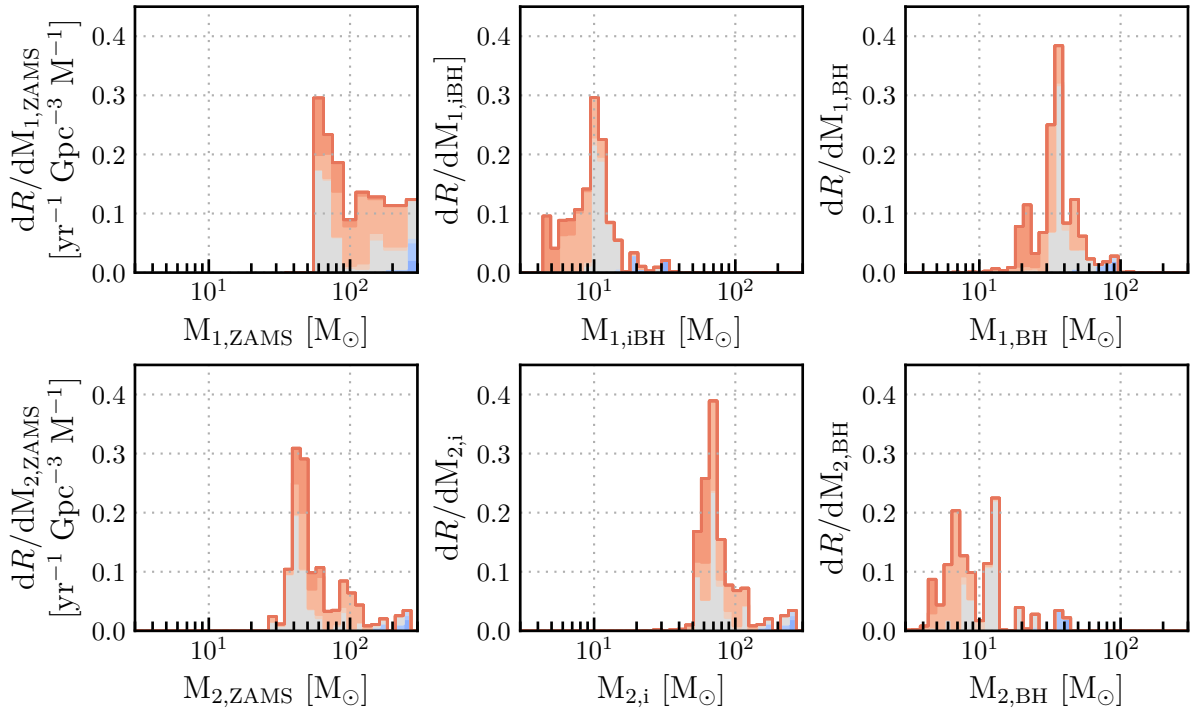

Figure 4.8: The evolution of the primary and secondary masses in the SMT+SMT channel separated by metallicity. The metallicity uses the same colouring as Figure 4.5. Standard binning (40 bins) is used, except for $M_{1,ZAMS}$, for which we use the values of the BPASS grid. The leftmost figures show the ZAMS distribution, the middle figures the masses right after the first SN, and the right figures the final remnant masses of the merging BBHs in this channel. The units of the vertical axis are the same for all plots.

its mass: by preventing its formation, the final core mass is greater than expected. This process is only revealed by the detailed evolution models.

With limited material available for the BH to grow during the second phase of SMT, $M_{1,BH}$ decreases with increasing metallicity. Due to this process, the $35\,M_\odot$ peak contains a metallicity distribution, whereas $M_{1,BH}$ increases, metallicity decreases. The combination of stellar wind, QHE, and stability criteria result in the placement of this peak near $35\,M_\odot$. Furthermore, $M_{2,i}$ has additional mass loss at higher metallicity due to stellar winds. Due to this, $M_{2,BH}$ decreases and the mass ratio of the final BBH systems increases. Moreover, these systems are also formed more recently and most require eccentric orbits to be able to merge within the Hubble time.

As a result of the double SMT, the mass ratio of systems in the $35\,M_\odot$ peak is around 0.2. However, altering the remnant mass prescription can result in more equal mass ratio systems. Moreover, since these models have experienced a reasonable amount of accretion, the primary BH is expected to have a spin. A more careful analysis of the accretion and spin of the BHs is required to determine in SMT can produce the $35\,M_\odot$ excess, which is not currently possible in BPASS V2.2.

4.2.2 The Formation of Upper Mass Gap BHs ($> 50\,M_\odot$)

The formation of high-mass BH is impeded by the PPISN and PISN mechanisms reducing the BH progenitors mass or completely disrupting its progenitor, respectively. Furthermore, the formation of a CE will shed a significant amount of stellar material from the system, further reducing the available mass for BH formation. In agreement with Neijssel et al. (2019) and van Son et al. (2022), we find that high-mass BH ($20 - 115\,M_\odot$) are increasingly formed through systems only undergoing SMT, as shown in Figure 4.1. However, we find significantly higher masses than predicted by rapid population synthesis codes, who have ZAMS masses up to $150\,M_\odot$ (Bavera et al. 2021; Olejak & Belczynski 2021; van Son et al. 2022).

This is a direct result of super-Eddington accretion onto the BH, which results in no mass loss from the system during accretion, except for wind drive mass loss. However, van Son et al. (2020) and Bavera et al. (2021) have shown that a super-Eddington accretion rate onto a BH leads to fewer mergers within the Hubble time due to reduced mass and angular momentum loss from the system. Thus, for the systems to be able to merge, their periods need to shrink sufficiently during the systems evolution. This can either happen through angular momentum loss from the system, mass transfer from the more massive star to its lower mass companion, or tidal synchronisation. Since

super-Eddington accretion limits the former, we focus our attention on the latter two.

The $M_{1,BH}$ distribution in Figure 4.5 shows that the high-mass BHs come from high-mass sub-QHE limit metallicity $M_{1,ZAMS}$ systems with massive $M_{2,ZAMS}$. During the initial phase of the evolution, mass is transferred to the companion, but the amount transferred is limited because QHE would limit further interactions, if accretion was more than 5% of the companion mass. The formed $M_{1,iBH}$ is, therefore, limited by (P)PISN. As a result of the SN, the systems have large mass ratios ($q_{2,final} \sim 5 - 10$). But because $M_{2,i}$ are massive, they are able to interact stably (see Section 5.1) and due to the interaction taking place on the main-sequence, a significant amount of material is transferred onto the BH.

Since the initial mass ratio was larger, mass is transferred from the most massive star to the less massive BH, which reduces the period. Furthermore, as a result of the high mass ratio, tidal forces are strong and further reduces the period. A CE is avoided by the 'fast' radial shrinkage of the donor star and the 'fast' increase of the BH mass due to the super-Eddington accretion. As a consequence, when the mass ratio approaches unity, the radius of the donor star does not reach the separation of the system.

4.3 Nature of the Envelope

As discussed in Section 1.3, a star can respond to mass loss by expanding or contracting, which depends on the properties of the envelope of the star. In general, if a star has a convective envelope, it expands due to adiabatic mass loss, while it contracts if the envelope is radiative (Hjellming & Webbink 1987; Soberman et al. 1997). However, work by Ge et al. (2010, 2015, 2020a,b) has shown that metallicity, radius and evolutionary phase also influence the mass transfer stability. Most rapid population synthesis BBH merger predictions do not take this into account (STARTRACK, MOBSE, COSMIC, COMPAS; Belczynski et al. 2016; Giacobbo et al. 2018; Breivik et al. 2020; Riley et al. 2022) and instead use an adiabatic model based on the evolutionary phase to determine the stability of mass transfer, as per Hurley et al. (2002). This leads to more unstable mass transfer since, for example, convective envelope criteria are applied to core-helium burning stars that can have radiative envelopes (for an overview, see Klencki et al. 2020, 2021). Furthermore, other detailed mass transfer simulations have shown that BH-star systems are more likely to undergo SMT (Pavlovskii et al. 2017; Marchant & Moriya 2020; Marchant et al. 2021), impacting population of merging BBHs (Gallegos-Garcia et al. 2021), and that the donor response is very different than the simplified adiabatic

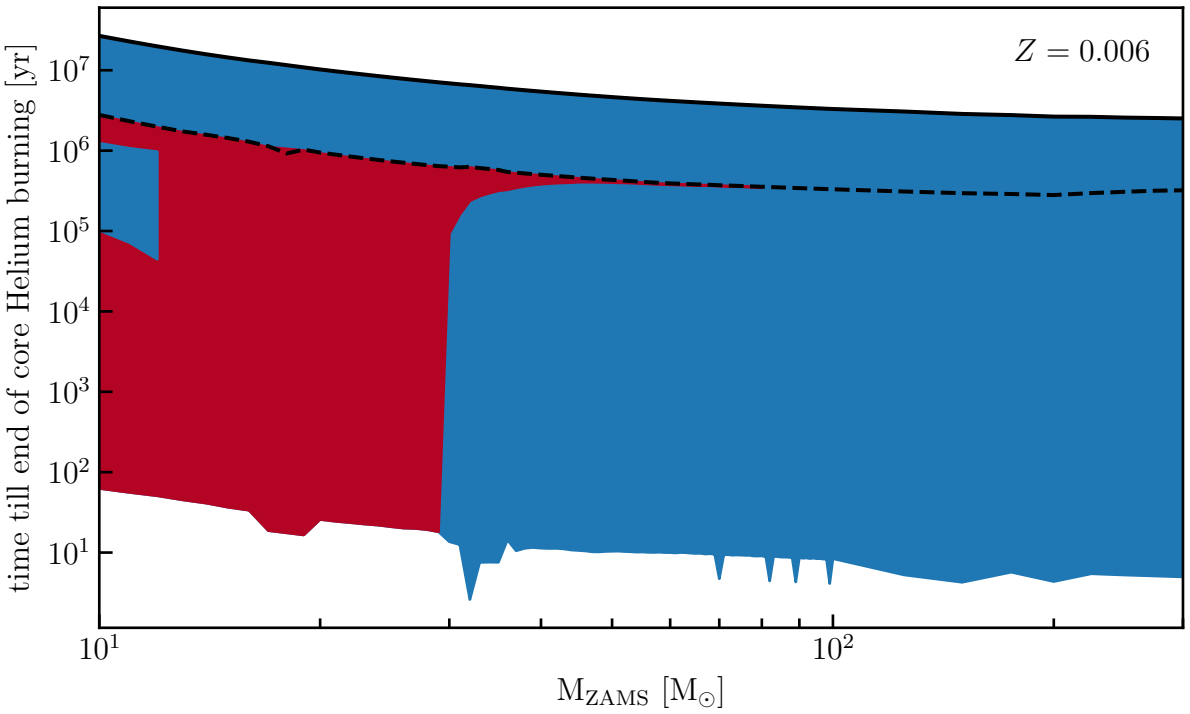

Figure 4.9: The radiative (blue) or convective (red) nature of the envelope of single stars at $Z = 0.006$ from ZAMS to the end of Helium core burning. The process for extraction from the SINGLE-STAR MODELS is discussed in the Supplementary material. For models that did not reach the end of core helium burning, we interpolate between ZAMS masses. We indicate the ZAMS (solid black line) and the end of the main-sequence (dashed black line).

model and holds across stellar codes (STARS, MESA, Heyney-type code Woods & Ivanova 2011; Passy et al. 2012).

Since BPASS STARS is based on the Cambridge STARS code, stability is determined by following the equations of stellar structure through mass loss, which allows us to determine the nature of the envelope and its response to mass loss over a large mass and metallicity range. Since mass transfer alters the stellar evolution and the internal structure of the donor star, we turn our attention to single stars to determine the convective or radiative nature of the donor envelope, because this is the structure of the star just before the onset of Roche lobe overflow. Figure 4.9 shows the energy transport in the envelope of the *single-star models* at $Z = 0.06$ (Appendix E contains the other BPASS metallicities). We find that nearly all massive stars spend their MS with a radiative envelope. The post-MS envelope depends on the initial mass and metallicity. At $Z > 0.002$, $M_{ZAMS} \leq 26$ have convective envelopes after core-helium burning initiates. Figure 4.9 shows this for $Z = 0.006$. Above this mass, the envelopes only have

a short period of convection before core-helium burning initiates, after which the star has a radiative envelope, which is similar to results found by Klencki et al. (2021). This indicates that interactions during this phase are more stable than estimated by rapid population synthesis codes, when considering the nature of the envelope as a proxy for mass transfer stability. Below $Z < 0.002$, the star becomes convective during core helium burning at $M_{ZAMS} \geq 21$. Below this limit, the absence of metals restricts the formation of a convective envelope until late in the core-helium burning phase. At $Z = 10^{-5}$, the convective zone is completely avoided at these low masses.

This shows that metallicity, age, and mass all influence the nature of the envelope in a single star. However, we cannot find a direct relation between the envelope of the donor star and the mass transfer stability. Moreover, in binaries, short mass transfer phases could alter the internal structure of the star in such a way that at later stages in the donor evolution, the envelope no longer becomes convective. Thus, without detailed treatment of the internal structure at the moment of mass transfer, BHs formed through SMT are missed in rapid population synthesis codes.

4.4 Mass Ratio Exploration

The resulting q values for SMT onto the BH in Figure 4.4 are more extreme than typically found in other detailed binary models (Marchant et al. 2021; Gallegos-Garcia et al. 2021). Although the mass ratios at the moment of mass transfer are less extreme, values up to $q = 23$ remain. As discussed in Section 1.3, tidal synchronisation should lead to mergers of such systems, but the mass transfer alters the mass ratio and prevents the merger. This could also indicate that our determination for CE is too constricting since our stability determination only considers the donor radius and the separation of the system. Although as we will see in Section 5.1 BPASS STARS undergoes more CE than detailed stellar models. Since much uncertainty in binary interactions remains, in this section, we explore how the high-mass features in $M_{1,BH}$ depend on the mass ratios and explore the extreme mass ratio systems.

4.4.1 Mass Ratio Cuts

Since the high-mass features predominantly come from the SMT+SMT channel, we perform two cuts at $q < 10$ and $q < 5$ based on the mass ratio at the moment of mass transfer onto the BH. The $q < 10$ cut in Figure 4.10 shows that large mass ratios ($q > 10$) are only a fraction of the SMT+SMT channel. Moreover, the cuts show that the $35\,M_\odot$

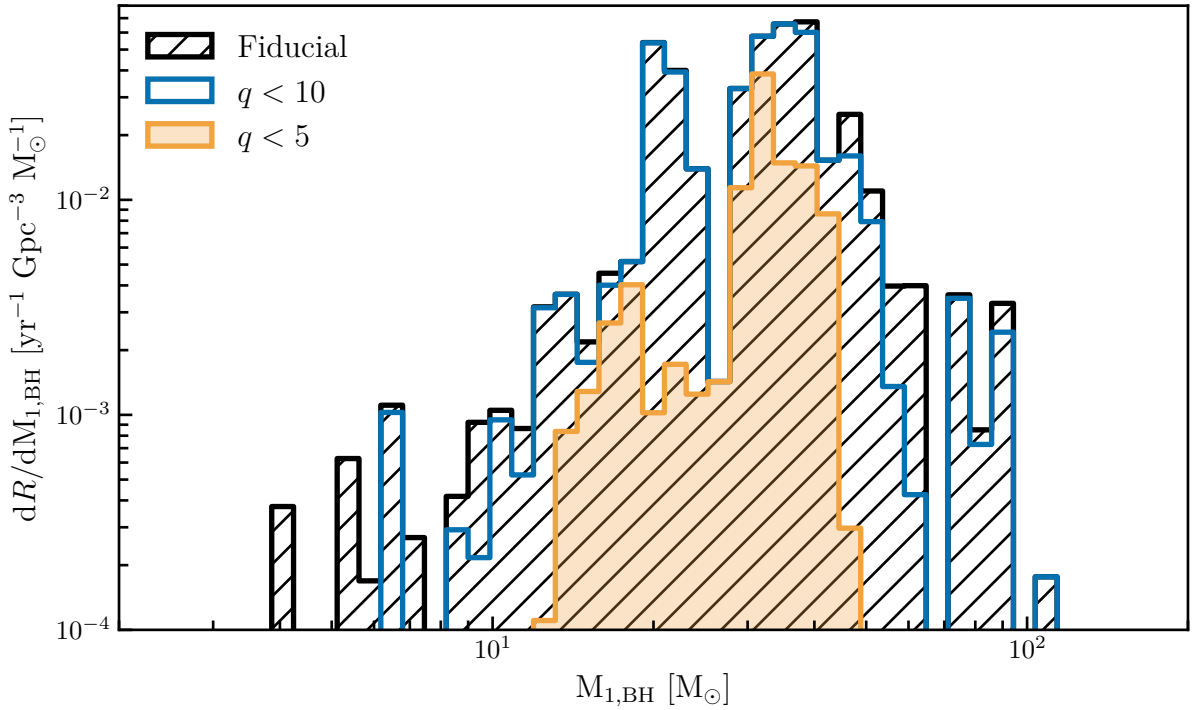

Figure 4.10: The primary BH mass ($\mathrm{M}_{1,\mathrm{BH}}$) distribution at $z = 0$ from the SMT+SMT channel with the fiducial model (black) and two cuts based on the mass ratios at the moment of mass transfer with $q < 10$ (blue) and $q < 5$ (orange).

peak is dominated by $q < 5$ systems, with the spread around the peak being a result of more extreme mass ratios ($q < 10$). As a consequence, the upper mass gap systems undergo SMT with mass ratios between 5 and 10, and our stability criteria could influence the existence of these systems. These mass ratios are larger than generally considered stable but are not unreasonable at low metallicity and high donor mass. In Section 5.1, we compare our stability criteria to other detailed work and describe why the mass transfer is stable.

Extreme Mass Ratios

Some BH-star systems undergoing SMT have extreme mass ratios with $q_{2,\mathrm{initial}}$ up to 25, as shown in Figure 4.4. The actual mass ratio at the moment of Roche lobe overflow is less extreme due to mass loss, but some $q > 15$ remain. These systems all interact on the main-sequence and occur between a small BH (3-6 $\mathrm{M}_{\odot}$) and a very massive star (70–140 $\mathrm{M}_{\odot}$) at $Z > 0.01$, a metallicity and mass regime where stellar winds are strong. As a result, the primary loses mass quickly, while the amount of Roche lobe overflow is small. This reduces the mass ratio and, thus, avoids the Darwin Instability. Due to the

strong stripping of the star, stellar winds become stronger and limit further interactions. Although these systems exist, their contribution to the $M_{1,BH}$ distribution is minimal and limited to the low mass regime.

4.5 Robustness of $M_{1,BH}$ Features

As discussed in Section 4.2, many aspects of stellar evolution come together to shape the features of the $M_{1,BH}$ distribution. The BBH rate and distribution are rather robust against some evolutionary parameters, such as the natal kick prescription (Broekgaarden et al. 2022a). This is further confirmed by Figure A3 in Ghodla et al. (2022), where the $35\,M_\odot$ overdensity and extended tail remain between different natal kick prescriptions. However, the BBH rate and distribution are very dependent on the star formation history and metallicity evolution (Chruslinska et al. 2019; Tang et al. 2020; Broekgaarden et al. 2022a). In Chapter 3, we have shown that the combination of BPASS and the TNG star formation history results in electromagnetic and GW transient close to observations. Moreover, the features in the high-mass $M_{1,BH}$ distribution remain when using the empirical star formation history from Briel et al. (2022). The stellar wind prescription can also alter the merging primary mass BH distribution by altering the mass available for mass transfer and the compact remnant (Broekgaarden et al. 2022a; Dorozsmai & Toonen 2022).

We have shown that using detailed stellar models with PPISN and super-Eddington accretion onto BHs leads to an extended mass tail up to $100\,M_\odot$ and an overdensity near $35\,M_\odot$, as observed by the LIGO/Virgo/KAGRA collaboration. These are both an effect of increased SMT. Because not only the BBH population is affected by the detailed treatment of mass transfer, we discuss the mass transfer stability in Chapter 5.1, and how BPASS compares to detailed stellar models and rapid population synthesis codes. In the following Sections, we explore how the QHE limit and remnant mass prescriptions influence the distribution.

4.5.1 Star Formation History Choice

In this chapter, we focused on the BBH population resulting from the CSFRD and metallicity evolution of the TNG-100 simulation. However, in Chapter 3, we saw that the metallicity evolution can have an impact on the predicted cosmic rates. As such, we implement the other CSFRD and plot their $M_{1,BH}$ distributions in Figure 4.11. While the distributions have different normalisations, the main features of a peak at $\sim 7\,M_\odot$

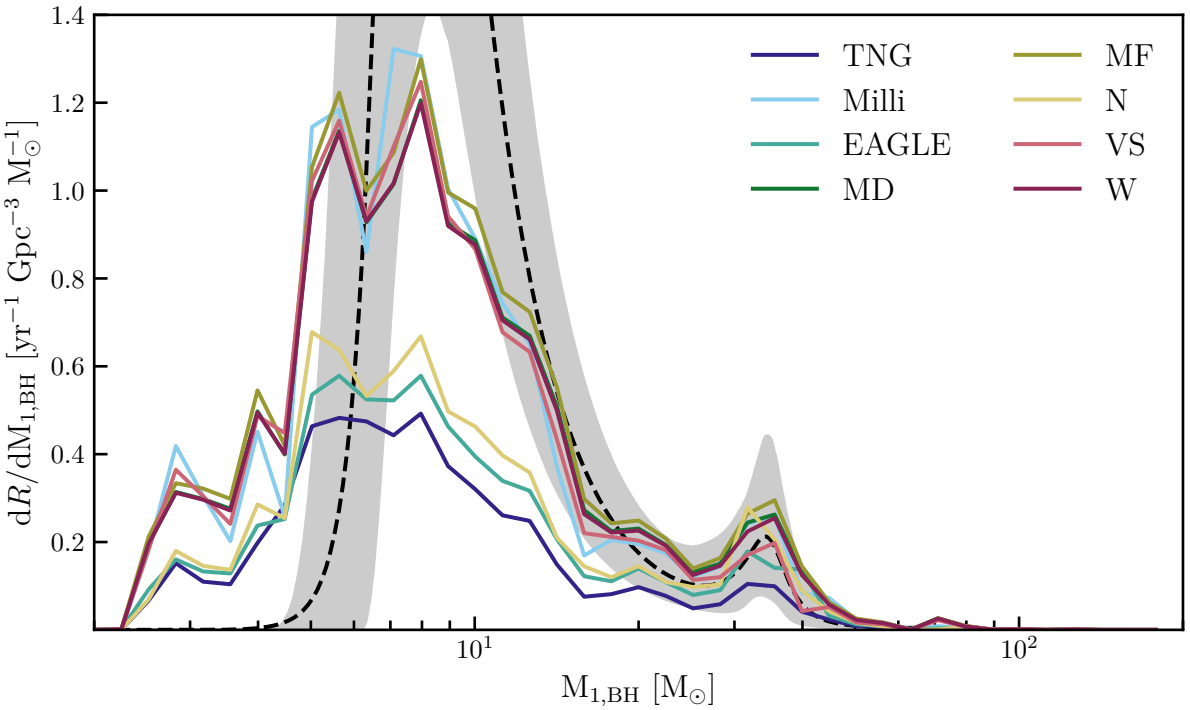

Figure 4.11: The primary BH mass distribution for the SFH prescriptions considered in this work. The black dashed line and grey area are the GWTC-3 90% credible interval (Abbott et al. 2023).

and $35\,M_\odot$ remain. The different SFH prescriptions have a large influence over the total rate of cosmic transients, but the choice of SFHs considered in this work does not impact the features in the primary BH mass distribution. For the low-mass BH regime, these findings are similar to van Son et al. (2023), but we do not see a dependence on high redshift low-metallicity star formation for the high-mass region. Section 4.5.4 shows that although the SMT+SMT channel does have long delay times and are redshift dependent, its rate increases with higher metallicity. As a result, these features are not as low-metallicity and early star formation dependent as found by van Son et al. (2023).

4.5.2 Quasi-Homogeneous Evolution Limit

The fiducial version of BPASS uses a hard QHE limit, where below $Z = 0.006$ QHE takes place if the companion star accretes more than 5% of its initial mass. Together with the stellar winds, this determines the upper edge of the $35\,M_\odot$ excess. As shown in Figure 4.12, lowering the QHE limit from $Z \leq 0.004$ to $Z \leq 0.001$ causes an increase in high-mass $M_{1,BH}$ around $40\,M_\odot$ and around the $10\,M_\odot$ peak, while pushing it towards higher BH masses. Furthermore, a plateau around $20\,M_\odot$ becomes clear as a result of

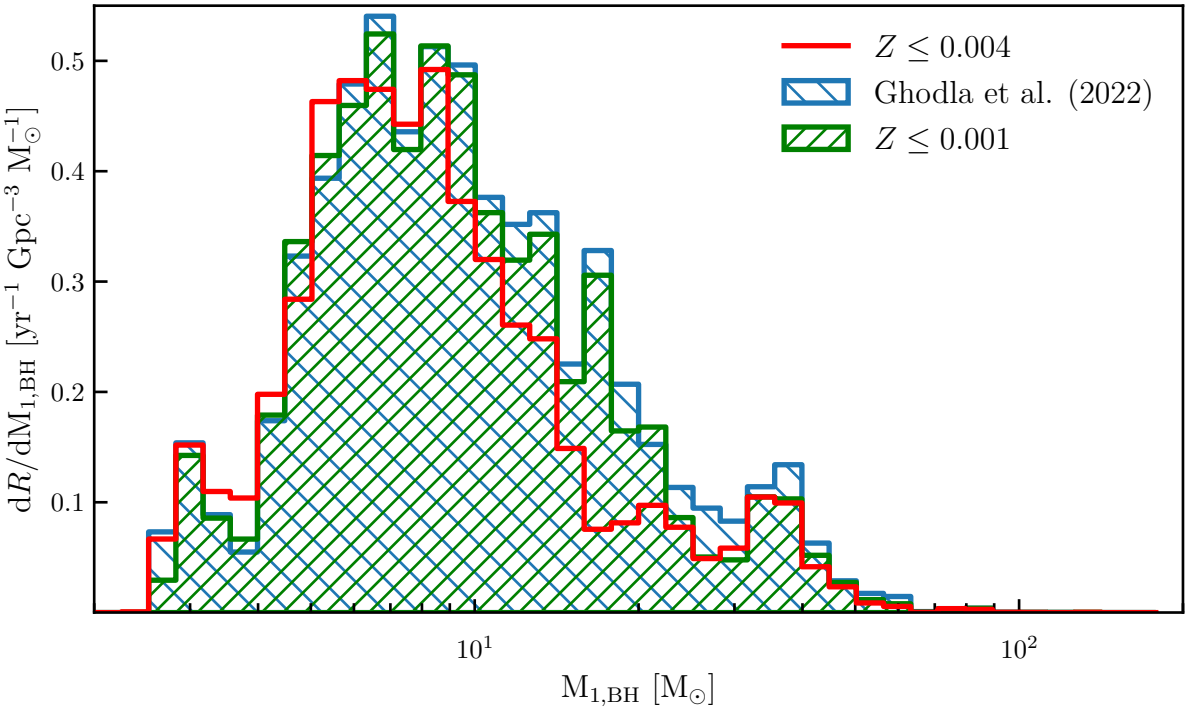

Figure 4.12: The $M_{1,BH}$ distribution at $z = 0$ for the QHE limit ($Z \leq 0.004$) implemented in standard BPASS (red), lowered to $Z \leq 0.001$ (green), and the accretion based QHE prescription from Ghodla et al. (2023) (blue).

SMT. While QHE is likely to occur at metallicities $0.001 \leq Z \leq 0.004$, this shows that QHE restricts the formation pathway for BBH in BPASS by limiting further binary interactions. Although this choice is physically motivated, in some cases, the star might spin down and still expand, resulting in binary interactions.

Instead of a hard limit, QHE through accretion is more likely to be a gradual process dependent on the mass and angular momentum accreted. Using a more detailed prescription for accretion QHE, created using MESA stellar evolution models, Ghodla et al. (2023) have shown that in BPASS, fewer systems undergo QHE, especially at low ZAMS masses. In the high ZAMS mass regime, QHE remains similar to the fiducial BPASS model. In Figure 4.12, we show the primary remnant mass distribution using the QHE prescription from Ghodla et al. (2023). The more detailed prescription adds additional systems to the high ends of the $10\,M_\odot$ peak and the $35\,M_\odot$ excess, shifting both to a slightly higher mass while the upper mass gap BHs remain.

4.5.3 Remnant Mass Prescriptions

While we are able to accurately predict the high end of the primary BH mass distribution, the lower end of our prediction does not align with observations. Since this regime is dominated by CE evolution, our prescription may need adjustment, but this is beyond the scope of this work. Another option could be the remnant mass prescription since this will mostly influence the lower mass regime, except for the (P)PISN prescriptions which influence the high mass regime. To explore the former, we implement the rapid and delayed remnant mass prescriptions of Fryer et al. (2012) in Figure 4.13, and we alter the (P)PISN prescriptions to show that the high mass features in the $M_{1,BH}$ distribution remain.

Fryer Rapid/Delayed

To explore the effect of the remnant mass prescription, we have implemented the rapid and delayed remnant mass prescription of Fryer et al. (2012) in Figure 4.13 (as discussed in Section 2.2.2). Note that these do not implement PPISN.

Both prescriptions increase the number of systems around $10\,M_\odot$, bringing the predicted distribution above the observed intrinsic rate. This is most likely a result of the fact that fiducial BPASS injects 10^{51} erg into the star, which could cause too much material to be ejected from low-mass stars. However, the Delayed prescription also increases the number of systems between 2 and 5 $M_\odot$, while Rapid does not include these systems and has a mass gap between 3 and $5\,M_\odot$ due to the implementation, as discussed in Section 2.2.2. Figure 2.4 shows that the Rapid and Delayed prescriptions are similar in the high mass regime since both assume full fallback onto the BH. In the low mass regime, the prescriptions differ significantly from each other and from the BPASS prescription. BPASS generally predicts smaller remnant masses for larger CO cores than both Fryer prescriptions and could result in the significantly different low $M_{1,BH}$ regime. Especially in this regime, the amount of fallback onto the proto compact object is unclear and could cause both NSs or BHs to be formed (Mandel et al. 2020; Mandel & Müller 2020). While the effect of the remant mass prescription makes it difficult to untangle the influence from CEE, it also shows that the extended tail and excess near $35\,M_\odot$ remain with other remnant prescriptions than implemented in fiducial BPASS.

(P)PISN

We have implemented the PPISN prescription from Farmer et al. (2019) for $M_{CO} \geq 38\,M_\odot$, which results in a smooth transition between different remnant mass prescriptions. van Son et al. (2020) found an additional bump at $30\,M_\odot$ as a result of a non-smooth transition between the CCSN and PPISN prescription. This is not present in our remnant mass distribution. Moreover, fiducial BPASS does not contain this PPISN prescription, but the $35\,M_\odot$ excess is still present.

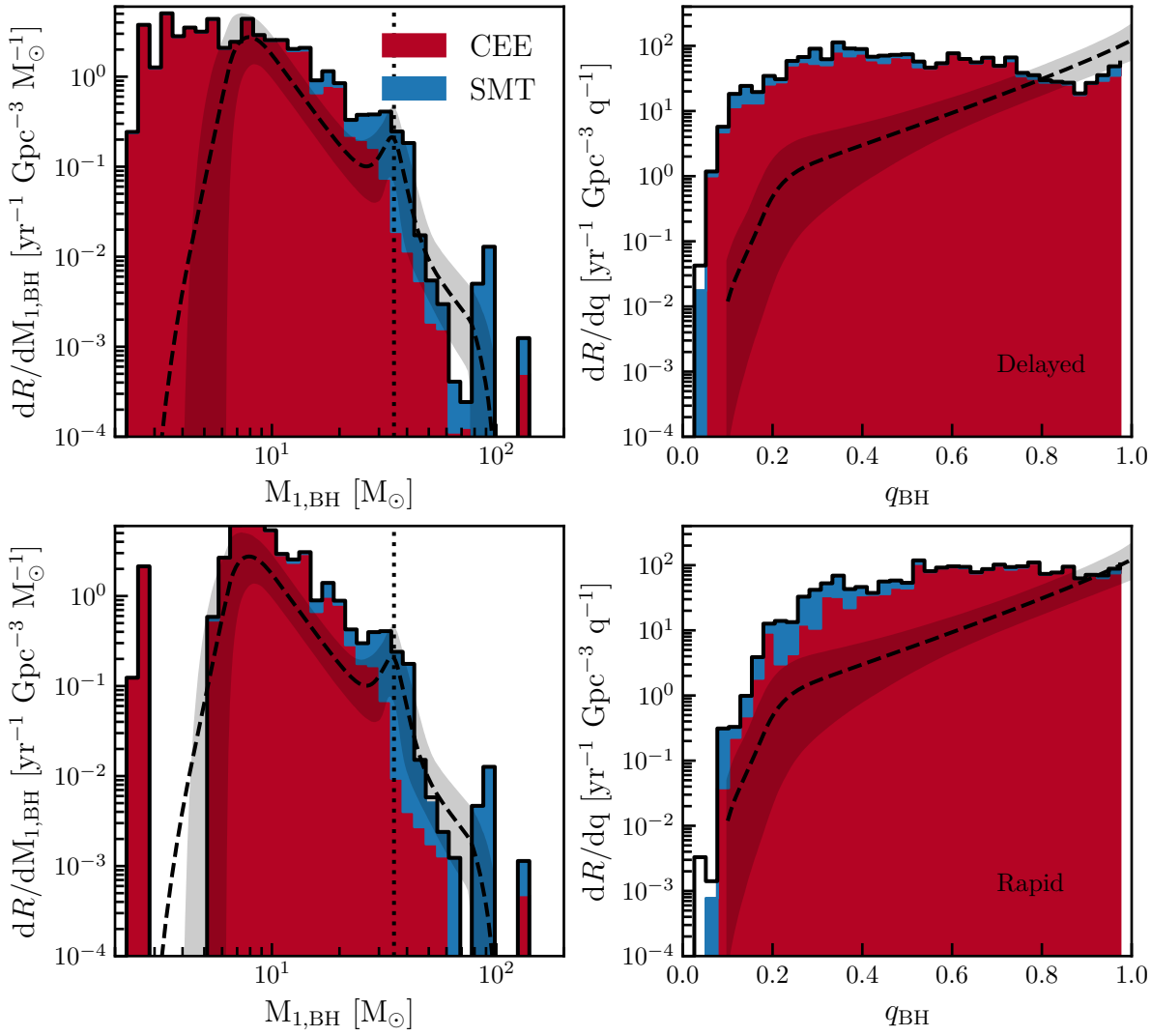

Figure 4.13: The primary BH mass (left) and mass ratio (right) distribution at $z = 0$ of the Fryer et al. (2012) delayed (top) and rapid (bottom) remnant mass prescriptions, split into CEE and SMT formation channels. The Rapid prescription has some BHs with small primary masses, possibly due to accretion onto a NS, such that a BH is formed. $35\,M_\odot$ is marked with a dashed line.

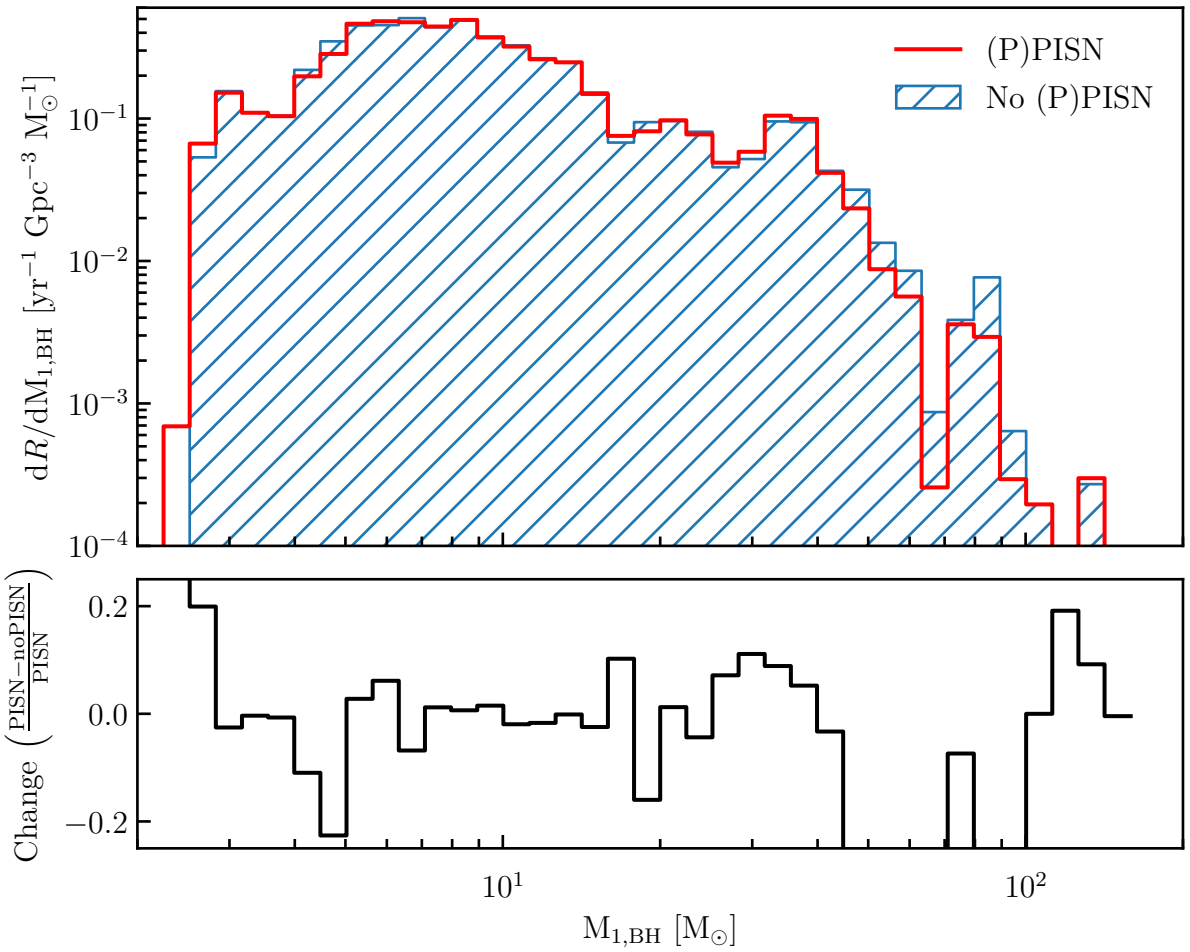

Figure 4.14: The $M_{1,BH}$ distribution at $z = 0$ of merging BBHs for the model presented in this work with PPISN and PISN (red) and for a model without PPISN and PISN (blue). The removal of (P)PISN does not influence the key observed features in BPASS, but does increase the number of mergers with upper mass gap BHs by a factor 2. This shows as the change dissapearing out of scale.

Furthermore, in Figure 4.14, we have removed the PPISN and PISN prescriptions from the population synthesis and find only subtle changes to the $35\,M_\odot$ excess with less than a 10% increase to the peak when including (P)PISN. This is in contrast to findings by Stevenson et al. (2019), who found that the (P)PISN influences the high-mass $M_{1,BH}$ regime. Because most of the high primary mass systems in BPASS are created through accretion onto BHs with initial masses between $10 - 30\,M_\odot$, the impact of (P)PISN is limited in BPASS, as those BHs do not come from progenitors experiencing PPISN.

4.5.4 Redshift Evolution

Up to this point, we have looked at the primary mass distribution at $z = 0$, but the BBH merger rate changes over redshift, as indicated in Figure 3.7. The formation pathways contributing to the BBH merger rate changes over redshift, as shown in Figure 4.15. The SMT+SMT channel increases similarly to the other rates initially, but below $z = 4$, it increases rapidly to 20% of the total BBH rate while the other channels start to decrease.

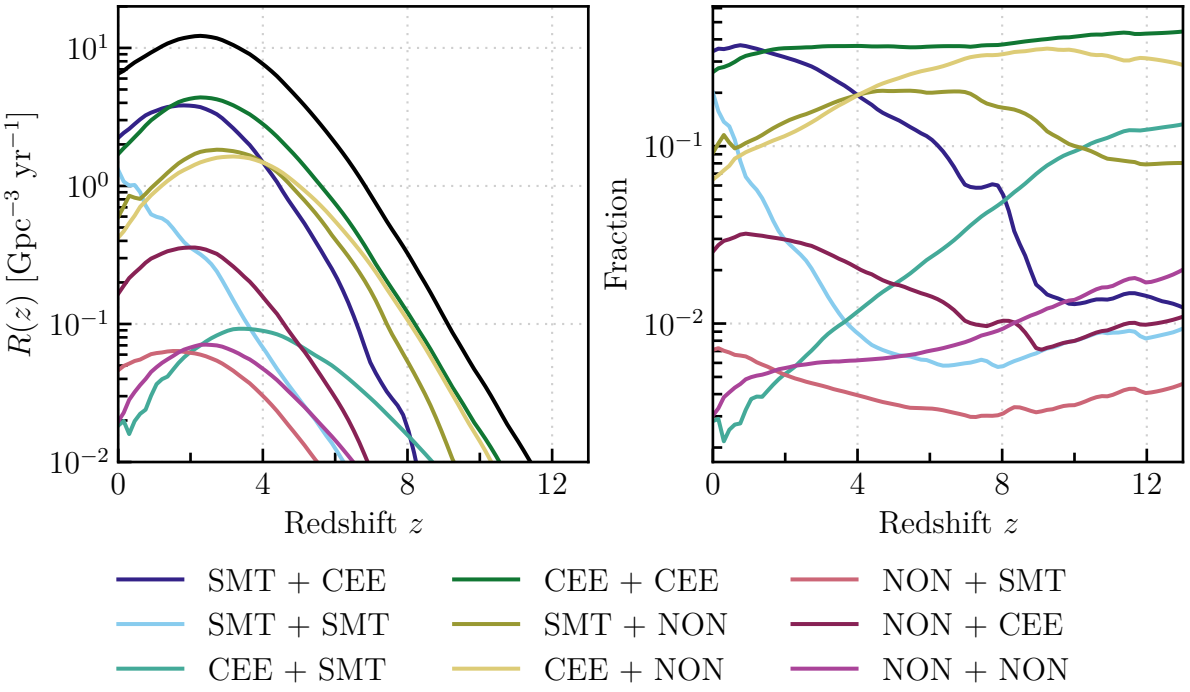

Figure 4.15: Merging BBH merger rate split up per formation channel with the rate (left) and as a fraction of the total rate (right).

The first reason for this behaviour is that the SMT+SMT channels delay times become constant and eventually increase above 10^8 yr, while most other channels continuously decrease, as shown in Figure 4.16. The SMT+NON channel is an exception to this, which experiences a slight increase at long delay times. Every metallicity in this channel exhibits the same constant behaviour, although the total rate is different between them. This results in an increase of SMT+SMT contribution at current time compared to at high redshift. The other reason for this behaviour is that the SMT+SMT channel increases with metallicity. In general, more stable mass transfer takes place between two stars, and a star and a compact at higher metallicities. This is most likely an effect of the increased stellar winds at higher metallicities. Furthermore, at higher

metallicities, fewer companions will undergo QHE after the first interaction, increasing the SMT+SMT channel in general.

Because the contribution of the SMT+SMT channel is increasing, so does the peak around $35\,M_\odot$. Figure 4.17 shows that the SMT+SMT creates the peak at $z = 0$ and that the peak is no longer present at $z = 2$. If the observed $35\,M_\odot$ excess is indeed caused by the SMT+SMT channel, it creates an avenue to calibrate the binary interactions. Furthermore, the very high mass BH systems are not present at high redshifts. Because the high mass systems are systems close to the QHE limit, at high redshifts, insufficient higher metallicity systems have been formed to contribute to the BBH rate.

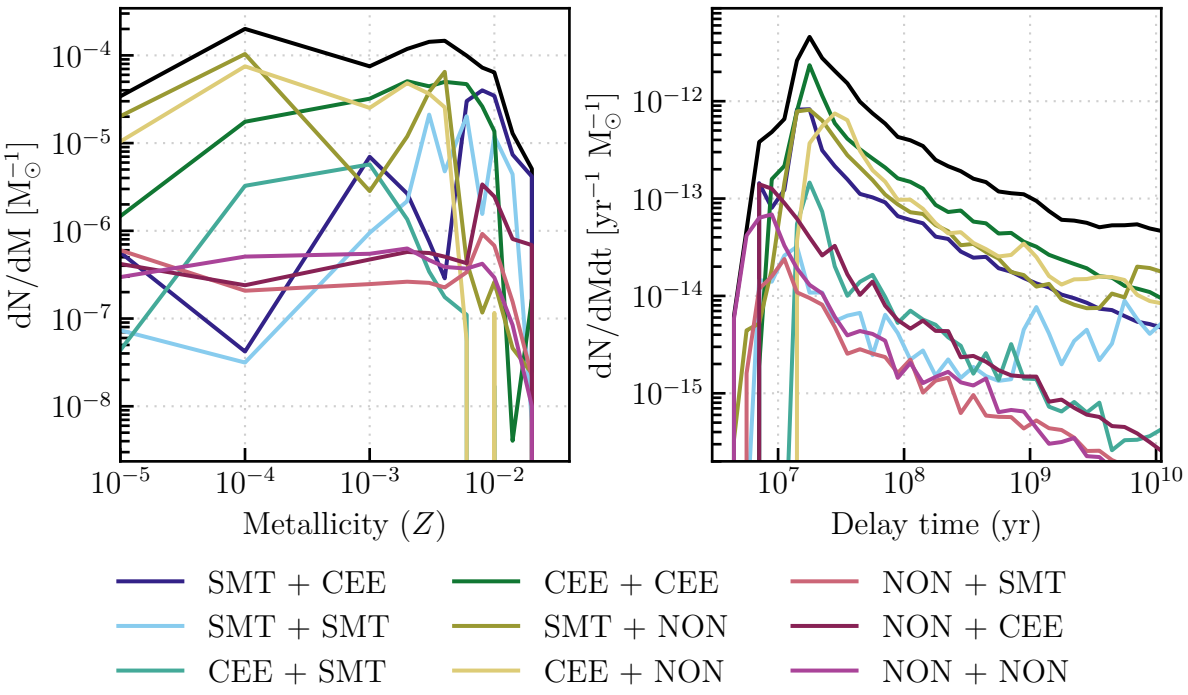

Figure 4.16: The merger efficiency over metallicity (left) and the delay time distribution (right) split per formation pathway. Black indicates the total rate. The right plot contains all metallicities together and is binned using the standard BPASS time bins.

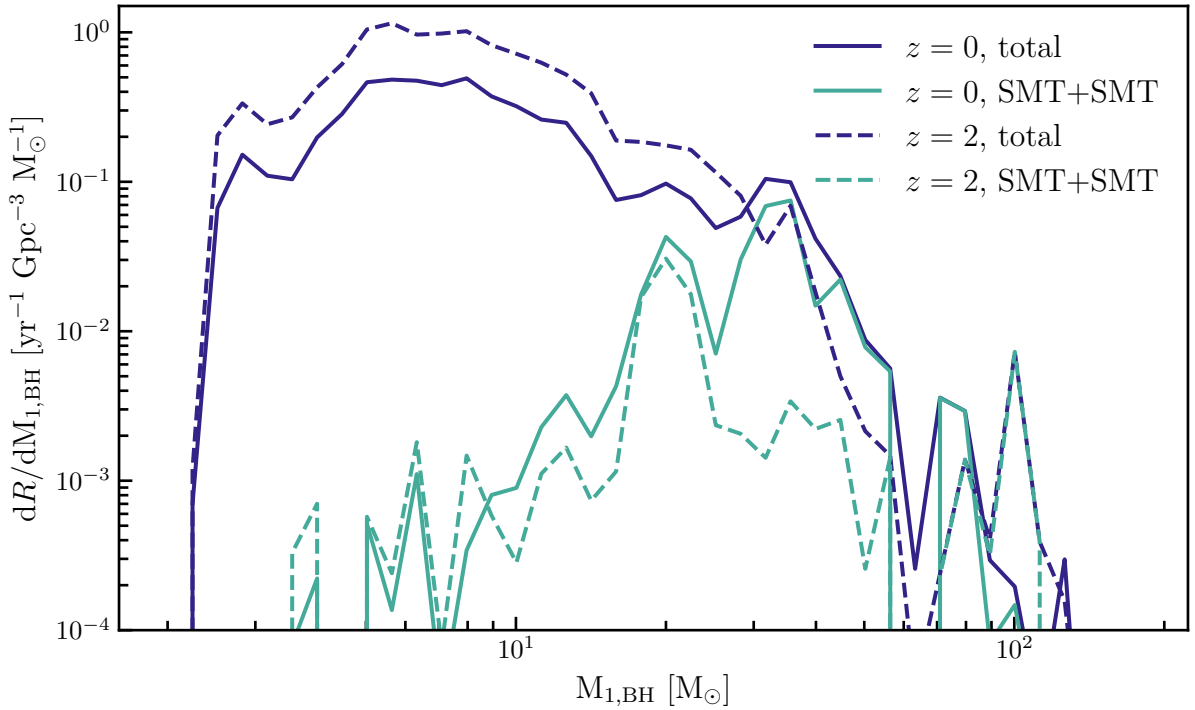

Figure 4.17: The primary BH mass distribution at $z = 0$ and $z = 2$ with the SMT+SMT channel separated. At $z = 0$, the $35\,\mathrm{M}_\odot$ excess is present, while at higher redshifts, this contribution decreases, and the peak disappears.

4.6 Caveats and Uncertainties

4.6.1 BH spin

Besides the stability of mass transfer, the efficiency of mass transfer is an important factor. To achieve high-mass BHs, we require stable mass transfer with super-Eddington accretion onto the BH. This can leave an imprint on the spin of the population since a large amount of material is accreted from the companion. This should lead to a non-negligible spin (Zevin & Bavera 2022) and even high spins for main-sequence stable mass transfer (Shao & Li 2022), albeit it is unclear if the BH remains rotating (Tchekhovskoy et al. 2012). BPASS does not currently track the spin of BHs. Thus, as an alternative, we look at the amount of accreted material onto the BH, which we use as a proxy for the spin.

From Figure 4.18, we find that most material is accreted by BHs in systems with $q \lesssim 0.5$, which would result in these BHs spinning with a positive spin. This is similar to the observed relation from LVK between $\chi_{\rm eff}$ and q, as shown by Callister et al. (2021).

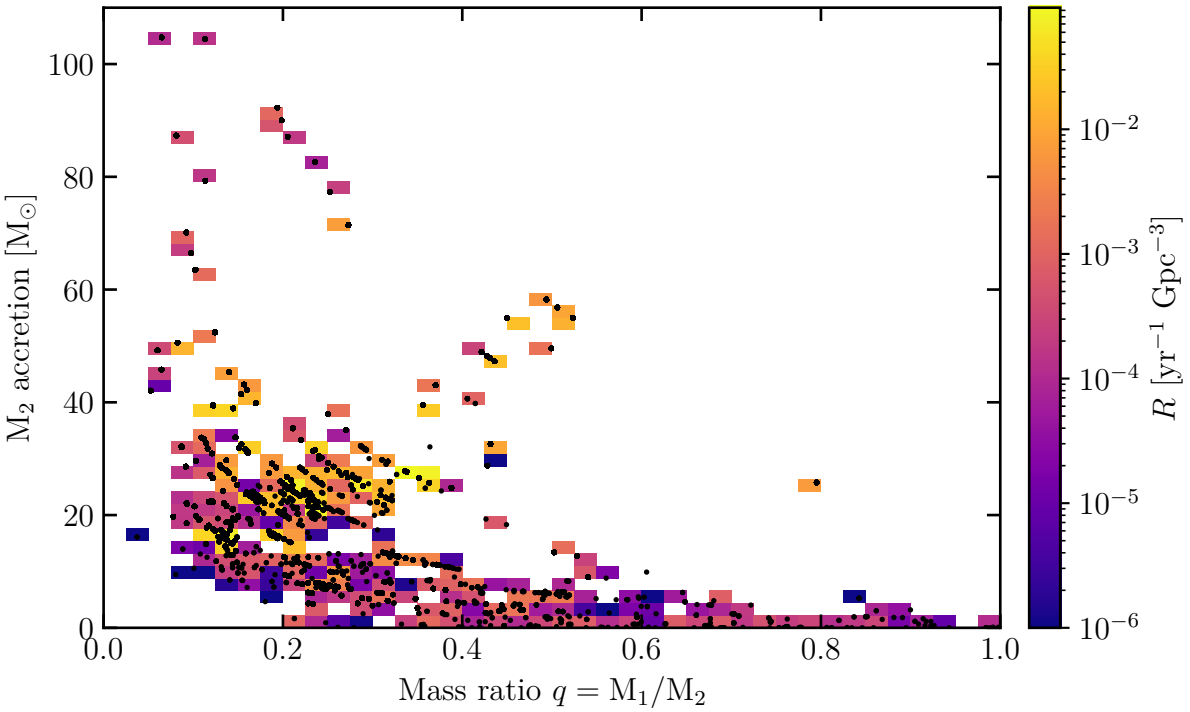

Figure 4.18: The accreted material by the BH in the SMT+SMT channel over the final mass ratio q. The mass ratio is split in 40 linear bins between 0 and 1, while the accretion rate is split in 51 linear bins between 0 and 110 M$_\odot$. The black dots indicate the location of individual models.

Furthermore, high chirp-mass systems have a lot of accreted material, as is expected, since the large chirp-mass systems require material to remain in the systems. These relations are in agreement with relations for SMT systems found by Zevin et al. (2021); Zevin & Bavera (2022), and could align the observed correlation between high chirp-masses ($\mathcal{M} > 40 M_{\odot}$) and a positive effective inspiral spin found by (Abbott et al. 2023) under the assumption of thin disk accretion (Bardeen 1970; King & Kolb 1999). However, if the BH progenitor star is rotating, this angular momentum could be transferred to the BH at formation, depending on assumption on the angular momentum transport (Spruit 2002; Batta & Ramirez-Ruiz 2019; Fuller & Ma 2019). This natal spin introduces additional dependencies on mass transfer and tidal interactions (for example, see Bavera et al. 2020), which is not modeled in BPASS. As such, it is uncertain if the current relations between mass ratio and accreted matter translates into a spin relationship; further analysis is required to find the spin of our predicted merging BBH systems.

Another observable could be the observed BH+star binaries, which are often quickly rotating, with BH masses around 10–20 $M_{\odot}$ and have high companion masses ($31-70\,M_{\odot}$; for an overview of systems, see conclusion of Shao & Li 2022). These systems might have been spun up during a previous mass transfer phase before the current observed mass transfer phase. This is similar to the interactions in our models, where an initial SMT interaction takes place on the main-sequence, followed by a SMT or CEE interaction during a later stage of the evolution. The observed companions are often a giant or supergiant, and have short periods (Miller-Jones et al. 2021; Orosz et al. 2007, 2009). Depending on the metallicity and mass ratio, our models undergo SMT if the star is in this phase. However, a detailed analysis of these BH binaries is required to determine their presence in BPASS and their relation to the BBH merger population.

4.6.2 Super-Eddington Accretion

Super-Eddington accretion is required to conserve enough mass in the binary system to form massive BHs, but also to allow for more stable mass transfer due to fast-changing mass ratios. For spherically symmetric accretion, the Eddington luminosity restricts the accretion rate onto a BH, as decribed in Section 2.1.1. The accretion rates onto the BH in our models are generally more than 100 times Eddington limited accretion and, on rare occasions, reach 10^4 times the Eddington rate. If the accretion is limited, it is uncertain whether or not the BH is still able to accrete similar amounts through longer accretion periods.

A radiation pressure-dominated disk could increase the accretion rate up to 10 times

Eddington (Begelman 2002; Ruszkowski & Begelman 2003), which can be sufficient to grow the BH. As shown by Mapelli et al. (2009) and Zampieri & Roberts (2009), marginal super-Eddington accretion could result in $30-80\,M_\odot$ BHs from low metallicity environments.

However, most BPASS models accrete at a higher rate. To achieve these, other accretion methods have to occur, such as near radial inflow, neutrino emission, advection into the event horizon, or semi-relativistic polar outflows (Popham et al. 1999; Begelman 2002; Ruszkowski & Begelman 2003; Sądowski & Narayan 2016; Takeo et al. 2020; Yoshioka et al. 2022). These can result in super-Eddington accretion rates between 100 and 1000 times the limit, which is where most of the accretion in our models occurs. More reasonable methods include photon trapping in a slim disk, which would allow for super-Eddington accretion at any rate above the Eddington limit (Begelman 1979; Johnson et al. 2022; Ghodla & Eldridge 2023).

Since the super-Eddington accretion takes place on a longer than thermal timescale, these systems spend a reasonable amount of time transferring mass at a super-Eddington rate. This should make it possible to observe these systems, especially because they could emit at a super-Eddington luminosity (Klencki et al. 2022). Observationally, these could be similar to very and ultraluminous X-ray sources, like Holmberg II X-1 (Cseh et al. 2014), M101 X-1 (Liu et al. 2013; Shen et al. 2015), M83 ULX-1 (Soria et al. 2012, 2015), and IC 342 X-1 (Das et al. 2021). These systems are thought to consist of a companion star and a stellar-mass BH with super-Eddington accretion (Ebisawa et al. 2003; Motch et al. 2014; Ogawa et al. 2021; Wielgus et al. 2022; Ambrosi et al. 2022), although this is an area of active discussion since it could also be an intermediate-mass BH (Ramsey et al. 2006).

4.6.3 Mass Ratio Reversal

Super-Eddington accretion does not only leave an imprint on the spin of the systems but also on the mass ratios. Under optimal conditions, up to 82% of BBH systems in theoretical populations without super-Eddington accretion undergo mass ratio reversal (Zevin et al. 2021; Broekgaarden et al. 2022b). In this process, the initially more massive star becomes the less massive BH in the BBH merger. Observationally, however, mass ratio reversal is thought to be limited, but this remains dependent on the model assumptions regarding spin (Mould et al. 2022). By implementing super-Eddington accretion onto the BH, this process becomes rare and only 4% of BBH systems reverse mass ratio in our population due to the material being accreted instead of blown away from the

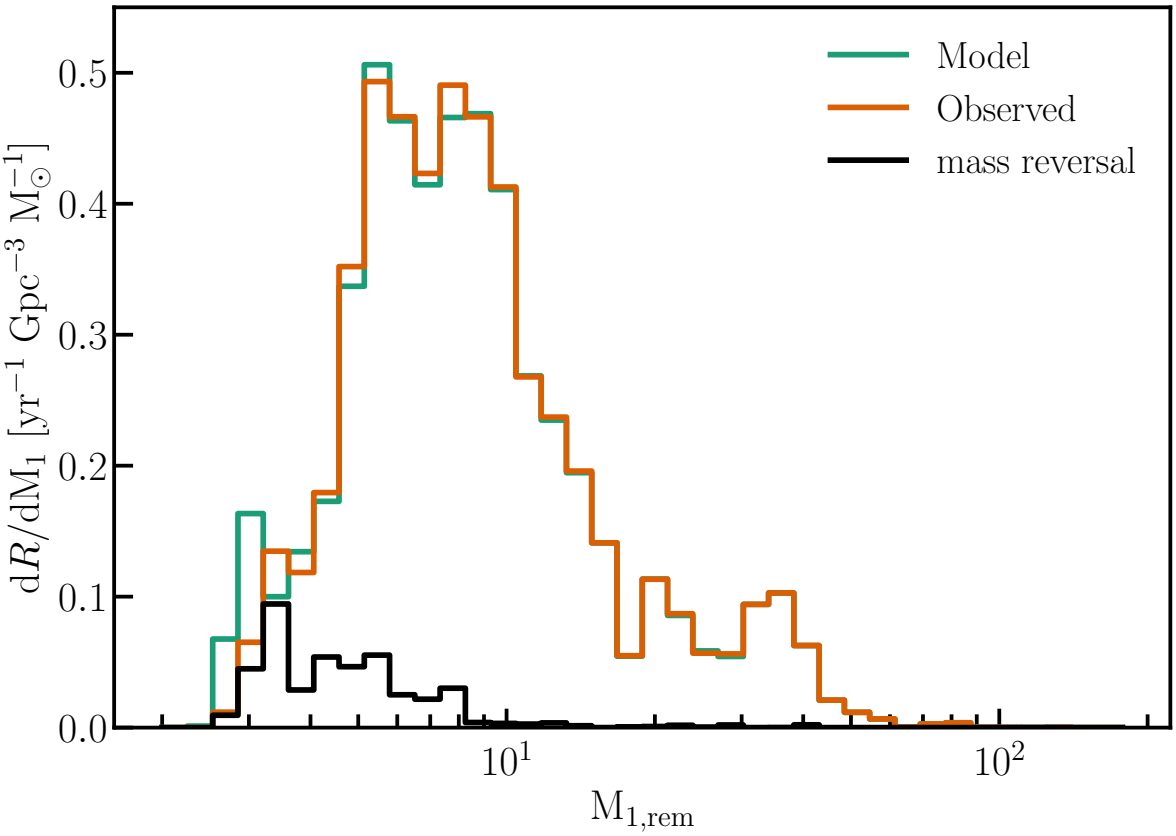

Figure 4.19: The primary BH mass distribution with the more massive BH at merger (orange) and the more massive ZAMS model (green). The distribution of models undergoing mass ratio reversal mostly consists of systems undergoing CEE (black).

system. The mass ratio reversal that does take place in BPASS is restricted to the low $M_{1,BH}$ regime below $\sim 9\,M_\odot$, with most being a result of CEE, as shown in Figure 4.19. Thus, super-Eddington accretion and more stable mass transfer lead to limited mass ratio reversal in merging BHs.

4.6.4 Additional Substructure in the $M_{1,BH}$ distribution

With GWTC-3, modest confidence for more substructure in the primary remnant mass distribution was found with a drop in merger rate at $14\,M_\odot$ (Abbott et al. 2023). The BPASS primary BH mass distribution has a reduced number of events at $18\,M_\odot$, as is visible in Figure 4.6. A drop in CEE systems while the SMT channel does not increase yet, causes this structure. This may be caused by SMT not being able to shrink the orbit of the system sufficiently for it to merge within the Hubble time, while a CE phase is avoided by our mass transfer stability criteria.

The substructure could also be explained by the explodibility of stripped stars (Schneider et al. 2023), which results in a bimodal feature in the mass distribution due to carbon and neon burning creating more compact BH progenitors. While BPASS takes into account the internal structure in the standard remnant mass prescription, the same amount is energy is injected into the structure to explore its explodibility. Furthermore, the same substructure remains between different remnant mass prescriptions, as can be seen in Figure 4.13, albeit less clearly. Interestingly, in Section 4.5.2 this substructure becomes a plateau when QHE is limited to lower metallicities. Further investigation of this substructure will be required in the future when the properties of the observed population are more constrained. Currently, the observed dip at $\sim 14\,M_\odot$ can be explained by noise (Farah et al. 2023).

4.6.5 Other Formation Pathways

Due to approximations made in BPASS models, the companion star will always be a main-sequence star before the first SN. This limits the ability to probe interactions of double-cored systems, where both stars in a binary have similar masses and have both evolved of the main-sequence before undergoing mass transfer (Brown 1995; Dewi et al. 2006; Vigna-Gómez et al. 2018; Qin et al. 2023). Since BPASS STARS assumes the companion is always on the main-sequence, such situations cannot be probed.

While we are able to predict high primary BH masses using isolated binary evolution, other formation pathways could contribute to the total BBH merger rate, such as dynamical interaction (for an overview, see Mapelli et al. 2021). These would leave their own imprint on the population of merging BBH holes, such as random spin alignment (Rodriguez et al. 2016; Zevin et al. 2021). However, due to uncertainties in other regions of compact object merger predictions, such as the stellar physics in the isolated binary evolution, care should be taken when constraining formation pathways (Broekgaarden et al. 2022a; Mandel 2021).

In the high primary BH mass regime, hierarchical mergers have been suggested as a possibility for their formation. However, this would lead to an isotropic-orientated spin distribution, which is not currently observed (Abbott et al. 2023) and could lead to an overabundance of high-mass mergers without fine-tuning (Barrett et al. 2018; Zevin et al. 2021; Zevin & Bavera 2022; Delfavero et al. 2023).

4.7 Conclusion

We have combined BPASS, a population synthesis code with detailed stellar models, with the metallicity evolution and star formation history of the TNG-100 simulation. On its own, the fiducial BPASS populations can self-consistently reproduce a number of massive star evolutionary characteristics, young and old stellar populations (see Eldridge & Stanway 2022, and references therein), and transients rates (See Chapter 3). Using the same population, we predicted the properties of the BBH populations and explored the influences of our assumptions.

1. We find that, similar to Neijssel et al. (2019) and van Son et al. (2022), high primary BH mass mergers are a result of stable mass transfer. Moreover, our stability determination and implementation of super-Eddington accretion results in an extended primary BH mass distribution up to $100\,\mathrm{M}_\odot$ with an excess at $35\,\mathrm{M}_\odot$.

2. The $35\,\mathrm{M}_\odot$ peak is not dominated by PPISN but is a result of stable mass transfer, QHE, and stellar winds. While PPISN systems contribute to this peak, it is not the major formation pathway for these systems. Instead, QHE limits the high end of the peak, while unstable mass transfer limits the lower edge. In combination with the stellar winds, this results in an excess at $35\,\mathrm{M}_\odot$, as discussed in Section 4.2.1.

3. The PISN mass gap BHs are a result of super-Eddington accretion in BH+star systems with $5 < q < 10$ (see Section 4.2.2). These systems are able to merge within the Hubble time due to tidal forces during Roche lobe overflow bringing the system together. Orbital shrinkage due to mass loss and the efficient accretion by the BH, which flips the mass ratio, allows this interaction to be stable. These high-mass systems create a disconnect between the excess and the cut-off of the primary BH mass distribution, as observed.

4. Super-Eddington accretion also restricts the amount of mass ratio reversal to 4%, with most occurring in systems undergoing CEE (Section 4.6.3). Furthermore, the large amount of mass transferred onto the primary BH could leave an imprint on the spin of the BH, visible during the merger. While we are currently unable to predict the spin of the system, we find that most mass is transferred in merging systems with $q \lesssim 0.5$ and high chirp masses, similar to values found by Zevin et al. (2021), aligning with observations (Section 4.6.1).

5. Besides the standard BPASS remnant mass prescription, which injects 10^{51} erg into the star to determine the remnant mass, we also implement the Fryer et al. (2012) prescriptions without PPISN. Because the prescriptions are similar in the high CO core mass regime, the $35\,M_\odot$ and upper mass gap BHs remain, but the low mass regime of the $M_{1,BH}$ distribution and the mass ratio distribution changes significantly with Rapid prescription providing a closer match to the observed distributions.

6. The features in the BBH mass distribution are present in all SFH considered in this work, which have significantly different metallicity evolutions. However, the $35\,M_\odot$ peak is dependent on the redshift observed. At high redshift ($z \approx 1$), the peak disappears due to a longer delay time and the metallicity dependence of the SMT+SMT channel.

7. Completely removing the PPISN and/or PISN prescription only minimally impacts the $M_{1,BH}$ distribution because the majority of BBH progenitors in BPASS do not experience PPISN or PISN.

8. Quasi-homogeneous evolution is an essential physical process in shaping the $M_{1,BH}$ distribution. Altering the QHE selection does significantly alter the $M_{1,BH}$ distribution, as discussed in Section 4.5.2. If a high amount of mass is transferred to the companion before the first SN, further interactions are limited due to QHE. Allowing for less QHE, the rate of the $35\,M_\odot$ excess increases and shifts to higher masses. Implementing a detailed determination of the accretion QHE from Ghodla et al. (2023) based on the amount of material accreted only slightly alters the final $M_{1,BH}$ distribution.

9. Because we use detailed stellar models, we model the response of the donor star due to mass loss instead of implementing prescriptions based on the evolutionary phase of the star. We find that the stability of mass transfer depends on metallicity, mass, and age, similar to Ge et al. (2010, 2015, 2020a,b). For comparison, we show the nature of the envelope for our SINGLE-STAR MODELS over a large range of metallicity, ZAMS masses, and ages. Most importantly, the envelope during core-helium burning is often radiative, while rapid population synthesis codes based on Hurley et al. (2002) often assume that these stars have a convective nature (for more detail, see Klencki et al. 2021). As a result, more systems undergo nuclear timescale stable mass transfer in BPASS, especially at larger mass ratios between a BH and stellar companion.

While the evolution of single stars is complex and non-linear, the evolution of binary stars is even more extreme. All relevant factors have to be taken into account, with QHE and the stability and efficiency of mass transfer being essential in understanding the high-mass regime of the primary BH mass distribution. Besides constraining other observable properties of the population synthesis, such as (ultra-luminous) X-Ray binaries, future GW observations will be able to further constraint the properties of the merging BBH population and restrict the formation pathways.

We have provided the strongest constraints on the formation pathways of BBH mergers. We have seen that mass transfer is an essential component in shaping the primary mass distribution of BBH mergers. As such, in the next chapter, we turn our attention to the stability and efficiency of mass transfer in BPASS STARS.

Chapter 5

Binary Mass Transfer Discussion

As we saw in Chapter 4, the BBH mass distribution is shaped by mass transfer and its stability. Furthermore, other observables, such as the Type Ia rate, are also significantly affected by binary interaction (Li et al. 2023). This raises the question how reasonable the assumptions in BPASS STARS are and how they compare to detailed binary grid and other population synthesis models.

BPASS V2.2 has a unique place in population synthesis codes due to its use of detailed stellar models. This brings complexity to its comparison against rapid or parametric population synthesis codes, which implement approximations to stellar evolution and binary interactions. Because of the additional layer of detail, relations present in other codes might not translate well to the BPASS V2.2 results. For example, suppose a transient is no longer produced through a CE due to the unique implementation of mass transfer stability. In that case, a relation to the CE parameters in Equation 1.10 will no longer be present. However, it is impossible to cover all regimes in which the stability criteria of BPASS V2.2 will affect the outcome of the binary evolution because that would cover almost all binary observables (for an overview of some binary observables, see Han et al. 2001; Negu & Tessema 2015; Belloni & Schreiber 2023). Instead, we compare the BPASS V2.2 grid against other binary grids; detailed model grids in Section 5.2 and rapid population synthesis grids in Section 5.3, because 1D detailed stellar models are able to provide a direct measure of the response of a donor star to mass loss, which is often absent in the rapid population synthesis codes. Although Section 1.3 discusses the response of the donor star and mass transfer stability in general terms, Section 5.1 contains an overview and discussion of stability criteria used in detailed binary evolution.

5.1 Mass Transfer Stability

To be able to compare grids, we should be aware of the assumptions made for each grid because these can drastically impact if and how binary interactions take place. Choices in internal stellar physics, such as mixing length and convection parameters, affect the radial expansion and entropy profile inside the star (Marchant et al. 2021) and if a star will fill its Roche lobe (For an overview of differences between stellar codes, see Agrawal et al. 2022). Besides the single-star physics, the binary interaction parameters and the criteria for CE define stability (Negu & Tessema 2015).

Even using 1D detailed stellar models, it is difficult to determine if a binary system undergoes a CE, because there are no definite criteria for when a CE initiates. As such, detailed stellar codes have to make assumptions on the mass transfer stability, which are often physically motivated. These differ between grids and codes and are the first choice in determining mass transfer stability. Common criteria for systems undergoing a CE are:

- Mass transfer rate limit (Marchant et al. 2021)
- L_2/L_3 outflow (Paczynski 1976; Pavlovskii & Ivanova 2015; Misra et al. 2020)
- Photon-trapping radius (Begelman 1979; Fragos et al. 2023)
- Radius of donor expanding past orbital separation (Eldridge et al. 2017)
- Dynamical mass transfer (Pavlovskii & Ivanova 2015; Pavlovskii et al. 2017; Temmink et al. 2023)
- Thermal readjustment of surface layers (Temmink et al. 2023)

For a comparison of several of these stability criteria at 1-8 $M_\odot$, see Temmink et al. (2023). No one definition might describe the boundary between stable and unstable mass transfer correctly. However, it has been shown that outer Lagrangian outflow does not have to lead to unstable mass transfer (Marchant et al. 2021; Temmink et al. 2023), and dynamical mass transfer can occur stably (Temmink et al. 2023). L_2/L_3 outflow can still alter the evolutionary outcome based on the angular momentum and mass loss, resulting in tighter binaries (Marchant et al. 2021). Such additional outflow is not considered in BPASS. Together with the choice in BPASS to use the radius of the donor expanding past the separation of the binary, the CE initialisation criteria might be too relaxed. However, because of numerical stability, the mass loss rate is limited

to $0.1\,M_\odot/yr$, which is one of the CE limits used by Fragos et al. (2023). As a result of limiting $\dot{M}$, some stars continue to expand instead of being restricted by the mass loss rate and enter a CE. Even if the first interaction is stable, the binary can undergo unstable mass transfer at larger evolutionary stages.

With the criteria for unstable mass transfer chosen, the mass loss rate and accretion efficiency are the binary parameters that determine what models meet these criteria. For example, altering the mass transfer rate impacts the radial expansion into the Roche lobe and how quickly the star can respond to mass transfer (Marchant et al. 2021). Moreover, the L_2/L_3 outflow can be restricted and give a different outcome to the mass transfer (Marchant et al. 2021).

The more non-conservative the mass transfer is, the more stable the mass transfer is if the mass and angular momentum is lost from the system (Soberman et al. 1997; Tauris 1996; Tauris & Savonije 1999). Thus, fully conservative mass transfer describes a minimum state for stable mass transfer for a specific set of model parameters. While some grids have chosen fixed values for their accretion efficiency (For example, see Han 1998; Petrovic et al. 2005), others use the thermal timescale (Hurley et al. 2002), the critical rotation limit of the accretor (Fragos et al. 2023), or Eddington limit for compact objects (Marchant et al. 2017) to limit the accretion onto the companion. The latter options fit better with observations based on the wide range of mass transfer efficiencies that have been observed in a wide range of systems (De Greve & Linnell 1994; Nelson & Eggleton 2001; de Mink et al. 2007; Petrovic et al. 2005; Vinciguerra et al. 2020; Wang et al. 2021b) and that the mass transfer efficiency is not constant throughout the interaction (Van Rensbergen et al. 2006).

As mentioned in Section 2.1.1, BPASS STARS limits the accretion by the thermal timescale of the accretor and the Eddington rate for NSs. The accretion onto BHs is unrestricted, which we discussed in Section 4.6.2. We do not consider spin up due to the accreted material. As a result, more efficient accretion for massive stars is allowed than by rotational limited accretion (Packet 1981; Petrovic et al. 2005; de Mink et al. 2013), but it might still be possible depending on the angular momentum transport in the star.

With these considerations in mind, we split our comparison further based on the companion being a star or compact object (WD/NS/BH), i.e. *primary* and *secondary models*, respectively.

5.2 Detailed Models

5.2.1 Primary

A variety of double star models have been created throughout the years to probe the many binary system observables, examples include Algols (Nelson & Eggleton 2001; Sen et al. 2022, 2023), stellar rotation (de Mink et al. 2013; Wang et al. 2023), contact binaries (Wellstein et al. 2001; Menon et al. 2021; Rickard & Pauli 2023), Wolf-Rayet star populations (Pauli et al. 2022; Sen et al. 2023), Be systems (Schootemeijer et al. 2018; Wang et al. 2023), and core-collapse supernovae (Eldridge et al. 2018b; Sravan et al. 2020; Vartanyan et al. 2021). Even more binary models have been created to match individual double star systems, such as WR+O (Petrovic et al. 2005) and blue stragglers (Sun et al. 2021). However, very few cover such a large mass range and metallicity as BPASS and have shown the mass transfer stability. For example, the grids by (Sen et al. 2022, 2023) and (Menon et al. 2021) cover a large mass range, but are either limited to shorter periods or do not report the stability of the mass transfer. Therefore, we compare the BPASS grid against grids from Temmink et al. (2023), Pauli et al. (2022), and Fragos et al. (2023) at $Z = 0.020$. No large grids at other metallicities are currently available in the literature.

Figure 5.1 shows the mass transfer stability over donor mass for four metallicities. We take all *primary models* over the initial period and mass ratios, as defined in Section 2.2 and determine the type of interaction in each model. If a CE occurs in the model, as defined in Secion 2.1.1, where the donor radius is larger than the separation of the system, it is tagged as a CEE system. If a model contains multiple mass transfer phases, it will be tagged as CEE if this condition is met in any of the mass transfer phases. For each donor mass, we determine the fraction of each model undergoing either interaction pathway or merge.

Independent of metallicity, models with $M_d \lesssim 7\,M_\odot$ mostly interact through stable mass transfer, while between 7 and $60\,M_\odot$, most interactions lead to a CE. Only at high masses does SMT become the dominant formation pathway again. This upper mass limit is determined by the stellar winds, which increase the stability of the interactions for very massive stars. However, the winds also stop interactions from taking place if they get too strong.

Looking closer at the stability grid of six representative example donor masses at $Z = 0.02$ in Figure 5.2. The low mass stars ($M_{donor} \lesssim 7\,M_\odot$) only undergo CE at small mass ratios, if they interact at all. Otherwise, most interactions are stable up to $7\,M_\odot$.

This is unexpected due to the convective envelope on the main-sequence for $1\,M_\odot$ stars and post-MS for $3-5\,M_\odot$ stars. A contributing factor to this increased stability below $5\,M_\odot$ is the use of the $5\,M_\odot$ mass loss rate in the mass transfer calculation. Since the thermal timescale on the main-sequence differ significantly with small mass changes (see Appendix B) and the mass loss rate is higher than expected for a less than $5\,M_\odot$ star,

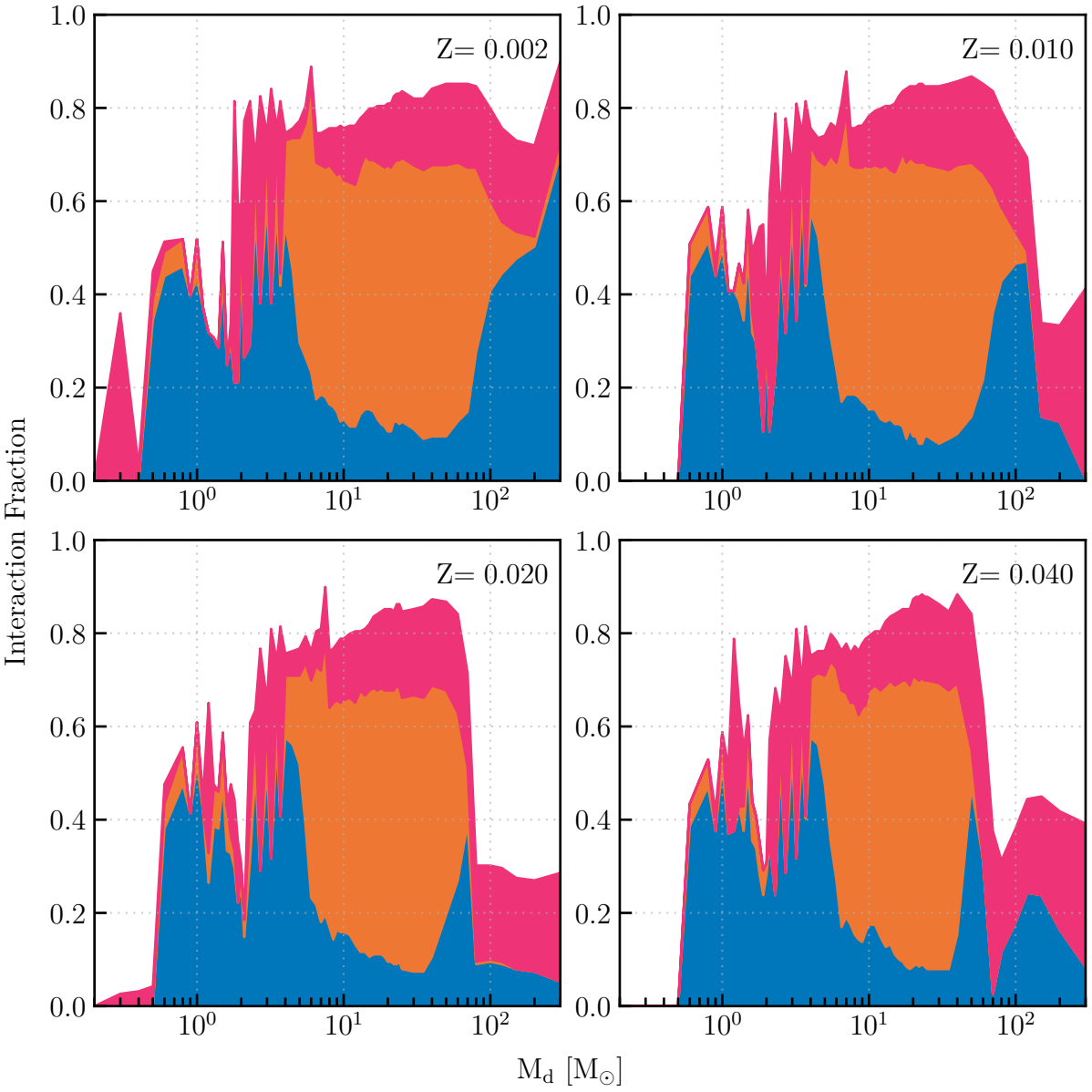

Figure 5.1: Mass transfer channel fraction for $Z = 0.002, 0.010, 0.020, 0.040$ over donor masses for the *primary models*. Each donor mass is normalised using the number of total model at that M_d, 12663 models per metallicity. Orange and blue indicate CE and SMT, respectively, while pink indicates merging models.

the companion cannot accrete the stellar material. Thus, the material and its angular momentum is lost from the system, widening the orbit and stabilising the interaction. Although further analysis and recalculation of the stellar models is required to determine if the interaction remains stable, the combination of evolutionary timescale and increased mass loss explain the observed mass transfer efficiencies in the BPASS V2.2 low mass binary models.

The grid by Temmink et al. (2023) covers the same low mass regime with $1\,M_\odot \leq M_d \leq 8\,M_\odot$ at $Z = 0.02$ and generates a lower bound (q_{crit}) for the stability of mass transfer using the local thermal timescale. They find similar results to a single star grid created by Ge et al. (2010, 2015, 2020a,b), who calculated the critical mass ratio for CE by using the global thermal timescale and the adiabatic assumption. Both grids assume fully-conservative mass transfer and are, thus, a lower bound to the stability of mass transfer.

Figure 5.3 show that the accretion efficiency ($\Delta M_2/\Delta M_1$) for the low mass models, in general, is low. Thus, increasing the stability of mass transfer compared to Temmink et al. (2023) and Ge et al. (2010, 2015, 2020a,b). At $1\,M_\odot$, a trend with mass ratio and period is present. If the mass ratio is close to unity, the accretor star is larger and more massive and can accrete more material, thus increasing the efficiency with increasing q. The trend with period is mostly visible with q close to 1. As the period increases, the efficiency decreases as well. Once a star evolves off the main-sequence, it evolves on a shorter timescale. The mass loss will be more rapid and the accretor is unable to accrete the material efficiently. Similar trends between the mass transfer efficiency, mass ratio and period have been found by Petrovic et al. (2005), de Mink et al. (2007), Schneider et al. (2015).

Due to the increase in mass loss rates below $5\,M_\odot$, most systems undergo stable mass transfer. The interaction remains stable due to the mass and angular momentum lost from the system, which widens the system slightly. Even though the star has a convective envelope, it does not expand rapidly after starting Roche lobe overflow, possibly due to the fast stripping of the envelope due to the increased mass loss rate.

Li et al. (2023) have shown that a more detailed treatment of mass transfer stability leads to a DWD population almost exclusively formed through stable mass transfer during the primary evolution. Furthermore, they find that non-conservative SMT can lead to a DWD population matching several observations that are harder to explain through conventional formation pathways as an alternative to the γ-prescription (Han 1998; Woods et al. 2012; Toonen et al. 2012). We find this non-conservative SMT in the

WD progenitor regime without imposing a maximum accretion efficiency, as done by Li et al. (2023). A more detailed analysis of the DWD population formation channels could provide insight into the stable mass transfer criteria and the mechanisms that dominate the low mass regime, which might affect the observable LISA population (Thiele et al. 2023). Other effects in this regime include the Type Ia rate (Toonen et al. 2014a) and the blue straggler population (Leiner & Geller 2021). The former, we discuss in Section 6.1. Recently, it has been shown that the blue straggler population cannot be reproduced by rapid population synthesis codes Leiner & Geller (2021) and detailed treatment of binary interaction is required (Sun et al. 2021). BPASS, with the detailed stellar models, might be able to reproduce the observed blue straggler to red supergiant population and

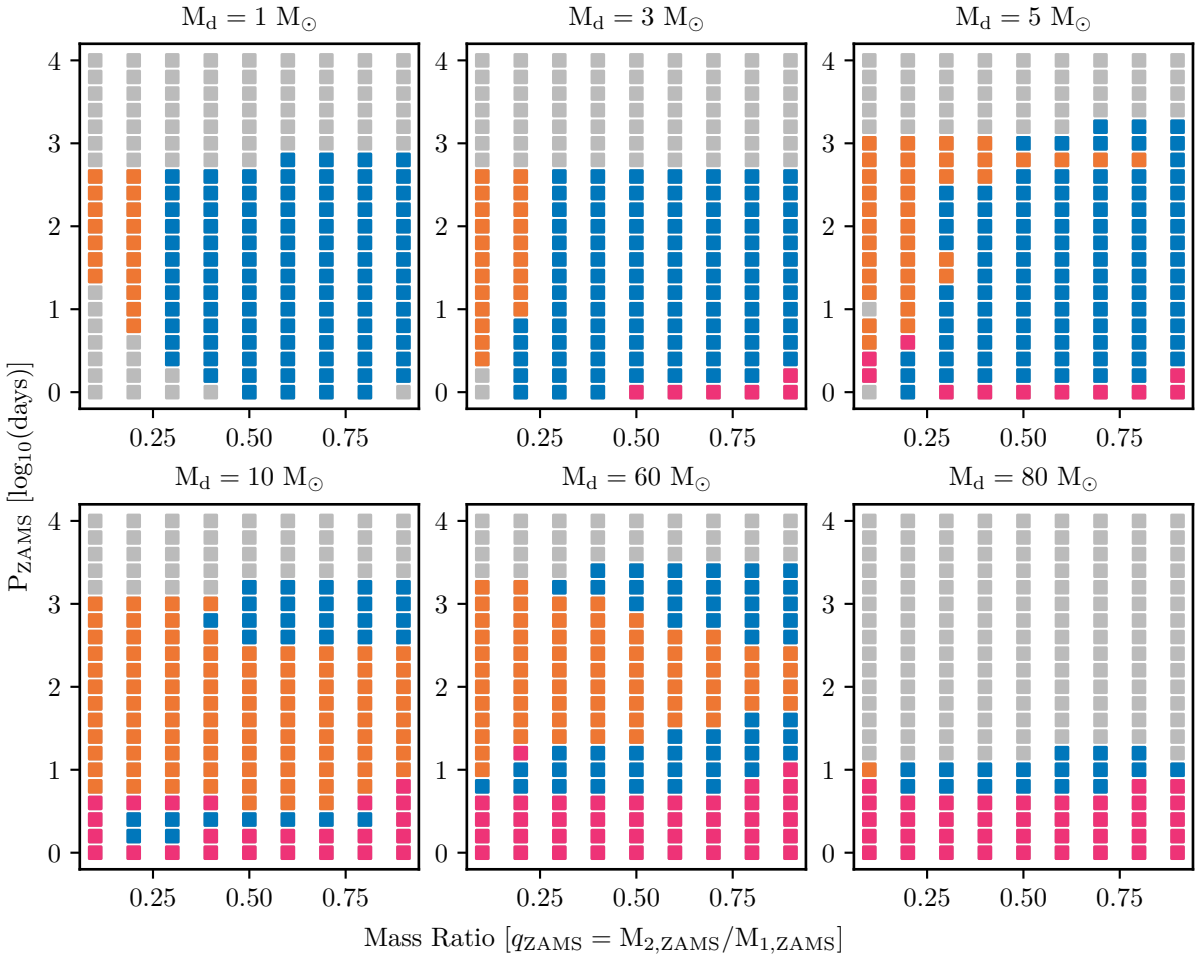

Figure 5.2: The mass transfer stability grid for the *primary models* at 6 donor masses at $Z = 0.02$. Blue and orange indicate stable mass transfer and CE evolution, respectively, while pink is merger models. Grey models do not interact. The models in the bottom left at 1,3, and 5 $M_\odot$ should lead to mergers, but do not interact and might be a code artefact.

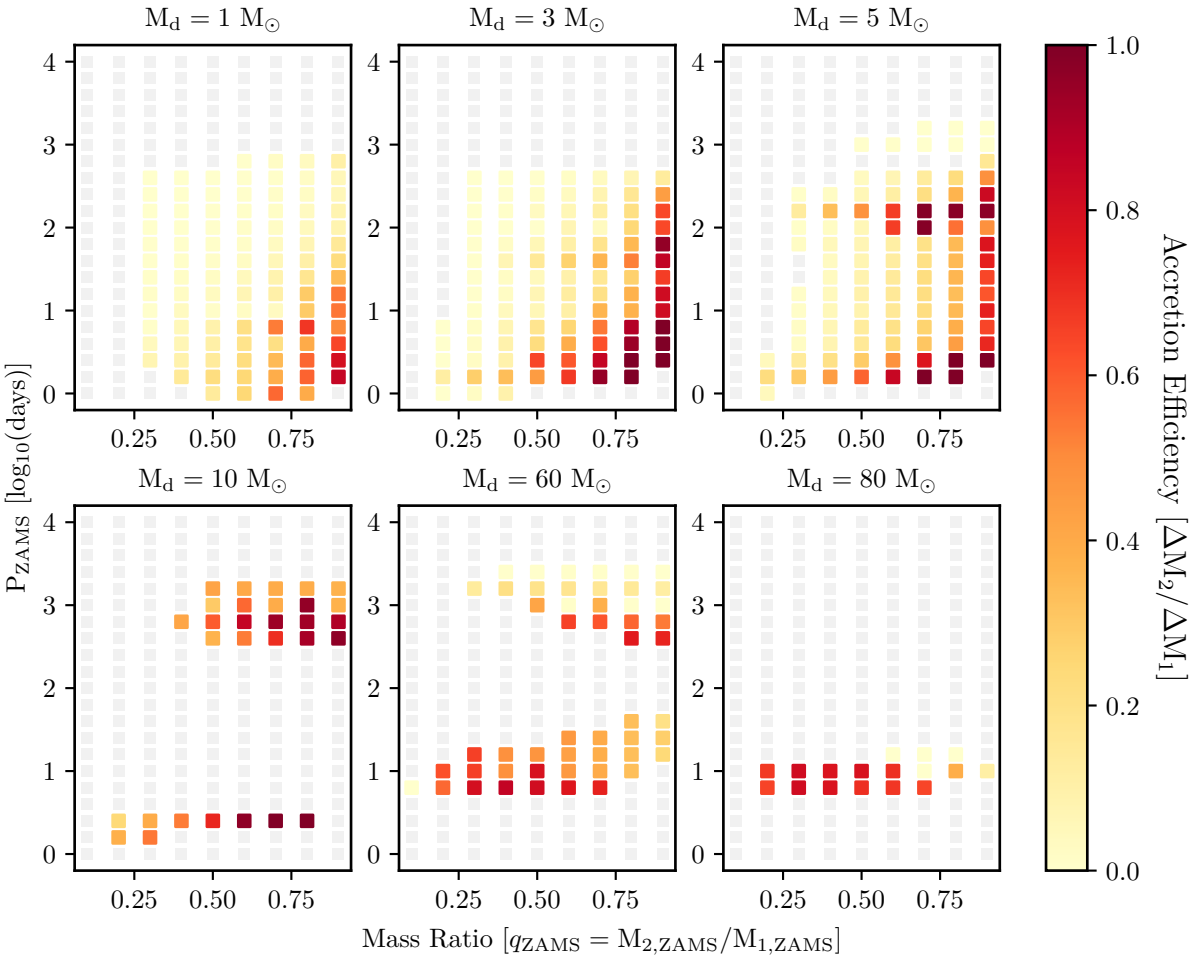

Figure 5.3: The mass transfer efficiency over the first mass transfer phase, if the *primary model* undergoes stable mass transfer at $Z = 0.02$. Grey models do no interact, undergo CE or merge.

their age distribution. However, this is beyond the scope of this work.

Between 3 and 5 $M_\odot$, the same trends in accretion efficiency can be found at $1\,M_\odot$, with the accretion efficiency increasing as a result of a larger thermal timescale of the accretor. However, an additional island of conservative mass transfer starts to take shape at higher periods and equal mass ratios ($P \approx 100$ days at $5\,M_\odot$), which shifts to larger periods at higher masses. This island of stability is a result of helium ignition, causing the star to start to evolve on a longer timescale and limiting the mass loss at which the Roche lobe overflow occurs. As such, the accretor is able to accrete the material from the companion efficiently at these periods, which flips the mass ratios and stabilises the interaction.

Once we move to more massive stars $M > 5\,M_\odot$, the non-conservative mass transfer

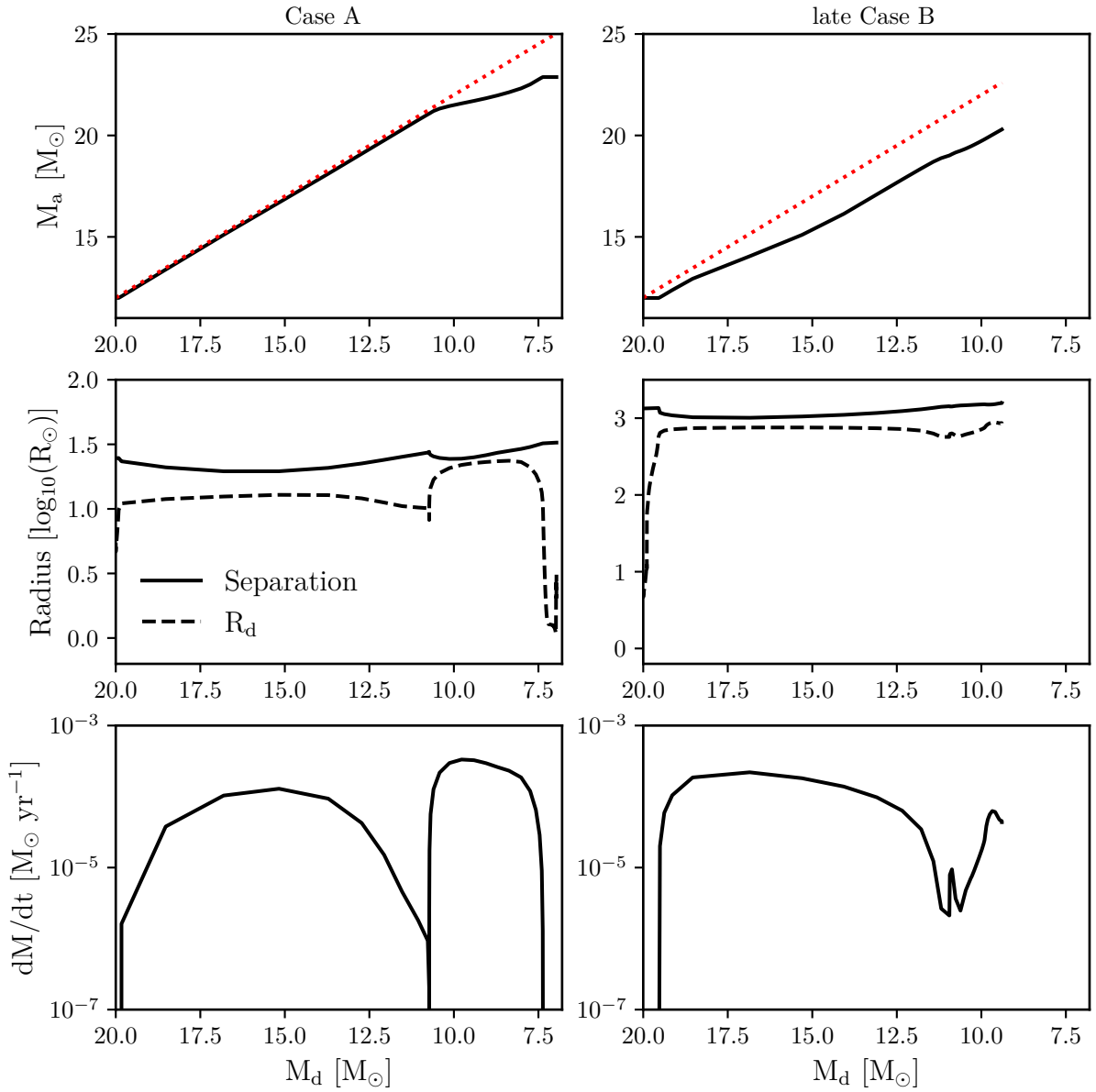

Figure 5.4: Case A (left) and late Case B (right) stable mass transfer at $Z = 0.001$ for a $M_d = 20$ and $q = 0.6$ with P= $10^{0.4}$ and P= 10^3, respectively. The red dashed line in the top figures indicated fully conservative mass transfer.

can no longer expand the orbit sufficiently in BPASS to counteract the radial expansion of the donor. As a result, the donor expands further past its Roche lobe, and many of the non-conservative mass transfer systems suddenly undergo a CE evolution, as shown at $10\,M_\odot$ in Figure 5.2. The mass loss rate now follows the donor mass but is insufficient in stabilising the system.

Only Case A and late Case B mass transfer regions that were initially conservative

remain stable. Due to similar thermal timescales, when Case A mass transfer occurs, the mass is transferred efficiently, quickly flipping the mass ratio. Because material is now transferred from the less massive primary to the more massive companion, the interaction slows down to a nuclear timescale, further increasing the accretion efficiency. SSN 7 is a massive binary expected to have undergone this interaction (Rickard & Pauli 2023). At low metallicity, these models will undergo QHE due to the large amount of stellar material being transferred to the companion. These interactions continue during the whole main-sequence of the donor. The efficiency of mass transfer will leave an imprint on the mass ratio distribution of Algol systems (van Rensbergen et al. 2005).

In the situation of a late Case B mass transfer, the star is nearing its maximum radius before helium ignition, slowing down its evolutionary timescale. Again, the mass ratio flips and the interaction remains stable and conservative. In many cases, this late Case B mass transfer stops the first dredge-up from happening and increases the helium core mass. The conservative nature of this interaction is promising for the formation of Be star and X-ray source binary, which requires a high accretion efficiency to match observation (Vinciguerra et al. 2020). This population and the WR star population would be able to provide further insight into the stability of mass transfer (Bodensteiner et al. 2020; Pauli et al. 2022).

As shown in Figure 5.1, CE continues to dominate the binary interactions up to $\sim$60 $M_\odot$ and the interaction grids look identical to the 10 $M_\odot$ example in Figure 5.2. Depending on metallicity, at approximately 60 $M_\odot$, the island of stability start to expand again towards each other at equal mass ratios. This is a direct result of stellar winds removing material from the stars, thus widening the orbit before interaction.

Together with the interactions occurring at later evolutionary stages, where the mass transfer is inefficient and stellar winds strong, stability increases again, as the 60 $M_\odot$ example in Figure 5.1 shows. Eventually, the stellar winds become strong enough to stop the donor star from interacting after the main-sequence.

Interestingly, at these high masses, initially, more equal mass ratio systems are not efficient accretors as systems with larger mass ratios, as can be seen in the 80 $M_\odot$ example in Figure 5.3. With thermal timescales at these high masses being near equal, the larger mass ratio allows for the system to spend more time in a state where the donor is the more massive star in the binary. Because when the donor becomes the less massive star, the orbit widens with mass transfer, and stellar winds prevent the star from interacting again. Thus, the more time the donor spends as the more massive star in the system, the more mass is transferred instead of lost by stellar winds. At metallicities where

Low-Mass Stars $M_d < 7\,M_\odot$
Case A: Mass ratio reversal **Other:** Non-conservative mass transfer.
Intermediate-Mass & Massive Stars $7\,M_\odot \leq M_d \lesssim 60\,M_\odot$
Case A: Mass ratio reversal **Late Case B:** Helium ignition shrinks the donor
Very Massive Stars $M_d \gtrsim 70\,M_\odot$
Case A: Stellar wind and mass ratio reversal **Other:** Similar thermal timescales

Table 5.1: The dominant physics that stabilises binary mass transfer in BPASS in different mass regimes.

stellar winds play less of a dominant role, the interactions are predominantly stable due to conservative mass transfer at more equal mass ratio, even when the donor has left the main-sequence, and for donors near helium ignition. Depending on the metallicity and the donor mass, the models between 10 and 300 $M_\odot$ contribute to the BBH merger rate at $z = 0$.

In the end, the physics determining the stability of binary interaction in BPASS depends heavily on the mass regime. Table 5.1 summarises the dominant physics causing stable mass transfer in the BPASS models.

The massive and very massive donor star regime is covered by the grid from Pauli et al. (2022), who provide simulation grids plots at $31.6\,M_\odot$, $63.1\,M_\odot$, $79.4\,M_\odot$ donors. This grid is also used in (Sen et al. 2022, 2023) to find Algols and reverse Algols, which are also found in BPASS (Eldridge et al. 2018a). A comparison with respect to the formation of Wolf-Rayet stars can be found in Pauli et al. (2022), Appendix B.2. In general, the BPASS models that undergo SMT agree. However, compared to the $31.6\,M_\odot$ grid from Pauli et al. (2022), the BPASS grid at $30\,M_\odot$ and $Z = 0.004$ mostly exists of systems undergoing a CE, which results in a brighter Wolf-Rayet star due to faster stripping of the hydrogen envelope. This will also have an effect on the predicted Type Ib/c fraction of the population (Shenar et al. 2019).

The island of late Case B stable mass transfer falls within a regime where the maximum mass transfer rate of 0.1 $M_\odot$/yr is reached in Pauli et al. (2022) models. This difference is most likely a result of the CONTACT mass transfer rate (Marchant et al. 2016), which keeps the radius of the donor within its Roche lobe by removing mass outside of it. Since the star after the main-sequence expands rapidly, the mass transfer rate

in Pauli et al. (2022) increases rapidly when the star interacts after the main-sequence and a CE is expected to happen. However, the CONTACT scheme does not treat the extended envelope correctly (Fragos et al. 2023). At higher masses, more interactions in the models by Pauli et al. (2022) in the high period regime deplete helium without reaching their maximum mass transfer rate, but comparison at this regime is difficult due to the high number of numerical convergence issues.

A more recent and detailed primary grid has been presented by the POSYDON collaboration, where MESA is used to model both stars in detail (Fragos et al. 2023). We show BPASS grid slices at similar parameters in Figure 5.5, and the POSYDON grids in Figure 5.6. While the BPASS covers a slightly larger parameter space in the low mass regime, the POSYDON grid contains more models. In BPASS, most of the low-mass models do not interact because their main-sequence lifetime is longer than the age of the universe. Eventually, some systems will start to interact through stable mass transfer as donor mass increases. Around the helium flash $M_1 \approx 1.3\,M_\odot$, low mass ratio systems merge instead of interact. Further investigation is required why around 2 and $3\,M_\odot$ these models all merge. At q=0.3 in the low mass regime (5.5 to $10\,M_\odot$), most POSYDON binaries undergo unstable mass transfer, similar to BPASS. However, a region of stable mass transfer is missed by POSYDON due to their lower mass limit of $6.23\,M_\odot$, since they are interested in the formation of compact objects. Furthermore, as the donor mass increases, POSYDON models experience stable mass transfer in systems with a period around 100 days, which decreases with donor mass. This behaviour is completely absent in BPASS. Moreover, POSYDON shows a large regime of stable mass transfer between 30 and 70 $M_\odot$, which is most likely cut off due to stellar winds prescriptions in BPASS. Stable Case A mass transfer at very massive stars is present in both grids. Interestingly, the stability criteria in POSYDON, which include a mass transfer rate limit and L_2 outflow, lead to similar stability regions at $q = 0.3$. This is in contrast to the stability regions predicted by Pauli et al. (2022), which is also a result of using the CONTACT scheme (Marchant et al. 2016) for interactions post-MS. Since POSYDON does not apply this method for stars after the main-sequence, interactions do not reach the $0.1\,M_\odot$/yr mass transfer rate limit and the interaction can occur stably in POSYDON.

At q=0.7, POSYDON predicts nearly fully stable mass transfer for masses above $\sim 5.5\,M_\odot$ and periods larger than $\sim$3 days, as shown in Figure 5.6. While the amount of stable mass transfer does increase in BPASS, a region of unstable mass transfer remains at intermediate and massive donor masses. This difference is most likely a result of the difference in mass loss rate from the donor due to mass transfer. POSYDON restricts a

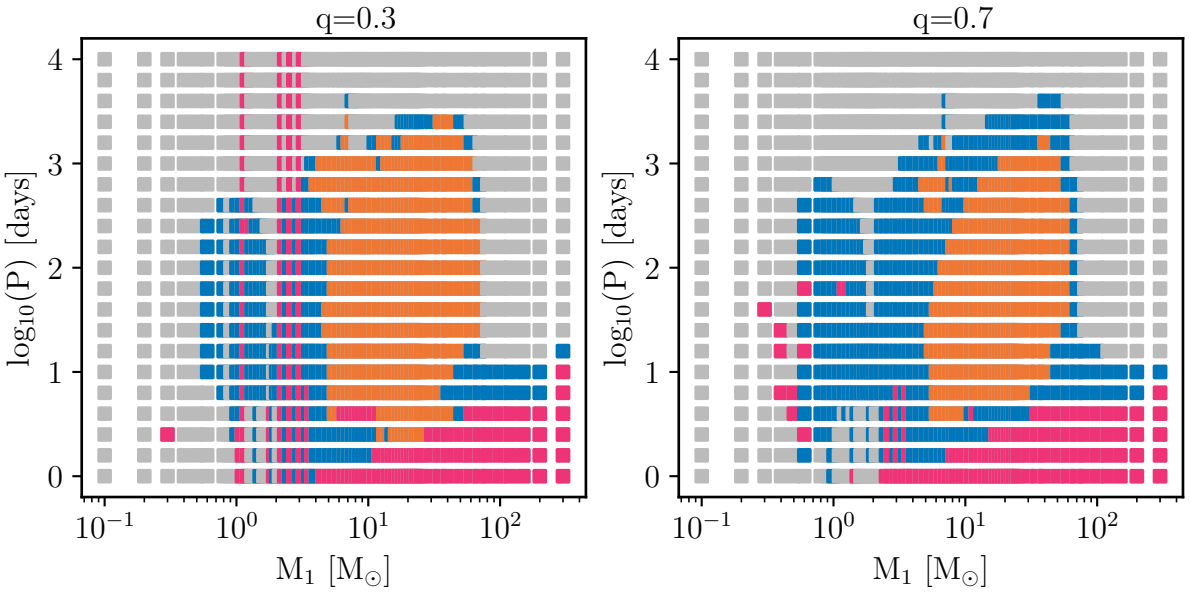

Figure 5.5: The stability of mass transfer over donor mass M_1 and P for the *primary models*. Grey indicates non-interacting models and pink indicates mergers. Orange and blue are CE and SMT interactions, respectively. The mass ratios, q = 0.3 and q = 0.7, are chosen to compare against the POSYDON grids from Fragos et al. (2023), as shown in Figure 5.6.

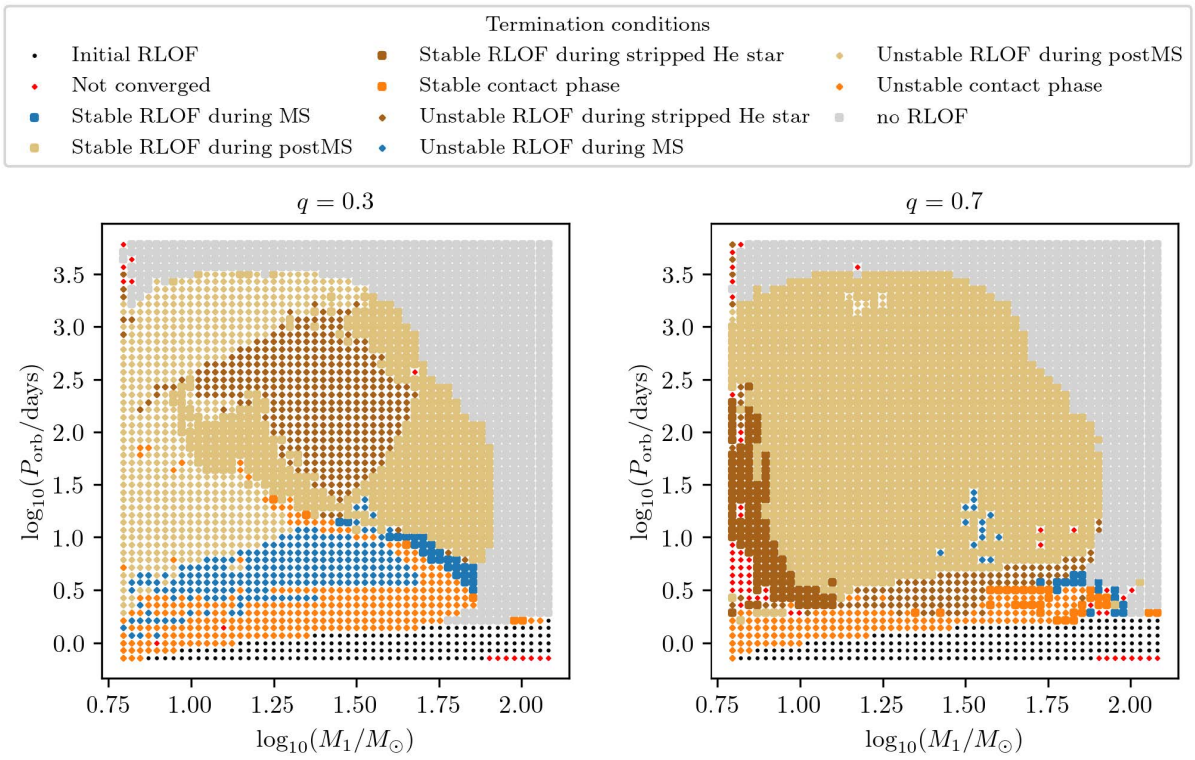

Figure 5.6: The termination conditions of the POSYDON grid at $q = 0.3$ and $q = 0.7$ for comparison against the BPASS grid in Figure 5.5. The SMT channel is indated with thick squares, while unstable mass transfer are smaller diamonds. Figure taken from Fragos et al. (2023).

main-sequence donor to its Roche lobe, while BPASS does not. For mass transfer post-MS, expansion into the Roche lobe is allowed, but a majority still undergoes stable mass transfer, which could be a result of a different treatment mass and angular momentum loss due to stellar winds. Moreover, POSYDON boosts the stellar winds to limit stellar rotation to below the critical threshold, which is not done in BPASS. This allows for additional widening of the binary, stabilising the mass transfer.

An additional stabilising factor can be the mass transfer rate prescription. For example, if the mass transfer rate increases more rapidly than in BPASS, the interaction might be stable due to additional mass loss. However, many of the binary models in Pauli et al. (2022) grid undergo non-conservative stable mass transfer but lack the luminosity to eject the material from the binary. As such, a circumbinary disk might form or the system might undergo a CE. While BPASS might not reach the instability for the right reason, it appears to describe the instability region for massive stars reasonably well, although details in stability regions might be missed compared to more detailed mass transfer and stability criteria (Fragos et al. 2023).

We also note that there is a slight dependence on q for the systems that interact. In BPASS, models at masses below $1\,\mathrm{M}_\odot$ interact more at $q = 0.7$ than at $q = 0.3$. Furthermore, a few models around $40\,\mathrm{M}_\odot$ interact at larger separation at $q = 0.7$ than $q = 0.3$, which might be caused by a reduced strength of the stellar winds in BPASS compared to POSYDON, thus limiting the orbital widening.

In general, the POSYDON and BPASS results agree at low mass ratios $q = 0.3$ but differ at more equal masses $q = 0.7$, which is most likely a result of stellar winds stabilising interactions more strongly in POSYDON than in BPASS. The stability of the models from Pauli et al. (2022) do not agree with BPASS or POSYDON due to their treatment of post main-sequence mass transfer. At lower masses, the models from Temmink et al. (2023) generally agree with the BPASS models. However, BPASS has significantly increased stability due to non-conservative mass transfer. A larger exploration of the input parameter space and comparison against more observables is required to determine accuracy of the binary interactions inside the models. However, it is promising that despite the simple stability criteria in BPASS, similar results for the stability of stellar mass transfer are found compared to the more detailed criteria in POSYDON.

So far, we have ignored much of what happens to the abundances of the accretor. While BPASS includes rejuvenation and quasi-homogeneous evolution, it does not accurately keep track of elemental abundances in mass transfer. This can be especially important when comparing stable mass transfer to observations of specific systems (Renzo

& Götberg 2021). Detailed modelling of the companion is required for this, which is not currently done in BPASS V2.2 but could provide another constraint in determining mass transfer stability and efficiency.

5.2.2 Secondary

The interaction between two stars is different than those between a star and compact object, be that a WD, NS or BH. This is an area with a significant amount of research because it is easier to numerically calculate the interaction between a simulated star and a point mass, which is an often made assumption for the compact object. As such, we have several works to compare the BPASS V2.2 models against. In BPASS, the accretion onto a WD is limited by the thermal timescale, a NS by the Eddington luminosity (Eldridge et al. 2017), and BH accretion is unrestricted, as discussed in Section 2.1.1, which makes the mass transfer for BH accretors fully conservative.

We perform a similar analysis to the stellar mass transfer and create stability grids for the BPASS *secondary models*, as shown in Figure 5.7. Although the grids are less uniform than the primary grid and prevent us from creating a Figure 5.1 for the *secondary models*, similar trends are present in the individual grids. As metallicity increases, more systems undergo SMT and eventually stop interacting due to strong stellar winds.

At low masses, most interactions are stable unless the mass ratio ($q = \mathrm{M_{accretor}}/\mathrm{M_{donor}}$) is very small, similar to interactions with stellar companions. As the donor mass increases, more interactions are unstable at equal mass ratios. At $Z = 0.020$ in Figure 5.7, a $5\,\mathrm{M_\odot}$ shows different stability for interactions with an Eddington limited compact object and a BH. The unrestricted accretion onto a BH allows for fast mass ratio reversal, stabilising the interaction. However, for larger masses, interactions during the Hertzsprung gap result in a CE even when $q > 1$. Similar to the *primary models*, Case A and late Case B can still occur stably with small mass ratios ($q \sim 0.1$).

Stable Case A mass transfer has been proposed by Shao & Li (2022) as a possible formation mechanism for fast-spinning massive BH binaries under the assumption of mildly super-Eddington accretion. These models are present in BPASS and Figure 5.8 shows a BPASS model undergoing a similar interaction at $\mathrm{M_d} = 70\,\mathrm{M_\odot}$, $\mathrm{M_{BH}} = 31.6228\,\mathrm{M_\odot}$, and $P = 10^{0.2}$ days at $Z = 0.001$. This model is chosen to be close to the model from Shao & Li (2022). This model contains a similar fast initial mass transfer followed by a slower continuous mass transfer. However, increasing the period to the next available period, $P = 10^{0.8}$, removes this slow mass transfer phase, because the star reaches the Hertzsprung Gap before this slow phase can initiate. Although the slow Case A

mass transfer from Shao & Li (2022) is present in the BPASS V2.2 models, the exact parameters, such as mass and period, differ from theirs. Moreover, we do not include the calculation of the BH spin in BPASS. The slow Case A mass transfer can lead to fast-spinning high-mass X-ray binaries (Shao & Li 2022). On the other hand, the BBH merger population does not spin rapidly (Abbott et al. 2020b) and might prefer more

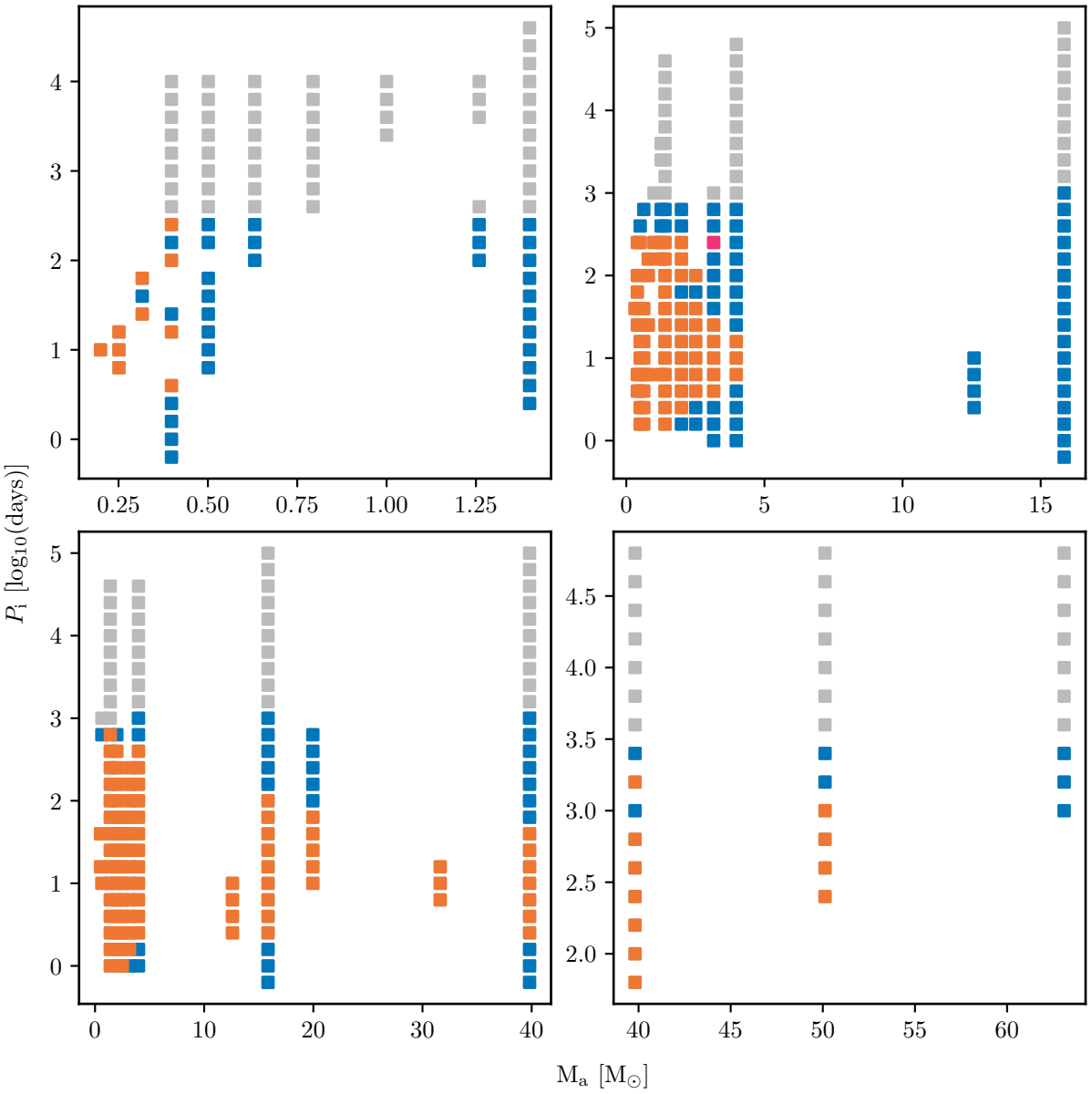

Figure 5.7: Mass transfer stability for the secondary models at $Z = 0.020$, where orange models undergo CEE, blue models experience SMT, pink models merge, and grey models do not interact. Four different donor masses are taken $M_d = 1, 5, 10, 80$. This grid is sparser due to how BPASS generates a stellar population.

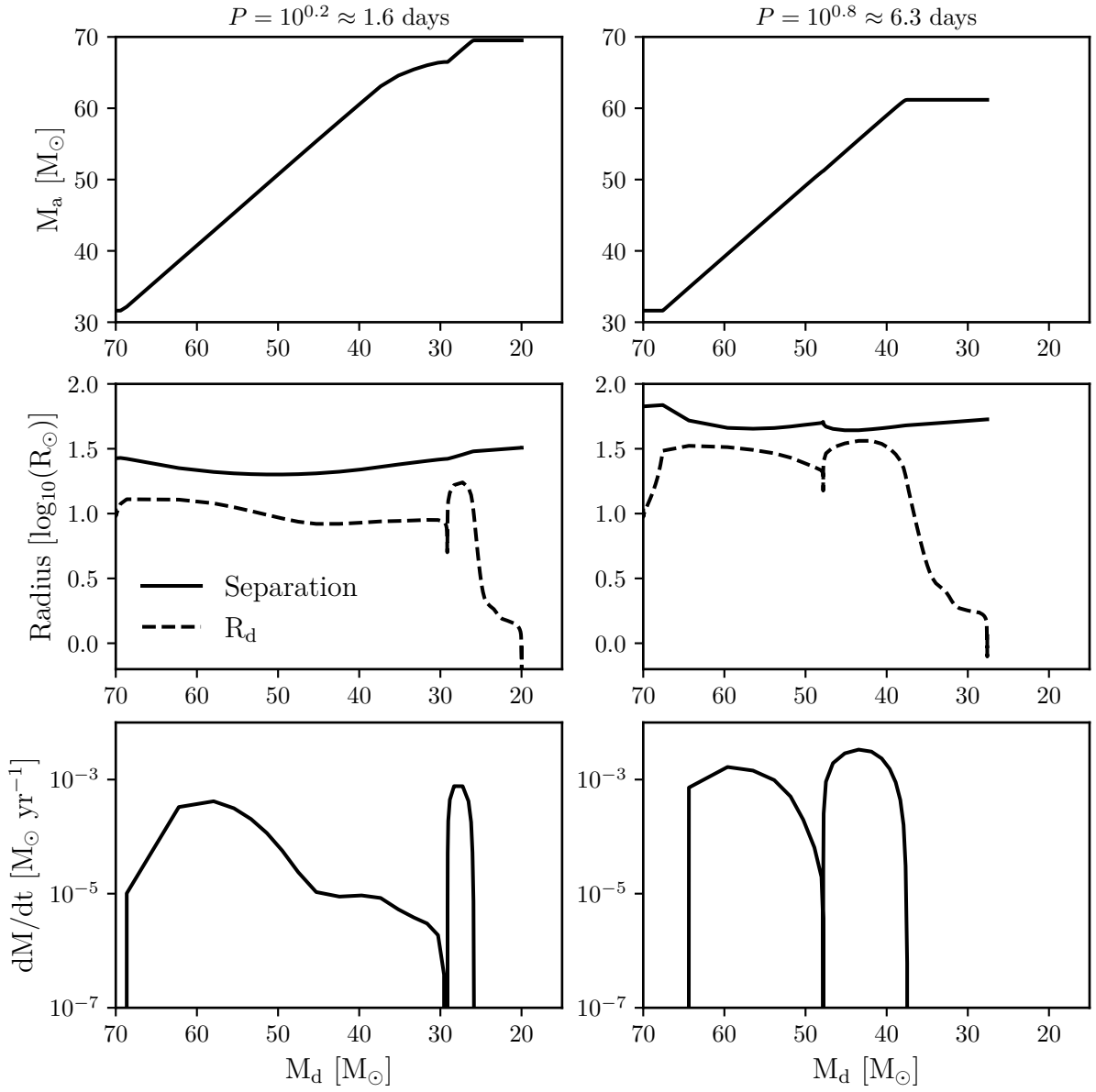

Figure 5.8: Case A mass transfer, resulting in a slow mass transfer phase (left) when the interaction occurs early on the main-sequence with $P = 10^{0.2}$. Or late in main-sequence when no slow mass transfer phase occurs (right) with $P = 10^{0.8}$.

equal mass ratio systems (Farah et al. 2022; Oh et al. 2023). The high-mass X-ray binary and BBH merger populations might originate from different progenitors (Liotine et al. 2023; Romero-Shaw et al. 2023). Depending on model uncertainty, only 11% of Case A HMXRB are expected to result in a BBH merger even when considering detailed mass transfer (Gallegos-Garcia et al. 2022a). Because some $q \approx 0.04$ systems undergo SMT and the $q \approx 0.1$–0.2 for the high-mass $M_{1,BH}$ is higher than conventional main-sequence

interactions undergoing stable mass transfer, we compare this to the literature.

Marchant et al. (2021) explored the stability of mass transfer using detailed treatment of the mass flow through L_1 and mass loss through the outer Lagrangian point of the donor star (L_2/L_3) using MESA (Paxton et al. 2011, 2013, 2015, 2018, 2019) at a metallicity of $Z = 0.00142$ and a $M_d = 30\,M_\odot$. Figure 5.9 shows their results with overlapped the stability of the BPASS models at the closest metallicity ($Z = 0.001$) at $M_{\rm donor} = 30\,M_\odot$. Although the overlap between the simulations is limited, BPASS V2.2 contains CE in regions where SMT is predicted by Marchant et al. (2021). This is most likely due to the synchronisation of the donor spin with the orbit when Roche lobe overflow takes place, which shrinks the orbital separation and, in general, leads to more frequent CE, which is not considered in Marchant et al. (2021). Interestingly, none of the CE interaction at this metallicity and mass in BPASS lead to a merger, but they do not probe far into the CE merger regime from Marchant et al. (2021).

In BPASS V2.2, SMT occurs pre-dominantly during the main-sequence and during core-helium burning when the envelope of the donor star is radiative and the star evolves on a nuclear timescale. When the mass ratio is reversed ($M_d \lesssim M_{BH}$), the system can interact stably during the Hertzsprung gap at $Z = 0.001$ and donor mass. However, the stability during this phase is highly dependent on the donor mass, metallicity, and mass ratio. A larger donor mass range using similar stellar evolution was explored by Gallegos-Garcia et al. (2021) at $Z = 0.00142$. As with Marchant et al. (2021), we find that more CE takes place due to the tidal forces and that more SMT takes place on the main-sequence. Furthermore, similar to Gallegos-Garcia et al. (2021), we find that for higher donor masses, the stability on the main-sequence increases. While the above comparison indicates that BPASS has more CE at the donor masses explored by Marchant et al. (2021) and Gallegos-Garcia et al. (2021), the majority of companion masses in the BBH formation channel have masses $\gtrsim 30\,M_\odot$ and are at a metallicity higher than $Z = 0.001$, see Figure 4.5.

While the grid shown by Fragos et al. (2023) does not contain larger BH masses, it does contain a larger grid of donor masses and a NS accretor of $1.43\,M_\odot$ at $Z = 0.020$. Figure 5.10 shows the closest BPASS models for the grid presented by POSYDON. For the BH, we find an increase in CE in BPASS due to no mass loss from the system, similar to the grids from Marchant et al. (2021) and Gallegos-Garcia et al. (2021). The NS accretor, however, exhibits very similar behaviour in the POSYDON and BPASS grids. Up to $\approx 3\,M_\odot$, interactions are stable, after which almost all interactions experience a CE. Since a BNS merger requires a donor mass above $8\,M_\odot$ to form a NS, we expect most

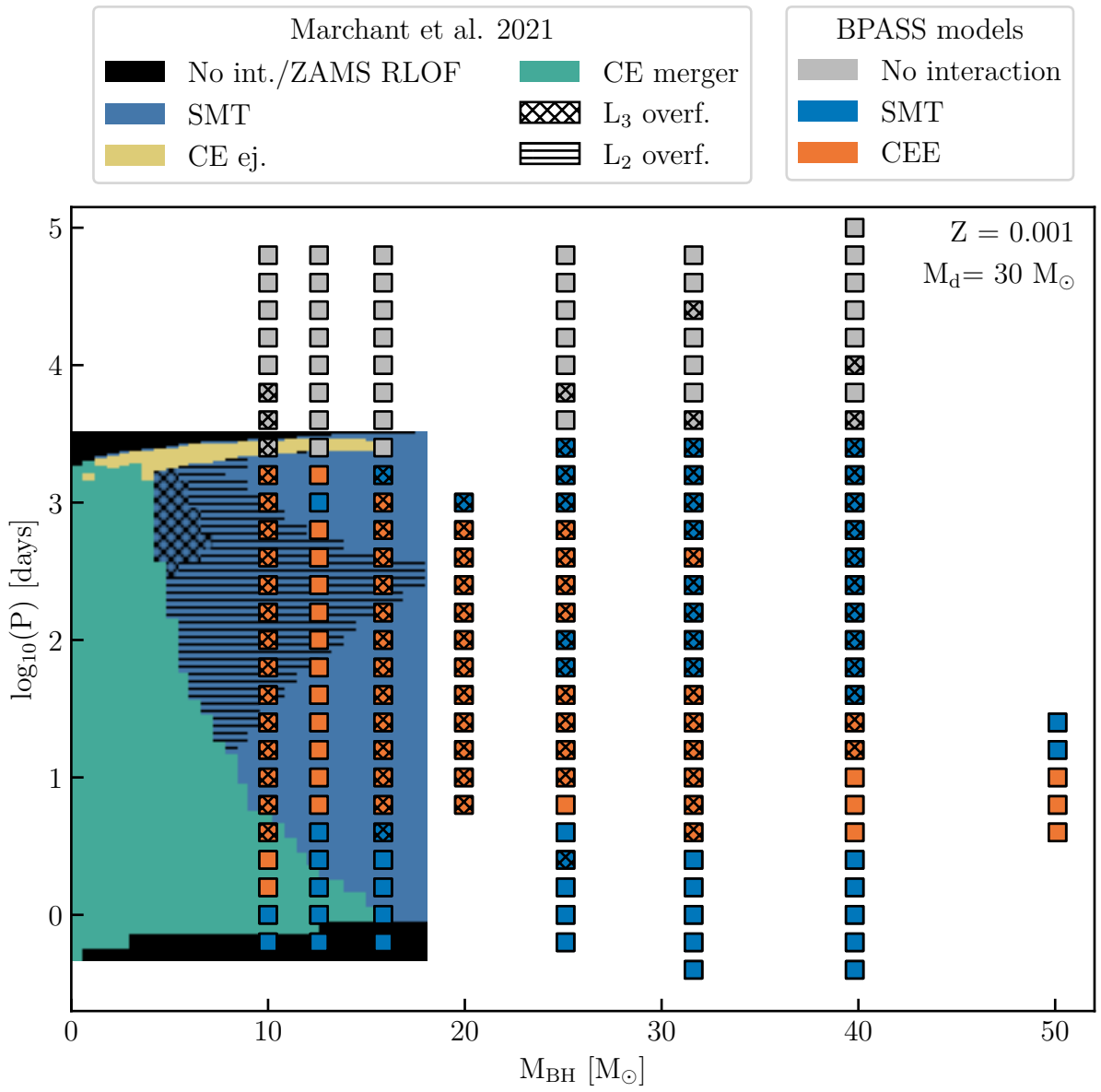

Figure 5.9: Mass transfer stability comparison between Marchant et al. (2021) models ($Z = 0.00142$) and the BPASS models ($Z = 0.001$). The Marchant et al. (2021) CE and SMT interactions leading to BBH mergers within the Hubble time have been grouped together to those taking longer. The hatched squares mark the models contributing at the event rate at $z = 0$, while the normal squares do not contribute to the BBH merger rate.

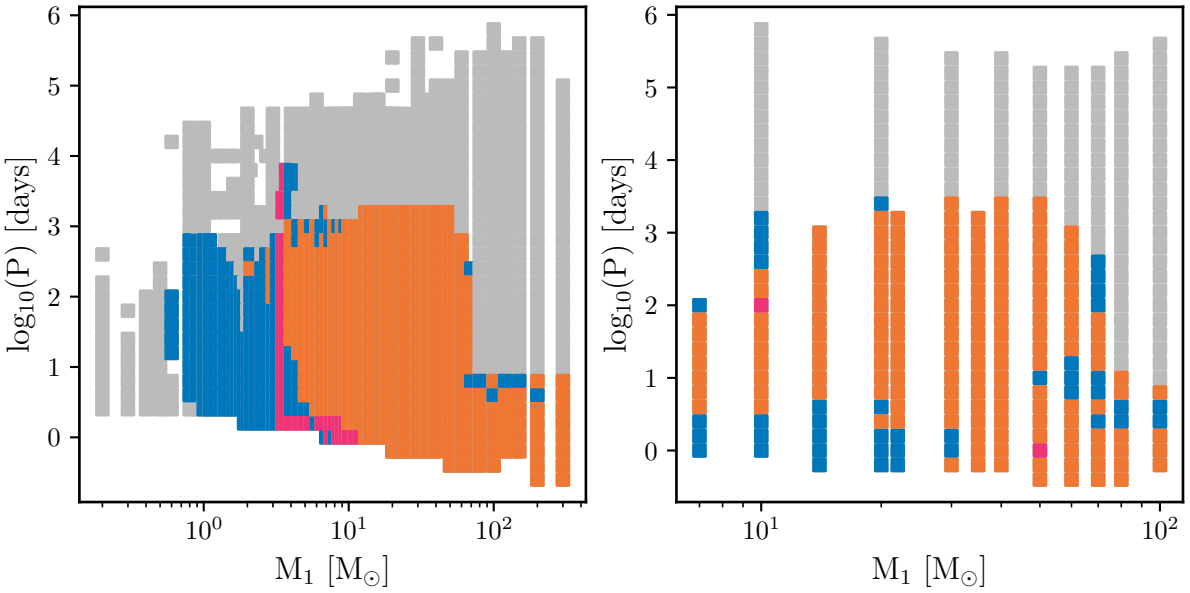

Figure 5.10: The stability of mass transfer over donor mass M_1 and P for the *secondary models*. Grey indicates non-interacting models and pink indicates mergers. Orange and blue are CE and SMT interactions, respectively. The accretor masses are $M_a = 1.4\,M_\odot$ (left) and $M_a \approx 7.9\,M_\odot$ (right).

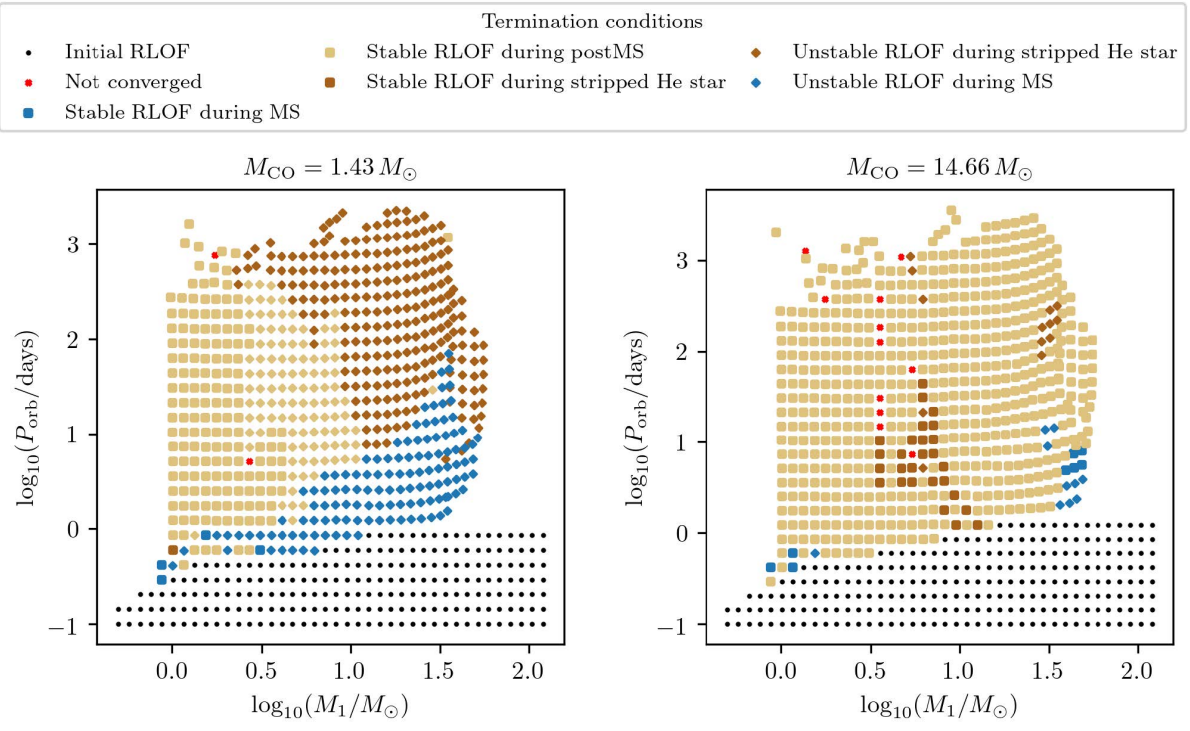

Figure 5.11: The termination conditions of the POSYDON grid at $M_{rem} = 1.43\,M_\odot$ and $14.66\,M_\odot$ for comparison against the BPASS grid in Figure 5.10. The SMT channel is indated with thick squares, while unstable mass transfer are smaller diamonds. Instead of the initial orbital parameters, the period at the moment of interaction is used. Figure taken from Fragos et al. (2023).

BNS progenitors to undergo a CE (Bhattacharya & van den Heuvel 1991; Tauris & van den Heuvel 2006; Postnov & Yungelson 2014; Gallegos-Garcia et al. 2022b; Belczynski et al. 2018b,a; Chruslinska et al. 2018; Vigna-Gómez et al. 2018; Tauris et al. 2017). In the lower mass regime where stable mass transfer occurs, these systems could lead to low mass or intermediate mass X-Ray binaries (Wiktorowicz et al. 2014) and eventually NS+WD systems (Misra et al. 2020) with the initiation moment of mass transfer determining the resulting WD type. Other NS+WD systems are also thought to be the progenitors of ultra-compact X-ray binaries (Bobrick et al. 2017). The outcome of these interactions could provide essential information in determining the stability criteria of mass transfer in the low and intermediate-mass regimes.

Ge et al. (2020a) explores thermal timescale mass transfer and L_2 overflow at an even larger range of donor masses and at a higher metallicity ($Z = 0.02$). Since nearly all of our BBH interactions take place on a longer than thermal timescale, we look at the critical mass ratio from L_2 overflow (their figure 9). All the donor stars in our *secondary models* that lead to BBH mergers at $z = 0$ lie on the right of their figure 9. In general, we find that if the star fills its Roche lobe while evolving on a thermal timescale, such as during the Hertzsprung gap, the system undergoes CE. The BPASS models interact stably during their main-sequence evolution and in the late stages with a few exceptions.

When the star interacts with the BH during the main-sequence, the critical mass ratio is less than in the later stages of the evolution according to Ge et al. (2020a). However, it is important to note that the stability criteria are defined at $Z = 0.02$, while the SMT in the *secondary model* in BPASS comes from lower metallicities, especially when considering the upper mass gap BHs. At lower metallicities, the opacity and thus the radius is small. As such, the L_2 overflow could take place at a higher mass ratio on the main-sequence. However, a more detailed analysis of the interactions is required.

BPASS does not treat outflow out of the outer Lagrangian point, which could result in more CE and mergers, but also the opportunity for more SMT systems to reach periods that can merge within the Hubble time. However, in BPASS, the CE that occurs early in the HG appears very different to those that occur with a deep convective envelope. In the former, the orbit radius changes little, while in the latter, significant orbit shrinkage occurs. This would be similar to mass loss through the L_2 point with not much mass transfer occurring and the orbit remaining constant compared to the strong CE we expect at higher periods and separations. Furthermore, whether or not the star expands past its outer Lagrangian point is determined by the mass loss rate due to mass transfer. Marchant et al. (2021) showed that a more detailed prescription of this rate could increase

the mass loss and reduce the expansion of the star, which limits the L_2 outflow. However, the interplay between the mass loss rate due to mass transfer and outflow through the L_2 point impacts the evolution of the systems non-linearly. It has not been explored at the donor masses and metallicities that form the high-mass regime of the $M_{1,BH}$ distribution. A more detailed investigation is required to understand the influences of the mass transfer rate at high donor star masses at low metallicity and their impact on the observed BBH merger rate, but this is beyond the scope of this work.

Besides the observations of mass transfer or post-mass transfer systems, non-interacting systems can provide additional insight into binary evolution. For example, the analysis of VFTS243 has drastically different formation pathways based on the assumed stellar physics (Shenar et al. 2022; Stevance et al. 2023b). Using more non-interacting compact object systems, such as those from the GAIA observations (Wiktorowicz et al. 2020; Shikauchi et al. 2023), could help us restrict systems undergoing mass transfer.

5.3 Rapid Population Synthesis

Up to this point, we have compared the BPASS against other detailed stellar models because these provide the most detail in the mass transfer. They are, however, computationally expensive. As a result, many other population synthesis codes use approximations in stellar physics and mass transfer stability. Many of these approximations originate from Hurley et al. (2002), on which many rapid population synthesis codes are based, but have included new mass transfer stability criteria. These include

- ζ_d is selected based on the evolutionary phase of the donor star. (Riley et al. 2022)
- A q_{crit} is defined. This takes care of delayed dynamical instabilities. However, it is only valid for a set of mass transfer parameters. (Belczynski et al. 2008; Breivik et al. 2020; Riley et al. 2022; Giacobbo & Mapelli 2018, 2019, 2020; Iorio et al. 2023)
- Radius of the donor star, compared to more detailed models. A unique approach without ζ based on L_2 outflow (Olejak et al. 2021)

The ζ approach sets a ζ for different evolutionary stages of the star based on the convective or radiative nature of the stellar envelope. The first approximation in this approach is the correlation between stellar type to a convective envelope, which does not hold across mass and metallicity (Klencki et al. 2021, 2022). Furthermore, the ζ is set

based on condensed polytropic models by Hjellming & Webbink (1987), Soberman et al. (1997), and newer models include a single value from Ge et al. (2015). This approach removes metallicity, donor mass, and envelope structure as a dependence for the stability of mass transfer. As a result, it misses many stabilities and instabilities (for example, see Woods & Ivanova 2011; Ge et al. 2022).

Especially problematic are delay dynamical instabilities, where the mass transfer is initially stable, but as material is stripped from the star, a region within the envelope is reached where it expands rapidly (Ge et al. 2010), thus resulting in a CE. This can be solved by using a critical mass ratio, which is set as specific mass ratio above which interactions are unstable. This approach implicitly takes into account these delayed instabilities but comes at a cost of $q_{\rm crit}$ only being valid for a specific set of mass transfer parameters, such as mass loss and accretion rate, which does not mimic the large range of observed mass transfer efficiencies (see references in Section 5.1). Moreover, the critical mass ratio can change significantly per evolutionary phase, metallicity and donor mass (Ge et al. 2010, 2015, 2020a,b), which is only minimally implemented.

This final approach considers the radius of the donor star in determining the stability (Olejak et al. 2021) based on the expansion and convective instabilities from detailed stellar models (Pavlovskii et al. 2017). This approach combines checks on the donor type, mass ratio, and radius to determine the stability of mass transfer. The combination of metallicity-dependent mass ratio and radius selection mimics the results found in BPASS V2.2. However, due to the sparseness of the models by Pavlovskii et al. (2017), it does not include the stable late Case B mass transfers nor super-Eddington accretion. Moreover, in the regime of $\rm M_d < 18\,M_\odot$, the old stability criteria using $q_{\rm crit}$ are applied. This results in a population that only extents up to $\sim$55 $\rm M_\odot$ and is limited by PISNe.

It is clear that rapid population synthesis codes miss details in the binary interactions by approximating the stability with ζ or $q_{\rm crit}$. BPASS contains an more self-consistent radial response from the donor star, but also makes approximations that have less theoretical foundation than specific-purpose detailed binary grids do, such as the mass transfer rate. Despite these drawbacks, no other population synthesis code contains this amount of detail in the stellar evolution over a large metallicity range. This detail is essential in properly modelling binary stellar populations and their observables, such as the blue straggler, double WDs, and BBH merger populations. Understanding the uncertainties associated with the binary interaction and seeing how BPASS V.2.2 compares to other binary grids and population synthesis codes, we turn our attention to other caveats and uncertainties in our stellar transient and BBH population predictions in Chapter 6.

Chapter 6

Caveats and Conclusions

By combining detailed binary population synthesis and detailed SFH from cosmological simulations, we made predictions for a large variety of electromagnetic and GW transients, which we presented in Chapter 3. We used this population of stellar transients to explore the properties and formation pathways of BBH mergers (see Chapter 4). While each chapter contains a discussion related to the physics directly related to that chapter's topics and Chapter 5 discusses the mass transfer in BPASS V2.2, several assumptions can impact all our predicted stellar transients. For example, altering the remnant mass prescription for CCSNe can change the number of NS and BHs formed. These systems will not disappear but will shift accordingly, thus altering the BBH, BHNS, and BNS rates simultaneously.

The strength of this thesis is the large number of transients predicted from the same stellar population, limiting the impact of the stellar environment. However, it also complicates the analysis of the implemented stellar physics since the transients originate from completely different progenitors and mass ranges. We start with a discussion on the transient determination in Section 6.1, while Section 6.2 describes how the remnant mass prescription influences the compact object merger mass distributions. Sections 6.3 and 6.4 discuss the influence of the SN natal kick and CE prescription, respectively. We summarise the conclusions of Chapters 3, 4, and 5 in Section 6.5 and discuss the future direction of GW population synthesis.

6.1 Transient Determination

CCSN

Without fully modelling the stellar model to and through iron core-collapse, we have to link the properties of the stellar models to the observational classifications. Massive stars have been observed as progenitors to CCSNe (Smartt 2015), but much remains

unknown about their pre-explosion internal structure and the details of the explosion mechanisms (e.g. Foglizzo et al. 2015; Burrows & Vartanyan 2021). As such, linking the internal properties of theoretical models to the observational categories introduces uncertainty, especially at the boundaries between classifications.

The Type Ib/c classification used in this thesis is based on the hydrogen and helium fraction in the progenitor model. These values were originally chosen to match the observed rates of Type Ib/c SNe (Eldridge et al. 2011, 2013, 2018a). However, in this thesis, the predicted rates no longer match the observed fractions; either SESN should be classified as Type II SNe or some SESNe fail to produce a typical CCSN signal. If the latter is the case, the SN progenitor directly collapses into a BH and vanishes with no or a limited electromagnetic signal (Smartt et al. 2009), for which several observational candidates have been found (Gerke et al. 2015; Smartt 2015; Adams et al. 2017a,b; Basinger et al. 2021; Neustadt et al. 2021). This could lead to a ∼25% decrease in the Type II rate (Disberg & Nelemans 2023) and a ∼16% decrease in the total CCSN rate (Neustadt et al. 2021; Byrne & Fraser 2022). To account for such a large fraction of failed SNe, the predicted CCSNe rate in our work should be over-estimating observations, which is currently not the case, as shown in Figure 3.2, although some failed SNe might still be visible as a sub-luminous outburst (Antoni & Quataert 2023). Uncertainty in the current observations makes it impossible to draw strong conclusions if this indicates the possibility for failed SNe.

Since linking theoretical progenitor models to the SN observations categories remains difficult, misidentifications between subcategories are also likely to occur, especially between the Type Ib and Type Ic SN categories. Whilst it is difficult to hide hydrogen in a SN spectrum due to its easy excitation, large amounts of helium can remain unseen if limited nickel is produced during the SN (Lucy 1991; Dessart et al. 2012a). With limited observations of Type Ib/c progenitors (Smartt 2015), the distinction between Type Ib and Type Ic SNe based on the amount of helium in the ejecta of the theoretical model without modelling the radiative transfer of the explosion is a likely area for uncertainty in the predicted rates. For example, Chrimes et al. (2020) found a different hydrogen mass ($M_H < 5 \times 10^{-4} M_\odot$) and helium fraction ($M_{He}/M_{ejecta} < 0.2$) for the Type II/I and Ib/Ic boundaries, when matching BPASS models to the latest subtype fraction observations over metallicity whilst assuming BH formation does not lead to a SN.

Care should be taken when interpreting the CCSN subcategories because of the uncertainty in linking progenitor models to the observational classes. Fully self-consistent

Reference	Criteria
Fiducial	$M_{CO} > 36$ & $M_{He} < 130$
M_{CO} lower limit only	$M_{CO} > 36$
Heger & Woosley (2002)	$M_{He} > 60$ & $M_{He} < 130$
Marchant et al. (2019))	$M_{He} > 38$
Eldridge et al. (2019)	$M_{He} > 60$ & $M_{He} < 130$ & $M_{ONe} > 0.1$

Table 6.1: The boundaries of the core sizes for systems undergoing PISN according to different prescriptions. Their metallicity bias function is shown in Figure 6.1.

modelling of the progenitor model to and through the SN explosion could provide better constraints on its classification, although model uncertainty remains (Foglizzo et al. 2015; Burrows & Vartanyan 2021).

LGRB

As discussed in Section 3.3, in this thesis, we have only considered the QHE channel for LGRB formation, while other formation pathways contribute significantly to the cosmic rate (Chrimes et al. 2020; Briel et al. 2022). We decided not to include this contribution in this thesis to retain self-consistency in the transient predictions. Chrimes et al. (2020) determine the angular momentum reservoir in Type Ic progenitors and determine a cut-off where these become LGRBs. As a result, this additional LGRB channel increases the LGRB rate, especially at low redshifts. However, since the LGRB rate normalisation is ill-defined, we cannot use it to determine the contribution from this channel. Although beyond the scope of this thesis, the shape of the LGRB rate and the Type Ic rate and their metallicity evolution could be used as a better constraint on the physical parameters of LGRBs.

PISN

The determination of PISN limits based on theoretical properties has been an active area of research, as it is expected to impact the BBH mass distribution, as discussed in Section 2.2.1. Although we do not find a significant dependence of the BBH distribution on the PISN prescription (see Section 4.5.3), we have limited ourselves to a single PISN prescription.

Figure 6.1 shows the metallicity bias function of multiple commonly used PISN prescriptions, as described in Table 6.1. These events are rare enough that the selection criteria minimally impact their distribution over metallicity and total rate. In the fidu-

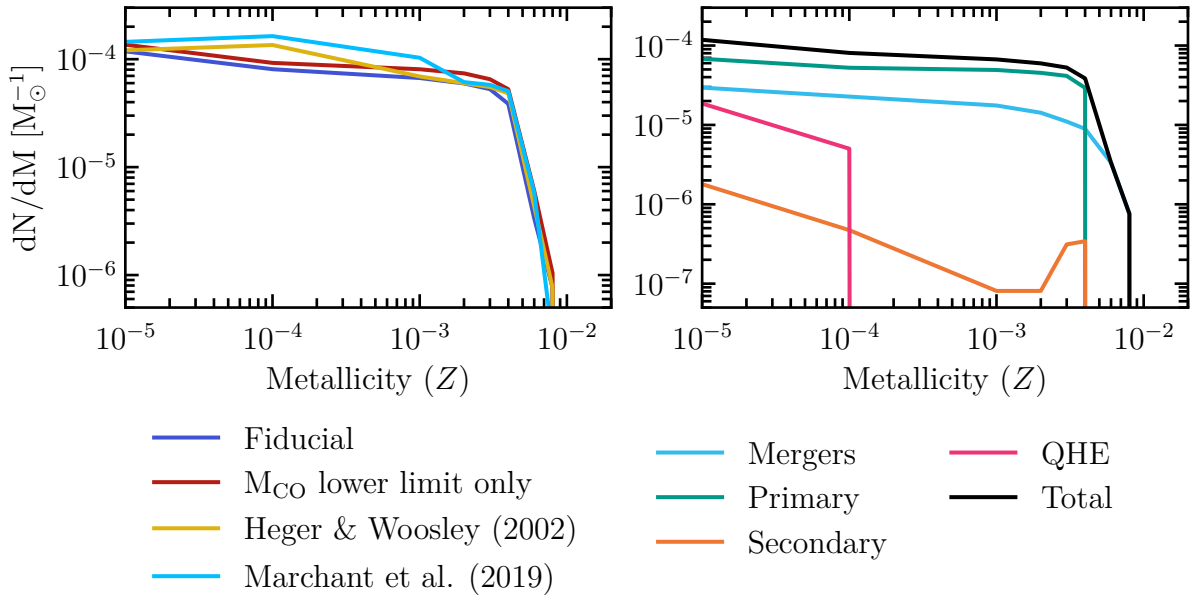

Figure 6.1: (left) The metallicity bias function of multiple PISN prescriptions based on the He or CO core size. (right) The fiducial PISN tagging is split between model types.

cial prescription of this thesis, a flat distribution with metallicity is present up to 0.008, which is unusual since stellar winds are expected to strip massive stars to make a PISN impossible. Figure 6.1 also shows that these high metallicity PISNe originate from merger products. While this is not unusual and could lead to more PISN at higher metallicity, some merger models at high metallicities undergoing PISN are going outside the boundaries of the implemented stellar winds prescriptions in BPASS V2.2. As a result, the star no longer loses mass due to the stellar wind and becomes more massive than it should. Correcting for these failed models would decrease the PISN rate at $z = 0$, where metallicity is high. Since the rest of the PISN models mostly consists of the primary star undergoing a PISN, their outcome and the low-metallicity rates are unlikely to change.

While the core selection criteria on the He or CO core barely impact the PISN predictions from the BPASS V2.2 models, the metallicity bias functions here are significantly different than those included in the BPASS V2.2 data release. Due to the removal of selection criteria for an ONe core to be present, which is not required for a massive star to reach the PPI regime, the PISN rate has increased significantly. We compare the BPASS V2.2 distribution and the prescription in this thesis in Appendix D. An determination based on the internal density and pressure profile in the stellar model would provide the best identification for explodibility. While this is possible using the unreleased BPASS internal structure files, it is beyond this thesis.

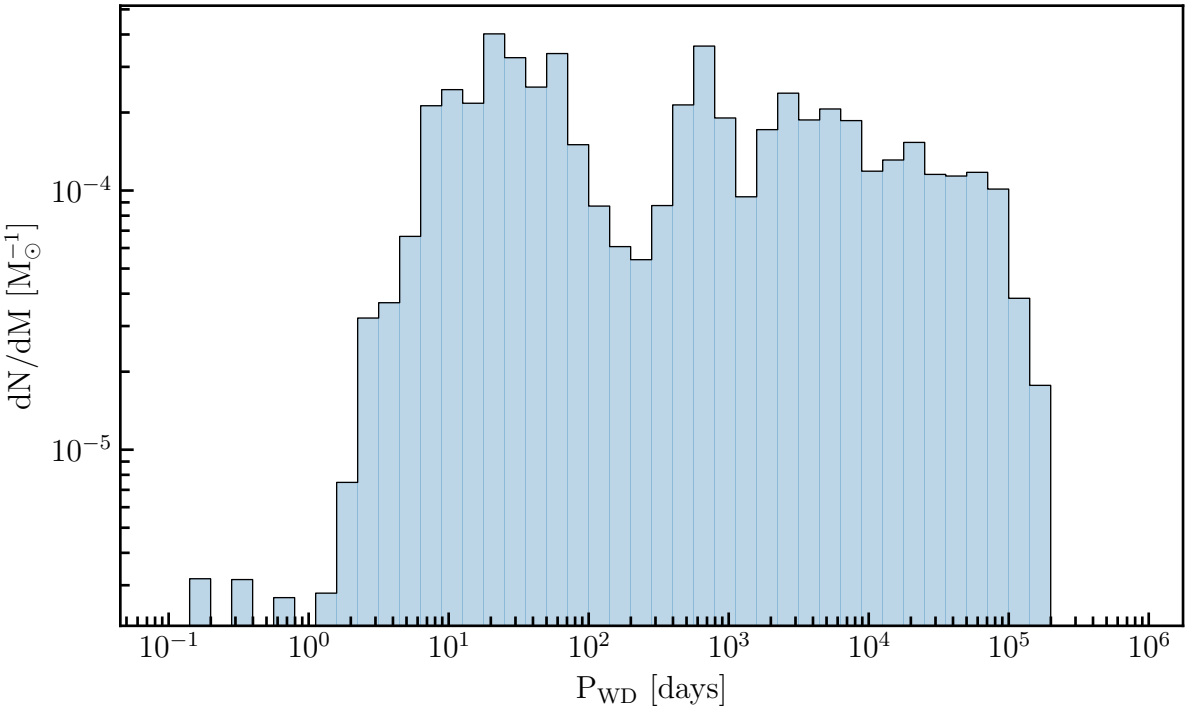

Figure 6.2: The period distribution of double WD systems at their formation that form within the age of the Universe from a simple stellar population at $Z = 0.020$. The period is binned in 0.15 dex bins between -1 and 6.

Type Ia

Type Ia SNe are one of the more uncertain transients in the BPASS models, especially with no DD Type Ia progenitors. While no unambiguous DD Type Ia progenitor has been observed (see Rebassa-Mansergas et al. 2017; Brown et al. 2022, and references therein), a contribution to the rate is expected based on the observed double WD population (Badenes & Maoz 2012; Maoz et al. 2018). The short and sub-day period double WDs in the observed populations (see Brown et al. 2022, and reference therein) are expected to merge within the age of the Universe. Figure 6.2 shows that in the period distribution of the double WDs from a simple stellar population at $Z = 0.020$ from TUI, these close double WDs are missing. On the contrary, these sub-day double WDs were present in the population from BPASS V2.2, which also contains a DD Type Ia contribution.

TUI contains improvements to the mass and period determination at primary WD formation compared to BPASS V2.2. Between the end of the *primary model* and WD formation, additional fusion and envelope removal can still occur, which is taken into account by averaging the Helium and CO core masses to determine the mass of the resulting WD. Compared to BPASS V2.2, the He core mass is correctly taken into account,

which increases the mass of the produced WDs. This process decreases the additional mass lost from the system, and it links the *primary models* to new *secondary models*, where not all short periods are available on the BPASS grid. As a consequence, a *primary model* with, for example, a final period of $10^{0.4}$ days links to a *secondary model* of $10^{2.4}$ days. The short-period binaries are, thus, excluded in the TUI stellar population, which explains the absence of sub-day double WD binaries.

Although the incorrect period transformation between the *primary* and *secondary models* can account for the missed DD Type Ia population in the predictions in this thesis, the implementation of mass transfer and its stability could also lead to fewer short-period binaries. Section 5.2 discussed how increased mass transfer stability in the *primary models* could result in wider double WD systems due to more potential progenitors undergoing SMT, where the increased mass transfer rate will result in additional orbital widening. If the progenitor system undergoes a CE, on the other hand, its orbit will shrink depending on the efficiency of transferring orbital energy into envelope ejection. For BPASS STARS, this efficiency is high, especially in the *secondary models*, as we describe in Section 6.4, resulting in limited orbital shrinkage. The mass transfer implementation and stability in BPASS STARS result in less tight binaries. Furthermore, BPASS STARS does not include the effects of magnetic wind braking, and this can also shift double WD systems to shorter periods. These effects on the double WD population cannot be accurately analysed without correcting the model linking first, which is beyond the scope of this thesis.

As shown in Chapter 3, the SD channel is able to match observations reasonably well depending on the chosen SFH, but additional contributions are expected. Besides the missing DD contribution, triple systems could contribute a similar number of Type Ia SNe as the SD and DD combined, although these predictions are model-dependent (Toonen et al. 2018a; Hamers & Thompson 2019; Di Stefano 2020; Michaely 2021; Rajamuthukumar et al. 2023). If these additional contributions contribute a non-negligible amount to the Type Ia SN rate, underpredicting SFHs are more likely than matching once. On the other hand, we do not account for the accretion rate in determining the explodability of the WD, which could reduce the Type Ia rate originating from this population, although the BPASS accretion rates for SD Type Ias are close to these limits (Eldridge et al. 2019). These improvements can be implemented in BPASS but are beyond the scope of this thesis.

The formation pathway of Type Ia SNe has been an active area of research in the past years, with the delay time distribution indicating a t^{-1} relationship, which is easily

reproduced through the DD channel. However, as we saw in Section 2.2, the BPASS DTD are able to reproduce a similar trend using only the SD channel, which might be an artefact of the incorrect linking between *primary* and *secondary models* too. Although this is unlikely, we cannot draw strong conclusions on the formation channels of the Type Ia SNe and improvements to the TUI population synthesis are required.

Additional Observables

We have predicted a large number of transients from a stellar population originating from detailed stellar models, but we could split the electromagnetic transients into more specific SNe types. For example, an NS-WD merger might result in a peculiar Type Ic-like (Toonen et al. 2018b). However, observations from such sub-populations are harder to come by, as we already see with the Type Ib/c rates. Another avenue would be the evolution of elemental abundances, where the predicted Type Ia, BNS, and BHNS rates contribute to the metallicity evolution of the Universe. Kobayashi et al. (2023) have shown that BPASS V2.2 Type Ia and BNS rates can reproduce abundances closest to the observed values compared to other population synthesis codes.

Uncertainty in the transient determination will remain until our theoretical understanding catchup to the observations, but complementary observables, such as those applied in this thesis, are able to provide confidence in the predictions made due to their self-consistent nature. Additional observables, like the X-ray binaries or double WD population discussed in Chapter 5, can further constrain the physics implemented in the stellar population predicted in this thesis. Besides uncertainty in the link between observables and theoretical predictions, implemented stellar evolution physics impacts the predicted populations and should be analysed. Thus, we turn our attention now to several components of the stellar evolution that could impact the predicted stellar transient populations.

6.2 Remnant Mass Prescription

Closely related to the GW transient determination is the remnant mass prescription, as discussed in Section 2.2.2. In Section 4.5.3, we showed that the high-mass BBH mass distribution is minimally altered by the chosen prescription due to the nearly full fallback in this regime. At lower masses, however, significant differences are present in the BBH, BHNS, and BNS mergers, where this does not occur.

Figure 6.3 shows the full primary mass compact object merger remnants for the

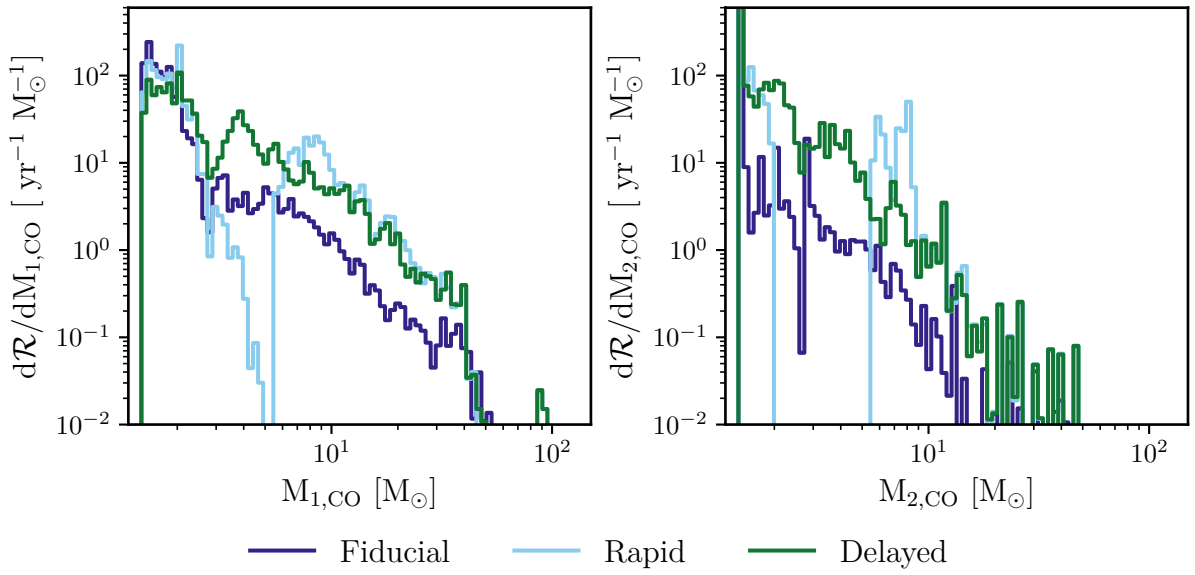

Figure 6.3: The remant mass distributions of merging GW sources from the Fiducial, and Fryer et al. (2012) remnant mass prescriptions split into 100 logarithmic bins between 1 and 200 $M_\odot$.

Fiducial and Fryer prescriptions. The former describes the remnant mass prescription in this thesis, as described in Section 2.2.1. The Fiducial and Delayed prescriptions show a continuous remnant mass distribution without a mass gap between 2 to 5 $M_\odot$. The Fryer et al. (2012) Delayed prescription contains many systems in the lower mass gap regime compared to the Fiducial prescription, which should make these systems more likely to be observed depending on detector sensitivity. The Rapid prescription does contain a lower mass gap between 2 and 5 $M_\odot$ in the compact object formation, but some merging systems still occupy the space between 2 and 4 $M_\odot$ due to mass transfer. Besides changing the full compact object mass distributions, the remnant mass prescriptions also alter the rates and mass distributions of the BNS, BHNS, and BBH populations. However, the compact objects do not disappear; they merely shift between the different GW transients and undergo different evolutionary pathways, for example, causing some systems to merge or others might no longer interact.

Ghodla et al. (2022) showed that the remnant mass prescription influences the cosmic GW transient merger rates, which is also observed here as the GW merger rates at $z = 0$ in Table 6.2 shows. Here, we extend the analysis by showing its impact on the mass distributions of each merger rate and the detailed formation pathways for BBH mergers.

Figures 6.4, 6.5, and 6.6 show the mass distributions of the merging BNS, BHNS (NSBH), and BBH populations for the three remnant mass prescriptions, respectively.

	Fiducial	Rapid	Delayed
Total BBH rate	6.50	57.12	48.04
Total BHNS+NSBH rate	27.01	70.38	84.68
Total BNS rate	93.41	80.17	61.63
BBH formation pathways [%]			
SMT + CEE	35 .29	41.29	35.35
SMT+SMT	20.08	9.73	10.88
CEE+SMT	0.28	0.87	1.29
CEE+CEE	26.16	42.00	45.69
SMT+NON	9.15	2.45	2.97
CEE+NON	6.48	2.19	2.20
NON+SMT	0.71	0.34	0.32
NON+CEE	2.54	0.84	0.85
NON + NON	0.30	0.28	0.45

Table 6.2: The $z = 0$ GW transient rates for the remnant mass prescription in this work (Fiducial) and from Fryer et al. (2012). The detailed formation pathways of the BBH mergers are also shown.

They have a kernel density function applied to them to smooth out the distributions because the BPASS models occupy a finite grid of masses leading to bumpy distributions, especially for the BNS rate. The BNS distribution remains mostly unchanged, except for a decrease in the low mass NS around $\sim$1.5 $M_\odot$. Most secondary NS are at 1.4 $M_\odot$ since BPASS V2.2 forms NS at this mass, and no interactions take place after the second NS is formed, except for GW emission.

This effect is also visible as a peak at 1.4 $M_\odot$ in the BHNS rate in Figure 6.5, where the NS is formed second in the system. The BH mass distribution of the BHNS rate peaks at different masses depending on the chosen remnant mass prescription. The Fryer et al. (2012) prescriptions spread out the NS distributions and caused the BH mass to peak at $\sim$8 $M_\odot$ and $\sim$4 $M_\odot$ for the Rapid and Delayed prescriptions, respectively. At the same time, the Rapid prescription increases the number of NS at 1.4 $M_\odot$ by almost a factor of 2. The choice of remnant mass prescription significantly alters the BHNS mass distribution. Moreover, its cosmic rate at $z = 0$ is more than 2.5 times the fiducial BHNS rate.

Although more systems are formed with the BH first, if the NS is formed first, as is the case in the NSBH channel, it undergoes interactions and forms more massive NS peaking around 2.1 $M_\odot$ in Figure 6.5. While the extreme peaked nature of the NSBH rate is most likely not realistic, a build-up of systems would be expected if the supernova causes the mass gap, but the BH mass distributions follow similar trends as the BHNS

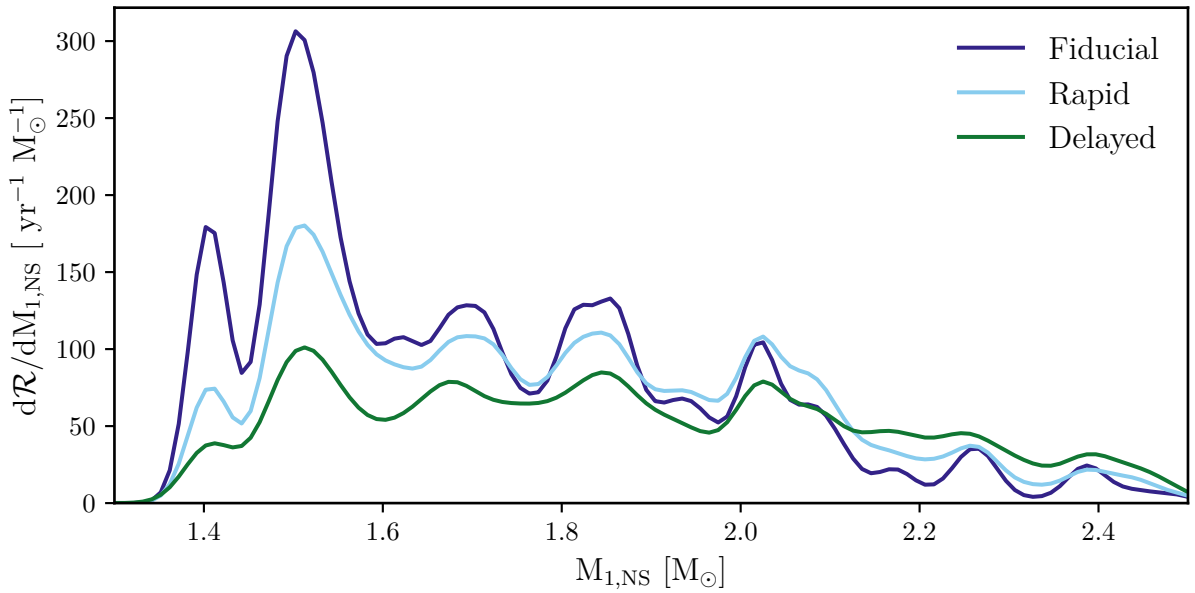

Figure 6.4: The BNS mass distribution of the primary, first formed NS for the fiducial BPASS and Fryer et al. (2012) prescriptions with a KDE applied to the individual events. Most *secondary models* in BPASS have a mass of $1.4\,M_\odot$ due to the finite grid of remnant masses.

rate. Since the impact of the SFH prescription on the feature in the BHNS and NSBH distribution is minimal (Broekgaarden et al. 2021), these could be used to determine the remnant masses left behind from a SN.

Section 4.5.3 discussed the impact of the remnant mass prescription on the primary mass of the BBH distribution. Here we also present the mass distribution of the secondary, which follows a similar trend to the primary mass distribution, only shifted to lower masses. The Rapid prescription is able to accurately predict the peak location of the merging BBH primary mass, although it overpredicts the rate by a factor of ∼2.5, as shown in Section 4.5.3. As a result of the mass gap, the Rapid prescription barely contains models below $5\,M_\odot$. Because CE evolution is dominant in this regime, the models shift to different formation pathways, as shown in Table 6.2.

While it is clear that altering the remnant mass prescription drastically alters the rate and the mass distributions of the compact object merger rates, we have limited ourselves to these commonly used remnant mass prescriptions. A more detailed analysis using a prescription with the compactness parameter (Schneider et al. 2023), internal structure (Patton et al. 2022), or a mix between the rapid and delayed models (Fryer et al. 2022b) would be possible. However, due to the limited observations of BHNS and BNS mergers, it is not currently possible to determine which remnant mass prescription fits

observations best, although the BBH distributions might provide a small window into the remnant mass prescriptions at this moment. It is important to consider multiple observables when exploring the parameter space of remnant mass prescriptions since the compact object mass distribution can be altered significantly in a non-trivial way. However, the remnants are expected to shift between types, although this can also shift their evolutionary pathways.

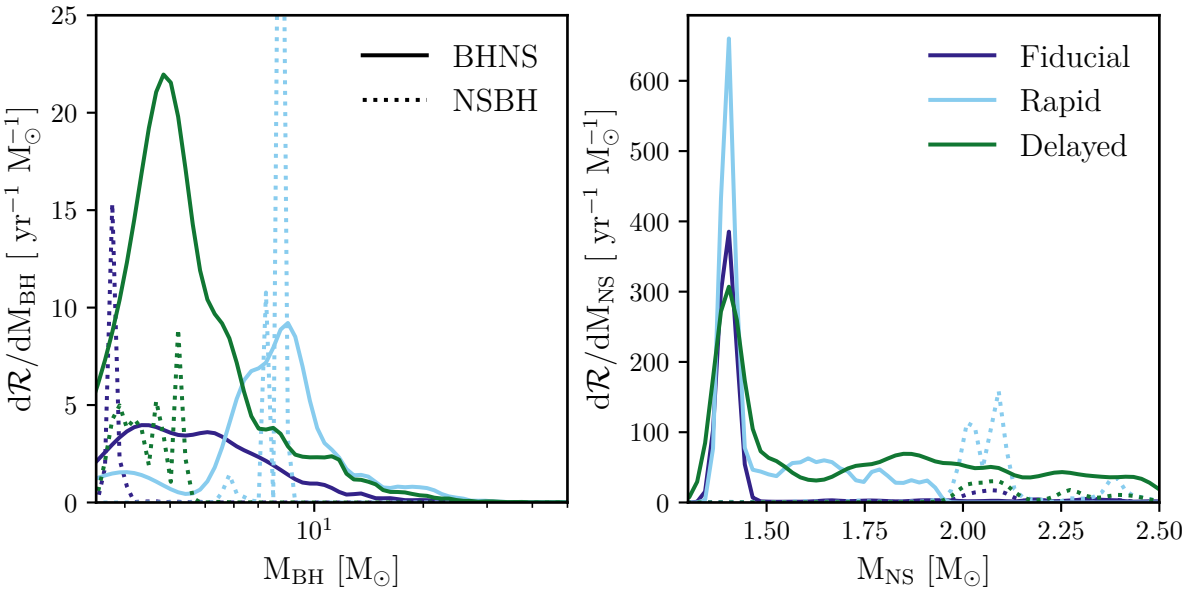

Figure 6.5: The BHNS mass distributions for the BH (left) and NS (right) for the fiducial BPASS and Fryer et al. (2012) prescriptions with a KDE applied to the individual events. In the BHNS channel (solid lines), the BH is formed first, while in the NSBH channel (dashed lines), the NS is formed first. Most secondary NSs in BPASS have a mass of $1.4\,M_\odot$ due to the code forming NS at this mass.

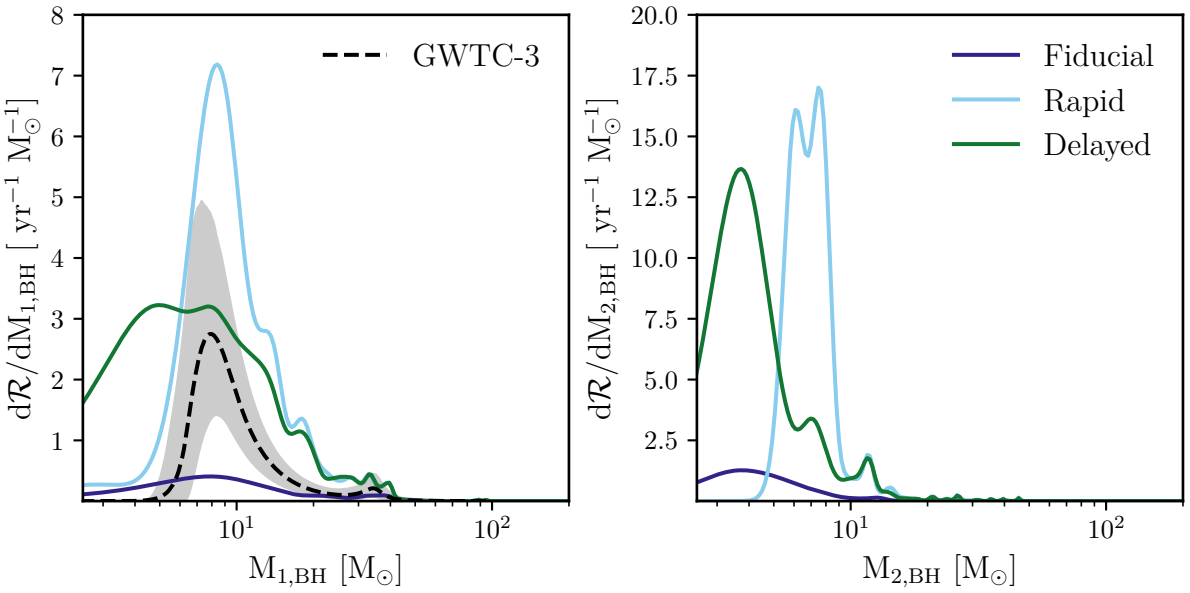

Figure 6.6: The BBH primary (left) and secondary (right) mass distributions for the fiducial BPASS and Fryer et al. (2012) prescriptions with a KDE applied to the individual events. GWTC-3 results are depicted in the left figure with their uncertainty (Abbott et al. 2023).

6.3 Supernova Kick Prescriptions

One of the uncertainties in the stellar population is the natal kick the compact object gets during the supernovae. It introduces eccentricity and alters the orbital distribution of the remnants. This natal kick is essential in the BHNS and BNS rates but minimally affects the BBH rate (Giacobbo & Mapelli 2018; Tang et al. 2020; Broekgaarden et al. 2021, 2022a) due to the BH's more massive nature. The number of BNS mergers impacts the r-process elements produced (van de Voort et al. 2022; Kobayashi et al. 2023).

The effect of the natal kick is already present in the Galactic BNS eccentricity and period distribution (Vigna-Gómez et al. 2018; Richards et al. 2023), and pulsar velocity distribution (Willcox et al. 2021; Richards et al. 2023). In this thesis, we have only implemented a Hobbs kick (Hobbs et al. 2005). While a bimodal SN kick distribution is preferred to match the Galactic BNS population (Vigna-Gómez et al. 2018; Chu et al. 2022), mass ejecta has also been suggested as a better alternative (Bray & Eldridge 2016; MacLeod et al. 2018). Either way, the details of our population are affected by the natal kick. The influence of an ejecta-dependent kick in BPASS has been explored by Richards et al. (2023) and includes an analysis of the velocity distribution of pulsars, which had already been matched using the Hobbs kick by Eldridge et al. (2011).

Although the kick will not influence Type Ia SNe, it could affect the number of CCSN, Type Ib/c fraction, GW mergers, and their distribution in the host galaxy (Eldridge et al. 2011; Zapartas et al. 2017). The kick distribution alters the period and eccentricity distribution (Vigna-Gómez et al. 2018; Richards et al. 2023), which can alter the mass transfer after the first SN. Furthermore, the implementation of orbital change in the mass transfer creates a degeneracy with the natal kick. For example, the natal kick can undo orbital shrinkage from CE. Disentangling the influence from the natal kick is non-trivial, but predictions of pulsar velocities from the same stellar population can provide validation of the natal kick.

6.4 Common Envelope Prescription

The common envelope prescription plays an important role in determining the period distribution of DWD and, in recent years, gained interest as a formation pathway for BBH mergers. However, much uncertainty exists in the parameters and prescriptions used (Ivanova et al. 2013). As discussed in Section 1.3.3, the γ and $\alpha_{\rm CE}\lambda$ prescriptions are the two main prescriptions used. In population synthesis codes, the $\alpha_{\rm CE}\lambda$ prescription is most common and values of alpha are often explored to best match compact object merger rates (for example, see Chu et al. 2022). However, the CE efficiency is not universal across binary systems (Iaconi & De Marco 2019; Politano 2021) with inefficient CE in low-mass stars (Parsons et al. 2017; Zorotovic & Schreiber 2022; Scherbak & Fuller 2023) and $\alpha \approx 1$ in GW progenitors (Wilson & Nordhaus 2022).

To match the merger rate and Galactic population of BNSs, values of $\alpha \approx 10$ are required (Giacobbo & Mapelli 2018; Chu et al. 2022). Additional energy can come from other sources inside the star, such as recombination energy, or additional mass transfer before or after the CE (Hirai & Mandel 2022). However, other uncertainties could skew the image of CE. For example, Woods & Ivanova (2011); Woods et al. (2012) have shown that non-conservative stable mass transfer can mimic inefficient common envelope interactions. Furthermore, different population synthesis codes provide evidence for a high α and low α (Bavera et al. 2021; Delfavero et al. 2023) for BBH progenitors. The most observables are at low mass, where the internal structure of the star is different than in the high mass regime (Wilson & Nordhaus 2022), with different efficiencies accordingly. The combination parameter alpha-lambda has been explored in BPASS and leads to values between 2 and 10 for the *primary models* and 10 and 50 for the *secondary models* (Stevance et al. 2023a). The difference might result from how tides are treated

or additional mass transfer after the common envelope widens the orbit (Hirai & Mandel 2022). If these additional parameters are taken into account, the efficiency of CE can be higher than 1, which means that systems that originally could not survive might be able to survive without losing too much mass, such as BH1 and BH2 (El-Badry et al. 2023a,b). These BH + star systems cannot have undergone SMT due to the elemental abundances on the star but require at least $\alpha = 1$ not to merge. These additional energy sources or interactions allow for a more efficient CE. However, such efficiencies are still higher than the often predicted from 3D simulations or low mass observations (Lau et al. 2022a,b).

The implementation of the CE prescription in BPASS is described in Section 2.1.1, but the exact relation between dJ, the angular momentum (AM), and the lost material

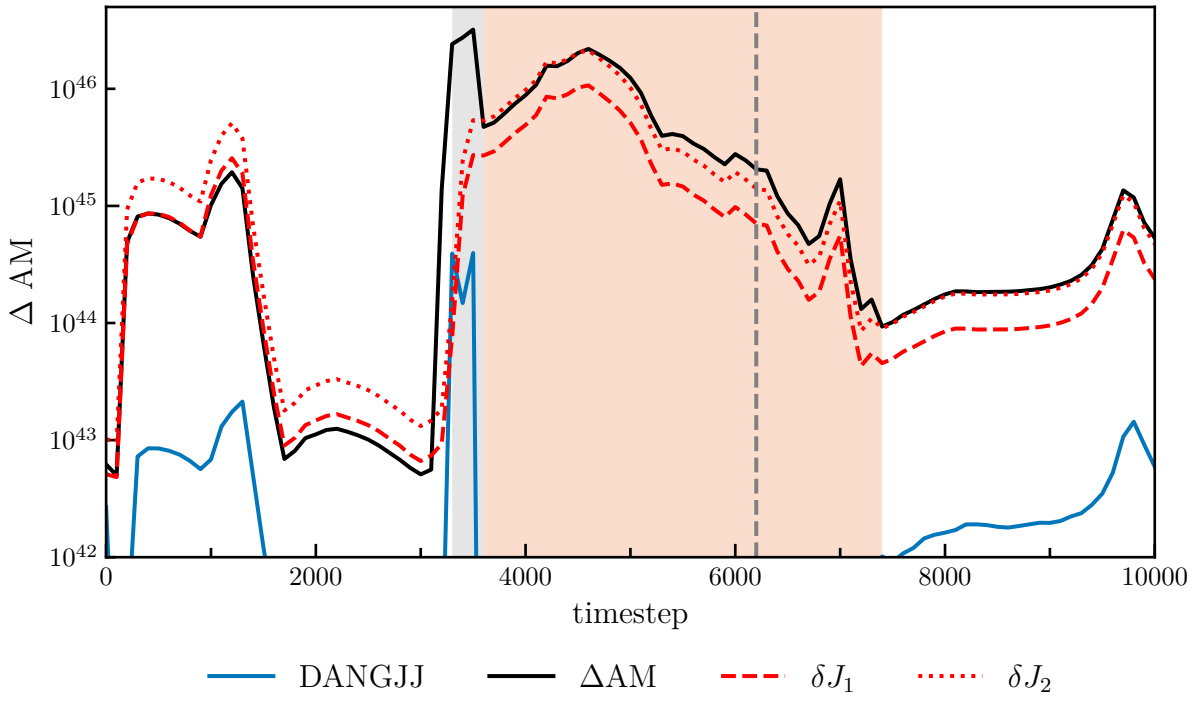

Figure 6.7: The angular momentum change in a $Z = 0.020$ binary with $M_1 = 20\,M_\odot$, $q = 0.7$, and $P = 10^2$ days. The system undergoes mass transfer in the grey area and the CE prescription is enabled in the orange region. The radius of the donor becomes smaller than the separation at the grey line. DANGJJ is the angular momentum change output from the model (blue line), while ΔAM is the change in the total angular momentum in the system (black line). δJ_1 (red dashed) and δJ_2 (red dotted) are post-processing calculations, which use the masses and normalised masses by 1/1.9891, respectively. Because only 1 in every 100 models is stored, we miss some details in the AM calculation. However, it is clear that a normalisation change occurs when the CE prescription has been initiated.

still need to be defined. Although the binary losses material according to Equation 2.1, the amount of angular momentum this material loses from the binary changes due to the tidal implementation.

Figure 6.7 shows the AM change in a binary in BPASS STARS. The output parameter for the angular momentum change, DANGJJ, does not align with the actual angular momentum change, ΔAM, in the binary. A factor 100 difference is present for the change outside the region where the CE prescription is present. During the CE, DANGJJ does not follow the AM change correctly due to the implementation of the CE prescription, although this does not impact the CE evolution itself.

Furthermore, the AM calculation from the masses and AM change is altered after the tides have been initiated. Before the tides, the AM change can be calculated using Equation 2.4 with the outputted M_1, M_2, and AM, which is shown as the dashed red line in Figure 6.7. After the tides have been initiated, the AM change requires the masses to be normalised with 1/1.9891 to match the model AM, as the dotted red line shows in Figure 6.7. This factor is used in the code such that the mass of the Sun inside the code is unity (Ball 2012), and as a result, the AM loss from the binary is increased during and after the tides. This could result in additional orbital alterations depending on the mass ratio. While the expected impact on a population scale is small, the outcome for an individual model could be significant and requires further analysis beyond this thesis.

Another essential aspect in CE evolution is the moment the unstable mass transfer initiates and ends. In BPASS, the CE starts when the radius of the primary is larger than the separation of the system. The CE ends, however, when the star shrinks back into its Roche lobe to ensure the interaction has ended. Since accretion is turned off during the CE, this removes the possibility for conservative mass transfer onto the companion after the donor star shrinks back to below the separation of the system. This missed accretion can influence the orbital separation and perceived CE efficiency (Hirai & Mandel 2022).

The benefit of this approach is the non-predetermined stripping of the star, which allows for BPASS V2.2 stars to be partially stripped with some non-negligible fraction of hydrogen left on their surface. Rapid population synthesis codes often assume full stripping of the hydrogen envelope during CE, but other detailed modelling has also found that some hydrogen is expected to remain (Fragos et al. 2019). However, the implementation needs further analysis and improvement to be confident the features described in this section do not significantly affect the population properties. The common envelope evolution will remain an area of active research, and several questions are still unanswered (see references in Spera et al. 2022).

6.5 Conclusions

GW mergers have become a new observational window into the evolution of massive binaries with almost a decade of observations. Still, much remains unknown about their exact formation pathways and the observed features in the GW populations. Theoretical predictions are focused on exploring the parameter space of the input physics instead of constraining it. With the purpose of gaining a better understanding of the GW merger population, we have combined detailed binary population synthesis with SFHs from cosmological simulations to make predictions of stellar transients. This is the first time this prediction has been done self-consistently from a single cosmological stellar population with detailed binary population synthesis and detailed star formation and metallicity evolution over the age of the Universe. By estimating GW and stellar transients from the same population, we are able to identify influences from the SFR, metallicity, stellar and binary physics since each transient probes different areas of stellar evolution or star formation. For example, the Type Ia and LGRB rates are impacted by binary physics, while the CCSN and PISN probe the evolution of massive stars, the NS and BH progenitors. Similarly, the metallicity dependence of the LGRB, PISN, and Type Ib/c rates provided insight into the metallicity evolution at different moments in the life of the Universe. If the stellar population is able to match the observed rates of these stellar transients, it gives confidence in the prediction for GW mergers from the same population.

6.5.1 Cosmic Transient Populations

Chapter 3 explored these transient rates for multiple SFH prescriptions from empirical and cosmological simulation origin to identify differences in the predicted populations. There we found that the non-metallicity dependent transient rates, such as the Type Ia and CCSN, match observations using most of the SFHs, because each of the selected CSFRDs generally follow similar evolution over the age of the Universe. The Type Ia rate probes older star formation and matched observations up to $z = 2.5$, indicating that the total amount of star formation before this is well described by the SFH, although binary, thermonuclear explosion physics, and linking between *primary* and *secondary models* remains uncertain, see Chapter 5 and Section 6.1, respectively. The early star formation at low metallicity is essential in the formation of merging BBH. While the total amount of star formation might be accurate, the merging BBH are thought to predominantly come from low metallicity environments, although in this thesis, the BBH merger rate

remains nearly constant up to $Z = 0.01$, after which no BBH merge (see Section 2.2.3).

To probe the star formation in more detail, metallicity-dependent transients are used to characterise the metallicity evolution of the star formation. For example, PISNe come from very massive stars, occur only several Myr after their formation, and are limited to low metallicities (see Section 2.2.3 for more details). We see in Section 3.4 that the metallicity evolution of the Neijssel et al. (2019) SFH does not match the observed SLSN-I rates indicating that its metallicity evolution does not accurately describe the cosmic population, although PISNe cannot explain all SLSN-I. Since the cosmological simulations have metallicity-specific CSFRD with reduced early star formation and faster enrichment than the empirical prescription, this left an imprint on the metallicity-dependent transient rates by boosting the Type Ib/c to Type II fraction at earlier ages and decreasing the BBH merger rate. However, the metallicity-dependent transients are still poorly observed, and new observations in the coming years, as mentioned in Section 3.8, should be able to provide us with a better understanding of the transient rates and metallicity evolution over redshift (Fryer et al. 2022a).

6.5.2 BBH Population

The predicted GW mergers from the same cosmic populations are reasonably well estimated, partially due to the uncertainty in the observed population, with the BBH rate being underestimated by most prescriptions. Moreover, its redshift evolution is too shallow to match the observed increase in BBH rate. However, observations rely highly on the assumed population, and this thesis only considers isolated binary evolution. Additional formation channels, such as dynamical mergers (see Section 3.7), can provide additional mergers to their cosmic merger rate.

With confidence in the predicted stellar population, we analysed more thoroughly the properties and formation pathways of the merging BBH population in Chapter 4. We show that the predicted population matches the observed features of a $35\,\mathrm{M}_\odot$ peak and extended tail up to $100\,\mathrm{M}_\odot$ in the primary BH mass distribution. No population synthesis code has been able to match these features using only isolated binary evolution before. Moreover, we find that these features do not result from (P)PISN, as previously thought, but instead originate from the interplay between mass transfer stability, quasi-homogeneous evolution, stellar winds, and super-Eddington accretion. This is a new self-consistent explanation of these poorly understood features in the mass distribution, which previously required additional dynamical formation pathways to be explained.

The extended tail and PISN mass gap BHs are a result of super-Eddington accretion

onto the BH and increased mass transfer stability. Super-Eddington accretion systems were originally thought to not merge within the age of the Universe due to orbital widening after the donor star becomes the less massive object in the binary. However, due to the increased stability, more extreme mass ratios interact in a stable manner, resulting in strong orbital shrinking tides and a longer time of orbital shrinkage before the mass ratios reverse. Both effects combined allow the super-Eddington BHs to merge within the Hubble time and upper mass gap. The $35\,M_\odot$ excess is also a result of increased mass transfer stability and further depends on the choice of QHE and stellar winds, as described in Section 4.2. Although PPISN systems contribute to the high-end of the excess, they do not shape the peak, and its presence is independent of remnant mass prescription and SFH choice. The former alters the low-mass regime and mass ratio distribution, which we cannot fully match, possibly due to our CE implementation, as discussed in Section 6.4.

6.5.3 Binary Interactions

Overall, we find that the binary interaction treatment is essential in forming these mass distribution features and compare the mass transfer treatment in BPASS V2.2 against detailed binary evolution grids and rapid population synthesis codes in Chapter 5. We find that BPASS V2.2 more closely matches the detailed grids and that rapid population synthesis codes miss essential physics related to the stability of mass transfer, resulting in BBH populations without the observed features. The stability of mass transfer is mostly independent of the radiative or convective nature of the envelope. Instead, we find that the stability of mass transfer depends on metallicity, mass, and age, similar to Ge et al. (2010, 2015, 2020a,b). Specifically during core-helium burning, the stellar envelope is often radiative, while rapid population synthesis codes based on Hurley et al. (2002) often assume that these stars have a convective nature (for more detail, see Klencki et al. 2021). As a result, more systems undergo nuclear timescale stable mass transfer in BPASS V2.2, especially at larger mass ratios between a BH and stellar companion.

6.5.4 Future Outlook

Detailed binary population synthesis provides unique insights into the cosmic population of merging BBH that have not been accessible before with rapid population synthesis code, even if the exploration of the implemented physics is limited. In this thesis, we have explored a large range of stellar transients related to GW mergers to account for

the uncertainty in the stellar evolution of merging BBH progenitors. Although we have been unable to match every observable, these indicate areas of improvement and where stronger constraints from observations are required.

The implementation of binary interactions in rapid population synthesis codes needs to include more detailed stability criteria to capture its impact on the predicted population. While population synthesis codes with detailed stellar models, should include accurate modeling of the accretor and improve upon the implemented physics, such as the common envelope phase and mass loss rate during mass transfer. Moreover, a collection of observables from the same population should be used to constrain the implemented physics, such as those presented here. With many population binary synthesis codes available now, their focus should be on explaining the physics shaping the observed features to allow for thorougher understanding of the detailed stellar and binary physics.

More observations of other stellar populations, such as the double WD population, can further help understand the impact of mass transfer stability on the predicted populations. The future Laser Interferometer Space Antenna (LISA; Amaro-Seoane et al. 2017) will provide a picture of the living double WD population in our galaxy by measuring the GWs they emit (Kremer et al. 2017; Lamberts et al. 2019; Wang et al. 2021a), extreme mass ratio inspirals (Gair et al. 2017; Babak et al. 2017), supermassive BBHs (Filloux et al. 2011; Chen et al. 2020), and many other possible observables (for an overview, see Amaro-Seoane et al. 2017).

The findings in this thesis provide new insight into the BBH population properties, and more confidence in this prediction can be gained by looking at other evolutionary phases to the formation of merging BBH, such as X-ray binaries or dark companions. Future observations from the LIGO/Virgo/KAGRA collaboration will provide more BBH mergers and better population constraints as time goes on. At the same time, the future GW observatories, the Einstein Telescope (Punturo et al. 2010) and Cosmic Explorer (Evans et al. 2021), are in their preparation phases and will detect mergers over cosmic time and in more detail, providing a larger window into binary physics and the formation pathways of GW mergers (see Maggiore et al. 2020, and references therein). The future of binary population synthesis is bright, with a new era of detailed population synthesis, and many current and future observations around the corner.

Appendix A

Delay Time Distributions

This section contains the delay time distributions for the 13 metallicities in BPASS. Furthermore, the CCSN and Type Ia subtypes have been given their own figures to show differences within these rates.

A.1 All transients

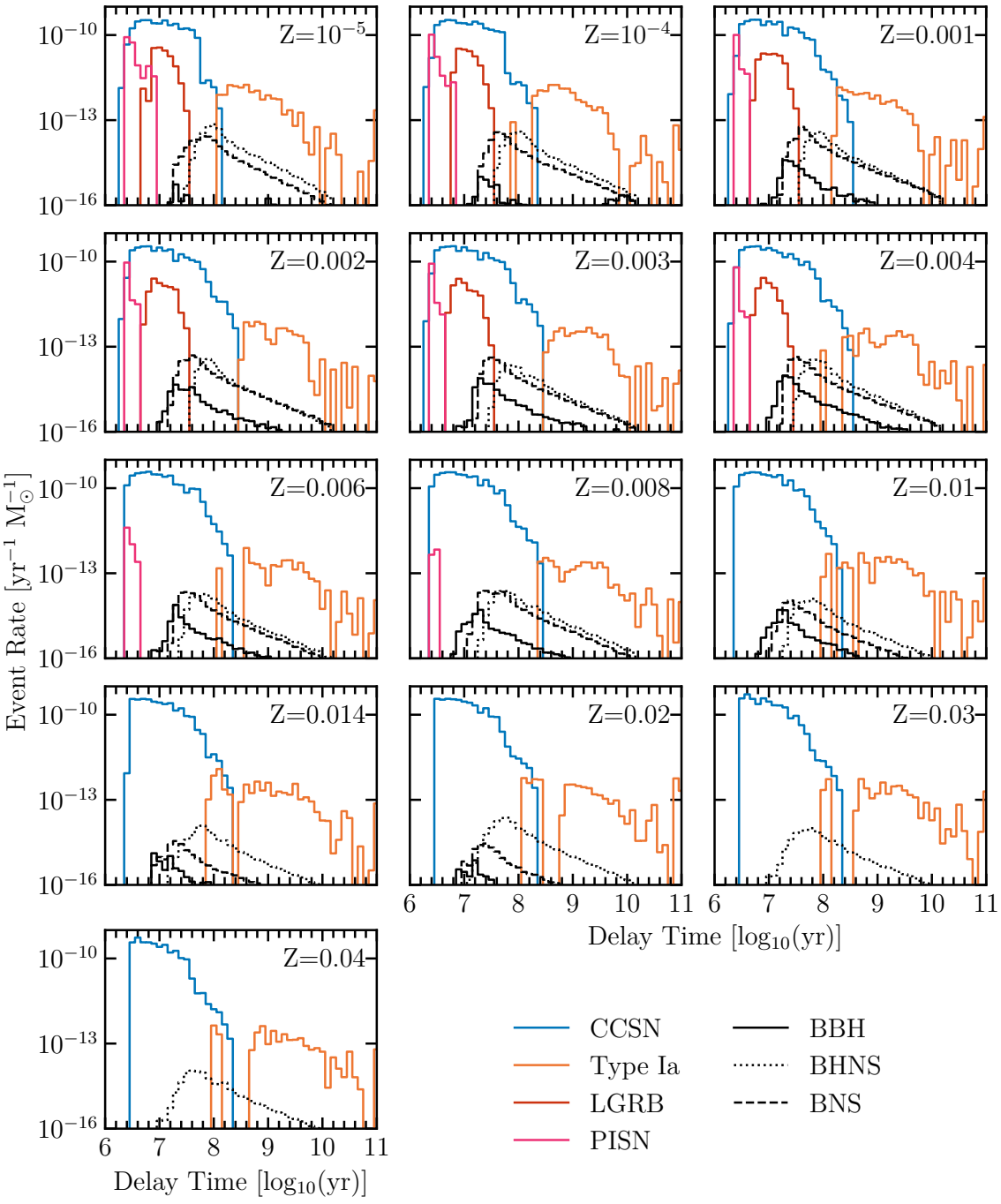

Figure A.1: The DTDs over all 13 BPASS metallicities for the main electromagnetic and gravitational wave transients considered in this work. The events are binned in 0.1 dex wide bins between 10^6 and 10^{11} yr.

A.2 CCSN subtypes

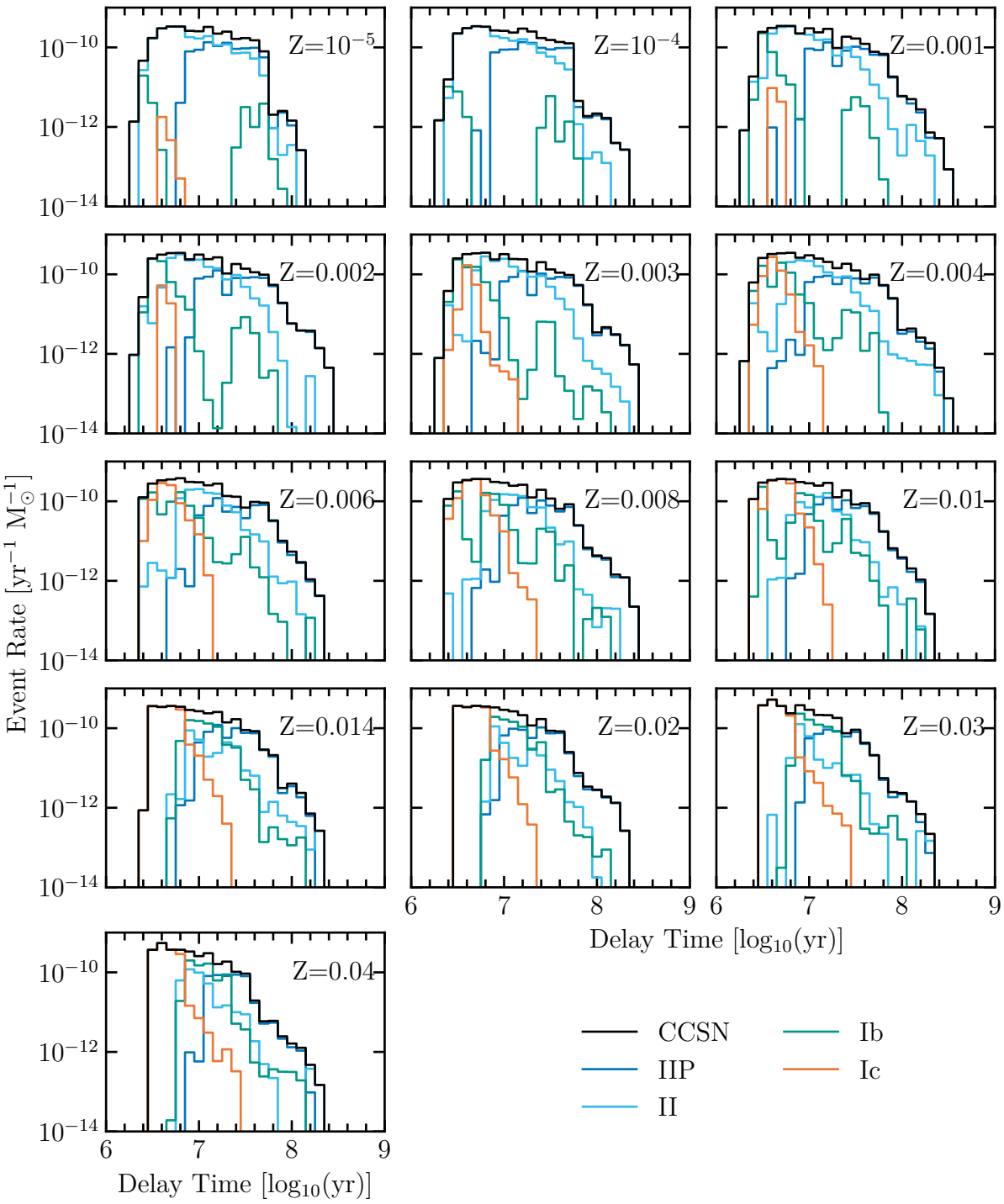

Figure A.2: The DTDs over all 13 BPASS metallicities for the CCSN subtypes. The black line is the toatal CCSN rate and overlaps the other rates.

A.3 Type Ia subtypes

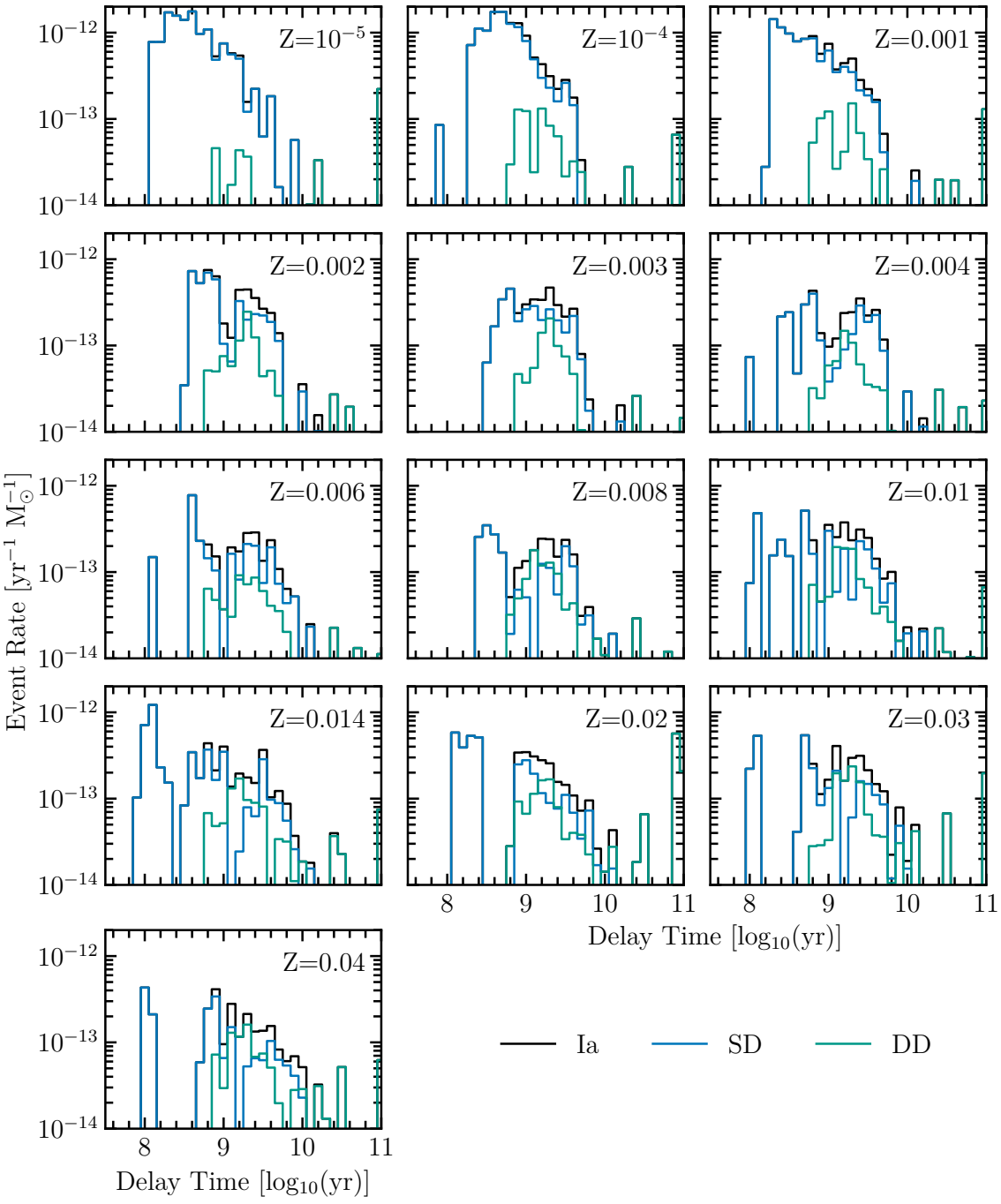

Figure A.3: The DTDs over all 13 BPASS metallicities for the Type Ia subtypes. Black is the total Type Ia SN rate. If the rate consists of only or almost only SD or DD, their lines might overlap the total SN DTD.

Appendix B

Homology

In the context of mass transfer the thermal timescale of the star are important because it limits the accretion onto the companion star. Within BPASS this limit is $\dot{\mathrm{M}} = \mathrm{M}_2/\tau_{\mathrm{KH}}$. Thus, the timescale at which the primary loses the mass and at which the secondary star can accrete this material determines the mass lost from the system. To be able to get massive BHs, it is essential that material remains in the system and that the timescales are similar. To understand the behaviour of the stellar models, we use homology relations to determine the dependence of the thermal timescale on mass between different stars (found in most stellar structure text books, such as Eldridge & Tout 2019). The thermal timescale is proportional to the mass, luminosity and radius of the star, as per Equation B.1.

$$\tau_{\mathrm{KH}} \propto \frac{M^2}{RL} \tag{B.1}$$

To determine the dependence solely on mass, we setup a few basic scaling relations that approximate the behaviour of massive stars before turning our attention to specific regimes. From the first two stellar structure equations, we get the following main homology relations in which ρ_c and P_c are the central temperatures of the star with mass M and radius R.

$$\rho_c \propto \frac{M}{R^3} \tag{B.2}$$

$$P_c \propto \frac{M^2}{R^4} \tag{B.3}$$

We use the stelar structure equation of radiative energy transport and electron scattering ($\kappa \propto 1 + X$) for the star. After applying Equation B.2, we get Equation B.4.

$$\frac{T_c}{R} \propto \frac{\kappa \rho_c L}{R^2 T_c^3} \longrightarrow L \propto T_c^4 \frac{R^4}{M} \frac{1}{1+X}, \tag{B.4}$$

where T_c is the central temperature, L the luminosity of the star, and X the hydrogen fraction.

Finally, we use the energy generation of the star to get Equation B.5. Since the main energy generation for massive stars is through the CNO-cycle, we have $\nu \approx 18$.

$$\frac{L}{R} \propto R^2 \rho_c^2 T_c^\nu \longrightarrow L \propto \frac{M^2}{R^3} T_c^{18} \tag{B.5}$$

B.1 Gas pressure dominated

At the low end of massive stars, the star is dominated by gas pressure and the equation of state follows the ideal gas law, where μ is the mean molecular weight in the star.

$$P_c \propto \frac{\rho_c T_c}{\mu} \longrightarrow T_c \propto \mu \frac{M}{R} \tag{B.6}$$

This allows us to transform Equations B.4 into

$$L \propto \frac{\mu^4}{1+X} M^3 \tag{B.7}$$

And combine it with B.5 to get:

$$L \propto \mu^{18} \frac{M^{20}}{R^{21}} \longrightarrow \frac{\mu^4}{1+X} M^3 \propto \mu^{18} \frac{M^{20}}{R^{21}} \tag{B.8}$$

Eventually, we get the relation between radius and mass.

$$R \propto \mu^{18/21} (1+X) M^{17/21} \tag{B.9}$$

Combining Equations B.7, B.8, B.9 with Equation B.1, we find that for the ideal gas equation of state, the thermal timescale scales as follows:

$$\tau_{\mathrm{KH}} \propto \frac{M^2}{M^{17/21} M^3} \propto M^{-38/21} \propto M^{-1.81} \tag{B.10}$$

B.2 Radiation pressure dominated

At higher masses, radiation pressure plays an essential role in supporting the star. Thus, the ideal gas equation of state is no longer valid. While the actual dynamics will be a combination of radiation and gas pressure, we can look at the extreme example with only radiation pressure. Instead of Equation B.6, we get the following relation for the

central temperature

$$P_c \propto T_c^4 \longrightarrow T_c^4 \propto \frac{M^2}{R^4} \tag{B.11}$$

This gives us the following equations for the luminosity and radius.

$$L \propto \frac{1}{1+X} M \tag{B.12}$$

$$L \propto \frac{M^{10}}{R^{21}} \longrightarrow \frac{M}{1+X} \propto \frac{M^{10}}{R^{21}} \longrightarrow R \propto M^{10/21} \tag{B.13}$$

Using them we find the relation between the thermal timescale and mass in radiation pressure only regime.

$$\tau_{\mathrm{KH}} \propto M^{11/21} \propto M^{0.52} \tag{B.14}$$

B.3 Relations within the BPASS models

The previous two sections cover two extreme cases. In reality, both the gas and radiation pressure contribute to the total internal pressure in the star. However, the difference in thermal timescale dependence on the mass is significant and means that at higher masses, where radiation pressure dominates, the thermal timescale becomes constant with mass.

To verify this, we plot the thermal timescale at ZAMS of all BPASS single star models in Figure B.1. At sub-solar metallicity, where BBH mergers are though to originate from (Belczynski et al. 2010; Stevenson et al. 2017, 2019; Santoliquido et al. 2021), the thermal timescale becomes close to constant for high masses. Thus, if mass is lost on a thermal timescale, most of it can be accreted by the companion, because the timescales are similar. At higher metallicities, the timescales no longer become constant, which is most likely due to the change in the opacity of the star.

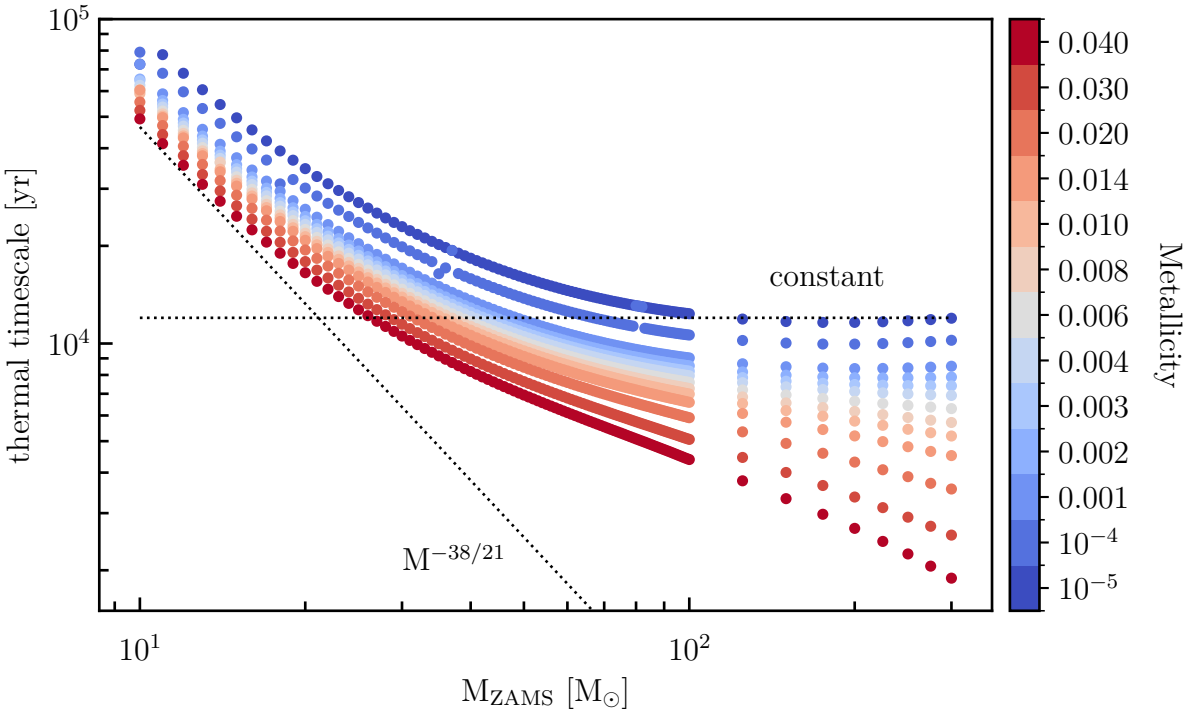

Figure B.1: The thermal timescale at ZAMS of all BPASS SINGLE-STAR MODELS per metallicity. The dashed lines indicate a $\tau_{KH} \propto M^{-38/21}$ relation and the thermal timescale being constant.

Appendix C

BBH Mass Distribution Uncertainties

BPASS is based on a limited number of stellar models (250.000), and one concern could be the number of models contributing to the $M_{1,BH}$ distribution. To this end, we calculate the number of models after the natal kick (465.047) contributing to each bin in the $M_{1,BH}$ distribution and calculate the Poisson error for each bin. The number of models after the natal kick is larger due to sampling of the natal kick distribution. The resulting Poisson errors are insignificant and, except for the lowest mass bin, are unnoticeable when added to Figure 4.1.

Because the ZAMS mass grid at high masses is sparse in BPASS, we have selected a logarithmic binning for the $M_{1,BH}$ space to combine the systems in this regime. In Figure C.1, we show the $M_{1,BH}$ distribution with linear bins of a $2\,M_\odot$ width. As can be seen, the high-mass regime is sparsely populated, but the number of models contributing to each bin still results in insignificant errors. Furthermore, the $35\,M_\odot$ excess and a substructure at $20\,M_\odot$ are still present.

Instead of binning the BPASS output, we can apply a kernel density estimate (KDE) to the individual $M_{1,BH}$ merger samples. Using Scott's rule for bandwidth determination (Scott 1979), we get the solid black line in Figure 4.1. The KDE fluctuates significantly due to the undersampling of masses in the high-mass regime and small event rates. The $35\,M_\odot$ peak is wider and slightly higher, and the substructure at $20\,M_\odot$ is clearly visible. This indicates that these features are part of the distribution and not a binning artefact. Furthermore, we perform 1000 resamplings of the data by redrawing the same number of models as the original $M_{1,BH}$ distribution, with each model weighted equally. We run the new populations through the KDE, which shows as the thick solid black line in Figure C.1. Although some statistical uncertainty is present, it does not significantly impact the $M_{1,BH}$ distribution or its features.

The features in the $M_{1,BH}$ distribution remain when changing bins and applying a kernel density estimation. While the high $M_{1,BH}$ range is undersampled, sufficient models contribute to each mass for the statistical error to be negligible. Of course, this does not

take into account uncertainty based on the implemented physics.

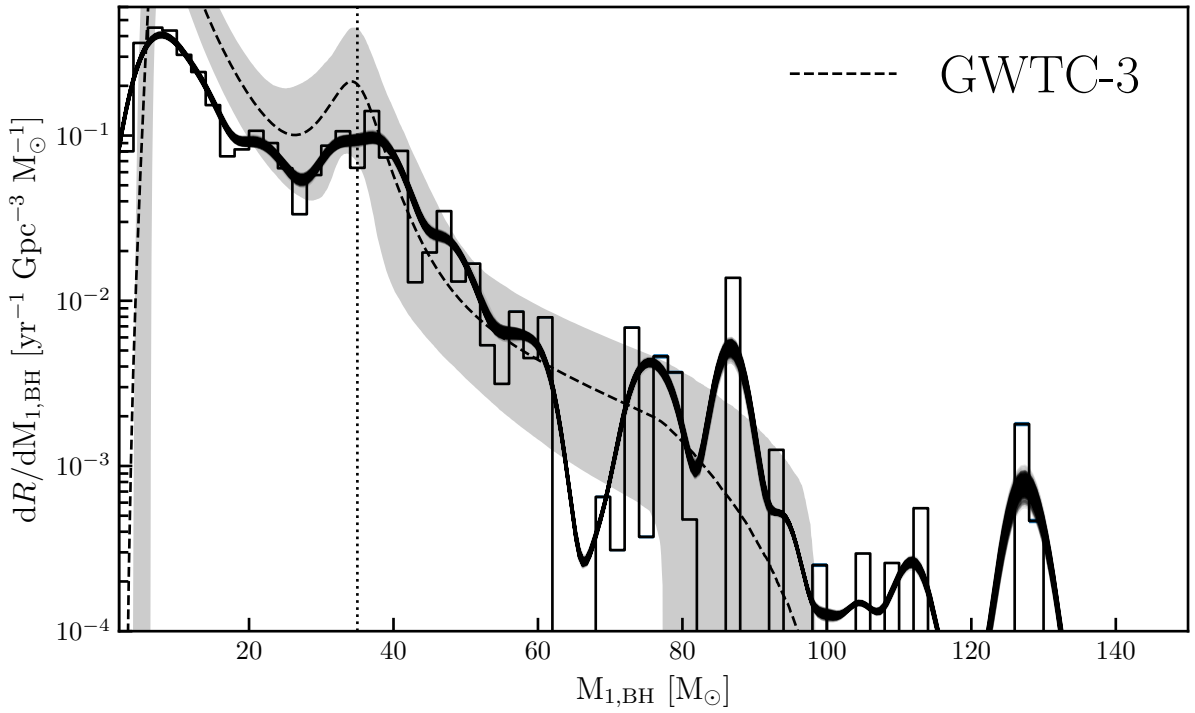

Figure C.1: The $M_{1,BH}$ distribution using linear bins with a width of $2\,M_\odot$. The vertical dotted line indicates $35\,M_\odot$, and the dashed line with the grey area is the GWTC-3 intrinsic population and the 95 per cent confidence interval using their PP model (Abbott et al. 2023). The thick black line is kernel density estimates from 1000 resampled populations.

Appendix D

BPASS Alterations

Within this work, we have altered sections of the code compared to the standard BPASS outputs. These include the SN determination, GW mergertime calculation, PPISN inclusion, and PISN alteration. Moreover, several aspects of the BPASS code are slightly different than described in previous works or undescribed. In this section, we describe what is different than previously thought and how it is adapted.

As described in Section 2.1.1 the mass transfer rate in BPASS STARS is defined as

$$\dot{\mathrm{M}} = 3 \times 10^{-6} \mathrm{max}(\mathrm{M_d}, 5\,\mathrm{M_\odot})^2 \ln(R_\mathrm{d}/R_\mathrm{RL})^3, \tag{D.1}$$

where $\mathrm{M_d}$ and R_d are the mass and radius of the donor star, respectively, and R_RL is the Roche lobe radius of the donor in the binary, as described by the Eggleton approximation (Eggleton 1983). This definition differs from Eldridge et al. (2017) and (Hurley et al. 2002) and causes additional mass loss at low mass systems, as described in Section 5.1.

Furthermore, a common envelope is initiated when R_d expands pasts its Roche lobe and the companion does not accrete material when CEE takes place nor does it lose mass due to stellar winds. δM is calculated based on the Roche lobe overflow amount and follows Equation 2.1 and is limited to 0.1 $\mathrm{M_\odot/yr}$. The material is removed like a stellar winds and carries away angular momentum from the orbit using the following equation:

$$\delta J \approx J \times \frac{\delta M}{M_1 + M_2}$$

Essential to mention is that the normalisation of the angular momentum loss after a CE has occured changed by a factor 1/1.9891 compared to before the CE. This is a code bug and can result more angular momentum loss, as discussed in Section 6.4.

The CE prescription is ended when R_d shrinks back into its Roche lobe. However, because the mass loss rate still follows equation 2.1 the mass transfer prescription still holds. On the other hand, the material is no longer accreted by the companion, which could play an important role in widening the orbit (Hirai & Mandel 2022).

D.1 Supernova Determination

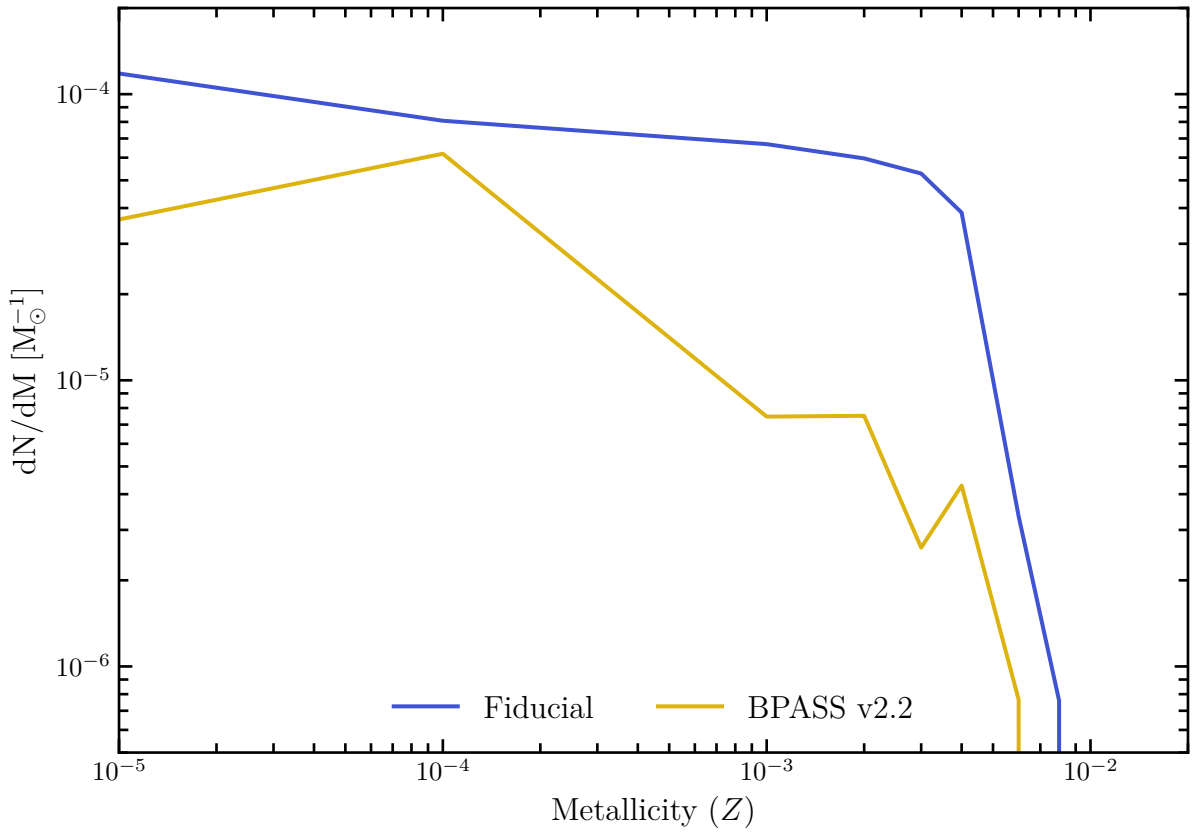

Figure D.1: The BPASS v2.2 (yellow) and this work (blue) PISN tagging as the metallicity bias function.

In BPASS v2.2., the core-collapse supernova determination includes selection criteria based on the presence of the ONe core. Since some BPASS models do not reach this point, we have slightly altered the selection criteria to account for this. Moreover, this selection criterion was also present for the PISN determination. Figure D.1 shows the metallicity bias functions of the original and new PISN determinations. Table D.1 shows how the SN determinations have changed compared to BPASS v2.2.

v2.2.	This work
CCSN	
$M_1 > 1.5\,M_\odot$	$M_1 > 1.5\,M_\odot$
$M_{CO} > 1.38\,M_\odot$	$M_{CO} > 1.38\,M_\odot$
$M_{ONe} > 0.1\,M_\odot$	if $M_{CO} < 3\,M_\odot$, then $M_{ONe} > 0\,M_\odot$
PISN	
CCSN criteria	$M_{CO} \geq 60\,M_\odot$
$M_{He} > 64\,M_\odot$	$M_{He} < 133\,M_\odot$
$M_{He} < 133\,M_\odot$	
Single Degenerate Type Ia	
age $\leq 10^{11}$yr	
$M_{2,initial} \leq 1.2\,M_\odot$	$M_{2,initial} \leq 1.08\,M_\odot$
$M_{2,initial} \geq 0.1\,M_\odot$	$M_{2,initial} \geq 0.1\,M_\odot$
$M_2 \geq 1.4\,M_\odot$	$M_2 \geq 1.4\,M_\odot$
Double Degenerate Type Ia	
$M_{1,rem} \leq 300\,M_\odot$	age > 0 yr
$M_2 < 300\,M_\odot$	
$M_2 \geq 0.1\,M_\odot$	
$M_{CO} <= 1.38\,M_\odot$	$M_{CO} <= 1.38\,M_\odot$
$M_1 \leq 1.5\,M_\odot$	$M_1 \leq 1.5\,M_\odot$
$M_2 < 1.3\,M_\odot$	$M_2 < 1.4\,M_\odot$
	$M_{He} > 0\,M_\odot$
	Standard Type Ia
	$0.6\,M_\odot \leq M_1 \leq 1.08\,M_\odot$
	$0.6\,M_\odot \leq M_2 \leq 1.08\,M_\odot$
	sub-luminous Type Ia
	$M_1 < 0.6\,M_\odot$ with $0.6\,M_\odot \leq M_2 \leq 1.08\,M_\odot$
	$M_2 < 0.6\,M_\odot$ with $0.6\,M_\odot \leq M_1 \leq 1.08\,M_\odot$
	Accretion induced collapse
	$M_1 > 1.08\,M_\odot$ with $M_2 \leq 1.08\,M_\odot$
	$M_2 > 1.08\,M_\odot$ with $M_1 \leq 1.08\,M_\odot$

Table D.1: Changes in the supernova determination in this work compared to the BPASS v2.2 determination.

Appendix E

Nature of the Envelope

During mass transfer the radiative or convective nature of the envelope of the donor star can influence how the interaction progresses. Generally, a convective envelope star expands, while a star with a radiative envelope shrinks as a response to mass loss.

Because of the large grid of detailed stellar models required for population synthesis, we can determine the nature of the envelope of single stars over a large range of initial masses and metallicities using our adapted BPASS version of the Cambridge STARS code. This can be useful in determining the stability of mass transfer in binary interactions and comparison against other other work.

The BPASS STARS code only provides the mass coordinates of convective boundaries, but not which regions are convective or radiative. We determine this using the semi-convective boundaries, which are included in the mass coordinates. We do have to assume that the core of the star is convective at the start of the model. In the mass regime considered here ($M_{ZAMS} > 10\,M_{\odot}$), this is reasonable, but does not necessarily hold at smaller masses (Eldridge & Tout 2019).

We define a convective envelope if a star has a convective region that is at most $0.1\,M_{\odot}$ below the surface of the star and is at least $1\,M_{\odot}$ deep. Our automatic tagging is not guaranteed to work in all situations due changes in the convective boundaries array that are numerical and not physical. Thus, we check every model to determine if the tagging of the convective envelope was successful. While most models are tagged successfully, if the tagging fails, we adjust the convective regions manually. Because the tagging does not work well in later stages of the evolution, we only look at the envelope structure until the end of core Helium burning. We define the end of core Helium burning, when the location of the convective core during core-Helium burning moves above $0.1\,M_{\odot}$. For models that did not reach this, we use the age of the closest model as the end of core Helium burning.

Figure E shows the nature of the envelope over initial masses at $Z = 0.00001$ till the end of core helium burning. Red areas indicate a convective envelope, while blue

indicates a radiative envelope. Models that do not reach the end of core helium burning are indicated with a black cross and the final time of the previous (lower mass) star is used to approximate its end point. The end of the ZAMS is indicated by the dashed line and is found by looking at when the helium luminosity starts to increase. Because we are limited by the indicator available in STARS, the end of core Hydrogen and Helium burning might not be the actual moment this occurs, but should be similar.

On the Main-Sequence all stars in this mass regime are radiative. Beyond the main-sequence the nature of the envelope depend on the initial mass and metallicity of the star. At $Z = 0.0001$ below $M_{ZAMS} \leq 21\,M_\odot$, the star remains radiative. Above this limit, the star becomes convective during the core helium burning phase and more massive stars become convective earlier in the phase.

As metallicity increases (see additional Figures), the low mass stars do become convective after entering the core-helium burning phase. At the same time, higher mass stars become radiative during core helium burning after a short phase of convection after the end of the MS. Eventually, stars below $26\,M_\odot$ are mostly convective during core-helium burning, while higher mass stars are radiative, agreeing with results found by Klencki et al. (2021). Indicating that interactions during this phase are more stable than estimated by rapid population synthesis codes. With a shorter period of convection as the ZAMS mass increases until it eventually disappears in the high mass regime. This is most likely a result of strong winds stripping most of the star and no convective envelope forming.

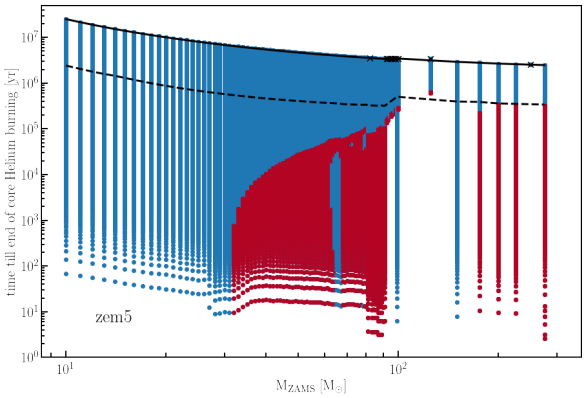

Figure E.1: The radiative (blue) or convective (red) nature of the envelope from a single star over different ZAMS masses up to the end of core helium burning at $Z = 10^{-5}$. The end of the main-sequence is indicated (black dashed) and so are models that did not converge (black crosses).

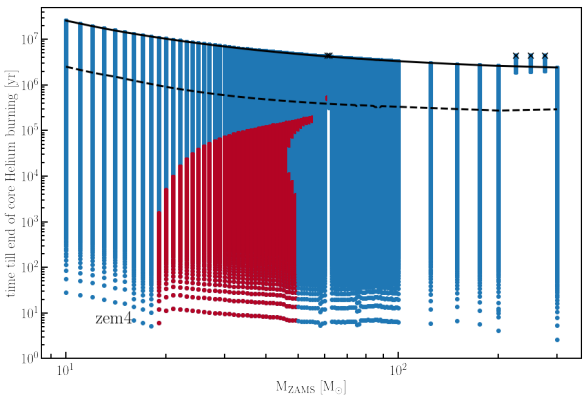

Figure E.2: $Z = 0.0001$.

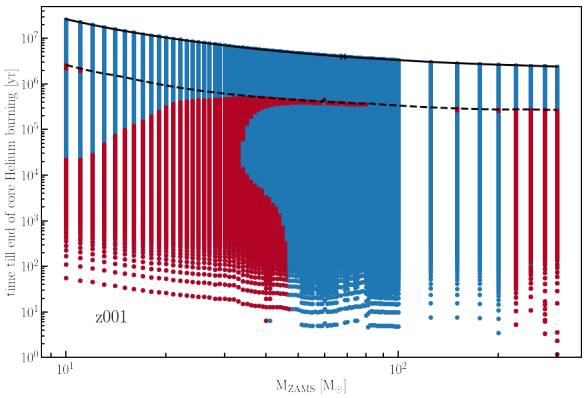

Figure E.3: $Z = 0.001$.

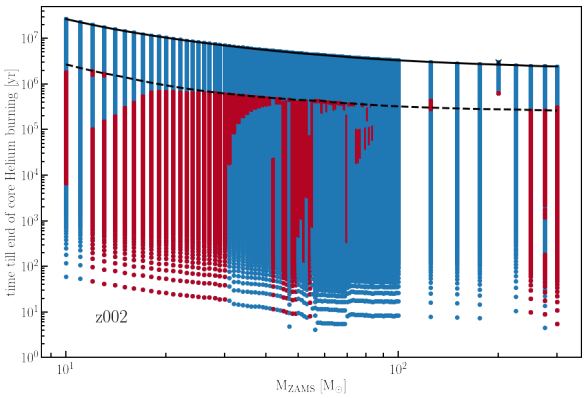

Figure E.4: $Z = 0.002$.

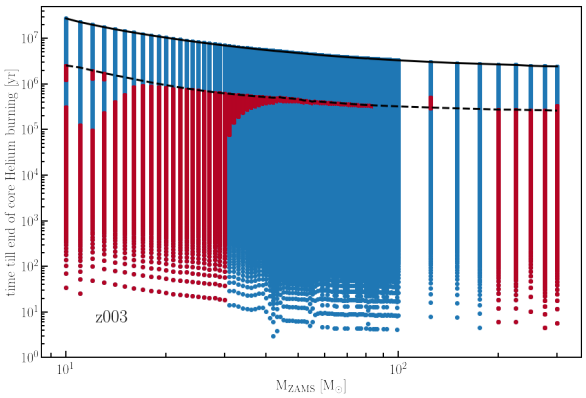

Figure E.5: $Z = 0.003$.

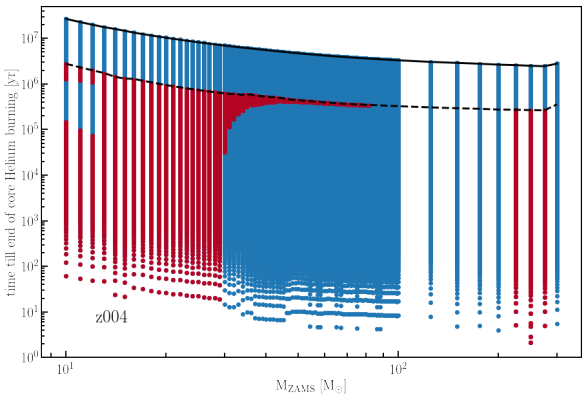

Figure E.6: $Z = 0.004$.

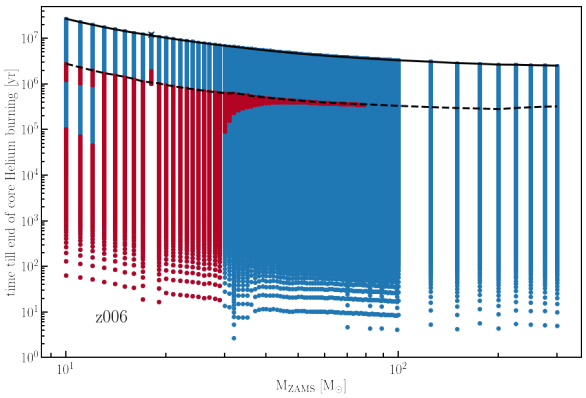

Figure E.7: $Z = 0.006$.

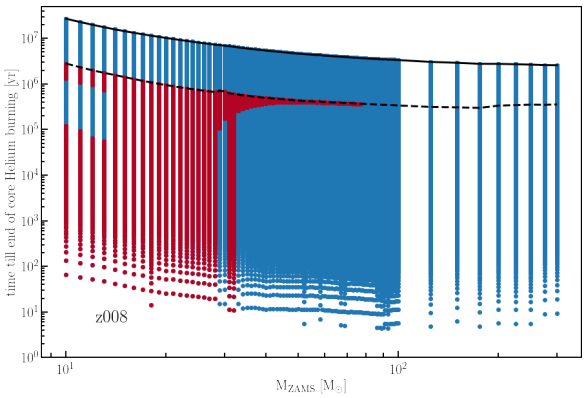

Figure E.8: $Z = 0.008$.

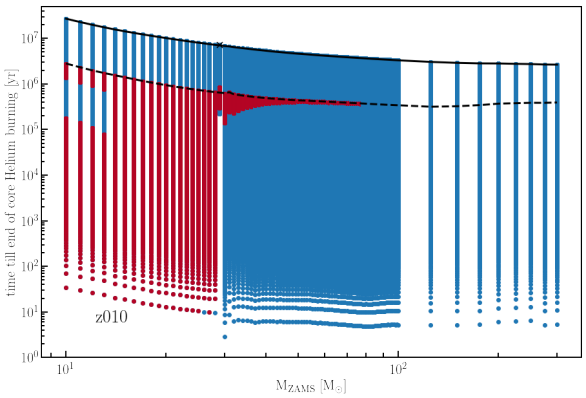

Figure E.9: $Z = 0.01$.

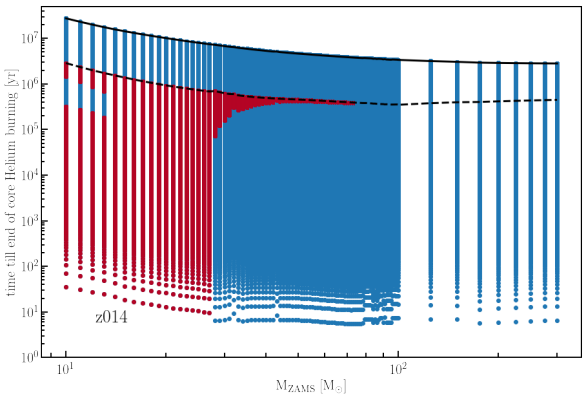

Figure E.10: $Z = 0.014$.

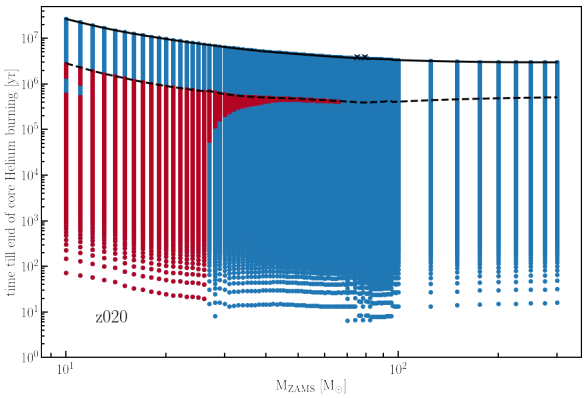

Figure E.11: $Z = 0.02$

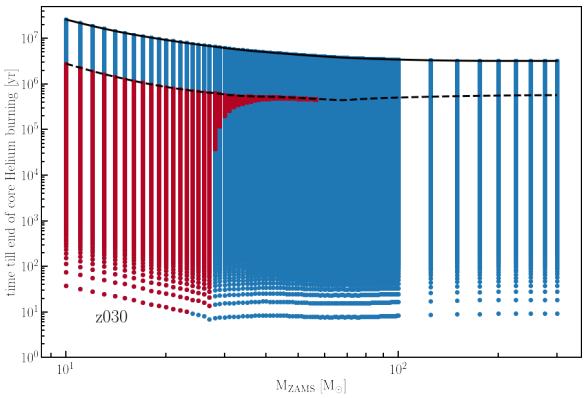

Figure E.12: $Z = 0.03$.

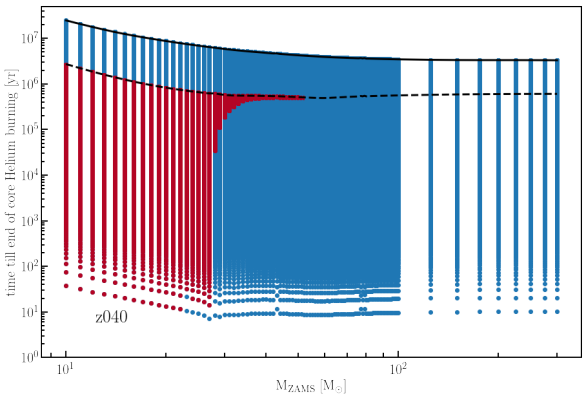

Figure E.13: $Z = 0.04$.

Appendix F

Observational Data

Throughout this work, we have used observational data to compare our predictions against. These tables contain the values and sources of these observations.

Redshift	**Rate**	**Uncertainty**		**Reference**
		$[10^5\ h^3\ \mathrm{yr}^{-1}\ \mathrm{Gpc}^{-3}]$		
0	0.77	-0.10 (-0.13)	0.10 (0.13)	Li et al. (2011b)
0.01	0.82	-0.26 (N.A.)	0.26 (N.A.)	Cappellaro et al. (1999)
0.03	0.82	-0.32 (N.A.)	0.32 (N.A.)	Mannucci et al. (2005)
0.025-0.050	0.81	-0.24 (N.A.)	0.33 (0.04)	Dilday et al. (2010)
0.073	0.71	-0.08 (-0.06)	0.08 (0.10)	Frohmaier et al. (2019)
0.05-0.15	1.60	-0.85 (-0.58)	1.46 (0.58)	Cappellaro et al. (2015)
0.075-0.125	0.76	-0.13 (0.00)	0.15 (0.08)	Dilday et al. (2010)
0.11	1.08	-0.29 (N.A.)	0.29 (N.A.)	Strolger (2003)
0.11	0.72	-0.18 (-0.09)	0.08 (0.05)	Graur & Maoz (2013)
0.13	0.58	-0.20 (-0.15)	0.20 (0.15)	Blanc et al. (2004)
0.15	0.93	-0.67 (-0.17)	0.67 (0.67)	Rodney & Tonry (2010)
0.125-0.175	0.90	-0.10 (-0.01)	0.11 (0.10)	Dilday et al. (2010)
0.16	0.41	-0.26 (-0.35)	0.26 (0.17)	Perrett et al. (2012)
0.175-0.225	1.01	-0.09 (-0.02)	0.09 (0.24)	Dilday et al. (2010)
0.2	0.58	-0.23 (N.A.)	0.23 (N.A.)	Horesh et al. (2008)
0.25	1.05	-0.76 (-1.02)	1.75 (0.35)	Rodney et al. (2014)
0.15-0.35	1.14	-0.35 (-0.29)	0.38 (0.29)	Cappellaro et al. (2015)
0.225-0.275	1.06	-0.08 (-0.03)	0.09 (0.53)	Dilday et al. (2010)
0.26	0.82	-0.20 (-0.20)	0.20 (0.17)	Perrett et al. (2012)
0.3	0.99	-0.44 (N.A.)	0.47 (N.A.)	Botticella et al. (2008)
0.275-0.325	1.27	-0.10 (-0.05)	0.11 (1.15)	Dilday et al. (2010)

0.35	0.99	-0.55 (-0.09)	0.55 (0.55)	Rodney & Tonry (2010)
0.35	1.05	-0.17 (-0.17)	0.17 (0.15)	Perrett et al. (2012)
0.42	1.34	-0.93 (-0.38)	1.22 (0.29)	Graur et al. (2014)
0.44	0.76	-0.39 (-0.35)	0.67 (0.17)	Okumura et al. (2014)
0.45	0.90	-0.44 (-0.12)	0.44 (0.44)	Rodney & Tonry (2010)
0.45	1.05	-0.17 (-0.15)	0.17 (0.12)	Perrett et al. (2012)
0.35-0.55	1.52	-0.38 (-0.47)	0.32 (0.47)	Cappellaro et al. (2015)
0.46	1.40	-0.50 (N.A.)	0.50 (N.A.)	Tonry et al. (2003)
0.47	1.22	-0.17 (-0.26)	0.17 (0.38)	Neill et al. (2006)
0.47	2.33	-0.79 (-0.76)	1.08 (4.84)	Dahlen et al. (2008)
0.55	0.93	-0.41 (-0.20)	0.41 (0.41)	Rodney & Tonry (2010)
0.55	1.40	-0.17 (-0.15)	0.17 (0.12)	Perrett et al. (2012)
0.55	1.52	-0.26 (N.A.)	0.29 (N.A.)	Pain et al. (2002)
0.62	3.76	-1.66 (-0.82)	2.57 (0.79)	Melinder et al. (2012)
0.65	1.40	-0.15 (-0.17)	0.15 (0.12)	Perrett et al. (2012)
0.55-0.75	2.01	-0.52 (-0.79)	0.55 (0.79)	Cappellaro et al. (2015)
0.65	1.43	-0.50 (-0.23)	0.50 (0.50)	Rodney & Tonry (2010)
0.74	2.30	-1.20 (N.A.)	0.96 (N.A.)	Graur et al. (2011)
0.75	1.49	-0.55 (-0.55)	0.79 (0.67)	Rodney et al. (2014)
0.75	1.98	-0.61 (-0.41)	0.61 (0.61)	Rodney & Tonry (2010)
0.75	1.69	-0.17 (-0.20)	0.17 (0.15)	Perrett et al. (2012)
0.8	2.45	-0.54 (-0.35)	0.67 (0.17)	Okumura et al. (2014)
0.83	3.79	-0.79 (-1.49)	0.96 (2.13)	Dahlen et al. (2008)
0.85	2.27	-0.64 (-0.47)	0.64 (0.64)	Rodney & Tonry (2010)
0.85	1.66	-0.15 (-0.20)	0.15 (0.17)	Perrett et al. (2012)
0.94	1.31	-0.55 (-0.17)	0.64 (0.38)	Graur et al. (2014)
0.95	2.22	-0.73 (-0.76)	0.73 (0.73)	Rodney & Tonry (2010)
0.95	2.24	-0.23 (-0.35)	0.23 (0.29)	Perrett et al. (2012)
1.05	2.30	-0.82 (-1.20)	0.82 (0.82)	Rodney & Tonry (2010)
1.1	2.16	-0.35 (-0.38)	0.35 (0.29)	Perrett et al. (2012)
1.14	2.06	-0.53 (-0.30)	0.70 (0.30)	Okumura et al. (2014)
1.21	3.85	-0.85 (-0.93)	1.05 (1.11)	Dahlen et al. (2008)
1.23	2.45	-0.82 (N.A.)	0.73 (N.A.)	Graur et al. (2011)
1.25	1.87	-0.64 (-0.67)	0.90 (0.99)	Rodney et al. (2014)
1.59	1.31	-0.64 (-0.26)	0.99 (0.15)	Graur et al. (2014)

1.61	1.22	-0.67 (-0.41)	1.14 (0.55)	Dahlen et al. (2008)
1.69	2.97	-1.08 (N.A.)	1.57 (N.A.)	Graur et al. (2011)
1.75	2.10	-0.87 (-0.82)	1.31 (1.46)	Rodney et al. (2014)
2.25	1.43	-1.11 (-0.70)	2.77 (1.31)	Rodney et al. (2014)

Table F.1: The observations used for Type Ia comparison. Adapted from Strolger et al. (2020) with additional observations from Melinder et al. (2012) and Li et al. (2011b), redshift ranges if available, and updated rates for Madgwick et al. (2003) from from Graur & Maoz (2013). Uncertainty is split between the statistic and systematic uncertainty. If the separate numbers are available, the latter is in between brackets

Redshift	**Rate**	**Uncertainty**		**Reference**
	$[h^3\ \mathrm{yr}^{-1}\ \mathrm{Gpc}^{-3}]$			
0.17	102	-38	73	Frohmaier et al. (2021)
0.17	89	-73	215	Quimby et al. (2013)
0-1.6	117	N.A.	N.A.	Zhao et al. (2021)
1.13	265	-105	222	Prajs et al. (2017)
2.0-4.0	1118	-559	559	Cooke et al. (2012)
2.5-3.5	1166	-1166	1166	Moriya et al. (2019)

Table F.2: The observed SLSN Type I rates from literature with the combined statistical and systematic uncertainties are given. Adapted from Frohmaier et al. (2021).

Redshift	**Rate**	**Uncertainty**		**Reference**
	$[10^5\ h^3\ \mathrm{yr}^{-1}\ \mathrm{Gpc}^{-3}]$			
0	1.15	-0.36 (N.A.)	0.36 (N.A.)	Li et al. (2011b)
0.15-0.35	2.01	-0.52 (-0.70)	0.47 (0.70)	Cappellaro et al. (2015)

Table F.3: The observed Type II rates from literature. Uncertainty is split between the statistic and systematic uncertainty. If the separate numbers are available, the latter is in between brackets.

Redshift	**Rate**	**Uncertainty** $[10^5\ h^3\ \mathrm{yr}^{-1}\ \mathrm{Gpc}^{-3}]$		**Reference**
0	1.81	-0.20 (-0.44)	0.20 (0.50)	Li et al. (2011b)
0.01	1.25	-0.50 (N.A.)	0.50 (N.A.)	Cappellaro et al. (1999)
0.028	2.65	-0.37 (N.A.)	0.45 (N.A.)	Frohmaier et al. (2021)
0.03-0.09	3.09	-0.32 (-0.44)	0.32 (0.44)	Taylor et al. (2014)
0.05-0.15	3.29	-1.55 (-1.43)	1.81 (1.43)	Cappellaro et al. (2015)
0.075	3.03	-0.76 (-0.32)	0.96 (0.12)	Graur et al. (2015)
0.1-0.5	8.75	-2.74 (-1.66)	3.73 (3.03)	Dahlen et al. (2012)
0.1-0.5	6.21	-1.57 (N.A.)	2.33 (N.A.)	Strolger et al. (2015)
0.1-0.5	9.59	-5.19 (-4.23)	8.98 (5.77)	Melinder et al. (2012)
0.15-0.35	3.53	-0.79 (-1.37)	0.79 (1.37)	Cappellaro et al. (2015)
0.21	3.35	-0.99 (-1.05)	1.25 (1.22)	Botticella et al. (2008)
0.26	6.41	-2.04 (N.A.)	2.33 (N.A.)	Cappellaro et al. (2005)
0.3	4.14	-0.87 (-0.70)	0.87 (-0.93)	Bazin et al. (2009)
0.4-0.9	8.16	-5.83 (N.A.)	13.12 (N.A.)	Petrushevska et al. (2016)
0.5-0.9	10.73	-2.10 (N.A.)	2.80 (N.A.)	Strolger et al. (2015)
0.5-0.9	21.55	-4.43 (-4.66)	5.42 (9.33)	Dahlen et al. (2012)
0.5-0.9	18.66	-9.10 (-6.15)	15.45 (10.64)	Melinder et al. (2012)
0.5-1.0	20.12	-15.74 (N.A.)	28.86 (N.A.)	Graur et al. (2011)
0.9-1.3	8.95	-1.92 (N.A.)	3.09 (N.A.)	Strolger et al. (2015)
0.9-1.3	27.90	-8.16 (-8.16)	10.96 (14.46)	Dahlen et al. (2012)
0.9-1.4	30.03	-17.78 (N.A.)	33.53 (N.A.)	Petrushevska et al. (2016)
1.3-1.7	9.48	-3.85 (N.A.)	5.92 (N.A.)	Strolger et al. (2015)
1.4-1.0	31.49	-25.95 (N.A.)	71.14 (N.A.)	Petrushevska et al. (2016)
1.7-2.1	9.21	-5.16 (N.A.)	9.83 (N.A.)	Strolger et al. (2015)
2.1-2.5	17.99	-10.26 (N.A.)	19.71 (N.A.)	Strolger et al. (2015)

Table F.4: The observed CCSN rates from literature. Uncertainty is split between the statistic and systematic uncertainty. If the separate numbers are available, the latter is in between brackets.

Bibliography

Abbott B. P., et al., 2016, Phys. Rev. Lett., 116, 061102

Abbott B. P., et al., 2017a, Phys. Rev. Lett., 119, 161101

Abbott B. P., et al., 2017b, ApJ, 848, L12

Abbott B. P., et al., 2017c, ApJ, 848, L13

Abbott R., et al., 2020a, Phys. Rev. Lett., 125, 101102

Abbott B. P., et al., 2020b, ApJ, 892, L3

Abbott R., et al., 2021a, Phys. Rev. X, 11

Abbott R., et al., 2021b, ApJ, 913, L7

Abbott R., et al., 2021c, ApJ, 915, L5

Abbott R., et al., 2023, Phys. Rev. X, 13, 011048

Adams S. M., et al., 2017a, MNRAS, 468, 4968

Adams S. M., et al., 2017b, MNRAS, 469, 1445

Ade P. A. R., et al., 2015, A&A, 594, 63

Aghanim N., et al., 2020, A&A, 641, A6

Agrawal P., et al., 2022, MNRAS, 512, 5717

Aguilera-Dena D. R., et al., 2023, A&A, 671, A134

Ahmad Q. R., et al., 2002, Phys. Rev. Lett., 89

Amaro-Seoane P., et al., 2017, arXiv e-prints

Ambrosi E., et al., 2022, MNRAS, 509, 4694

Anand S., et al., 2021, Nature Astronomy, 5, 46

Andreoni I., et al., 2019, PASP, 131, 068004

Antoni A., Quataert E., 2023, arXiv, 2301.05237

Arca-Sedda M., et al., 2020, ApJ, 894, 133

Arca-Sedda M., et al., 2023, MNRAS, 520, 5259

Archinal B. A., Hynes S. J., 2003, Star Clusters. Willmann-Bell

Arnett W. D., 1980, ApJ, 237, 541

Artale M. C., et al., 2020, MNRAS, 491, 3419

Asplund M., et al., 2009, ARA&A, 47, 481

Asplund M., Amarsi A. M., Grevesse N., 2021, A&A, 653, A141

Babak S., et al., 2017, Physical Review D, 95, 103012

Badenes C., Maoz D., 2012, ApJ, 749, L11

Bahcall J. N., 1964, Phys. Rev. Lett., 12, 300

Bailyn C. D., et al., 1998, ApJ, 499, 367

Ball W. H., 2012, STARS

Ballone A., et al., 2023, MNRAS, 519, 5191

Banerjee S., 2022, A&A, 665, A20

Bardeen J. M., 1970, Nature, 226, 64

Barrett J. W., et al., 2018, MNRAS, 477, 4685

Basinger C. M., et al., 2021, MNRAS, 508, 1156

Batta A., Ramirez-Ruiz E., 2019, arXiv e-prints

Bavera S. S., et al., 2020, A&A, 635, A97

Bavera S. S., et al., 2021, A&A, 647, A153

Bazin G., et al., 2009, A&A, 499, 653

Begelman M. C., 1979, MNRAS, 187, 237

Begelman M. C., 2002, ApJ, 568, L97

Behroozi P. S., Wechsler R. H., Conroy C., 2013, ApJ, 770, 57

Belczynski K., et al., 2008, ApJS, 174, 223

Belczynski K., et al., 2010, ApJ, 715, L138

Belczynski K., et al., 2016, ApJ, 819, 108

Belczynski K., et al., 2018a, A&A, 615, A91

Belczynski K., et al., 2018b, arXiv, 2301.05237

Belczynski K., et al., 2022, ApJ, 925, 69

Belloni D., Schreiber M. R., 2023, Handbook of X-ray and Gamma-ray Astrophysics

Bethe H. A., 1939a, Phys. Rev., 55, 434

Bethe H. A., 1939b, Phys. Rev., 55, 103

Bethe H. A., Marshak R. E., 1939, Reports on Progress in Physics, 6, 1

Bhattacharya D., van den Heuvel E. P. J., 1991, Phys. Rep., 203, 1

Biscoveanu S., Landry P., Vitale S., 2023, MNRAS, 518, 5298

Blaauw A., 1961, Bulletin of the Astronomical Institutes of the Netherlands, 15, 265

Blanc G., et al., 2004, A&A, 423, 881

Bobrick A., Davies M. B., Church R. P., 2017, MNRAS, 467, 3556

Bodensteiner J., Shenar T., Sana H., 2020, A&A, 641, A42

Botticella M. T., et al., 2008, A&A, 479, 49

Bouffanais Y., et al., 2021, MNRAS, 507, 5224

Branch D., Wheeler J. C., 2017, in Branch D., Wheeler J. C., eds, Astronomy and Astrophysics Library, Supernova Explosions. Springer, Berlin, Heidelberg, pp 245–265, doi:10.1007/978-3-662-55054-0_12

Bray J. C., Eldridge J. J., 2016, MNRAS, 461, 3747

Breivik K., et al., 2020, ApJ, 898, 71

Briel M. M., et al., 2022, MNRAS

Briel M. M., Stevance H. F., Eldridge J. J., 2023, MNRAS, 520, 5724

Broekgaarden F. S., et al., 2021, MNRAS, 508, 5028

Broekgaarden F. S., et al., 2022a, MNRAS, 516, 5737

Broekgaarden F. S., Stevenson S., Thrane E., 2022b, ApJ, 938, 45

Brown G. E., 1995, ApJ, 440, 270

Brown J. M., et al., 2011, ApJ, 730, 67

Brown W. R., et al., 2022, ApJ, 933, 94

Budding E., 1989, Space Sci. Rev., 50, 205

Burrows A., Vartanyan D., 2021, Nature, 589, 29

Byrne R. A., Fraser M., 2022, MNRAS, 514, 1188

Callister T. A., Farr W. M., Renzo M., 2021, ApJ, 920, 157

Calzetti D., et al., 2000, ApJ, 533, 682

Cantiello M., et al., 2007, A&A, 465, L29

Cappellaro E., Evans R., Turatto M., 1999, A&A, 351, 459

Cappellaro E., et al., 2005, A&A, 430, 83

Cappellaro E., et al., 2015, A&A, 584, A62

Cassinelli J. P., 1979, ARA&A, 17, 275

Cehula J., Pejcha O., 2023, MNRAS, 524, 471

Chabrier G., 2003, PASP, 115, 763

Chabrier G., Baraffe I., 1997, A&A, 327, 1039

Chandrasekhar S., 1931, ApJ, 74, 81

Chen Y., Yu Q., Lu Y., 2020, ApJ, 897, 86

Chrimes A. A., Stanway E. R., Eldridge J. J., 2020, MNRAS, 491, 3479

Chruslinska M., et al., 2018, MNRAS, 474, 2937

Chruslinska M., Nelemans G., Belczynski K., 2019, MNRAS, 482, 5012

Chu Q., Yu S., Lu Y., 2022, MNRAS, 509, 1557

Conroy C., 2013, ARA&A, 51, 393

Cooke J., et al., 2012, Nature, 491, 228

Costa G., et al., 2022, MNRAS

Coughlin M. W., et al., 2020, MNRAS, 492, 863

Crain R. A., et al., 2015, MNRAS, 450, 1937

Croton D. J., et al., 2006, MNRAS, 365, 11

Cseh D., et al., 2014, MNRAS: Letters, 439, L1

Cucchiara A., et al., 2011, ApJ, 736, 7

Curti M., et al., 2023, MNRAS, 518, 425

Dabrowny M., Giacobbo N., Gerosa D., 2021, Rendiconti Lincei. Scienze Fisiche e Naturali, 32, 665

Dahlen T., Strolger L.-G., Riess A. G., 2008, ApJ, 681, 462

Dahlen T., et al., 2012, ApJ, 757, 70

Dalrymple G. B., 1991, The Age of the Earth. Stanford University Press, Stanford

Das S., et al., 2021, MNRAS, 507, 2777

Davis R., 1964, Phys. Rev. Lett., 12, 303

De Greve J. P., Linnell A. P., 1994, A&A, 291, 786

De Lucia G., Blaizot J., 2007, MNRAS, 375, 2

De S., et al., 2020, ApJ, 897, 130

Delfavero V., et al., 2023, arXiv, 2303.05436

Dessart L., et al., 2012a, MNRAS, 424, 2139

Dessart L., et al., 2012b, MNRAS: Letters, 426, L76

Dessart L., et al., 2013, MNRAS, 428, 3227

Dessart L., et al., 2020, A&A, 642, A106

Dewi J. D. M., Podsiadlowski Ph., Sena A., 2006, MNRAS, 368, 1742

Di Carlo U. N., et al., 2020, MNRAS, 498, 495

Di Stefano R., 2020, MNRAS, 493, 1855

Dilday B., et al., 2010, ApJ, 713, 1026

Disberg P., Nelemans G., 2023, arXiv, 2306.14332

Doherty C. L., et al., 2015, MNRAS, 446, 2599

Doherty C. L., et al., 2017, PASA, 34, e056

Dolag K., et al., 2009, MNRAS, 399, 497

Dominik M., et al., 2012, ApJ, 759, 52

Dominik M., et al., 2013, ApJ, 779, 72

Dorozsmai A., Toonen S., 2022, arXiv, 2207.08837

Drozda P., et al., 2022, A&A, 667, A126

Ebisawa K., et al., 2003, ApJ, 597, 780

Eddington A. S., 1917, The Observatory, 40, 290

Eggleton P. P., 1971, MNRAS, 151, 351

Eggleton P. P., 1983, ApJ, 268, 368

Eggleton P., 2011, Evolutionary Processes in Binary and Multiple Stars. Cambridge University Press, Cambridge, UK

Eggleton P. P., Tokovinin A. A., 2008, MNRAS, 389, 869

El-Badry K., et al., 2023a, MNRAS, 518, 1057

El-Badry K., et al., 2023b, MNRAS, 521, 4323

Eldridge J. J., 2005, PhD thesis, University of Cambridge, doi:10.48550/arXiv.astro-ph/0502046

Eldridge J. J., Stanway E. R., 2016, MNRAS, 3313, 3302

Eldridge J. J., Stanway E. R., 2022, ARA&A, 60, 455

Eldridge J. J., Tout C. A., 2004a, MNRAS, 348, 201

Eldridge J. J., Tout C. A., 2004b, MNRAS, 353, 87

Eldridge J. J., Tout C. A., 2019, The Structure and Evolution of Stars. World Scientific Publishing Co. Pte. Ltd, doi:10.1142/p974

Eldridge J. J., Izzard R. G., Tout C. A., 2008, MNRAS, 384, 1109

Eldridge J. J., Langer N., Tout C. A., 2011, MNRAS, 414, 3501

Eldridge J. J., et al., 2013, MNRAS, 436, 774

Eldridge J. J., et al., 2015, MNRAS, 446, 2689

Eldridge J. J., et al., 2017, PASA, 34, e058

Eldridge J. J., et al., 2018a, Research Notes of the AAS, 2, 236

Eldridge J. J., et al., 2018b, PASA, 35, e049

Eldridge J. J., Stanway E. R., Tang P. N., 2019, MNRAS, 482, 870

Evans M., et al., 2021, arXiv, 2109.09882

Fan Y.-Z., et al., 2023, arXiv e-prints

Farag E., et al., 2022, ApJ, 937, 112

Farah A., et al., 2022, ApJ, 931, 108

Farah A. M., et al., 2023, arXiv, 2301.00834

Farmer R., et al., 2019, ApJ, 887, 53

Farr W. M., et al., 2011, ApJ, 741, 103

Fattoyev F. J., et al., 2020, Phys. Rev. C, 102, 065805

Filippenko A. V., 1988, AJ, 96, 1941

Filippenko A. V., 1997, ARA&A, 35, 309

Filloux Ch., et al., 2011, International Journal of Modern Physics D, 20, 2399

Foglizzo T., et al., 2015, PASA, 32, e009

Foucart F., 2012, Phys. Rev. D, 86, 124007

Foucart F., Hinderer T., Nissanke S., 2018, Phys. Rev. D, 98, 081501

Fowler W. A., Hoyle F., 1964, ApJS, 9, 201

Fragione G., Loeb A., Rasio F. A., 2021, ApJ, 918, L38

Fragos T., et al., 2019, ApJ, 883, L45

Fragos T., et al., 2023, ApJS, 264, 45

Freundlich J., Maoz D., 2021, MNRAS, 502, 5882

Frohmaier C., et al., 2019, MNRAS, 486, 2308

Frohmaier C., et al., 2021, MNRAS, 500, 5142

Fryer C. L., Woosley S. E., Heger A., 2001, ApJ, 550, 372

Fryer C. L., et al., 2012, ApJ, 749, 91

Fryer C. L., et al., 2022a, ApJ, 929, 111

Fryer C. L., Olejak A., Belczynski K., 2022b, ApJ, 931, 94

Fuller J., Ma L., 2019, ApJ Letters, 881, L1

Gair J. R., et al., 2017,] 10.1088/1742-6596/840/1/012021, 840, 012021

Gal-Yam A., et al., 2009, Nature, 462, 624

Gallegos-Garcia M., et al., 2021, ApJ, 922, 110

Gallegos-Garcia M., et al., 2022a, App Letters, 938, L19

Gallegos-Garcia M., Berry C. P. L., Kalogera V., 2022b, arXiv, 2211.15693

Ge H., et al., 2010, ApJ, 717, 724

Ge H., et al., 2015, ApJ, 812, 40

Ge H., Webbink R. F., Han Z., 2020a, ApJS, 249, 9

Ge H., et al., 2020b, ApJ, 899, 132

Ge H., et al., 2022, ApJ, 933, 137

Gerke J. R., Kochanek C. S., Stanek K. Z., 2015, MNRAS, 450, 3289

Ghodla S., Eldridge J. J., 2023, MNRAS, 523, 1711

Ghodla S., et al., 2022, MNRAS, 511, 1201

Ghodla S., et al., 2023, MNRAS, 518, 860

Giacobbo N., Mapelli M., 2018, MNRAS, 480, 2011

Giacobbo N., Mapelli M., 2019, MNRAS, 486, 2494

Giacobbo N., Mapelli M., 2020, ApJ, 891, 141

Giacobbo N., Mapelli M., Spera M., 2018, MNRAS, 474, 2959

Goldstein D. A., et al., 2019, ApJ, 881, L7

Gomez S., et al., 2019, ApJ, 881, 87

Graur O., Maoz D., 2013, MNRAS, 430, 1746

Graur O., et al., 2011, MNRAS, 417, 916

Graur O., et al., 2014, ApJ, 783, 28

Graur O., Bianco F. B., Modjaz M., 2015, MNRAS, 450, 905

Grevesse N., Noels A., Sauval A. J., 1996, in Astronomical Society of the Pacific Conference Series. Astronomical Society of the Pacific, College Park, Maryland, p. 117

Grieco V., et al., 2012, MNRAS, 423, 3049

Gunn J. E., Ostriker J. P., 1970, ApJ, 160, 979

Hamers A. S., Thompson T. A., 2019, ApJ, 882, 24

Han Z., 1998, MNRAS, 296, 1019

Han Z., Podsiadlowski Ph., 2006, MNRAS, 368, 1095

Han Z., et al., 2001, in Evolution of Binary and Multiple Star Systems. ASP, p. 205

Heger A., Woosley S. E., 2002, ApJ, 567, 532

Heger A., et al., 2002, New Astron. Rev., 46, 463

Heger A., et al., 2003, ApJ, 591, 288

Helmholtz H., 1856, The London, Edinburgh, and Dublin Philosophical Magazine and Journal of Science, 11, 489

Hemler Z. S., et al., 2021, MNRAS, 506, 3024

Henyey L. G., Lelevier R., Levee R. D., 1959, ApJ, 129, 2

Hillebrandt W., et al., 2013, Frontiers of Physics, 8, 116

Hirai R., Mandel I., 2022, ApJ, 937, L42

Hjellming M. S., Webbink R. F., 1987, ApJ, 318, 794

Hobbs G., et al., 2005, MNRAS, 360, 974

Hogg D. W., 1999, arXiv, 9905116

Horesh A., et al., 2008, MNRAS, 389, 1871

Hosseinzadeh G., et al., 2019, ApJ, 880, L4

Howell D. A., 2011, Nature Communications, 2, 350

Howell D. A., 2017, Handbook of Supernovae, p. 431

Hoyle F., Fowler W. A., 1960, ApJ, 132, 565

Hurley J. R., Pols O. R., Tout C. A., 2000, MNRAS, 315, 543

Hurley J. R., Tout C. A., Pols O. R., 2002, MNRAS, 329, 897

Iaconi R., De Marco O., 2019, MNRAS, 490, 2550

Iben I. J., Livio M., 1993, PASP, 105, 1373

Iben Jr. I., Tutukov A. V., 1984, ApJS, 54, 335

Igoshev A. P., et al., 2021, MNRAS, 508, 3345

Inserra C., et al., 2013, ApJ, 770, 128

Iorio G., et al., 2023, MNRAS, 524, 426

Ivanova N., et al., 2013, The A&A Review, 21, 59

Izzard R. G., Jermyn A. S., 2023, MNRAS, 521, 35

Izzard R. G., et al., 2004, MNRAS, 350, 407

Jermyn A. S., et al., 2023, ApJS, 265, 15

Jha S. W., Maguire K., Sullivan M., 2019, Nature Astronomy, 3, 706

Johnson J. L., Sanderbeck P. R. U., 2022, ApJ, 934, 58

Johnson J. W., Kochanek C. S., Stanek K. Z., 2022, arXiv, 2210.01818

Jones S., Hirschi R., Nomoto K., 2014, ApJ, 797, 83

Jonker P. G., et al., 2021, ApJ, 921, 131

Joyce M., Tayar J., 2023, Galaxies, 11, 75

Kanas N., 2012, Star Maps. Springer, New York, NY, doi:10.1007/978-1-4614-0917-5

Kasen D., Bildsten L., 2010, ApJ, 717, 245

Kasen D., Woosley S. E., 2009, ApJ, 703, 2205

Kawai Y., Saio H., Nomoto K., 1987, ApJ, 315, 229

Kewley L. J., Ellison S. L., 2008, ApJ, 681, 1183

Khokhlov A. M., 1991, A&A, 245, 114

King A. R., Kolb U., 1999, MNRAS, 305, 654

Kippenhahn R., Weigert A., Weiss A., 2013, Stellar Structure and Evolution. Springer Berlin Heidelberg, Berlin, Heidelberg, doi:10.1007/978-3-642-30304-3

Klencki J., et al., 2018, A&A, 619, A77

Klencki J., et al., 2020, A&A, 638, A55

Klencki J., et al., 2021, A&A, 645, 27

Klencki J., et al., 2022, A&A, 662, A56

Kobayashi C., et al., 2023, ApJ, 943, L12

Kochanek C. S., 2014, ApJ, 785, 28

Kochanek C. S., 2015, MNRAS, 446, 1213

Kolb U., Ritter H., 1990, A&A, 236, 385

Kozyreva A., Blinnikov S., 2015, MNRAS, 454, 4357

Kozyreva A., et al., 2021, MNRAS, 503, 797

Kragh H., 2016, European Physical Journal H, 41

Kreidberg L., et al., 2012, ApJ, 757, 36

Kremer K., et al., 2017, ApJ, 846, 95

Kroupa P., 2001, MNRAS, 322, 231

Kroupa P., Tout C. A., Gilmore G., 1993, MNRAS, 262, 545

Kruckow M. U., et al., 2018, MNRAS, 481, 1908

Kumar S. S., 1963, ApJ, 137, 1121

Kwitter K. B., Henry R. B. C., 2022, PASP, 134, 022001

Lamberts A., et al., 2018, MNRAS, 480, 2704

Lamberts A., et al., 2019, 16, 1

Landau L. D., 1932, Phys. Zs. Sowjet, 1, 285

Langer N., 2012, ARA&A, 50, 107

Langer N., Norman C. A., 2006, ApJ, 638, L63

Laplace E., et al., 2020, A&A, 637, A6

Laplace E., et al., 2021, A&A, 656, A58

Lau M. Y. M., et al., 2022a, MNRAS, 512, 5462

Lau M. Y. M., et al., 2022b, MNRAS, 516, 4669

Leiner E. M., Geller A., 2021, ApJ, 908, 229

Lemson G., 2006, arXiv, 0608019

Lequeux J., 2013, Birth, Evolution and Death of Stars. World Scientific Publishing Co. Pte. Ltd, doi:10.1142/8820

Li W., et al., 2011a, MNRAS, 412, 1441

Li W., et al., 2011b, MNRAS, 412, 1473

Li Z., et al., 2023, A&A, 669, A82

Liotine C., et al., 2023, ApJ, 946, 4

Lipunov V. M., Postnov K. A., Prokhorov M. E., 1996, The Scenario Machine: Binary Star Population Synthesis. Harwood Academic Publishers, Amsterdam

Lipunov V. M., et al., 2009, Astronomy Reports, 53, 915

Liu J.-F., et al., 2013, Nature, 503, 500

Livne E., Arnett D., 1995, ApJ, 452, 62

Lucy L. B., 1991, ApJ, 383, 308

MacLeod M., Ostriker E. C., Stone J. M., 2018, ApJ, 868, 136

Madau P., Dickinson M., 2014, ARA&A, 52, 415

Madau P., Fragos T., 2017, ApJ, 840, 39

Madgwick D. S., et al., 2003, ApJ, 599, L33

Maeder A., 1987, A&A, 178, 159

Magg E., et al., 2022, A&A, 661, A140

Maggiore M., et al., 2020, Journal of Cosmology and Astroparticle Physics, 2020, 050

Mandel I., 2021, Research Notes of the AAS, 5, 223

Mandel I., Broekgaarden F. S., 2022, Living Reviews in Relativity, 25, 1

Mandel I., Farmer A., 2022, Phys. Rep., 955, 1

Mandel I., Müller B., 2020, MNRAS, 499, 3214

Mandel I., et al., 2020, MNRAS, 500, 1380

Mannucci F., et al., 2005, A&A, 433, 807

Maoz D., Graur O., 2017, ApJ, 848, 25

Maoz D., Mannucci F., 2012, PASA, 29, 447

Maoz D., Mannucci F., Nelemans G., 2014, ARA&A, 52, 107

Maoz D., Hallakoun N., Badenes C., 2018, MNRAS, 476, 2584

Mapelli M., Colpi M., Zampieri L., 2009, MNRAS, 395, L71

Mapelli M., et al., 2017, MNRAS, 472, 2422

Mapelli M., et al., 2019, MNRAS, 487, 2

Mapelli M., et al., 2021, MNRAS, 505, 339

Mapelli M., et al., 2022, MNRAS, 511, 5797

Marchant P., Moriya T. J., 2020, A&A, 640, L18

Marchant P., et al., 2016, A&A, 588, A50

Marchant P., et al., 2017, A&A, 604, A55

Marchant P., et al., 2019, ApJ, 882, 36

Marchant P., et al., 2021, A&A, 650, A107

Margalit B., Metzger B. D., 2017, ApJ, 850, L19

Marinacci F., et al., 2018, MNRAS, 480, 5113

Mattila S., et al., 2012, ApJ, 756, 111

McAlpine S., et al., 2016, Astronomy and Computing, 15, 72

McCrea W. H., 1964, MNRAS, 128, 147

McKee C. F., Ostriker E. C., 2007, ARA&A, 45, 565

Mehta A. K., et al., 2022, ApJ, 924, 39

Melinder J., et al., 2012, A&A, 545, A96

Mennekens N., Vanbeveren D., 2014, A&A, 564, A134

Mennekens N., Vanbeveren D., 2016, A&A, 589, A64

Mennekens N., et al., 2010, A&A, 515, A89

Menon A., et al., 2021, MNRAS, 507, 5013

Mestel L., 1952, MNRAS, 112, 583

Metha B., Cameron A. J., Trenti M., 2021, MNRAS, 504, 5992

Meynet G., Maeder A., 2007, A&A, 464, L11

Michaely E., 2021, MNRAS, 500, 5543

Miller-Jones J. C. A., et al., 2021, Science, 371, 1046

Minkowski R., 1941, PASP, 53, 224

Misra D., et al., 2020, A&A, 642, A174

Mitalas R., Sills K. R., 1992, ApJ, 401, 759

Miyaji S., et al., 1980, PASJ, 32, 303

Moe M., Di Stefano R., 2017, ApJS, 230, 15

Moe M., Kratter K. M., Badenes C., 2019, ApJ, 875, 61

Moriya T. J., et al., 2019, ApJS, 241, 16

Moriya T. J., et al., 2021, ApJ, 908, 249

Moriya T. J., et al., 2022a, A&A, 666, A157

Moriya T. J., Quimby R. M., Robertson B. E., 2022b, ApJ, 925, 211

Motch C., et al., 2014, Nature, 514, 198

Mould M., et al., 2022, MNRAS, 517, 2738

Naiman J. P., et al., 2018, MNRAS, 477, 1206

Negu S. H., Tessema S. B., 2015, International Journal of A&A, 05, 222

Neijssel C. J., et al., 2019, MNRAS, 490, 3740

Neill J. D., et al., 2006, AJ, 132, 1126

Nelemans G., et al., 2000, A&A, 360, 1011

Nelson C. A., Eggleton P. P., 2001, ApJ, 552, 664

Nelson D., et al., 2018, MNRAS, 475, 624

Nelson D., et al., 2019, Comput. Astrophys., 6, 2

Neustadt J. M. M., et al., 2021, MNRAS, 508, 516

Nomoto K., 1984, ApJ, 277, 791

Nomoto K., Iben Jr. I., 1985, ApJ, 297, 531

Nomoto K., Thielemann F. K., Yokoi K., 1984, ApJ, 286, 644

Nugis T., Lamers H. J. G. L. M., 2000, A&A, 360, 227

Ogawa T., et al., 2021, PASJ, 73, 701

Oh M., et al., 2023, arXiv

Okumura J. E., et al., 2014, PASJ, 66, 49

Olejak A., Belczynski K., 2021, ApJ, 921, L2

Olejak A., Belczynski K., Ivanova N., 2021, A&A, 651, 17

Orosz J. A., et al., 2007, Nature, 449, 872

Orosz J. A., et al., 2009, ApJ, 697, 573

Özel F., et al., 2010, ApJ, 725, 1918

Packet W., 1981, A&A, 102, 17

Paczynski B., 1976, in Structure and Evolution of Close Binary Systems. D. Reidel Publishing Co., Cambridge, England, p. 75

Paczyński B., Sienkiewicz R., 1972, Acta Astronomica, 22, 73

Pain R., et al., 2002, ApJ, 577, 120

Pakmor R., et al., 2010, Nature, 463, 61

Pakmor R., et al., 2012, ApJ, 747, L10

Palla F., 2002, Physics of Star Formation in Galaxies. No. 1999 in Saas-Fee Advanced Course 29 Lecture Notes, Springer, Berlin

Pankow C., et al., 2020, ApJ, 902, 71

Pannarale F., Tonita A., Rezzolla L., 2011, ApJ, 727, 95

Parsons S. G., et al., 2017, MNRAS, 471, 976

Passy J.-C., Herwig F., Paxton B., 2012, ApJ, 760, 90

Patton R. A., Sukhbold T., Eldridge J. J., 2022, MNRAS, 511, 903

Pauli D., et al., 2022, A&A, 667, A58

Pavlovskii K., Ivanova N., 2015, MNRAS, 449, 4415

Pavlovskii K., et al., 2017, MNRAS, 465, 2092

Paxton B., et al., 2011, ApJS, 192, 3

Paxton B., et al., 2013, ApJS, 208, 4

Paxton B., et al., 2015, ApJS, 220, 15

Paxton B., et al., 2018, ApJS, 234, 34

Paxton B., et al., 2019, ApJS, 243, 10

Peletier R., 2013, Stellar Populations. Secular Evolution of Galaxies, Cambridge University Press, Cambridge, UK

Perley D. A., et al., 2016a, ApJ, 817, 7

Perley D. A., et al., 2016b, ApJ, 817, 8

Perley D. A., et al., 2020, ApJ, 904, 35

Perrett K., et al., 2012, AJ, 144, 59

Pescalli A., et al., 2016, A&A, 587, A40

Peters P. C., 1964, Phys. Rev., 136, B1224

Petrovic J., Langer N., van der Hucht K. A., 2005, A&A, 435, 1013

Petrushevska T., et al., 2016, A&A, 594, A54

Phillips M. M., 1993, ApJ, 413, L105

Pillepich A., et al., 2018a, MNRAS, 473, 4077

Pillepich A., et al., 2018b, MNRAS, 475, 648

Podsiadlowski P., 2001, in Evolution of Binary and Multiple Star Systems; A Meeting in Celebration of Peter Eggleton's 60th Birthday. p. 239

Politano M., 2021, A&A, 648, L6

Pols O., 2011, Lecture Notes: Stellar Structure and Evolution. Astronomical Institute Utrecht, Utrecht

Pols O. R., et al., 1995, MNRAS, 274, 964

Popham R., Woosley S. E., Fryer C., 1999, ApJ, 518, 356

Popov D. V., 1993, ApJ, 414, 712

Portegies Zwart S. F., Verbunt F., 1996, A&A, 309, 179

Postnov K. A., Yungelson L. R., 2014, Living Reviews in Relativity, 17, 3

Prajs S., et al., 2017, MNRAS, 464, 3568

Punturo M., et al., 2010, Classical and Quantum Gravity, 27, 194002

Qin Y., et al., 2023, Astronomy & Astrophysics, 671, A62

Quimby R. M., et al., 2013, MNRAS, 431, 912

Rajamuthukumar A. S., et al., 2023, ApJ, 950, 9

Rakavy G., Shaviv G., 1967, ApJ, 148, 803

Ramsey C. J., et al., 2006, ApJ, 641, 241

Rasio F. A., 1995, ApJ, 444, L41

Rebassa-Mansergas A., et al., 2011, MNRAS, 413, 1121

Rebassa-Mansergas A., et al., 2017, MNRAS, 466, 1575

Renzo M., Götberg Y., 2021, ApJ, 923, 277

Renzo M., Zapartas E., 2020, Contributions of the Astronomical Observatory Skalnaté Pleso, 50, 472

Renzo M., et al., 2020a, MNRAS, 493, 4333

Renzo M., et al., 2020b, A&A, 640, A56

Renzo M., et al., 2020c, ApJ, 904, L13

Rhoades C. E., Ruffini R., 1974, Phys. Rev. Lett., 32, 324

Richards S. M., et al., 2023, MNRAS, 522, 3972

Rickard M. J., Pauli D., 2023, A&A, 674, A56

Riley J., et al., 2022, ApJS, 258, 34

Ritter A., 1898, ApJ, 8, 293

Rodney S. A., Tonry J. L., 2010, ApJ, 723, 47

Rodney S. A., et al., 2014, AJ, 148, 13

Rodriguez-Gomez V., et al., 2015, MNRAS, 449, 49

Rodriguez C. L., et al., 2016, ApJ, 832, L2

Rodriguez C. L., et al., 2019, Phys. Rev. D, 100, 043027

Romero-Shaw I., et al., 2023, MNRAS, 524, 245

Ruiter A. J., 2019, Proceedings of the International Astronomical Union, 15, 1

Ruiter A. J., Belczynski K., Fryer C. L., 2009, ApJ, 699, 2026

Ruiter A. J., et al., 2011, MNRAS, 417, 408

Ruszkowski M., Begelman M. C., 2003, ApJ, 586, 384

Sądowski A., Narayan R., 2016, MNRAS, 456, 3929

Saio H., Nomoto K., 1985, A&A, 150, L21

Salaris M., 2005, Evolution of Stars and Stellar Populations. Chichester, West Sussex, England ; Hoboken, NJ, USA : J. Wiley

Salpeter E. E., 1955, ApJ, 121, 161

Sana H., et al., 2012, Science (New York, N.Y.), 337, 444

Sana H., et al., 2013, A&A, 550, A107

Santoliquido F., et al., 2020, ApJ, 898, 152

Santoliquido F., et al., 2021, MNRAS, 502, 4877

Scalo J. M., 1986, Fundamentals of Cosmic Physics, 11, 1

Schaye J., et al., 2015, MNRAS, 446, 521

Scherbak P., Fuller J., 2023, MNRAS, 518, 3966

Schlegel E. M., 1990, MNRAS, 244, 269

Schmidt M., 1959, ApJ, 129, 243

Schneider F. R. N., et al., 2015, ApJ, 805, 20

Schneider F. R. N., Podsiadlowski P., Laplace E., 2023, ApJ, 950, L9

Schönberg M., Chandrasekhar S., 1942, ApJ, 96, 161

Schootemeijer A., et al., 2018, A&A, 615, A30

Schulze S., et al., 2023, arXiv, 2305.05796

Schwab J., Quataert E., Kasen D., 2016, MNRAS, 463, 3461

Scott D. W., 1979, Biometrika, 66, 605

Sen K., et al., 2022, A&A, 659, A98

Sen K., et al., 2023, A&A, 672, A198

Shao Y., Li X.-D., 2021, ApJ, 920, 81

Shao Y., Li X.-D., 2022, ApJ, 930, 26

Shao D.-S., et al., 2020, Phys. Rev. D, 101

Shapiro S. L., Teukolsky S. A., 1983, Black Holes, White Dwarfs and Neutron Stars. The Physics of Compact Objects. A Wiley-Interscience Publication, Wiley, New York, doi:10.1002/9783527617661

Shaviv G., 2008, New Astron. Rev., 51, 803

Shen K. J., et al., 2012, ApJ, 748, 35

Shen R.-F., et al., 2015, MNRAS: Letters, 447, L60

Shenar T., et al., 2019, A&A, 627, A151

Shenar T., et al., 2022, Nature Astronomy, 6, 1085

Shikauchi M., et al., 2023, arXiv, 2301.07207

Shivvers I., et al., 2017, PASP, 129, 054201

Shu F. H., Lubow S. H., Anderson L., 1979, ApJ, 229, 223

Siegel J. C., et al., 2022, arXiv, 2209.06844

Siess L., 2006, A&A, 448, 717

Smartt S. J., 2015, PASA, 32, e016

Smartt S. J., et al., 2009, MNRAS, 395, 1409

Smith M. D., 2004, The Origin of Stars. Imperial College Press, London

Smith N., et al., 2011, MNRAS, 412, 1522

Smith K. W., et al., 2020, PASP, 132, 085002

Soberman G. E., Phinney E. S., van den Heuvel E. P. J., 1997, A&A, pp 620–635

Somerville R. S., Primack J. R., Faber S. M., 2001, MNRAS, 320, 504

Soria R., et al., 2012, ApJ, 750, 152

Soria R., et al., 2015, ApJ, 799, 140

Spera M., Mapelli M., 2017, MNRAS, 470, 4739

Spera M., Trani A. A., Mencagli M., 2022, Galaxies, 10, 76

Spergel D., et al., 2015, Technical report, Wide-Field InfrarRed Survey Telescope-Astrophysics Focused Telescope Assets WFIRST-AFTA 2015 Report. Science Definition Team of the Wide-Field Infrared Survey Telescope mission

Springel V., et al., 2001, MNRAS, 328, 726

Springel V., et al., 2005, Nature, 435, 629

Springel V., et al., 2018, MNRAS, 475, 676

Spruit H. C., 2002, A&A, 381, 923

Sravan N., et al., 2020, ApJ, 903, 70

Stanway E. R., Eldridge J. J., 2018, MNRAS, 479, 75

Stanway E. R., et al., 2018, MNRAS, 475, 1829

Stępień K., 2011, A&A, 531, A18

Stevance H. F., et al., 2023a, Nature Astronomy, 7, 444

Stevance H. F., et al., 2023b, MNRAS, 520, 4740

Stevenson S., et al., 2017, Nature Communications, 8, 14906

Stevenson S., et al., 2019, ApJ, 882, 121

Strolger L.-G., 2003, Thesis (Ph.D.), Univeristy of Michigan

Strolger L.-G., et al., 2015, ApJ, 813, 93

Strolger L.-G., et al., 2020, ApJ, 890, 140

Sun M., et al., 2021, ApJ, 908, 7

Takeo E., Inayoshi K., Mineshige S., 2020, MNRAS, 497, 302

Tang P. N., et al., 2020, MNRAS: Letters, 493, L6

Tang S.-P., et al., 2021, Physical Review D, 104, 063032

Tanvir N. R., et al., 2021, Exp. Astron., 52, 219

Tassoul J.-L., Tassoul M., 2004, A Concise History of Solar and Stellar Physics. Princeton University Press

Taubenberger S., 2017, The Extremes of Thermonuclear Supernovae. Springer International Publishing AG, doi:10.1007/978-3-319-21846-5_37

Tauris T. M., 1996, A&A, 315, 453

Tauris T. M., Savonije G. J., 1999, A&A, 350, 928

Tauris T. M., van den Heuvel E. P. J., 2006, Formation and Evolution of Compact Stellar X-ray Sources. Cambridge Astrophysics Series Vol. 39, Cambridge University Press, Cambridge, UK, doi:10.48550/arXiv.astro-ph/0303456

Tauris T. M., et al., 2017, ApJ, 846, 170

Taylor J. H., Weisberg J. M., 1982, ApJ, 253, 908

Taylor M., et al., 2014, ApJ, 792, 135

Tchekhovskoy A., McKinney J. C., Narayan R., 2012, Journal of Physics: Conference Series, 372, 012040

Temmink K. D., et al., 2023, A&A, 669, A45

Terreran G., et al., 2017, Nature Astronomy, 1, 713

Thiele S., et al., 2023, ApJ, 945, 162

Thomson W., 1862, The London, Edinburgh, and Dublin Philosophical Magazine and Journal of Science, 23, 158

Timmes F. X., Woosley S. E., Taam R. E., 1994, ApJ, 420, 348

Tonry J. L., et al., 2003, ApJ, 594, 1

Toonen S., Nelemans G., Portegies Zwart S., 2012, A&A, 546, A70

Toonen S., Voss R., Knigge C., 2014a, MNRAS, 441, 354

Toonen S., et al., 2014b, A&A, 562, A14

Toonen S., Hamers A., Portegies Zwart S., 2016, Comput. Astrophys., 3, 1

Toonen S., Perets H. B., Hamers A. S., 2018a, A&A, 610, A22

Toonen S., et al., 2018b, A&A, 619, A53

Toonen S., et al., 2020, A&A, 640, A16

Torrey P., et al., 2019, MNRAS, 484, 5587

Totani T., et al., 2008, PASJ, 60, 1327

Tutukov A. V., Yungelson L. R., 1981, Nauchnye Informatsii, 49, 3

Umeda H., et al., 1999, ApJ, 522, L43

Van Oeveren E. D., Friedman J. L., 2017, Phys. Rev. D, 95, 083014

Van Rensbergen W., Loore C. D., Jansen K., 2006, A&A, 446, 1071

Vanbeveren D., De Loore C., 1994, A&A, 290, 129

Vartanyan D., et al., 2021, ApJ, 916, L5

Vigna-Gómez A., et al., 2018, MNRAS, 481, 4009

Vinciguerra S., et al., 2020, MNRAS, 498, 4705

Vink J. S., 2022, ARA&A, 60, 203

Vink J. S., de Koter A., Lamers H. J. G. L. M., 2001, A&A, 369, 574

Walmswell J. J., Tout C. A., Eldridge J. J., 2015, MNRAS, 447, 2951

Wang B., Han Z., 2012, New Astron. Rev., 56, 122

Wang X., et al., 2021a, arXiv:2106.06690 [astro-ph]

Wang L., et al., 2021b, AJ, 161, 248

Wang C., et al., 2023, A&A, 670, A43

Ward-Thompson D., 2011, An Introduction to Star Formation. University Press, Cambridge

Webbink R. F., 1984, ApJ, 277, 355

Weinberger R., et al., 2017, MNRAS, 465, 3291

Wellstein S., Langer N., Braun H., 2001, A&A, 369, 939

Whelan J., Iben Jr. I., 1973, ApJ, 186, 1007

Wielgus M., et al., 2022, MNRAS, 514, 780

Wiersma R. P. C., et al., 2009, MNRAS, 399, 574

Wiktorowicz G., Belczynski K., Maccarone T. J., 2014, in Binary Systems, Their Evolution and Environments. Mongolia-Japan Centre, Ulaanbaatar, Mongolia, doi:10.48550/arXiv.1312.5924

Wiktorowicz G., et al., 2020, ApJ, 905, 134

Wilkins S. M., et al., 2016, MNRAS, 455, 659

Wilkins S. M., et al., 2018, MNRAS, 473, 5363

Wilkins S. M., Lovell C. C., Stanway E. R., 2019, MNRAS, 490, 5359

Willcox R., et al., 2021, ApJ, 920, L37

Wilson E. C., Nordhaus J., 2022, MNRAS, 516, 2189

Wongwathanarat A., Janka H.-T., Müller E., 2013, A&A, 552, A126

Woods T. E., Ivanova N., 2011, ApJ, 739, L48

Woods T. E., et al., 2012, ApJ, 744, 12

Woosley S. E., 2010, ApJ, 719, L204

Woosley S. E., 2017, ApJ, 836, 244

Woosley S. E., Heger A., 2021, ApJ, 912, L31

Woosley S. E., Weaver T. A., 1994, ApJ, 423, 371

Woosley S. E., Heger A., Weaver T. A., 2002, Rev. Mod. Phys., 74, 1015

Woosley S. E., Blinnikov S., Heger A., 2007, Nature, 450, 390

Wyrzykowski Ł., Mandel I., 2020, A&A, 636, A20

Yang Y., et al., 2019, Phys. Rev. Lett., 123, 181101

Yoon S.-C., 2015, PASA, 32, e015

Yoon S. C., Langer N., 2005, A&A, 443, 643

Yoon S.-C., Langer N., Norman C., 2006, A&A, 460, 199

Yoon S.-C., Woosley S. E., Langer N., 2010, ApJ, 725, 940

Yoon S. C., Dierks A., Langer N., 2012, A&A, 542, A113

Yoon S.-C., et al., 2022, IAU Symposium, 366, 39

Yoshida T., et al., 2016, MNRAS, 457, 351

Yoshioka S., et al., 2022, PASJ, 74, 1378

Yusof N., et al., 2010, in Proceedings of the 11th Symposium of Nuclei in the Cosmos. Heidelberg, Germany (arxiv:1012.3649), doi:10.48550/arXiv.1012.3649

Yusof N., et al., 2013, MNRAS, 433, 1114

Zahid H. J., et al., 2014, ApJ, 791, 130

Zampieri L., Roberts T. P., 2009, MNRAS, 400, 677

Zapartas E., et al., 2017, A&A, 601, A29

Zevin M., Bavera S. S., 2022, ApJ, 933, 86

Zevin M., et al., 2020, ApJ, 899, L1

Zevin M., et al., 2021, ApJ, 910, 152

Zhao W.-C., Xue X.-X., Cao X.-F., 2021, New Astronomy, 83, 101506

Zorotovic M., Schreiber M., 2022, MNRAS, 513, 3587

Zou Z.-C., Zhou X.-L., Huang Y.-F., 2020, Res. Astron. Astrophys., 20, 137

de Jager C., Nieuwenhuijzen H., van der Hucht K. A., 1988, A&A Supplement Series, 72, 259

de Mink S. E., Pols O. R., Hilditch R. W., 2007, A&A, 467, 1181

de Mink S. E., et al., 2013, ApJ, 764, 166

du Buisson L., et al., 2020, MNRAS, 499, 5941

van Rensbergen W., De Loore C., Vanbeveren D., 2005, in Interacting Binaries: Accretion, Evolution, and Outcomes.. AIP Conference Proceedings, eprint: arXiv:astro-ph/0410583, pp 301–306, doi:10.1063/1.2130247

van Son L. A. C., et al., 2020, ApJ, 897, 100

van Son L. A. C., et al., 2022, ApJ, 931, 17

van Son L. A. C., et al., 2023, ApJ, 948, 105

van Zeist W. G. J., 2018, BSc(Hons), University of Auckland, Auckland

van de Voort F., et al., 2022, MNRAS, 512, 5258